

AN ANALYSIS AND MODULATION OF  
RE-CIRCULATION ZONE BEHIND A  
SUBMERGED SQUARE OBSTRUCTION  
IN AN OPEN CHANNEL TURBULENT  
FLOW

*Manas Kumar Bhukta*

---



AN ANALYSIS AND MODULATION OF  
RE-CIRCULATION ZONE BEHIND A  
SUBMERGED SQUARE OBSTRUCTION  
IN AN OPEN CHANNEL  
TURBULENT FLOW

*Thesis submitted by*

MANAS KUMAR BHUKTA

Doctor of Philosophy  
(Engineering)

DEPARTMENT OF MECHANICAL ENGINEERING  
FACULTY COUNCIL OF ENGINEERING & TECHNOLOGY  
JADAVPUR UNIVERSITY  
KOLKATA, INDIA  
2025



**JADAVPUR UNIVERSITY**  
**KOLKATA-700032, INDIA**

**INDEX No. 256/18/E**

**1. Title of the Thesis:**

AN ANALYSIS AND MODULATION OF RE-CIRCULATION ZONE  
BEHIND A SUBMERGED SQUARE OBSTRUCTION IN AN OPEN CHAN-  
NEL TURBULENT FLOW

**2. Name, Designation & Institution of the Supervisor(s):**

Dr. Snehamoy Majumder  
Professor, Department of Mechanical Engineering,  
Jadavpur University, Kolkata-700032

**3. List of Publications:**

- (a) **Bhukta, M.K.**, Singh, S.K., Debnath, K., and Majumder, S., "Modulation of recirculation zone behind a cubical obstruction by the vertically placed turbulent multijets in the form of shower," in *International Journal of Fluid Mechanics Research*, 2022, DOI: 10.1615/InterJFluidMechRes.2023046305. [**ESCI, Scopus**]
- (b) **Bhukta, M.K.**, Singh, S.K., Majumder, S., and Debnath, K., "Modulation of re-circulation zones behind a square obstruction by blower-induced suction force" in *Journal of the Brazilian Society of Mechanical Sciences*, 2024, DOI: 10.1007/s40430-024-04976-x [**SCIE, Scopus**]
- (c) **Bhukta, M.K.**, Singh, S.K., Majumder, S., and Debnath, K., "Modulation of re-circulation zone behind a square obstruction by single inclined turbulent wall jet with varying angle of attack" in *Engineering Research Express*, 2024, <https://doi.org/10.1088/2631-8695/ad6af3>. [**ESCI, Scopus**]

**4. List of Patents: Nil**

---

5. **List of Presentations in National/International Conferences:**

- (a) **Bhukta, M.K.**, Singh, S.K., Debnath, K., and Majumder, S., "Modulation of re-circulation zone behind a square obstruction by single inclined turbulent wall jet with varying angle of attack" 2nd International Conference on Energy Resources and Technologies for Sustainable Development (**ICERTSD 2023**), organized by the Department of Mechanical Engineering IEST, Shibpur

6. **List of Book Chapters:** Nil

**Candidate:**

---

(Manas Kumar Bhukta)

**Supervisor:**

---

(Dr. Snehamoy Majumder)

**JADAVPUR UNIVERSITY  
FACULTY OF ENGINEERING AND TECHNOLOGY**

**STATEMENT OF ORIGINALITY**

I, **MANAS KUMAR BHUKTA**, registered on 04<sup>th</sup> **MAY 2018**, do hereby declare that this thesis entitled "**AN ANALYSIS AND MODULATION OF RE-CIRCULATION ZONE BEHIND A SUBMERGED SQUARE OBSTRUCTION IN AN OPEN CHANNEL TURBULENT FLOW**" contains literature survey and original research work done by the undersigned candidate as part of the Doctoral studies.

All information in this thesis has been obtained and presented in accordance with existing academic rules and ethical conduct. I declare that, as required by these rules and conduct, I have fully cited and referred all materials and results that are not original to this work.

I also declare that I have checked this thesis as per the "**Policy of Anti-Plagiarism, Jadavpur University, 2019**", and the level of similarity as checked by iThenticate software is **8%**.

**Signature of the candidate:**

\_\_\_\_\_  
(Manas Kumar Bhukta)

**Date:**

**Certified by Supervisor(s):**

(Signature with Date, Seal)

1. \_\_\_\_\_  
(Dr. Snehamoy Majumder)



**JADAVPUR UNIVERSITY  
FACULTY OF ENGINEERING AND TECHNOLOGY**

**CERTIFICATE FROM THE SUPERVISOR**

This is to certify that the thesis entitled “**AN ANALYSIS AND MODULATION OF RE-CIRCULATION ZONE BEHIND A SUBMERGED SQUARE OBSTRUCTION IN AN OPEN CHANNEL TURBULENT FLOW**” submitted by Sri **MANAS KUMAR BHUKTA**, who got his name registered on 04.05.2018 for the award of Ph.D. (Engineering) degree of Jadavpur University, is absolutely based upon his own work under the supervision of **Dr. SNEHAMOY MAJUMDER** and that neither his thesis nor any part of the thesis has been submitted for any degree/diploma or any other academic award anywhere before.

---

**(Dr. Snehamoy Majumder)**

Signature of the Supervisor and  
date with Official Seal



# Acknowledgment

---

---

I take the opportunity to express my sincere gratitude and indebtedness to my project guide, **Prof. Snehamoy Majumder** Department of Mechanical Engineering of, Jadavpur University, Kolkata-700032 for his resourceful guidance, constant encouragement, and enlightening discussions during this research work without which it would not have been possible for me to reach to this point. It is my privilege of great pleasure to convey my gratitude to my beloved sir **Dr. Koustuv Debnath** Department of Aerospace Engineering and Applied Mechanics of, Indian Institute of Engineering Science and Technology, Shibpur, Howrah-711103, **Dr. Santosh Kumar Singh** Department of Mechanical Engineering, SRM Institute of Science and Technology, Kattankulathur-603203 and **Dr. Supriyo Roy** Department of Mechanical Engineering, Haldia Institute of Technology, Haldia-721657 for their immense dedication towards my work, co-operations and supports for the continuation and completion of my project.

My deepest appreciation goes to my family for their unconditional love, encouragement, and understanding throughout this challenging process. Their unwavering support, patience, and belief in my abilities have been the cornerstone of my success. I am truly grateful for their sacrifices and constant motivation.

Finally, I would like to express my heartfelt gratitude to all the participants who volunteered their time and expertise for this study. This work would not have been possible without their willingness to contribute to my research.

In conclusion, I extend my sincere appreciation to all those mentioned above, as well as anyone else who has been involved in my academic journey, directly or indirectly. Your support and contributions have played a pivotal role in completing this thesis, and I am forever grateful.

Thank you all.

MANAS KUMAR BHUKTA



# Abstract

---

---

The thesis titled “An Analysis and Modulation of the Re-circulation Zone behind a Submerged Square Obstruction in an Open Channel Turbulent Flow” presents a comprehensive numerical study aimed at mitigating the re-circulation zone formed behind a submerged square obstruction in an open channel flow. The re-circulation zone, which typically forms in the wake of such obstructions, is characterized by flow separation, turbulence, and significant pressure drops. These phenomena can lead to flow-induced vibrations, which can adversely affect structures such as rectangular buildings or other submerged obstacles.

The study’s primary goal is to explore and develop effective methods for modulating or eradicating this re-circulation zone using plane turbulent jets, multi-jet configurations, and suction forces. The research is grounded in computational fluid dynamics (*CFD*) simulations using the two-phase Volume of Fluid (*VOF*) model with open channel boundary conditions. The turbulent flow is simulated using the standard  $k - \epsilon$  two-equation turbulence model, which solves the Reynolds-averaged Navier-Stokes (*RANS*) equations to capture the complex flow dynamics. In order to modulate the recirculation region several control techniques such as use of plane turbulent dual jet of three different Reynolds numbers, use of multi-jets in the form of showers and the use of suction force are adopted. The numerical model contains open channel flow with a square obstruction on the bottom surface of the channel within the fully developed region.

The presence of the re-circulation zone, indicated by negative stream-wise velocities, results in the generation of large-scale vortices and adverse pressure gradients. These vortices lead to vortex-induced vibrations (*VIV*), flow-induced vibrations (*FIV*), and wake-induced vibrations (*WIV*), which are detrimental to structural integrity. The thesis focuses on employing several control techniques to mitigate these effects, including the use of dual-plane jets at various Reynolds numbers, showers of jets distributed over the surface, and suction forces applied

---

near the wake region. Through a systematic investigation of these control strategies, the research demonstrates that varying jet velocities, the variation of the Jet-spread length ( $l$ ), and configurations can effectively modulate the re-circulation zone. The numerical simulations show that increasing the Reynolds number of the jet can significantly reduce or reallocate the re-circulation region. Additionally, the study explores the effects of different jet discharge velocities and spread lengths on the wake, revealing that these parameters have a direct impact on the size and intensity of the re-circulation zone.

A key finding of the research is the correlation between the jet's Reynolds number and the pressure distribution in the wake. As the jet velocity increases, the pressure drop behind the square obstruction diminishes, leading to an improved pressure recovery. This reduces the adverse pressure gradient and consequently mitigates the formation of large vortices. The study also finds that the turbulent kinetic energy ( $TKE$ ) and turbulent dissipation rate ( $TDR$ ) are closely linked to the modulation of the re-circulation zone. Controlling these turbulent properties can minimize flow-induced vibrations, leading to more stable flow conditions.

The practical implications of this research are significant, particularly in engineering applications where flow-induced vibrations pose a risk to structural stability. The modulation techniques studied in this thesis can be applied to optimize the design of hydraulic structures, improve the flow around buildings and bridges, and enhance environmental fluid dynamics in natural water bodies. By effectively controlling the recirculation zones in these scenarios, the study provides a pathway to reduce energy losses, enhance structural performance, and minimize environmental impacts.

**Keywords:** Open Channel, Square Obstruction, Re-circulation, Reynolds Number, Turbulent Kinetic Energy ( $TKE$ ),

*Dedicated to My Parents*

*Guide*

*My PC*

*And My Beloved Wife*



# Contents

---

---

<b>Certificate by the Supervisor</b>	<b>ix</b>
<b>Acknowledgement</b>	<b>ix</b>
<b>Abstract</b>	<b>xi</b>
<b>1 Introduction</b>	<b>1</b>
1.1 Motivation . . . . .	4
1.2 Background . . . . .	5
1.3 Research Issues . . . . .	7
1.4 Research Objectives . . . . .	8
1.5 Contributions . . . . .	10
1.6 Thesis Organization . . . . .	11
<b>2 Ch 2: open channel flow</b>	<b>13</b>
2.1 Introduction . . . . .	13
2.2 Uniform & non-uniform open channel flow . . . . .	14
2.3 The Reynolds averaged Navier-Stokes modeling . . . . .	14
2.4 Reynolds stress distribution in open channel . . . . .	16
2.5 Different types of flow layers . . . . .	17
2.6 Velocity distribution . . . . .	19
2.6.1 Linear-law in viscous sub-layer . . . . .	19
2.6.2 Logarithmic-law in turbulent outer-layer . . . . .	21
2.7 Flow characteristics . . . . .	22
2.8 Viscous model . . . . .	24
2.8.1 Turbulence model . . . . .	24

<b>3</b>	<b>Ch 3: Turbulent Jet</b>	<b>31</b>
3.1	Plane turbulent free jet . . . . .	33
3.1.1	Equation of motion . . . . .	33
<b>4</b>	<b>Ch 4: Numerical Methodology</b>	<b>39</b>
4.1	Turbulence Model . . . . .	39
4.2	Standard $k - \epsilon$ model . . . . .	39
4.2.1	Transport equations for standard $k - \epsilon$ model . . . . .	40
<b>5</b>	<b>Ch 5: Square Duct Flow with Suction Panel</b>	<b>43</b>
5.1	Problem definition . . . . .	43
5.1.1	Boundary conditions . . . . .	44
5.2	Mathematical Formulation . . . . .	45
5.3	Free Surface Equation . . . . .	48
5.4	Numerical Procedure . . . . .	48
5.5	Grid Independent Test . . . . .	50
5.6	Validation of Velocity Profile with Log Law . . . . .	52
5.7	Validation with Experimental Results . . . . .	53
5.8	Result and Discussion . . . . .	54
5.8.1	Variation of Vertical Normalized Mean-Velocity( $U = u/u_*$ ) Component along x-Direction . . . . .	54
5.8.2	Variation of Vertical Normalized Mean-Velocity( $V = v/u_*$ ) Component along y-Direction . . . . .	57
5.8.3	Contour Pattern of Velocity . . . . .	57
5.8.4	Streamline Plot of the Flow Structure . . . . .	59
5.8.5	Contour plot of static pressure . . . . .	61
5.8.6	Contour Plot of Turbulent Kinetic Energy . . . . .	62
5.8.7	Contour Plot of Turbulent Dissipation Rate ( $\epsilon$ ) . . . . .	64
5.9	Conclusion . . . . .	66
<b>6</b>	<b>Ch 6: Wake Zone Modulation via Suction</b>	<b>69</b>
6.1	Formulation of the problem . . . . .	70
6.1.1	Boundary conditions . . . . .	70
6.1.2	Governing Equations . . . . .	72
6.1.3	Grid independence test . . . . .	73
6.2	Results and Discussion . . . . .	76
6.2.1	Verification of the velocity profile using the log-law principle . . . . .	76
6.2.2	Validation with the experimental results . . . . .	76

## CONTENTS

---

6.2.3	Variation of normalized mean velocity along $x$ -direction . . .	78
6.2.4	Variation of normalized mean velocity along $y$ -direction . . .	80
6.2.5	Contour plot of normalized mean velocity along $x$ -direction .	83
6.2.6	Representation of Streamlines of the flow pattern. . . . .	84
6.2.7	Instantaneous Vorticity Contours . . . . .	85
6.2.8	Time series of velocity components . . . . .	86
6.2.9	Vorticity spectra analysis . . . . .	87
6.2.10	Static pressure contour . . . . .	88
6.2.11	Contours of Turbulent Kinetic Energy ( $TKE$ ) . . . . .	90
6.3	Conclusion . . . . .	91
<b>7</b>	<b>Ch 7: Modulation of Wake by Inclined Wall Jet</b>	<b>95</b>
7.1	Formulation of the problem . . . . .	96
7.1.1	Boundary Conditions . . . . .	97
7.1.2	Turbulence model . . . . .	97
7.1.3	Governing Equation . . . . .	99
7.1.4	Free surface equation . . . . .	100
7.1.5	Grid Independence Test . . . . .	100
7.1.6	Variation of $y^+$ values . . . . .	101
7.2	Result and Discussion . . . . .	102
7.2.1	Validation of velocity profile against log-law . . . . .	102
7.2.2	Validation with the experimental results . . . . .	103
7.2.3	Velocity profile . . . . .	105
7.2.4	Streamline plot of the flow structure . . . . .	106
7.2.5	Pressure Contour Plot . . . . .	107
7.2.6	Variation of turbulent kinetic energy ( $TKE$ ) . . . . .	107
7.2.7	Contours of Turbulent Kinetic Energy ( $TKE$ ) . . . . .	109
7.2.8	Instantaneous vorticity variation . . . . .	110
7.2.9	Spectral analysis of vorticity magnitude . . . . .	111
7.3	Conclusion . . . . .	113
<b>8</b>	<b>Ch 8: Wake Control by Dual Wall Jets</b>	<b>115</b>
8.1	Formulation of the problem . . . . .	116
8.1.1	Boundary and initial conditions . . . . .	117
8.1.2	Governing Equations . . . . .	119
8.1.3	Free surface equation . . . . .	121
8.1.4	Grid independence test . . . . .	121

8.1.5	Numerical procedure . . . . .	123
8.2	Results and Discussion . . . . .	124
8.2.1	Validation of velocity profile with log-law . . . . .	124
8.2.2	Validation with the experimental results . . . . .	125
8.2.3	Variation of Vertical Normalized Mean-Velocity ( $\hat{U}$ ) Com- ponent along x-Direction . . . . .	126
8.2.4	Contour plot of velocity variation . . . . .	128
8.2.5	Streamline plot of the flow structure . . . . .	129
8.2.6	Instantaneous vorticity variation . . . . .	131
8.2.7	Vorticity spectra analysis . . . . .	131
8.2.8	Variation of pressure . . . . .	132
8.2.9	Variation of turbulent kinetic energy ( $TKE$ ) . . . . .	133
8.2.10	The $TKE$ contour plots . . . . .	135
8.2.11	Variation of Turbulent dissipation rate ( $TDR$ ) ( $\epsilon$ ) . . . . .	136
8.2.12	The $TDR$ contour plots . . . . .	137
8.3	Conclusion . . . . .	138
 <b>A Appendix</b>		 <b>141</b>
A.0.1	General . . . . .	141
A.0.2	Components of fluent . . . . .	142
A.0.3	Programing capabilities . . . . .	143
A.0.4	Upstream boundary condition . . . . .	146
A.0.5	Downstream boundary condition . . . . .	147
References . . . . .		149

# List of Abbreviations

---

---

VOF	Volume of Fluid
PSD	Power Spectral Density
PhD	Doctor of Philosophy
TKE	Turbulent Kinetic Energy
ASCETC	American Society of Civil Engineers Task Committee
CFD	Computational Fluid Dynamics
SIMPLE	Semi-Implicit Method for Pressure Linked Equations
QUICK	Quadratic Upstream Interpolation for Convective Kinematics
PDE	Partial Differential Equation
SST	Shear Stress Transport
PISO	Pressure-Implicit with Splitting of Operators
MRF	Multiple Reference Frame
ADV	Acoustic Doppler Velocimeter
LDV	Laser Doppler Velocimeter
PIV	Particle Image Velocimeter
FIV	Flow Induced Vibration
VIV	Vortex-Induced Vibration
RANS	Reynolds-averaged Navier–Stokes Equations
GCI	Grid Convergence Index
SWF	Standard Wall Function
AOA	Angle of Attack



# List of Figures

---

---

2.1	Shear stress components and distribution (Adopted from J Southard, 2006 [1]) . . . . .	17
2.2	Classification of flow region (layer thickness not to scale)(Adopted from J Southard, 2006 [1]) . . . . .	18
2.3	(a) Hydraulically smooth flow, (b) Hydraulically rough flow. . . . .	19
2.4	Velocity profile of uniform smooth open channel flow(Adopted from Alawadi, W. A. A. K et. al. 2019[2]) . . . . .	20
2.5	Velocity profiles in different flow layers . . . . .	20
2.6	Time series of $u$ . . . . .	22
3.1	Different examples of turbulent jets(Adopted from P. Koumoutsakos, et. al., 1999[3]) . . . . .	32
3.2	Definition sketch of Turbulent Jet(Adapted from A. Assouidi et. al., 2019[4]) . . . . .	32
3.3	Schematic of a plane turbulent free jet showing jet regions, velocity profiles, and coordinate system (adapted from Abdel-Rahman, A. 2010[5]) . . . . .	33
5.1	Schematic diagram of the computational setup with boundary conditions . . . . .	44
5.2	Normalized streamwise velocity plot for different grid elements . . . . .	51
5.3	Schematic of the simulation domain with mesh . . . . .	51
5.4	Validation with the Log-Law . . . . .	52
5.5	Validation of the Normalised x-velocity $U = u/u_*$ at different positions relative to the obstruction . . . . .	54
5.6	Variation of mean velocity along x-direction for without jet and with jet for a constant Reynolds number ( $Re = 70,000$ ) against the normalized vertical distance from the bed . . . . .	56

---

**LIST OF FIGURES**

5.7	Variation of mean velocity along y-direction for without jet and with jet for a constant Reynolds number ( $Re = 70,000$ ) against the normalized vertical distance from the bed . . . . .	58
5.8	Contour plot of stream-wise vertical depth average velocity $U$ in 2D against normalized horizontal distance along bed ( $x/d$ ) and the normalized vertical distance from the bed ( $y/h$ ) . . . . .	60
5.9	Streamline plot of stream-wise vertical depth average velocity ( $U$ ) in 2D against normalized horizontal distance along bed ( $x/d$ ) and the normalized vertical distance from the bed ( $y/h$ ) . . . . .	61
5.10	Contour plot of stream-wise static pressure ( $P$ ) in 2D against normalized horizontal distance along bed ( $x/d$ ) and the normalized vertical distance from the bed ( $y/h$ ) . . . . .	63
5.11	Contour plot of stream-wise turbulent kinetic energy ( $K$ ) profile in 2D against normalized horizontal distance along bed ( $x/d$ ) and the normalized vertical distance from the bed ( $y/h$ ) . . . . .	65
5.12	Contour plot of stream-wise vertical turbulent dissipation rate ( $\epsilon$ ) profile in 2D against normalized horizontal distance along bed ( $x/d$ ) and the normalized vertical distance from the bed ( $y/h$ ) . . . . .	67
6.1	The diagrams of computational configuration with boundary conditions. . . . .	71
6.2	Stream-wise normalized velocity profile plot for three different grid elements . . . . .	75
6.3	Diagram of the simulation domain featuring a mesh (Grid-3( $1848 \times 52$ )) . . . . .	75
6.4	Verification of the numerical model through comparison with the standard logarithmic law of wall . . . . .	77
6.5	Validation of normalized mean-velocity along x-direction ( $u/u_*$ ), along y-direction ( $v/u_*$ ) and normalized turbulent kinetic energy ( $k/(u_*^2)$ ) with experimental results (adopted from Singh and Deb-nath 2016) at various normalized locations relative to the square obstruction. . . . .	79
6.6	Representation of mean velocity along x- direction ( $u/u_*$ ) for bed without and with suction against $y/h$ from the bed. . . . .	81
6.7	Representation of mean velocity along y- direction ( $v/u_*$ ) for bed without and with suction against $y/h$ from the bed. . . . .	82

## LIST OF FIGURES

---

6.8	Representation of mean velocity along y- direction ( $v/u_*$ ) for bed without and with suction against $y/h$ from the bed. . . . .	84
6.9	Stream-line plot of normalized mean velocity ( $u/u_*$ ) depth for without and with suction. . . . .	85
6.10	Instantaneous vorticity contours for (a) $t = 1s$ , (b) $t = 8s$ , (c) $t = 16s$ and (d) $t = 20s$ . . . . .	86
6.11	Time series analysis of stream-wise ( $u$ ) and transverse ( $v$ ) velocity component . . . . .	87
6.12	Power spectral density of vorticity magnitude (a). Without suction, (b). With suction $l = 0.05$ , $u_i = 0.35, 0.70, 10.5$ m/s, (c). With suction $l = 0.10$ , $u_i = 0.35, 0.70, 10.5$ m/s and (d). With suction $l = 0.15$ , $u_i = 0.35, 0.70, 10.5$ m/s . . . . .	89
6.13	Contours of stream wise pressure ( $\hat{p}$ ) against non-dimensionlized abscissa along bed ( $x/d$ ) and the non-dimensionlized ordinate from bed ( $y/h$ ) . . . . .	90
6.14	Contour plot of stream wise Turbulent Kinetic Energy ( $\hat{k}$ ) against normalized horizontal distance along bed ( $x/d$ ) and the normalized vertical distance from the bed ( $y/h$ ). . . . .	92
7.1	Schematic diagram of the computational set-up with boundary conditions With varying Angle of Attack ( $\Phi_j = 45^0, 67.5^0, \text{ and } 90^0$ ). . .	97
7.2	Normalized velocity profile plot for three different grids. . . . .	102
7.3	Schematic of the simulation domain with mesh. . . . .	102
7.4	Wall $y^+$ for Grid-3 along x-direction . . . . .	103
7.5	Validation of $VOF$ model against the law of wall . . . . .	103
7.6	Validation of non-dimensionalized mean-velocity along x-direction( $\hat{u}$ ),non-dimensionalized mean-velocity along y-direction ( $\hat{v}$ ) with experimental results . . . . .	105
7.7	Stream wise vertical velocity $\hat{U}$ profile along x- direction for a constant Reynolds number ( $Re = 60000$ ) of main flow with jet having three different angles of attacks . . . . .	106
7.8	Stream line plot of streamwise vertical velocity $\hat{U}$ (a) without jet, (b) Flow with jet velocities $\hat{U}_i = 25^0$ and $AOA 45^0$ (c) Flow with jet velocities $\hat{U}_i = 25^0$ and $AOA 67.5^0$ (d). Flow with jet velocities $\hat{U}_i = 25^0$ and $AOA 90^0$ . . . . .	107

**LIST OF FIGURES**

7.9	Contour plot of streamwise static pressure $\hat{P}$ (a) without jet, (b) Flow with jet velocities $\hat{U}_i = 25^0$ and $AOA 45^0$ (c) Flow with jet velocities $\hat{U}_i = 25^0$ and $AOA 67.5^0$ (d). Flow with jet velocities $\hat{U}_i = 25^0$ and $AOA 90^0$ . . . . .	108
7.10	Stream wise plot of $TKE \hat{K}$ (a) without jet, (b) Flow with jet velocities $\hat{U}_i = 25^0$ and $AOA 45^0$ (c) Flow with jet velocities $\hat{U}_i = 25^0$ and $AOA 67.5^0$ (d). Flow with jet velocities $\hat{U}_i = 25^0$ and $AOA 90^0$ . . . . .	109
7.11	Contour plot of streamwise static turbulent kinetic energy $\hat{K}$ (a) without jet, (b) Flow with jet velocities $\hat{U}_i = 25$ and $AOA = 45^0$ (c) Flow with jet velocities $\hat{U}_i = 25$ and $AOA = 67.5^0$ (d). Flow with jet velocities $\hat{U}_i = 25$ and $AOA = 90^0$ . . . . .	111
7.12	Instantaneous vorticity (a) without jet, (b) Flow with jet velocities $\hat{U}_i = 25$ and $AOA = 45^0$ (c) Flow with jet velocities $\hat{U}_i = 25$ and $AOA = 67.5^0$ (d). Flow with jet velocities $\hat{U}_i = 25$ and $AOA = 90^0$	112
7.13	Power spectral density of vorticity magnitude (a) without jet, (b) Flow with jet velocities $\hat{U}_i = 25$ and $AOA = 45^0$ (c) Flow with jet velocities $\hat{U}_i = 25$ and $AOA = 67.5^0$ (d). Flow with jet velocities $\hat{U}_i = 25$ and $AOA = 90^0$ . . . . .	113
8.1	Schematic diagram of the computational set-up with boundary conditions . . . . .	117
8.2	Schematic of the jet behavior in the flow field . . . . .	118
8.3	Stream-wise normalized velocity profile plot for three different grid elements . . . . .	122
8.4	Schematic of the simulation domain with mesh (Grid-3(2257 $\times$ 54))	123
8.5	Validation of $VOF$ model against log law . . . . .	125
8.6	Validation of normalised mean-velocity along x-direction ( $u/u_*$ ), along y-direction ( $v/u_*$ ) and normalised turbulent kinetic energy ( $k/(u_*^2)$ ) with experimental results (from Singh and Debnath 2016) at different normalized locations relative to the square obstruction. . . . .	127
8.7	Normalized stream wise mean velocity $\hat{U}$ profile against $y/h$ for with and without jet. . . . .	128
8.8	Contour plot of stream wise vertical velocity ( $\hat{U}$ ) (a). without jet (b). Flow with dual jet velocities $\hat{U}_i = 25$ and $\hat{U}_j = 12.5$ (c). Flow with dual jet velocities $\hat{U}_i = 50$ and $\hat{U}_j = 25$ and (d). Flow with dual jet velocities $\hat{U}_i = 75$ and $\hat{U}_j = 37.5$ . . . . .	129

## LIST OF FIGURES

---

8.9	Stream line plot of stream wise vertical velocity ( $\hat{U}$ ) (a). without jet (b). Flow with dual jet velocities $\hat{U}_i = 25$ and $\hat{U}_j = 12.5$ (c). Flow with dual jet velocities $\hat{U}_i = 50$ and $\hat{U}_j = 25$ and (d). Flow with dual jet velocities $\hat{U}_i = 75$ and $\hat{U}_j = 37.5$ . . . . .	130
8.10	Instantaneous vorticity (a). without jet (b). Flow with dual jet velocities $\hat{U}_i = 25$ and $\hat{U}_j = 12.5$ (c). Flow with dual jet velocities $\hat{U}_i = 50$ and $\hat{U}_j = 25$ and (d). Flow with dual jet velocities $\hat{U}_i = 75$ and $\hat{U}_j = 37.5$ . . . . .	132
8.11	Power spectral density of vorticity magnitude (a). without jet (b). Flow with dual jet velocities $\hat{U}_i = 25$ and $\hat{U}_j = 12.5$ (c). Flow with dual jet velocities $\hat{U}_i = 50$ and $\hat{U}_j = 25$ and (d). Flow with dual jet velocities $\hat{U}_i = 75$ and $\hat{U}_j = 37.5$ . . . . .	133
8.12	Contour plot of stream wise static pressure ( $\hat{P}$ ) (a). without jet (b). Flow with dual jet velocities $\hat{U}_i = 25$ and $\hat{U}_j = 12.5$ (c). Flow with dual jet velocities $\hat{U}_i = 50$ and $\hat{U}_j = 25$ and (d). Flow with dual jet velocities $\hat{U}_i = 75$ and $\hat{U}_j = 37.5$ . . . . .	134
8.13	Contour plot of stream wise static pressure ( $\hat{P}$ ) (a). without jet (b). Flow with dual jet velocities $\hat{U}_i = 25$ and $\hat{U}_j = 12.5$ (c). Flow with dual jet velocities $\hat{U}_i = 50$ and $\hat{U}_j = 25$ and (d). Flow with dual jet velocities $\hat{U}_i = 75$ and $\hat{U}_j = 37.5$ . . . . .	135
8.14	Contour plot of stream wise Turbulent Kinetic Energy ( $\hat{K}$ ) (a). Plane bed without jet (b). Flow with dual jet velocities $\hat{U}_i = 25$ and $\hat{U}_j = 12.5$ (c). Flow with dual jet velocities $\hat{U}_i = 50$ and $\hat{U}_j = 25$ and (d). Flow with dual jet velocities $\hat{U}_i = 75$ and $\hat{U}_j = 37.5$ . . . . .	136
8.15	Stream wise vertical Turbulent Dissipation Rate ( $\hat{\epsilon}$ ) profile along x-direction for with and without jet. . . . .	137
8.16	Contour plot of stream wise Turbulent Dissipation Rate ( $\hat{\epsilon}$ ) (a). without jet (b). Flow with dual jet velocities $\hat{U}_i = 25$ and $\hat{U}_j = 12.5$ (c). Flow with dual jet velocities $\hat{U}_i = 50$ and $\hat{U}_j = 25$ and (d). Flow with dual jet velocities $\hat{U}_i = 75$ and $\hat{U}_j = 37.5$ . . . . .	138
A.1	Some elements of FLUENT uses . . . . .	142
A.2	Basic program structure of <i>FLUENT</i> . . . . .	143
A.3	Duct flow defining parameters . . . . .	145



# List of Tables

---

---

5.1	specification of the Channel . . . . .	45
5.2	Hydrodynamic parameters of open channel without jet . . . . .	45
5.3	Hydrodynamic parameters for open channel with jets . . . . .	46
6.1	specification of the Channel . . . . .	71
6.2	Hydrodynamic parameters for open channel without suction . . . . .	72
6.3	Hydrodynamic parameters for open channel with suction . . . . .	72
6.4	Grid convergence index test for grid density refinement . . . . .	74
7.1	specification of the Channel with hydraulic parameters . . . . .	97
7.2	solution domain with required boundary conditions . . . . .	99
7.3	Grid convergence index test for grid density refinement . . . . .	101
8.1	The modeled channel specification . . . . .	117
8.2	Hydrodynamic parameters for plane bed open channel . . . . .	119
8.3	Hydrodynamic parameters for open channel with jet . . . . .	119
8.4	Grid convergence index test for grid density refinement . . . . .	123



## Introduction

Research on turbulence is challenging but incredibly fascinating because the field is largely unexplored and contains many unsolved problems. The highly irregular, random, and fluctuating flow is called turbulent flow. In this work, we have modeled the problem based on the open channel flow by placing a cube at the fully developed region. The problem is confined to the numerical investigation over a cube mounted on the bed of an open channel with the addition of a plane turbulent jet. There are many practical applications based on such investigations in many areas of science and engineering like in several industrial and environmental processes. The most important applications come from the area of aeronautics design, the study of flow around buildings and obstacles, heating, cooling, ventilation, and environmental fluid dynamics. Though the cube is very simple in geometry, the flow around a cube succumbs to complexity which includes various flow separation and reattachment regions [6]. The presence of the square obstruction leads to complex flow patterns in the wake region, including flow separation, re-circulation, and reattachment zones. The obstruction also increases turbulence intensities, turbulent kinetic energy, and dissipation rate. In the wake region, behind the cube flow is dominated by large-scale flow structure and generation of vortex, such as horse-shoe vortices, which wrap around the cube [7]. The generation of vortex sheddings is a common phenomenon due to the occurrence of significant pressure drop in the

wake region which is very detrimental to the object (obstruction) as they cause unwanted vibrations whose effect is significant to the object. This vortex shedding is the cause of the formation of flow-induced-vibration (*FIV*) followed by vortex-induced vibration (*VIV*), wake-induced vibration (*WIV*), galloping, etc. [8, 9, 10]. Many researchers conducted several experiments to identify the flow structures in the re-circulation zones and their extent in the wake. The investigation and analysis of complex flow structures around submersed three-dimensional (3D) bluff bodies have been facilitated with the advent of recent powerful computers, numerical algorithms solution techniques (large eddy simulation) [11, 12, 13] and experimental techniques using Acoustic Doppler Velocimeter (*ADV*), Laser Doppler Velocimeter (*LDV*), and Particle Image Velocimeter (*PIV*) [14, 15]. All of these investigations primarily focused on analyzing the flow patterns around various geometrical shapes of obstructions, identifying re-circulation zones, flow separation, reattachment, vortex structures, and their impacts. It is worth mentioning that only a limited number of researchers have explored the modulation of the re-circulation zone behind surface-mounted obstructions using control measures. Many control measures were employed to manage the situation, including the utilization of magnetic forces [16, 17, 18], the usage of particles with varying diameters [19], the implementation of moving surface boundary-layer control [20], the deployment of jets with different impingement velocities [21], the exploration of different jet orientations such as longitudinal horizontal [22] and lateral horizontal [23]. Also, use of electrohydrodynamic actuators to control the near wake region is investigated by Artana et al. [24]. They reported that the flow regimen is analyzed with the systematic increase of the Reynolds number. Arcas and Chen et al. [25, 26] employed steady suction and blowing techniques as additional methods to investigate the fundamental mitigation of vortex-induced vibration (*VIV*). Additionally, synthetic jet control strategies were utilized to alleviate *VIV* [27, 28]. Hannemann and Oertel (1989) [29] used the bed-bleeding technology to control the same purpose. Beyond the basic and well-documented information on turbulence found in major books and publications, there is an extensive amount of research and specific studies on this topic, especially concerning the control of re-circulation in the wake and the structure of turbulent flow, in both laboratory and environmentally relevant conditions. This thesis will discuss a broad spectrum of specific

---

publications, including experimental and technical measurement techniques, as well as classical jet and plume theory. The most important step was Forthmann (1936) [30] who first carried out an experimental investigation of the flow field of a plane turbulent wall jet. Later Glauert (1956) [31] performed a theoretical analysis of radial and plane wall jets in the laminar and turbulent flow regimes and made a comparison with the experimental data. Self-preservation of jets within the range of experimental and that of the decay of the maximum velocity had been investigated by Bakke (1957) [32] by his experimental investigation on plane wall jets. He found the spread over of the jet within the limit which followed the simple power law ( $U_{max} \propto X^{-0.5}$  and  $Y_{0.5} \propto X$ ). Schneider (1984) [33] investigated the decay of momentum flux in submerged jets. He separately made his experiments on turbulent jet (plane and axisymmetric) and the laminar plane jet. He analyzed the axial velocity in the turbulent (plane and axisymmetric) jets which decreased more quickly than foretold classical boundary layer solutions. He also investigated the momentum flux which becomes zero since the distance from the nozzle tends to infinity whereas in the case of the laminar jet, he found little effect in the change of momentum flux. Liepmann and Ghacubes (1992) [34], in their paper investigated the role of structures in the near-field entrainment of round jets. The generation of stream-wise vorticity in the free shear layers of the braid region between primary vertical structures plays a role in the near-field entrainment process, resulting in a higher rate of fluid being entrained into the jet. With the downstream flow evolved the efficiency of the streamwise vorticity increased relative to that of the azimuthal vorticity. They identified with the aid of flow visualization techniques the process of entrainment controlled by the streamwise vorticity beyond the end of the potential core of the regime. Craft and Launder (1999) [35] investigated the behavior of a three-dimensional turbulent wall jet using various turbulence closure levels. Their goal was to understand the reasons behind the exceptionally high lateral spreading rates observed in experiments. Their calculations confirmed that this strong lateral spreading is due to the creation of stream-wise vorticity, rather than anisotropic diffusion. The source of this driving vorticity is the anisotropy of the Reynolds stresses in the plane perpendicular to the jet axis, not the bending of mean vortex lines. Given that the three-dimensional wall jet is highly sensitive to turbulence models, it would be beneficial to establish definitive experimental

or possibly simulation results for the fully developed flow.

Numerical study of turbulent wall jet over multiple- inclined flat surface had been investigated by Das and Pramanik (2014) [36]. Using a proper boundary-fitted coordinate system, they numerically solved the *RANS* equations for incompressible flow in a transformed geometry. Their objective was to study how three different inlet conditions—uniform, parabolic, and trapezoidal velocity profiles—affect the mean flow and turbulence characteristics of a jet flowing tangentially along multiple inclined solid walls.

## 1.1 Motivation

This study aims to eliminate the re-circulation zone formed behind a fully submerged square obstruction in open channel flow and assess the turbulent characteristics at high Reynolds numbers. The presence of this re-circulation zone can lead to undesired vibrations on the square obstruction, such as rectangular-shaped buildings and that may cause detrimental effects on the objects. This is the sought-after drawback of the study that should be minimized or eliminated to get the objects rid of these adverse effects.

To achieve this, various control techniques are employed, including the use of plane turbulent dual jets with different Reynolds numbers, multi-jets in the form of showers, and the application of suction forces. The numerical model simulates an open channel flow with a square obstruction on the channel's bottom surface within the fully developed region.

The specialty of this research stride is the continuation of the prolonged gap found in terms of the turbulent control techniques to control the re-circulation of the wake. To achieve this the soft-influenced technology of using jets or creating a vacuum in the wake in the form of showers by allowing through a series of small openings into the main flow domain without hampering the main flow structure too much. The practical alliance of this study demands the significance of the potential to optimize engineering design, control flow patterns, enhance system efficiency, ensure structural integrity, and minimize adverse environmental impacts. By effectively modulating the re-circulation zone behind a submerged square obstruction using different turbulent controlling forces, engineers can achieve improved per-

## 1.2 Background

---

formance, safety, and sustainability in a range of practical applications.

The re-circulation zone is recognized by the negative average stream-wise velocity, and the streamline contour charts are created to illustrate the re-circulation flow patterns. The study includes different control methods such as varying the jet discharge velocity and the jet-spread length ( $l$ ) to properly modulate the re-circulation region, either by reallocating or eliminating it. The simulation results demonstrate a gradual modulation of the re-circulation region with variations in these parameters.

Additionally, the study observes a significant pressure drop behind the square obstruction, resulting in an adverse pressure gradient within the wake region. The static pressure increases as the jet Reynolds number rises, and it approaches zero when the jet discharge velocity equals the mainstream flow velocity. Furthermore, the turbulent kinetic energy, turbulent intensity, and turbulent dissipation rate are analyzed.

In summary, this numerical study focuses on the modulation of the re-circulation region behind a fully submerged square obstruction in open channel flow. By employing various control techniques, the study aims to eliminate or redistribute the re-circulation zone. The results provide insights into the flow behavior, pressure distribution, and turbulent characteristics associated with these control methods.

## 1.2 Background

Flow patterns around submerged obstructions in open channels have been the subject of extensive research due to their significant implications in various engineering and environmental applications. In particular, the presence of a square obstruction in an open channel flow creates a re-circulation zone, characterized by reversed or stagnant flow, vortices, and adverse pressure gradients. This re-circulation zone can lead to adverse effects such as unwanted vibrations, increased drag forces, and structural integrity concerns. Thus, understanding and controlling the re-circulation zone behind submerged square obstructions are of great importance.

Previous studies have focused on investigating the characteristics and behavior of re-circulation zones. These studies have shed light on the formation, size, shape,

and stability of re-circulation zones under different flow conditions and obstruction geometries.

Many researchers in their works have analyzed the influence of various factors like flow velocity, obstruction size, flow depth, and behavior of the re-circulation zone. However, research specifically focusing on the modulation of the re-circulation zone using different turbulent controlling forces remains relatively limited.

The techniques of turbulent flow control offer the potential to modulate the re-circulation zone behind submerged square obstructions. Most of the techniques involved the use of external forces to exploit the flow patterns and disrupt the re-circulation zone. Previous researches investigated the techniques such as jets, vortex generators, and passive control mechanisms in changing the flow behavior and reducing the consequent effects associated with re-circulation zones. However, there is a need for further clarification of the optimal configuration and application of these turbulent controlling forces for achieving proper modulation.

The objective of this thesis work is to investigate the modulation of the re-circulation zone behind a submerged square obstruction by employing different turbulent controlling forces. The study will primarily depend on numerical simulations to analyze the behavior and characteristics of the re-circulation zone under various controlling force scenarios. Additionally, experimental investigations may be conducted to validate the numerical findings and provide real-world data for further analysis.

The outcomes of this research have practical importance for engineering design optimization, flow control strategies, system efficiency improvement, and structural integrity enhancement. Understanding and effectively modulating the re-circulation zone can lead to improved performance, reduced energy losses, enhanced safety, and minimized adverse environmental impacts in a range of applications such as river dams, coastal structures, and heat exchangers.

In summary, this thesis work aims to address the research gap concerning the modulation of the re-circulation zone behind a submerged square obstruction using different turbulent controlling forces. By exploring and analyzing the behavior and characteristics of the re-circulation zone, this research will contribute to the practical understanding and application of turbulent flow control techniques in various engineering and environmental contexts.

### 1.3 Research Issues

This research work will contribute to advancing the knowledge and practical application of modulating the re-circulation zone behind a submerged square obstruction using different turbulent controlling forces. By investigating the underlying mechanisms, optimizing control parameters, considering practical implementation, validating findings, and assessing environmental implications, this research aims to provide valuable insights and solutions for efficient and sustainable re-circulation zone modulation in various engineering and environmental contexts. Despite this, some issues can't be ignored.

- **Lack of Comprehensive Understanding:** One of the research issues in this thesis work is the lack of a comprehensive understanding of the modulation of the re-circulation zone behind a submerged square obstruction using different turbulent controlling forces. While previous studies have explored aspects such as the behavior of re-circulation zones and the influence of various factors, there is still a need for a deeper understanding of the
- **Optimization of Turbulent Controlling Forces:** Another research issue is the optimization of turbulent controlling forces for efficient re-circulation zone modulation. While previous research has investigated techniques such as jets, vortex generators, and passive control mechanisms, there is a need to explore the optimal configuration and application of these forces to achieve desired outcomes. Identifying the most effective combination of parameters, such as jet discharge velocity, jet-spread length, or vortex generator size, is crucial for the successful modulation of the re-circulation zone.
- **Practical Implementation and Engineering Design:** A research issue lies in the practical implementation and engineering design aspects of re-circulation zone modulation. Understanding how to translate the research findings into practical guidelines and recommendations for engineering design optimization is important. Exploring the applicability of different control techniques in real-world scenarios, such as river dams, coastal structures, and heat exchangers, requires further investigation to ensure the practical significance and feasibility of the proposed modulation strategies.

- **Validation and Real-World Data:** Validating the numerical simulations and experimental findings with real-world data is a research issue in this thesis work. While numerical simulations provide insights into the behavior of the re-circulation zone, experimental investigations are crucial for validation and providing reliable data. There is a need for comprehensive experimental studies to verify the numerical results and enhance the understanding of the actual flow behavior and characteristics during re-circulation zone modulation.
- **Environmental Considerations:** Considering the environmental impact is an important research issue in this thesis work. Exploring the effects of re-circulation zone modulation on sediment transport, water quality, and ecological systems is necessary to ensure sustainable engineering practices. Investigating the potential environmental implications of different control techniques and their long-term effects will contribute to a comprehensive assessment of re-circulation zone modulation strategies.

### 1.4 Research Objectives

This thesis objectives can be listed as follows:

- **Understand Flow Control Mechanisms:** Explore the effectiveness of suction as a flow control mechanism to manipulate re-circulation zones and reduce flow-induced vibrations. The objective is to assess how suction forces can alter flow structures and improve the stability of fluid flow around obstacles.
- **Modulation of the Re-circulation Zone:** The primary objective is to modulate the re-circulation zone behind the bed-mounted square obstruction using jet inputs to achieve pressure recovery and control unwanted vortex-induced vibrations.
- **Investigate the Influence of Suction Parameters:** The primary objective is to study how different control techniques including varying suction velocities, suction-panel lengths, and jet velocities impact flow patterns around

## 1.4 Research Objectives

---

square obstacles. This involves analyzing changes in velocity profiles, pressure distributions, and turbulence characteristics in the re-circulation zone.

- **Analyze Numerical Simulation Results:** Utilize computational fluid dynamics simulations to investigate the impact of suction and jet on flow behavior and validate the numerical results with experimental data. The objective is to compare simulation outcomes with physical observations to enhance the understanding of flow dynamics.
- **Optimize Design Parameters:** Evaluate the influence of suction-panel length, variation of suction, jet-spread distance and jet velocities, and orientation on flow patterns to optimize the design of flow control mechanisms. The objective is to determine the most effective configuration of suction parameters for minimizing re-circulation effects and enhancing flow efficiency.
- **Explore Practical Applications:** Investigate the practical implications of using suction or using jets for flow control in engineering applications. The objective is to identify potential benefits of implementing suction-based flow control strategies, such as reducing vibrations, improving performance, and enhancing fluid flow management in real-world scenarios.
- **Assessment of Energy Transfer Mechanisms:** To investigate the energy transfer mechanisms, turbulence structures, and flow stability in the presence of obstacles and jet-induced disturbances.
- **Optimization of Flow Control Strategies:** To provide insights for optimizing flow control strategies, enhancing pressure recovery, and minimizing adverse effects of turbulence and re-circulation zones in practical flow scenarios.
- **Contribute Insights to Flow Control Research:** Provide valuable insights into the role of suction in controlling flow patterns around obstacles and managing re-circulation zones. The objective is to contribute to the advancement of flow control research by offering new perspectives on optimizing flow behavior through suction mechanisms.

## 1.5 Contributions

1. **Novel Flow Control Strategy:** The thesis introduces a novel flow control strategy involving the modulation of the re-circulation zone behind a cubical obstruction using jet-induced turbulence. This innovative approach offers a promising method for achieving pressure recovery and minimizing adverse flow effects.
2. **Insights into Turbulence Dynamics:** By analyzing the turbulent properties, including turbulent kinetic energy distribution, turbulence intensity, and dissipation rates, the thesis provides valuable insights into the complex turbulence dynamics near obstacles in open channel flows under the influence of jet inputs.
3. **Optimization of Jet Parameters:** The study systematically evaluates the effects of jet parameters, such as jet-spread distance and jet velocity, on pressure recovery and turbulence characteristics. The findings contribute to optimizing jet configurations for enhanced flow control and improved flow stability.
4. **Enhanced Understanding of Energy Transfer Mechanisms:** Through the assessment of energy transfer mechanisms and turbulence structures in the presence of obstacles and jet-induced disturbances, the thesis enhances the understanding of energy dissipation processes and their impact on flow behavior in complex flow scenarios.
5. **Practical Implications for Flow Control:** The research outcomes offer practical implications for optimizing flow control strategies in real-world applications. The insights gained from the study can be applied to improve the efficiency, stability, and performance of flow systems subjected to challenging flow conditions.
6. **Contribution to Academic Knowledge:** The thesis contributes to the academic knowledge base by advancing the understanding of flow behavior around obstacles in open channel flows and providing valuable data on the

## 1.6 Thesis Organization

---

effects of jet-induced turbulence on flow characteristics. The research findings can serve as a foundation for further studies in the field of flow control and turbulence dynamics.

## 1.6 Thesis Organization

### Introduction

- Background and Motivation
- Research Objectives
- Thesis Outline

### Literature Review

- Overview of Flow Control Techniques
- Previous Studies on Suction Effects
- Relevance of Suction in Flow Control

### Methodology

- Computational Fluid Dynamics (CFD) Simulation Setup
- Description of the Flow Domain and Boundary Conditions
- Suction Panel Design and Parameters
- Numerical Methods and Models Used

### Experimental Validation

- Comparison of Simulation Results with Experimental Data
- Validation of Suction Effects on Flow Patterns
- Analysis of Flow Characteristics in the Re-circulation Zone

### Results and Discussion

- Impact of Suction Parameters on Flow Behavior
- Changes in Velocity Profiles and Pressure Distributions
- Analysis of Turbulence Characteristics with Suction

### **Optimization of Suction Design**

- Influence of Suction Panel Length and Velocities
- Optimization of Suction Parameters for Flow Control
- Design Guidelines for Efficient Flow Manipulation

### **Practical Implications**

- Application of Suction in Engineering Scenarios
- Benefits of Suction-Based Flow Control Strategies
- Case Studies and Practical Implementations

### **Conclusion**

- Summary of Key Findings
- Contributions to Flow Control Research
- Future Research Directions

### **References**

# OPEN CHANNEL FLOW

## 2.1 Introduction

Open channel flow refers to the movement of fluid in a channel that is not completely filled, resulting in a free surface between the flowing fluid, typically water, and the air above it. The primary driving force for this type of flow is gravity. Most open-channel flow relationships have been derived from small-scale laboratory models under conditions of uniform flow. Extensive research has been focused on open channel flow and its turbulence characteristics. The flow in open channels can be classified in various ways, such as developing, fully developed, uniform, non-uniform, laminar, or turbulent. The presence of a free surface allows the fluid to naturally adjust its configuration. This study focuses on uniform and non-uniform open channel flows, which are significant types to consider. An open channel flow is classified as uniform if the depth of flow ( $h$ ) remains constant along the channel, and as non-uniform if the depth changes along the channel. Additionally, depending on different conditions and the Reynolds number, open channel flow can be laminar, transitional, or turbulent.

## 2.2 Uniform & non-uniform open channel flow

Uniform flow is characterized by constant velocity and depth over a given distance. In contrast, non-uniform flow exhibits variations in both velocity and depth due to changes in the channel's cross-section. Consequently, uniform flow conditions are uncommon in both natural and artificial channels, as they require a constant cross-section, roughness, and slope in the flow direction. Non-uniform flow, on the other hand, can occur in channels with variable geometrical properties, whether man-made or natural. A pressure gradient is the primary cause of non-uniformity, exerting a significant influence on the flow. While moderate non-uniform open channel flows do exist, they are often approximated as uniform flows for simplicity. In river systems, the bed slope can cause variations in depth and velocity from upstream to downstream, resulting in a water surface that is not parallel to the bed. If the channel's cross-sectional area decreases downstream, the flow accelerates, creating a positive velocity gradient  $\frac{dU_e}{dX}$  and a negative pressure gradient. Conversely, if the channel's cross-sectional area increases, the flow decelerates, leading to negative velocity gradients and positive pressure gradients. According to Bernoulli's equation, pressure  $p(x)$  is mathematically linked to the free stream velocity  $U(x)$

$$\frac{dp}{dx} = -\rho U \frac{dU}{dx} \quad (2.1)$$

An accelerating flow, indicated by  $(\frac{dU}{dx} > 0)$ , corresponds to a negative or favorable pressure gradient. Conversely, a decelerating flow, where  $(\frac{dU}{dx} < 0)$ , results in a positive or adverse pressure gradient, which can cause the boundary layer to separate from the surface. In the case where  $(\frac{dU}{dx} = 0)$ , the flow is uniform, and there is no pressure gradient.

## 2.3 The Reynolds averaged Navier-Stokes modeling

To analyze the flow structure in an open channel, the governing equations used are the Continuity equation and the Reynolds-averaged Navier-Stokes (RANS) equations, which can be written in tensor notation as follows:

### 2.3 The Reynolds averaged Navier-Stokes modeling

---

**Continuity Equation:**

$$\frac{\partial \bar{u}_i}{\partial x_i} = 0 \quad (2.2)$$

**Reynolds-Averaged Navier-Stokes Equation:**

$$\frac{\partial \bar{u}_i}{\partial t} + \frac{\partial}{\partial x_j} (\bar{u}_j \bar{u}_i) = -\frac{1}{\rho} \frac{\partial \bar{p}}{\partial x_i} + \nu \frac{\partial^2 \bar{u}_i}{\partial x_j^2} - \frac{\partial}{\partial x_j} (\overline{u'_i u'_j}) \quad (2.3)$$

where the Reynolds averaged quantity is denoted by an over bar. Here,  $\bar{u}_i$  and  $u'_i$  represent the mean and fluctuating velocities in the  $x_i$  direction, respectively where  $i = 1, 2$ . This corresponds to the stream-wise  $x$  and vertical  $z$  directions; such that  $x_i = (x, z) \in x$ ;  $u_i = (u, w)$ ;  $\bar{u}_i = (\bar{u}, \bar{w}) \in (u, w)$ . Additionally,  $\nu$  denotes kinematic viscosity and  $p$  represents the kinematic pressure. When the Navier-Stokes is used as a time-averaged Navier-Stokes equation, it results in unknown correlations between the fluctuating velocities, known as Reynolds stresses. These stresses are represented by the tensor  $(\overline{u'_i u'_j})$ . Physically these correlations, multiplied by density ( $\rho$ ), i.e.  $\overline{\rho u'_i u'_j}$ , represent the transport of momentum in specific directions.

To solve for the mean values of velocity, pressure, and other quantities using equations such as Eq. 2.2 and Eq. 2.3, it is necessary to relate these turbulent correlations to mean velocity or pressure. This challenge is known as the closure problem in turbulence modeling. The resulting terms from three cross products of velocity fluctuations introduce additional stresses due to turbulence. These stresses are termed turbulent shear stresses or Reynolds stresses and can be expressed as a stress tensor called the Reynolds stress tensor.

$$\begin{bmatrix} \sigma'_x & \tau'_{xy} & \tau'_{xz} \\ \tau'_{yx} & \sigma'_y & \tau'_{yz} \\ \tau'_{zx} & \tau'_{zy} & \sigma'_z \end{bmatrix} = -\rho \begin{bmatrix} \overline{u'^2} & \overline{u'v'} & \overline{u'w'} \\ \overline{v'u'} & \overline{v'^2} & \overline{v'w'} \\ \overline{w'u'} & \overline{w'v'} & \overline{w'^2} \end{bmatrix} \quad (2.4)$$

In turbulent flow,  $\sigma'_x, \sigma'_y$ , and  $\sigma'_z$  represent normal stresses, while the remaining terms correspond to shear stresses. These additional stresses, known as apparent or virtual stresses, are specifically referred to as Reynolds stresses. Because they contribute to the overall stress like ordinary viscous stresses in laminar flow, they are often termed eddy viscosity. Typically, in turbulent flow, Reynolds stresses

are significantly greater than viscous stresses.

## 2.4 Reynolds stress distribution in open channel

For a steady flow with no pressure gradient in the stream-wise ( $x$ ) direction, the fundamental equations to consider are the continuity equation and the two components of the Reynolds equations. The continuity equation is inherently satisfied in this scenario. The  $z$ -component of the Reynolds equation (2.3) yields an expression for the Reynolds stress  $-\overline{\rho w' w'}$ . Meanwhile, the  $x$ -component of the Reynolds equation (2.3) simplifies to

$$\frac{\partial \bar{u}}{\partial t} + \bar{u} \frac{\partial \bar{u}}{\partial x} + \bar{w} \frac{\partial \bar{u}}{\partial z} = g_x - \frac{1}{\rho} \frac{\partial \bar{p}}{\partial x} + \nu \left( \frac{\partial^2 \bar{u}}{\partial x^2} + \frac{\partial^2 \bar{u}}{\partial z^2} \right) - \left( \frac{\partial \overline{u' u'}}{\partial x} + \frac{\partial \overline{u' w'}}{\partial z} \right) \quad (2.5)$$

As  $\frac{\partial \bar{u}}{\partial t} = 0$ ,  $\bar{w} = 0$ ,  $g_x = -g \sin \theta$  and  $\frac{\partial \bar{p}}{\partial x} = 0$ ,  $\bar{u}$  is a function of  $z$  only, where,  $g$  = gravitational acceleration and  $\theta$  = stream wise bed slope. Also,  $\frac{\partial \bar{u}}{\partial x} = 0$  for uniform flow. Therefore, Eq.2.5 becomes

$$\mu \frac{d^2 \bar{u}}{dz^2} + \frac{d(-\overline{\rho u' w'})}{dz} = -\rho g \sin \theta = -\rho g \frac{dh}{dx} \quad (2.6)$$

Where  $\mu$  = dynamic viscosity of fluid i.e.  $\rho \nu$  and  $h$  = flow depth. Eq. 2.6 can be written as

$$\frac{d}{dz} \left[ \mu \frac{d\bar{u}}{dz} + (-\overline{\rho u' w'}) \right] = -\frac{\tau_0}{h} \quad (2.7)$$

Where  $\tau_0$  = bed shear stress i.e.  $\rho g h \left( \frac{dh}{dx} \right)$ . The terms inside the parenthesis in LHS of Eq. 2.7 are expressed as

$$\mu \frac{d\bar{u}}{dz} + (-\overline{\rho u' w'}) = \tau_v + \tau_t = \tau \quad (2.8)$$

Where  $\tau_v$  = shear stress due to viscosity, i.e.  $\mu \frac{d\bar{u}}{dz}$ ;  $\tau_t$  = shear stress due to turbulence or Reynolds stress, i.e.  $(-\overline{\rho u' w'})$  and  $\tau$  = total shear stress. Therefore, Eq. 2.7 becomes

$$\frac{d\tau}{dz} = -\frac{\tau_0}{h} \quad (2.9)$$

## 2.5 Different types of flow layers

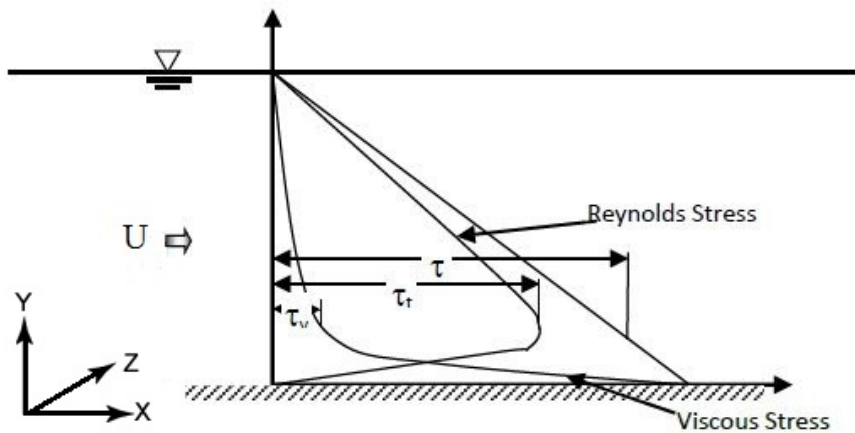


Figure 2.1: Shear stress components and distribution (Adopted from J Southard, 2006 [1])

Integrating Eq. 2.9 yields,

$$\tau = [1 - (z/h)]\tau_0 \quad (2.10)$$

## 2.5 Different types of flow layers

The flow of fluid over a solid boundary can be divided into several distinct layers, as illustrated in Fig. 2.2:

- **Viscous Sub-Layer:** This is an extremely thin layer located directly next to the boundary. The flow within this sub-layer is fully laminar, with no turbulence present.
- **Transition Layer or Buffer Layer:** This intermediate layer exhibits both viscous and turbulent effects, showing a combination of laminar and turbulent characteristics.
- **Turbulent Logarithmic Layer:** In this region, the effects of viscous shear stress are minimal, and the shear stress is predominantly due to turbulence.
- **Turbulent Outer Layer:** This layer, which constitutes about 80% to 90%

of the flow region, is characterized by nearly constant velocities and significant mixing due to large eddies.

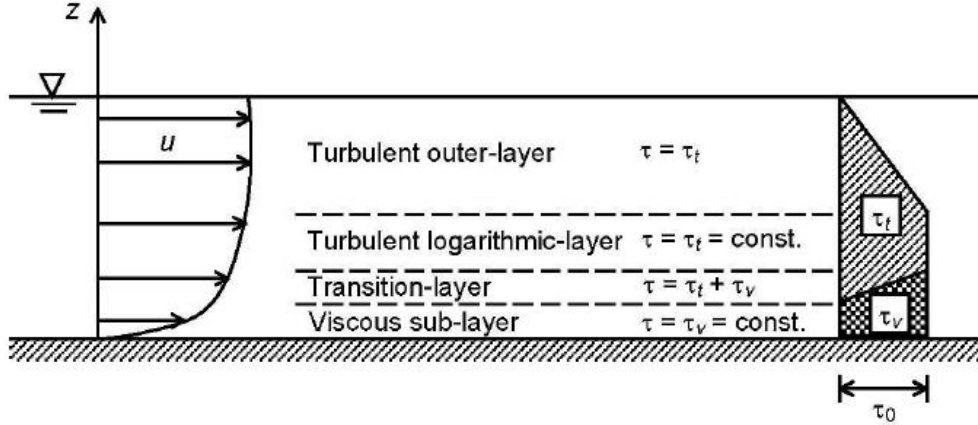


Figure 2.2: Classification of flow region (layer thickness not to scale)(Adopted from J Southard, 2006 [1])

The logarithmic velocity profile, modified using Prandtl's mixing-length concept, applies to both the buffer and outer layers. Comparisons between measured and computed velocities generally show good agreement. However, in the viscous sub-layers, boundary roughness significantly influences the velocity distribution. This effect was first explored by Nikuradse [37], who introduced the concept of equivalent roughness ( $\epsilon$ ), now known as Nikuradse's equivalent roughness. Based on Nikuradse's experimental data, flow conditions can be categorized as follows:

1. **Hydraulically smooth flow ( $Re_* \leq 5$ ):** In this regime, the bed roughness is much smaller than the thickness of the viscous sub-layer  $\delta_v$ , so it does not impact the velocity distribution.
2. **Hydraulically rough flow ( $Re_* \geq 70$ ):** Here, the bed roughness is sufficiently large to create eddies near the boundary, eliminating the viscous sub-layer.
3. **Hydraulically transitional flow ( $5 < Re_* < 70$ ):** In this intermediate regime, the velocity distribution is influenced by both bed roughness and viscosity. The particle Reynolds number  $Re_*$  is defined as  $u_*\epsilon/\nu$ , where  $u_*$

## 2.6 Velocity distribution

is shear velocity, given by  $(\tau_b/\rho)^{0.5}$ , and  $\tau_b$  represents the bed shear stress. Figure. 2.2 illustrates how bed roughness affects the flow regions.

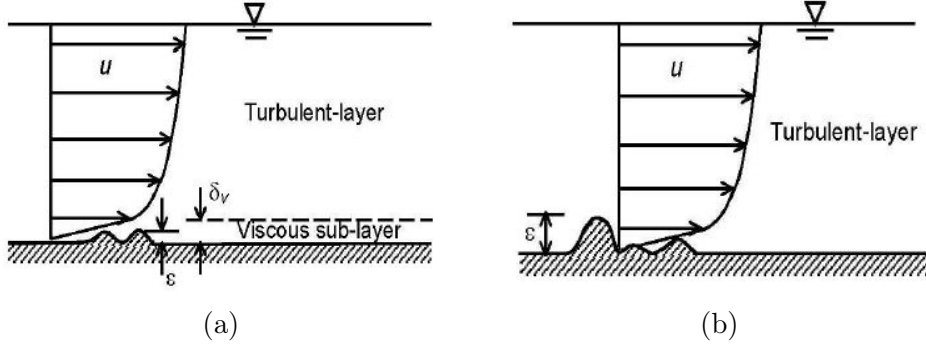


Figure 2.3: (a) Hydraulically smooth flow, (b) Hydraulically rough flow.

## 2.6 Velocity distribution

The flow zone over a boundary can be divided into two distinct layers: the inner layer and the outer layer. The inner layer, where turbulence is directly influenced by the bed roughness, includes the viscous sub-layer and the buffer layer. In contrast, the outer layer, where bed roughness impacts the flow indirectly, is further divided into the turbulent logarithmic layer and the turbulent outer layer. Figure 2.4 illustrates the velocity profiles in the vertical direction, while Fig. 2.5 outlines the various layers over a smooth boundary. The velocity distributions within these layers are detailed in the subsequent subsections.

### 2.6.1 Linear-law in viscous sub-layer

In the case of smooth boundary, the viscous shear stress ( $\tau_v$ ) is constant and equal to the bed shear stress ( $\tau_0$ ) i.e.

$$\tau_v = \rho\nu \frac{d\bar{u}}{dz} = \tau_0 \quad (2.11)$$

$$d\bar{u} = \frac{u_*^2}{\nu} dz \quad (2.12)$$

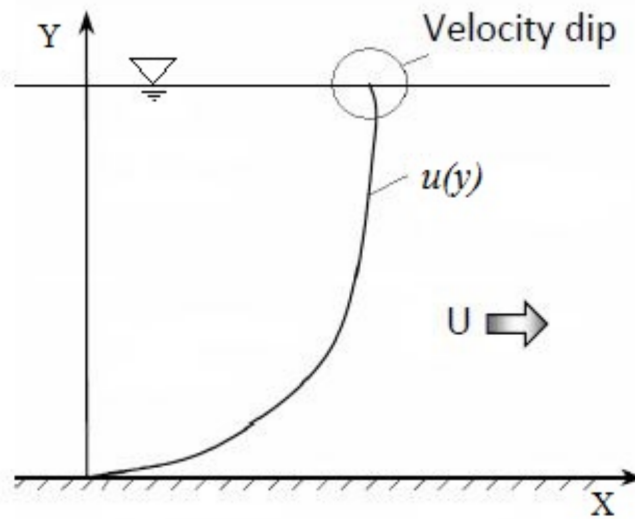


Figure 2.4: Velocity profile of uniform smooth open channel flow(Adopted from Alawadi, W. A. A. K et. al. 2019[2])

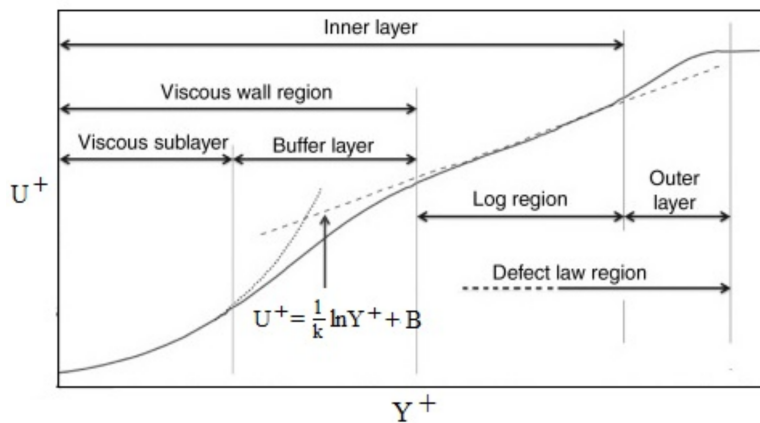


Figure 2.5: Velocity profiles in different flow layers

By integration and using no-slip condition at the boundary, i.e.  $u|_{z=0} = 0$ , results

$$u^+ = u_* z / \nu \quad (2.13)$$

Where  $u^+ = \frac{\bar{u}}{u_*}$ . Therefore, there is a linear velocity distribution in the viscous sub-layer as shown in Fig. 2.5 and Eq. 2.13 is valid within the range  $0 < u_* z / \nu \leq 5$ .

## 2.6 Velocity distribution

---

### 2.6.2 Logarithmic-law in turbulent outer-layer

In the turbulent outer layer, total shear stress  $\tau$  is the same as the turbulent shear stress ( $\tau_t$ ). According to Prandtl's mixing length theory.

$$\tau_t = \rho l^2 \left( \frac{d\bar{u}}{dz} \right)^2 \quad (2.14)$$

Putting  $l = Kz$ , gives

$$d\bar{u} = \frac{u_*}{Kz} dz \quad (2.15)$$

By integrating Eq. 2.15, the logarithmic velocity distribution can be written as

$$\frac{\bar{u}}{u_*} = \frac{1}{k} \ln \left( \frac{yu^*}{\nu} \right) + A \quad (2.16)$$

Using the boundary condition  $u = u_0$  and  $z = z_0$  i.e. zero velocity level gives

$$u^* = \frac{1}{k} \ln \frac{z}{z_0} \quad (2.17)$$

$$z_0 = 0.11 \frac{\nu}{u_*} \quad \text{for smooth flow} \quad Re_* \leq 5 \quad (2.18)$$

$$z_0 = 0.33\epsilon \quad \text{for rough flow} \quad Re_* \geq 70 \quad (2.19)$$

$$z_0 = 0.11 \frac{\nu}{u_*} + 0.33\epsilon \quad \text{for transition flow} \quad 5 < Re_* \leq 70 \quad (2.20)$$

In a report by The American Society of Civil Engineers Task Committee (*AS-CETC*) in 1963 found open channels with roughness comparable to that found in pipes, the resistance equations used for pipe flows are suitable. For flow over a smooth boundary, like a plane bed surface with a median grain size smaller than 0.25 mm, we can use Eq. 2.18 in Eq. 2.17 to obtain the relevant results.

$$u^+ = \frac{1}{k} \ln z^+ + Br \quad (2.21)$$

Where  $z^+ = z/\epsilon$ ;  $Br$  = constant of integration, i.e.  $-(1/k) \ln z_0^+$  and  $z^+ = z_0/\epsilon$ .

## 2.7 Flow characteristics

Fluid flow is generally classified into laminar flow and turbulent flow. Laminar flow occurs at relatively low velocities and is characterized by layers of fluid sliding smoothly over one another with varying velocities, without significant mixing or exchange of fluid particles perpendicular to the flow direction. As the flow velocity increases, the flow pattern changes dramatically, losing its stability and forming eddies that spread throughout the flow region. This highly irregular, random, and fluctuating flow is known as turbulent flow. A defining feature of turbulent flow is that the velocity and pressure at a fixed point in space do not remain constant over time but exhibit very irregular, high-frequency fluctuations. Generally, flows in rivers and streams are turbulent.

In the study of turbulent flow, hydrodynamic quantities are often described by separating the time-averaged values from their fluctuations or eddies. This method of breaking down an instantaneous hydrodynamic value is referred to as Reynolds decomposition. In the Cartesian coordinate system  $(x, y, z)$ , let the

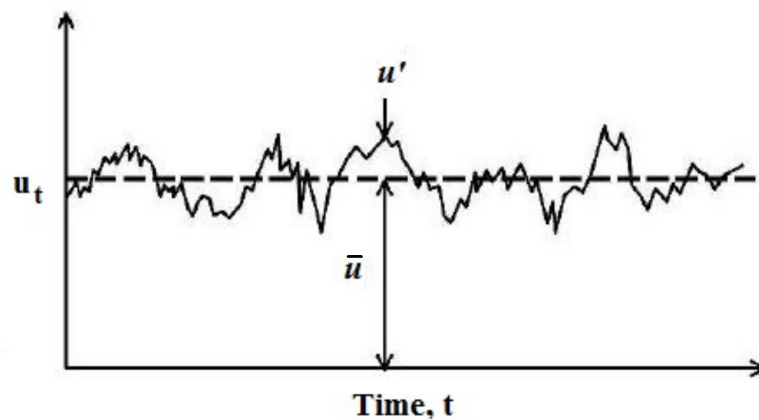


Figure 2.6: Time series of  $u$

time-averaged velocity components be denoted as  $\bar{u}, \bar{v}, \bar{w}$ , and their fluctuations as  $u', v', w'$ . Additionally, let  $\bar{p}$  and  $p'$  represent the time-averaged pressure and pressure fluctuations, respectively. Thus, the instantaneous velocity components

## 2.7 Flow characteristics

---

$(u, v, w)$  and the instantaneous pressure  $p$  are written as:

$$u = \bar{u} + u', \quad v = \bar{v} + v', \quad w = \bar{w} + w', \quad p = \bar{p} + p' \quad (2.22)$$

The time-averaged value of a hydrodynamic quantity, say  $\bar{u}$  is given by

$$\bar{u} = \frac{1}{t_1} \int_{t_0}^{t_0+t_1} u \, dt \quad (2.23)$$

$t_0$  is any arbitrary time and  $t_1$  is the period over which the average is calculated. The time  $t_1$  is chosen to be sufficiently long to obtain time-independent quantities. Mean values are taken over a long interval to ensure they are completely independent of time. Consequently, the time averages of all fluctuation quantities are zero i.e.

$$\overline{u'} = 0, \quad \overline{v'} = 0, \quad \overline{w'} = 0, \quad \overline{p'} = 0 \quad (2.24)$$

For the turbulent motion, the fluctuations  $(u', v', w')$  influence the mean motion  $(\bar{u}, \bar{v}, \bar{w})$  in that fashion, that the later exhibits an apparent increase in the resistance to deformation, which is called as Reynolds stresses or turbulent stresses.

The following relationships are known as the Reynolds conditions (Note: Bar denotes time-averaging), written with two quantities, say F and G

$$\overline{F + G} = \bar{F} + \bar{G} \quad (2.25)$$

$$\overline{constant \times F} = constant \times \bar{F} \quad (2.26)$$

$$\overline{constant} = constant \quad (2.27)$$

$$\frac{\partial \bar{F}}{\partial s_1} = \frac{\partial \bar{F}}{\partial s_1} \quad (2.28)$$

$$\overline{\bar{F} \cdot \bar{G}} = \bar{F} \cdot \bar{G} \quad (2.29)$$

$$\overline{\bar{F}} = \bar{F} \quad (2.30)$$

$$\overline{F \cdot G'} = \bar{F} \cdot \bar{G}' \quad \text{only if } F = \bar{F} \text{ (i.e., F is a mean quantity)} \quad (2.31)$$

Where  $s_1$  space and time coordinate, i.e.  $(x, y, z, t)$

## 2.8 Viscous model

### 2.8.1 Turbulence model

Turbulent flows exhibit fluctuating velocity fields, which mix transported quantities such as momentum, energy, and species concentration, leading to their fluctuations. These fluctuations' small-scale and high-frequency nature makes direct simulation in practical engineering scenarios computationally less practical. To address this, the instantaneous governing equations can be averaged over time, taken as ensemble averages, or otherwise manipulated to eliminate the small scales, resulting in a set of modified equations that are computationally more tractable. Nonetheless, these modified equations introduce new unknown variables, necessitating turbulence models to relate these variables to known quantities.

We have used the Standard  $K - \epsilon$  model. Here we are going to discuss the Standard  $K - \epsilon$  model.

**Continuity equation:**

$$\frac{\partial u_i}{\partial x_i} = 0 \quad (2.32)$$

**Navier-Stokes equation:**

$$\frac{\partial u_i}{\partial t} + u_j \frac{\partial u_i}{\partial x_j} = -\frac{1}{\rho} \frac{\partial p}{\partial x_i} + \nu \frac{\partial^2 u_i}{\partial x_j \partial x_j} \quad (2.33)$$

Using Reynolds Decomposition as  $u_i = \bar{u}_i + u'_i$ ;  $u_j = \bar{u}_j + u'_j$ ;  $p = \bar{p} + p'$

**For Continuity equation:**

$$\begin{aligned} \frac{\partial(\bar{u}_i + u'_i)}{\partial x_i} &= 0 \\ \text{or } \frac{\partial(\overline{\bar{u}_i + u'_i})}{\partial x_i} &= 0 \\ \text{or } \frac{\partial \bar{u}_i}{\partial x_i} + \frac{\partial \overline{u'_i}}{\partial x_i} &= 0 \quad [\because \overline{u'_i} = 0] \\ \text{or } \frac{\partial \bar{u}_i}{\partial x_i} &= 0 \end{aligned} \quad (2.34)$$

## 2.8 Viscous model

---

For Navier Stokes equation:

$$\frac{\partial(\bar{u}_i + u'_i)}{\partial t} + (\bar{u}_j + u'_j) \frac{\partial(\bar{u}_i + u'_i)}{\partial x_j} = -\frac{1}{\rho} \frac{\partial(\bar{p} + p')}{\partial x_i} + \nu \frac{\partial^2(\bar{u}_i + u'_i)}{\partial x_j \partial x_j}$$

By taking the time average, the above equation yields

$$\begin{aligned} \text{or } \frac{\partial(\overline{\bar{u}_i + u'_i})}{\partial t} + (\overline{\bar{u}_j + u'_j}) \frac{\partial(\overline{\bar{u}_i + u'_i})}{\partial x_j} &= -\frac{1}{\rho} \frac{\partial(\overline{\bar{p} + p'})}{\partial x_i} + \nu \frac{\partial^2(\overline{\bar{u}_i + u'_i})}{\partial x_j \partial x_j} \\ \text{or } \frac{\partial \bar{u}_i}{\partial t} + \frac{\partial \bar{u}'_i}{\partial t} + \bar{u}_j \frac{\partial \bar{u}_i}{\partial x_j} + \bar{u}_j \frac{\partial \bar{u}'_i}{\partial x_j} + \bar{u}'_j \frac{\partial \bar{u}_i}{\partial x_j} + \bar{u}'_j \frac{\partial \bar{u}'_i}{\partial x_j} &= -\frac{1}{\rho} \left( \frac{\partial \bar{p}}{\partial x_i} + \frac{\partial \bar{p}'}{\partial x_i} \right) \\ &+ \nu \left( \frac{\partial^2 \bar{u}_i}{\partial x_j \partial x_j} + \frac{\partial^2 \bar{u}'_i}{\partial x_j \partial x_j} \right) \\ \text{or } \frac{\partial \bar{u}_i}{\partial t} + \bar{u}_j \frac{\partial \bar{u}_i}{\partial x_j} + \bar{u}'_j \frac{\partial \bar{u}'_i}{\partial x_j} &= -\frac{1}{\rho} \frac{\partial \bar{p}}{\partial x_i} + \nu \frac{\partial^2 \bar{u}_i}{\partial x_j \partial x_j} \end{aligned} \quad (2.35)$$

[∴ As per rules of averaging 2<sup>nd</sup>, 4<sup>th</sup>, 5<sup>th</sup> terms of *RHS* and 2<sup>nd</sup>, 4<sup>th</sup> terms of *LHS* are equal to zero.]

In the above equation 3<sup>rd</sup> term of the *RHS* can be written

$$\begin{aligned} \bar{u}'_j \frac{\partial \bar{u}'_i}{\partial x_j} &= \frac{\partial \bar{u}'_i \bar{u}'_j}{\partial x_j} - \bar{u}'_i \frac{\partial \bar{u}'_j}{\partial x_j} \\ \text{or } \bar{u}'_j \frac{\partial \bar{u}'_i}{\partial x_j} &= \frac{\partial \bar{u}'_i \bar{u}'_j}{\partial x_j} [\because \frac{\partial \bar{u}'_j}{\partial x_j} = 0 \text{ due to continuity}] \end{aligned}$$

Now, Eq. 2.35 becomes

$$\begin{aligned} \frac{\partial \bar{u}_i}{\partial t} + \bar{u}_j \frac{\partial \bar{u}_i}{\partial x_j} &= -\frac{1}{\rho} \frac{\partial \bar{p}}{\partial x_i} + \nu \frac{\partial^2 \bar{u}_i}{\partial x_j \partial x_j} - \frac{\partial \bar{u}'_i \bar{u}'_j}{\partial x_j} \\ \text{or } \frac{\partial \bar{u}_i}{\partial t} + \bar{u}_j \frac{\partial \bar{u}_i}{\partial x_j} &= -\frac{1}{\rho} \frac{\partial \bar{p}}{\partial x_i} + \frac{\partial}{\partial x_j} \left[ \nu \frac{\partial \bar{u}_i}{\partial x_j} - \bar{u}'_i \bar{u}'_j \right] \end{aligned} \quad (2.36)$$

Let,  $\overline{u'_i u'_i} = \tau_{ij}$

So, 2.36 becomes

$$\text{or } \frac{\partial \bar{u}_i}{\partial t} + \bar{u}_j \frac{\partial \bar{u}_i}{\partial x_j} = -\frac{1}{\rho} \frac{\partial \bar{p}}{\partial x_i} + \frac{\partial}{\partial x_j} \left[ \nu \frac{\partial \bar{u}_i}{\partial x_j} - \bar{\tau}_{ij} \right] \quad (2.37)$$

Subtracting the Eq. 2.37 from Eq. 2.33, we get

$$\begin{aligned} \frac{\partial}{\partial t} (u_i - \bar{u}_i) + (\bar{u}_j + u'_j) \frac{\partial \bar{u}_i}{\partial x_j} (\bar{u}_j + u'_j) - \bar{u}_j \frac{\partial \bar{u}_i}{\partial x_j} &= -\frac{1}{\rho} \frac{\partial}{\partial x_i} (p - \bar{p}) + \nu \nabla^2 (u_i - \bar{u}_i) + \frac{\partial \tau_{ij}}{\partial x_j} \\ \text{or } \left[ \frac{\partial u'_i}{\partial t} + \bar{u}_j \frac{\partial u'_i}{\partial x_j} \right] &= -u'_j \frac{\partial \bar{u}_i}{\partial x_j} - u'_j \frac{\partial u'_i}{\partial x_j} - \frac{1}{\rho} \frac{\partial p'}{\partial x_i} + \nu \nabla^2 u'_i + \frac{\partial \tau_{ij}}{\partial x_j} \end{aligned} \quad (2.38)$$

Multiplying Eq. 2.38 by  $u'_k$  and time averaging we get,

$$\begin{aligned} \left[ \left( \overline{u'_k \frac{\partial u'_i}{\partial t}} \right) + \bar{u}_j \left( \overline{u'_k \frac{\partial u'_i}{\partial x_j}} \right) \right] &= -\overline{(u'_k u'_j)} \frac{\partial \bar{u}_i}{\partial x_j} - \overline{\left( u'_k u'_j \frac{\partial u'_i}{\partial x_j} \right)} - \frac{1}{\rho} \overline{\left( u'_k \frac{\partial p'}{\partial x_j} \right)} \\ &\quad + \nu \overline{\left( u'_k \nabla^2 u'_i \right)} + \overline{\left( u'_k \frac{\partial \tau_{ij}}{\partial x_j} \right)} \end{aligned} \quad (2.39)$$

[In the above Eq. 2.39  $\overline{u'_k} = 0$  as per averaging rule and Eq. 2.39 becomes]

$$\left[ \underbrace{\left( \overline{u'_k \frac{\partial u'_i}{\partial t}} \right)}_1 + \underbrace{\bar{u}_j \left( \overline{u'_k \frac{\partial u'_i}{\partial x_j}} \right)}_2 \right] = -\underbrace{\overline{(u'_k u'_j)} \frac{\partial \bar{u}_i}{\partial x_j}}_3 - \underbrace{\overline{\left( u'_k u'_j \frac{\partial u'_i}{\partial x_j} \right)}}_4 - \underbrace{\frac{1}{\rho} \overline{\left( u'_k \frac{\partial p'}{\partial x_j} \right)}}_5 + \nu \underbrace{\overline{\left( u'_k \nabla^2 u'_i \right)}}_6 \quad (2.40)$$

Since both  $i$  and  $k$  are free indices they can be interchanged to yield a  $2^{nd}$  equation as

$$\left[ \underbrace{\left( \overline{u'_i \frac{\partial u'_k}{\partial t}} \right)}_{(1)} + \underbrace{\bar{u}_j \left( \overline{u'_i \frac{\partial u'_k}{\partial x_j}} \right)}_{(2)} \right] = -\underbrace{\overline{(u'_i u'_j)} \frac{\partial \bar{u}_k}{\partial x_j}}_{(3)} - \underbrace{\overline{\left( u'_i u'_j \frac{\partial u'_k}{\partial x_j} \right)}}_{(4)} - \underbrace{\frac{1}{\rho} \overline{\left( u'_i \frac{\partial p'}{\partial x_j} \right)}}_{(5)} + \nu \underbrace{\overline{\left( u'_i \nabla^2 u'_k \right)}}_{(6)} \quad (2.41)$$

By adding Eq. 2.40 and Eq. 2.41 we get

## 2.8 Viscous model

---

Term-1 + (1)

$$\left[ u'_k \frac{\partial u'_i}{\partial t} + u'_i \frac{\partial u'_k}{\partial t} \right] = \frac{\partial}{\partial t} (\overline{u'_i u'_k})$$

Term-2 + (2)

$$\left[ \bar{u}_j \left( u'_k \frac{\partial u'_i}{\partial x_j} \right) + \bar{u}_j \left( u'_i \frac{\partial u'_k}{\partial x_j} \right) \right] = \bar{u}_j \frac{\partial}{\partial x_j} (\overline{u'_i u'_k})$$

Term-4 + (4)

$$\begin{aligned} & \left[ \left( u'_k u'_j \frac{\partial u'_i}{\partial x_j} \right) + \left( u'_i u'_j \frac{\partial u'_k}{\partial x_j} \right) \right] = \left[ u'_j \left( u'_k \frac{\partial u'_i}{\partial x_j} + u'_i \frac{\partial u'_k}{\partial x_j} \right) \right] = \left[ u'_j \frac{\partial}{\partial x_j} (\overline{u'_i u'_k}) \right] \\ & = \left[ \frac{\partial}{\partial x_j} (\overline{u'_j u'_i u'_k}) - (\overline{u'_i u'_k}) \frac{\partial u'_j}{\partial x_j} \right] = \left[ \frac{\partial}{\partial x_j} (\overline{u'_j u'_i u'_k}) \right] [\because \frac{\partial u'_j}{\partial x_j} = 0 \text{ due to continuity.}] \end{aligned}$$

Term-5 + (5)

$$\begin{aligned} & \frac{1}{\rho} \left[ \left( u'_k \frac{\partial p'}{\partial x_i} \right) + \left( u'_i \frac{\partial p'}{\partial x_k} \right) \right] = \frac{1}{\rho} \left[ \frac{\partial}{\partial x_i} (\overline{p' u'_k}) + \frac{\partial}{\partial x_k} (\overline{p' u'_i}) - p' \frac{\partial u'_k}{\partial x_i} - p' \frac{\partial u'_i}{\partial x_k} \right] \\ & = -\frac{1}{\rho} \left[ p' \left( \frac{\partial u'_i}{\partial x_i} + \frac{\partial u'_k}{\partial x_k} \right) \right] + \frac{1}{\rho} \left[ \frac{\partial}{\partial x_j} \left( (\overline{p' u'_k}) \delta_{ij} + (\overline{p' u'_i}) \delta_{kj} \right) \right] \end{aligned}$$

Term-6 + (6)

$$\begin{aligned} & \nu \left[ (\overline{u'_k \nabla^2 u'_i}) + (\overline{u'_i \nabla^2 u'_k}) \right] = \nu \left[ \left( \frac{\partial}{\partial x_j} u'_k \frac{\partial u'_i}{\partial x_j} - \frac{\partial u'_i}{\partial x_j} \frac{\partial u'_k}{\partial x_j} \right) - \left( \frac{\partial}{\partial x_j} u'_i \frac{\partial u'_k}{\partial x_j} - \frac{\partial u'_k}{\partial x_j} \frac{\partial u'_i}{\partial x_j} \right) \right] \\ & = \nu \left[ \left( \frac{\partial}{\partial x_j} \left( u'_k \frac{\partial u'_i}{\partial x_j} + u'_i \frac{\partial u'_k}{\partial x_j} \right) \right) - 2 \left( \frac{\partial u'_i}{\partial x_j} \frac{\partial u'_k}{\partial x_j} \right) \right] = \nu \left[ (\overline{\nabla^2 (u'_i u'_k)}) - 2 \left( \frac{\partial u'_i}{\partial x_j} \frac{\partial u'_k}{\partial x_j} \right) \right] \end{aligned}$$

Combining all the term we get,

$$\begin{aligned} \frac{\partial}{\partial t} (\overline{u'_i u'_k}) + \bar{u}_j \frac{\partial}{\partial x_j} (\overline{u'_i u'_k}) &= - \left[ (\overline{u'_k u'_j}) \frac{\partial \bar{u}_i}{\partial x_j} + (\overline{u'_i u'_j}) \frac{\partial \bar{u}_k}{\partial x_j} \right] - \frac{\partial}{\partial x_j} (\overline{u'_i u'_j u'_k}) + \\ \left[ \frac{p'}{\rho} \left( \frac{\partial u'_i}{\partial x_k} + \frac{\partial u'_k}{\partial x_i} \right) \right] - \frac{1}{\rho} \left[ \frac{\partial}{\partial x_j} \left( (\overline{p' u'_k}) \delta_{ij} + (\overline{p' u'_i}) \delta_{kj} \right) \right] &+ \nu (\overline{\nabla^2 (u'_i u'_k)}) - 2\nu \left( \frac{\partial u'_i}{\partial x_j} \frac{\partial u'_k}{\partial x_j} \right) \\ \text{or } \frac{\partial}{\partial t} (\overline{u'_i u'_k}) + \bar{u}_j \frac{\partial}{\partial x_j} (\overline{u'_i u'_k}) &= - \left[ (\overline{u'_k u'_j}) \frac{\partial \bar{u}_i}{\partial x_j} + (\overline{u'_i u'_j}) \frac{\partial \bar{u}_k}{\partial x_j} \right] + \left[ \frac{p'}{\rho} \left( \frac{\partial u'_i}{\partial x_k} + \frac{\partial u'_k}{\partial x_i} \right) \right] \\ - \frac{\partial}{\partial x_j} \left[ (\overline{u'_i u'_j u'_k}) + \frac{1}{\rho} \left[ (\overline{p' u'_k}) \delta_{ij} + (\overline{p' u'_i}) \delta_{kj} \right] \right] &+ \nu (\overline{\nabla^2 (u'_i u'_k)}) - 2\nu \left( \frac{\partial u'_i}{\partial x_j} \frac{\partial u'_k}{\partial x_j} \right) \end{aligned}$$

In the above equation  $i$  and  $k$  are both free indices. By contracting the free indices means replacing one free index in terms of the other free index. In this case we replace  $k$  in terms of  $i$ . we get

$$\begin{aligned} \frac{\partial}{\partial t} (\overline{u'_i u'_i}) + \bar{u}_j \frac{\partial}{\partial x_j} (\overline{u'_i u'_i}) &= -2 \left[ (\overline{u'_i u'_j}) \frac{\partial \bar{u}_k}{\partial x_j} \right] + \left[ \frac{p'}{\rho} \left( \frac{\partial u'_i}{\partial x_k} + \frac{\partial u'_k}{\partial x_i} \right) \right] \\ - \frac{\partial}{\partial x_j} \left[ (\overline{u'_i u'_j u'_j}) + \frac{2}{\rho} \left[ (\overline{p' u'_i}) \delta_{ij} \right] \right] &+ \nu (\overline{\nabla^2 (u'_i u'_i)}) - 2\nu \left( \frac{\partial u'_i}{\partial x_j} \frac{\partial u'_i}{\partial x_j} \right) \end{aligned} \quad (2.42)$$

$\therefore$  in the above equation,  $\frac{\partial u'_i}{\partial x_i} = 0$  due to continuity

$$\text{Kinetic energy: } k = \frac{1}{2} (\overline{u'_i u'_i}) \quad (2.43)$$

and

$$\text{Dissipation rate: } \epsilon = \nu \left( \frac{\partial u'_i}{\partial x_j} \frac{\partial u'_i}{\partial x_j} \right) \quad (2.44)$$

$\therefore$  The Eq.2.42 becomes

$$\frac{\partial k}{\partial t} + \bar{u}_j \frac{\partial k}{\partial x_j} = - \left[ (\overline{u'_i u'_j}) \frac{\partial \bar{u}_i}{\partial x_j} \right] - \frac{\partial}{\partial x_j} \left[ \frac{1}{2} (\overline{u'_i u'_i u'_j}) + \frac{1}{\rho} (\overline{p' u'_j}) \right] - \epsilon + \nu \nabla^2 k \quad (2.45)$$

The initial assumption in modeling the  $k$  equation is that the Boussinesq eddy viscosity hypothesis holds valid, allowing the Reynolds stresses to be represented

## 2.8 Viscous model

---

accordingly.

$$\tau_{ij} = -\rho(\overline{u'_i u'_j}) = \mu_t \left( \frac{\partial u_i}{\partial x_j} + \frac{\partial u_j}{\partial x_i} \right) - \frac{2}{3} \rho k \delta_{ij} \quad (2.46)$$

For an incompressible fluid, the concept used to determine the eddy viscosity in Eq. 2.46 is similar to that employed in algebraic models and is typically expressed as follows.

$$\mu_t \approx \rho k^{1/2} l \quad (2.47)$$

Here,  $l$  represents a turbulence length scale, which may be analogous to the mixing length. In Eq. 2.47, the characteristic velocity scale is chosen as the square root of  $k$ , because the turbulent fluctuations at a specific point within the flow field effectively represent the turbulent momentum transport. The formulation for  $\mu_t$  provided in Eq. 2.47 closely resembles that described by

$$\mu_t \approx \rho \nu_{mix} l_{mix} \quad (2.48)$$

In the algebraic or mixing length model, the kinematic viscosity due to mixing, denoted as  $\nu_{mix}$  is typically linked to a single velocity gradient within the flow. According to White (1991) [38], an eddy characterized by a size  $l$  and moving at a speed  $u$  should have its energy dissipation per unit mass approximated.

$$\epsilon \approx \frac{(drag)(velocity)}{mass} \approx \frac{(\rho u^2 l^2) u}{\rho l^3} \approx \frac{u^3}{l} \quad (2.49)$$

The dissipation is typically modeled by using the square root of the turbulent kinetic energy as the representative velocity scale and written as

$$\epsilon \approx \frac{k^{3/2}}{l} \quad (2.50)$$

The transport of turbulent kinetic energy ( $k$ ) and the pressure diffusion components are typically modeled by employing a gradient diffusion approach. In practice, the pressure fluctuation term, which tends to be minor in incompressible flows, is often combined with the gradient diffusion term. By making these assumptions, the modeling of turbulent kinetic energy transport and pressure fluc-

tuations can be expressed as follows.

$$\frac{\mu_t}{\sigma_k} \frac{\partial k}{\partial x_j} = -\frac{1}{2} \overline{\rho(u'_i u'_i u'_j)} - \overline{(p' u'_j)} \quad (2.51)$$

Where  $\sigma_k$  is a dimensionless constant and the value of  $\sigma_k = 1$ . Combining the modeled expressions for Reynolds stress, dissipation, turbulent diffusion, and pressure diffusion with the transient, convective, and viscous terms results in the formulated  $k$  equation as

$$\rho \frac{\partial k}{\partial t} + \rho \frac{\partial(k \bar{u}_j)}{\partial x_j} = - \left[ \rho \overline{(u'_i u'_j)} \frac{\partial \bar{u}_i}{\partial x_j} \right] + \frac{\partial}{\partial x_j} \left[ \left( \mu + \frac{\mu_t}{\sigma_k} \right) \frac{\partial k}{\partial x_j} \right] - \rho \epsilon \quad (2.52)$$

$$\text{or } \rho \frac{\partial k}{\partial t} + \rho \frac{\partial(k \bar{u}_j)}{\partial x_j} = \frac{\partial}{\partial x_j} \left[ \left( \mu + \frac{\mu_t}{\sigma_k} \right) \frac{\partial k}{\partial x_j} \right] + G_k - \rho \epsilon \quad (2.53)$$

In Eq. 2.53  $G_k = \frac{\partial}{\partial x_j} \left[ \left( \mu + \frac{\mu_t}{\sigma_k} \right) \frac{\partial k}{\partial x_j} \right]$ . The first term of the *RHS* of the Eq. 2.53 corresponds to the diffusion term,  $G_k$  represents the generation of turbulent kinetic energy due to the mean velocity gradients and the third one represents the destruction term.

---

## TURBULENT JET

The current report is focused on turbulent jets, their structures, and mixing properties. We will start by explaining the basic theory behind turbulent jets and then move on to various configurations, such as the plane turbulent free jet, the circular turbulent jet, and the turbulent wall jet. These configurations are described using equations of motion, the integral momentum equation, the integral energy equation, and the integral moment of momentum equation. Turbulent jets are fluid flows created through the expenditure of pressure drop via an orifice. In recent times, there has been increased attention from researchers on the mechanics of turbulent jets, leading to a better understanding of the process and its interaction with the surrounding fluid. Figure 3.1 presents examples of turbulent jets.

From an empirical standpoint, there is significant evidence indicating that the initial growth of turbulence is a direct result of large-scale motions generated at the boundaries of the jet. These large-scale motions are primarily responsible for jet noise production and the initial entrainment of ambient fluid. The basic sequence of axisymmetric jets appears to proceed as follows: near the orifice, the high-speed jet flow causes the production of a laminar shear layer. This shear layer becomes unstable and grows rapidly, forming ring vortices that carry turbulent jet flows into the surrounding ambient fluid. The generation of vortices is crucial in the initial dilution of the jet. Each vortex wraps ambient fluid around itself, and

as the vortices pair, the fusion process mixes the ambient and jet fluid. Circumferential instability, along with possible interaction with helical modes, leads to the apparent self-destruction of the large-scale structures, generating subsequent small-scale turbulent mixing.

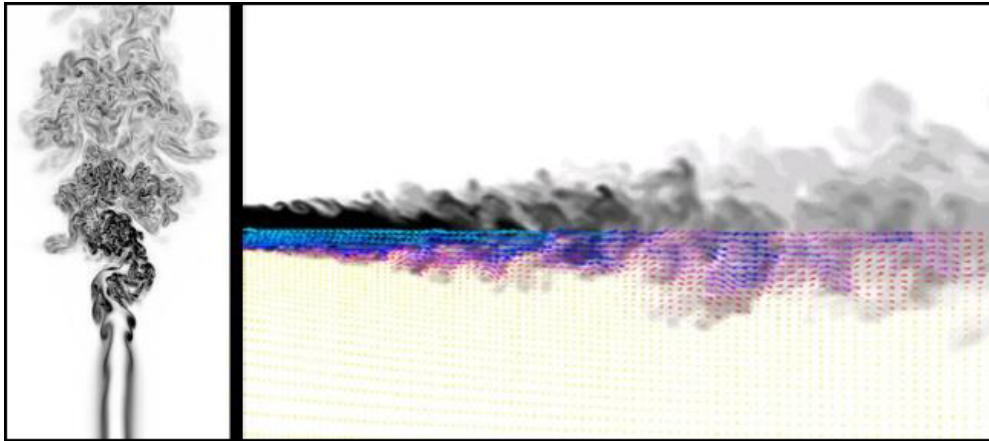


Figure 3.1: Different examples of turbulent jets(Adopted from P. Koumoutsakos, et. al., 1999[3])

Please make a note of the following text:

Figure. 3.2 depicts the various configurations of turbulent jets.

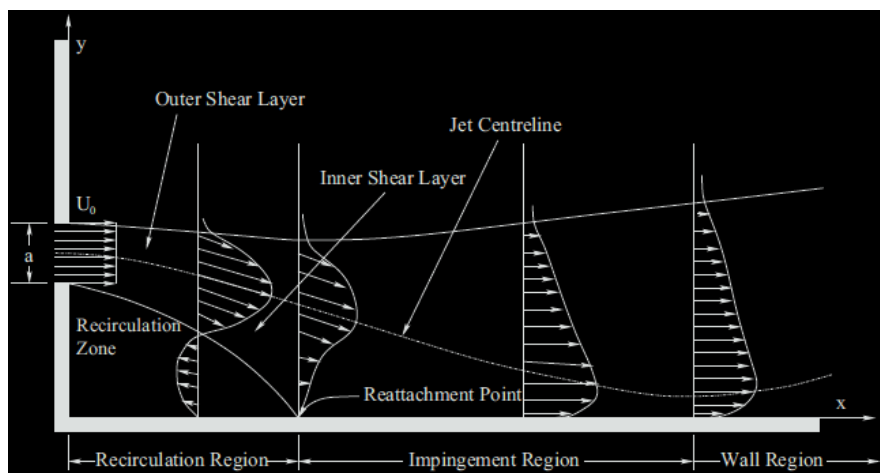


Figure 3.2: Definition sketch of Turbulent Jet(Adapted from A. Assoudi et. al., 2019[4])

### 3.1 Plane turbulent free jet

## 3.1 Plane turbulent free jet

A plane turbulent free jet can be exemplified by a stream of water emerging from a wide, flat nozzle into a large water body, or a stream of air flowing into a vast expanse. When using effective visualization techniques, it becomes evident that the jet interacts intensely with the surrounding fluid, leading to turbulence and an increase in the jet's thickness. Figure 3.3 illustrates a schematic representation of this jet configuration, commonly referred to as a plane turbulent free jet.

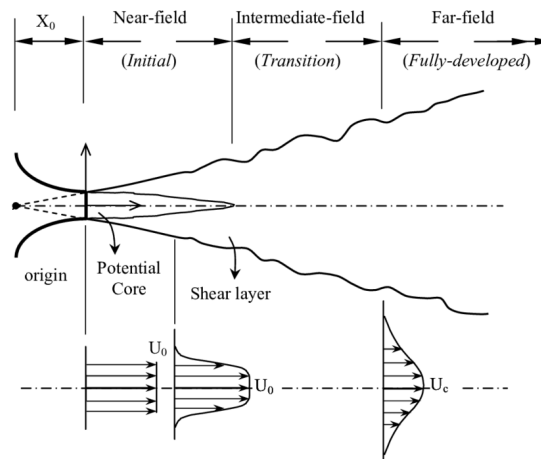


Figure 3.3: Schematic of a plane turbulent free jet showing jet regions, velocity profiles, and coordinate system (adapted from Abdel-Rahman, A. 2010[5])

Experimental observations of the mean turbulent velocity field show that the jet's axial direction is split into two distinct regions. The first region, located near the nozzle and called the flow development region, features a wedge-shaped area of constant mean velocity, equal to  $U_0$  which extends towards the jet's axis or center line. This area is referred to as the potential core and is flanked by a mixing layer above and below. In the second region, known as the fully developed flow region, turbulence has fully reached the axis, causing the potential core to dissipate.

### 3.1.1 Equation of motion

The Equations of motion for the plane turbulent free jet have been deduced from the Reynolds equation. In the Cartesian System, the Reynolds equations are

written as:

$$\frac{\partial u}{\partial t} + u \frac{\partial u}{\partial x} + v \frac{\partial u}{\partial y} + w \frac{\partial u}{\partial z} = -\frac{1}{\rho} \frac{\partial p}{\partial x} + \nu \left( \frac{\partial^2 u}{\partial x^2} + \frac{\partial^2 u}{\partial y^2} + \frac{\partial^2 u}{\partial z^2} \right) - \left( \frac{\overline{\partial u'^2}}{\partial x} + \frac{\overline{\partial u'v'}}{\partial y} + \frac{\overline{\partial u'w'}}{\partial z} \right) \quad (3.1)$$

$$\frac{\partial v}{\partial t} + u \frac{\partial v}{\partial x} + v \frac{\partial v}{\partial y} + w \frac{\partial v}{\partial z} = -\frac{1}{\rho} \frac{\partial p}{\partial y} + \nu \left( \frac{\partial^2 v}{\partial x^2} + \frac{\partial^2 v}{\partial y^2} + \frac{\partial^2 v}{\partial z^2} \right) - \left( \frac{\overline{\partial u'v'}}{\partial x} + \frac{\overline{\partial v'^2}}{\partial y} + \frac{\overline{\partial v'w'}}{\partial z} \right) \quad (3.2)$$

And:

$$\frac{\partial w}{\partial t} + u \frac{\partial w}{\partial x} + v \frac{\partial w}{\partial y} + w \frac{\partial w}{\partial z} = -\frac{1}{\rho} \frac{\partial p}{\partial z} + \nu \left( \frac{\partial^2 w}{\partial x^2} + \frac{\partial^2 w}{\partial y^2} + \frac{\partial^2 w}{\partial z^2} \right) - \left( \frac{\overline{\partial u'w'}}{\partial x} + \frac{\overline{\partial v'w'}}{\partial z} + \frac{\overline{\partial w'^2}}{\partial y} \right) \quad (3.3)$$

The continuity is written as:

$$\frac{\partial u}{\partial x} + \frac{\partial v}{\partial y} + \frac{\partial w}{\partial z} = 0 \quad (3.4)$$

In the analysis of jet flows, we define our coordinate system with the  $x$ -axis representing the axial direction of the jet. The  $y$ -axis is perpendicular to the  $x$ -axis and aligns with the height of the nozzle, while the  $z$ -axis completes the three-dimensional coordinate system. The variables  $u$ ,  $v$ , and  $w$  represent the turbulent mean velocities in the  $x$ ,  $y$ , and  $z$  directions respectively, whereas  $u'$ ,  $v'$ , and  $w'$  denote the corresponding fluctuating velocities. The mean pressure at any point is denoted by  $p$ , the kinematic viscosity by  $\nu$  the mass density of the fluid by  $\rho$ , and the time variable by  $t$ . Given that the mean flow is two-dimensional,  $w = 0$  and any mean quantity's partial derivative to  $z$  is zero ( $\frac{\partial}{\partial z}$ ). Additionally, the Reynolds stresses involving  $w$  are zero ( $\overline{u'w'} = 0$  and  $\overline{v'w'} = 0$ ). The steady nature of the mean flow implies that the partial derivatives of  $u$  and  $v$  for time are zero ( $\frac{\partial u}{\partial t} = 0$  and  $\frac{\partial v}{\partial t} = 0$ ).

Furthermore, in regions where the transverse extent of the flow is limited, the velocity component  $u$  is significantly larger than  $v$ . This implies that velocity and stress gradients in the  $y$ -direction are much greater than those in the  $x$ -direction. Considering these simplifications, the equation of motion for the jet flow can be significantly reduced to the following form:

### 3.1 Plane turbulent free jet

---

$$u \frac{\partial u}{\partial x} + v \frac{\partial u}{\partial y} = -\frac{1}{\rho} \frac{\partial p}{\partial x} + \nu \frac{\partial^2 u}{\partial y^2} - \frac{\partial \overline{u'v'}}{\partial y} - \frac{\partial \overline{u'^2}}{\partial x} \quad (3.5)$$

$$0 = -\frac{1}{\rho} \frac{\partial p}{\partial y} - \frac{\partial \overline{v'^2}}{\partial y} \quad (3.6)$$

$$\frac{\partial u}{\partial x} + \frac{\partial v}{\partial y} = 0 \quad (3.7)$$

On integration for  $y$  from  $\bar{y}$  to a point located outside the jet, differentiating and substituting, we get:

$$u \frac{\partial u}{\partial x} + v \frac{\partial u}{\partial y} = -\frac{1}{\rho} \frac{dp_\infty}{dx} + \nu \frac{\partial^2 u}{\partial y^2} - \frac{\partial \overline{u'v'}}{\partial y} - \frac{\partial}{\partial x} (\overline{u'^2} - \overline{v'^2}) \quad (3.8)$$

Where  $p_\infty$  is the pressure outside the jet.

The final term in the equation is significantly smaller than the others and can be disregarded. Therefore, the equation simplifies to:

$$u \frac{\partial u}{\partial x} + v \frac{\partial u}{\partial y} = -\frac{1}{\rho} \frac{dp_\infty}{dx} + \nu \frac{\partial^2 u}{\partial y^2} - \frac{\partial \overline{u'v'}}{\partial y} \quad (3.9)$$

And

$$\frac{\partial u}{\partial x} + \frac{\partial v}{\partial y} = 0 \quad (3.10)$$

To simplify notation, we denote  $p_\infty$  as  $p$ . Consequently, the last two terms can be reformulated as:

$$\frac{1}{\rho} \frac{\partial}{\partial y} \left( \mu \frac{\partial u}{\partial y} \right) + \frac{1}{\rho} \frac{\partial}{\partial y} (-\rho \overline{u'v'}) = \frac{1}{\rho} \frac{\partial}{\partial y} (\tau_l + \tau_t) \quad (3.11)$$

In free turbulent flows, the turbulent shear stress ( $\tau_t$ ) is significantly larger than the laminar shear stress ( $\tau_l$ ) because there are no solid boundaries. Consequently, the laminar shear stress ( $\tau_l$ ) can be considered negligible. Therefore, the equation simplifies to:

$$u \frac{\partial u}{\partial x} + v \frac{\partial u}{\partial y} = -\frac{1}{\rho} \frac{dp}{dx} + \frac{1}{\rho} \frac{\partial \tau_t}{\partial y} \quad (3.12)$$

Moreover, in many practical situations, the pressure gradient along the axial

direction is insignificantly small. To simplify the analysis of the jet under these conditions, we assume  $\frac{dp}{dx} = 0$ . Then:

$$u \frac{\partial u}{\partial x} + v \frac{\partial u}{\partial y} = \frac{1}{\rho} \frac{\partial \tau_t}{\partial y} \quad (3.13)$$

$$\frac{\partial u}{\partial x} + \frac{\partial v}{\partial y} = 0 \quad (3.14)$$

These are the established equations of motion for a plane turbulent free jet with no pressure gradient along the axial direction. To derive the integral momentum equation, one can multiply by  $\rho$  and then integrate over the range from  $y = 0$  to  $y = \infty$ :

$$\rho \int_0^\infty u \frac{\partial u}{\partial x} dy + \rho \int_0^\infty v \frac{\partial u}{\partial y} dy = \int_0^\infty \frac{\partial \tau}{\partial y} dy \quad (3.15)$$

Let us now consider the different terms of the above equation:

$$\rho \int_0^\infty u \frac{\partial u}{\partial x} dy = \frac{1}{2} \frac{d}{dx} \int_0^\infty \rho u^2 dy \quad (3.16)$$

$$\rho \int_0^\infty v \frac{\partial u}{\partial y} dy = -\rho \int_0^\infty u \frac{\partial v}{\partial y} dy \quad (3.17)$$

For  $y = 0$ , the conditions are  $u = u_m$  and  $v = 0$ . As  $y$  approaches infinity, the conditions change to  $u = 0$  and  $v = v_e$ , Where  $v_e$  is a finite value referred to as the "entrainment velocity."

Then:

$$\frac{d}{dx} \int_0^\infty \rho u^2 dy = 0 \quad (3.18)$$

The equation indicates that the momentum flux in the  $x$ -direction remains constant; in other words, the momentum flux in the  $x$ -direction is conserved.

Consider a plane jet emerging from an orifice with a height of  $2b_0$  and a uniform velocity of  $U_0$ . For each unit length of the orifice, the momentum flux,  $M_0$ , is given by  $2\rho b_0 U_0^2$ . We can conceptualize this momentum flux as originating from a line source positioned at a virtual origin, from which the  $x$ -coordinate is measured. Therefore, we have:

### 3.1 Plane turbulent free jet

---

$$2 \int_0^{\infty} \rho^2 dy = M_0 \quad (3.19)$$

The momentum flux  $M_0$  is a crucial parameter in determining the characteristics of the plane jet. It serves as a substitute for the specific values of  $b_0$  and  $U_0$ . We can devise a method to predict how the velocity and length scales will change by utilizing the integral momentum equation. It has been observed that in the fully developed region, the velocity distribution resembles that of a plane turbulent jet. i.e.

$$\frac{u}{u_m} = f(\eta) \quad \text{where } \eta = y/b \quad (3.20)$$

Let us assume simple forms for  $u_m$  and  $b$  as:

$$u_m \propto x^p \quad b \propto x^q \quad (3.21)$$

Where  $p$  and  $q$  are the unknown exponents to be evaluated. Substituting the last equations, we get:

$$\frac{d}{dx} \int_0^{\infty} \rho u_m^2 b f^2 d\eta = 0 \quad (3.22)$$

where  $f^2$  stands for  $f^2(\eta)$ . Rewriting

$$\frac{d}{dx} \rho u_m^2 b \int_0^{\infty} f^2 d\eta = 0 \quad (3.23)$$

Where  $\int_0^{\infty} f^2 d\eta = 0$  is a constant, then:

$$\frac{d}{dx} (b u_m^2) \quad (3.24)$$

We can say  $b u_m^2$  is independent of  $x$ . i.e.

$$b u_m^2 \propto x^0 \quad (3.25)$$



---

# NUMERICAL METHODOLOGY

## 4.1 Turbulence Model

Turbulent flows exhibit velocity fluctuations mixed with different transport quantities such as intensity, momentum, species density, etc. These variables, generally at small scales and high frequencies, make simulations straightforward is computationally inefficient for many industrial applications. by averaging to exclude small variations. This results in modified equations of the process that can be solved for further calculations. However, this simplified equation introduces additional unknown variables, and turbulence models need to be applied at known quantities to account for these variables

We have used Standard  $k - \epsilon$  and  $k - \omega$  SST models. Here we are going to discuss each of the models.

## 4.2 Standard $k - \epsilon$ model

The simplest “complete models” of turbulence are two-equation models, which solve two separate transport equations to independently determine turbulent velocity and length scales. The standard  $k - \epsilon$  model in *FLUENT* is an example of

this type of turbulence model. Its popularity in industrial flow and heat transfer simulations is due to its robustness, cost-effectiveness, and reasonable accuracy across a wide range of turbulent flows. This model is semi-empirical, with its equations derived through a combination of phenomenological considerations and empirical data [39].

The standard  $k - \epsilon$  model relies on transport equations for turbulence kinetic energy ( $k$ ) and its dissipation rate ( $\epsilon$ ). The transport equation for  $k$  is derived from the exact equation, whereas the transport equation for  $\epsilon$  is based on physical reasoning and only loosely resembles its mathematical counterpart. Typically, when the turbulence kinetic energy is required for modeling a specific term, it is obtained by taking the trace of the Reynolds stress tensor.

$$k = \frac{1}{2} \overline{u'_i u'_i} \quad (4.1)$$

In deriving the  $k - \epsilon$  turbulence model, it is assumed that the flow is entirely turbulent and the influence of molecular viscosity is minimal. Consequently, the standard  $k - \epsilon$  model applies only to fully turbulent flows.

#### 4.2.1 Transport equations for standard $k - \epsilon$ model

The standard kinetic energy  $k$  and its rate of dissipation  $\epsilon$ , are obtained from the following transport equations:

$$\frac{\partial}{\partial t}(\rho k) + \frac{\partial}{\partial x_i}(\rho k u_i) = \frac{\partial}{\partial x_j} \left[ \left( \mu + \frac{\mu_t}{\sigma_k} \right) \frac{\partial k}{\partial x_j} \right] + G_k + G_b - \rho \epsilon - Y_M + S_k \quad (4.2)$$

And

$$\frac{\partial}{\partial t}(\rho \epsilon) + \frac{\partial}{\partial x_i}(\rho \epsilon u_i) = \frac{\partial}{\partial x_j} \left[ \left( \mu + \frac{\mu_t}{\sigma_k} \right) \frac{\partial \epsilon}{\partial x_j} \right] + C_{1\epsilon} \frac{\epsilon}{k} (G_k + C_{3\epsilon} G_b) - C_{2\epsilon} \rho \frac{\epsilon^2}{k} + S_\epsilon \quad (4.3)$$

In these equations,  $G_k$  represents the generation of turbulence kinetic energy due to the mean velocity gradients, calculated as:

$$G_k = -\rho \overline{u'_i u'_j} \frac{\partial u_j}{\partial x_j} \quad (4.4)$$

## 4.2 Standard $k - \epsilon$ model

---

In Reynolds averaging, the solution variables in the instantaneous (exact) Navier-Stokes equations are decomposed into the mean (ensemble-averaged or time-averaged) and fluctuating components. For the velocity components:

$$u_i = \bar{u}_i + u'_i \quad (4.5)$$

Here  $\bar{u}_i$  and  $u'_i$  are the mean and fluctuating velocity components ( $i = 1, 2, 3$ ). Here  $\overline{\rho u'_i u'_j}$  is called Reynolds stress.  $G_b$  is the generation of turbulence kinetic energy due to buoyancy calculated as:

$$G_b = \beta g_i \frac{\mu_t}{Pr_t} \frac{\partial T}{\partial x_i} \quad (4.6)$$

In this context,  $Pr_t$  denotes the turbulent Prandtl number related to energy. The term  $g_i$  stands for the  $i^{th}$  component of the gravitational vector. The symbol  $\beta$  represents the thermal expansion coefficient. Meanwhile,  $Y_M$  accounts for the effect of fluctuating dilatation in compressible turbulence on the overall dissipation rate, and it is calculated as follows:

$$Y_M = 2\rho\epsilon M_t^2 \quad (4.7)$$

Where,  $M_t$  is the turbulent Mach number, defined as:

$$M_t = \sqrt{\frac{K}{a^2}} = \sqrt{\frac{K}{\gamma RT}} \quad (4.8)$$

$C_{1\epsilon}$  and  $C_{3\epsilon}$  are constants.  $\sigma k$  and  $\sigma\epsilon$  are turbulent Prandtl numbers for  $K$  and  $\epsilon$  respectively.  $S_k$  and  $S_\epsilon$  are user-defined source terms. We are not considering  $Y_M$  and  $G_B$  as the flow is considered completely incompressible and the effect of buoyancy is negligible. So finally the equation becomes

$$\frac{\partial}{\partial t}(\rho k) + \frac{\partial}{\partial x_i}(\rho k u_i) = \frac{\partial}{\partial x_j} \left[ \left( \mu + \frac{\mu_t}{\sigma_t} \right) \frac{\partial k}{\partial x_j} \right] + G_k + \rho\epsilon + S_k \quad (4.9)$$

and

$$\frac{\partial}{\partial t}(\rho\epsilon) + \frac{\partial}{\partial x_i}(\rho\epsilon u_i) = \frac{\partial}{\partial x_j} \left[ \left( \mu + \frac{\mu_t}{\sigma_t} \right) \frac{\partial \epsilon}{\partial x_j} \right] + C_{1\epsilon} \frac{\epsilon}{k} G_k - C_{2\epsilon} \rho \frac{\epsilon^2}{k} + S_\epsilon \quad (4.10)$$

The model constants have the following values:  $C_{1\epsilon} = 1.44$ ,  $C_{2\epsilon} = 1.92$ ,  $C_{3\epsilon} = 0.09$ ,  $\sigma_k = 1$  and  $\sigma_\epsilon = 1.3$

These default values are based on experimental results obtained from studies with air and water. These studies focused on basic turbulent shear flows, such as homogeneous shear flows and decaying isotropic grid turbulence. The values have proven to be effective across various wall-bounded and free-shear flows.

# MODELING DUCT FLOW WITH SQUARE AND JET SUCTION PANEL

The numerical simulation process introduces mathematical modeling which is based on a set of assumptions about the variation of the problem variables and constitutive relation. We have modeled our problems in *ANSYS FLUENT* based on the open channel flows providing a square obstacle followed by horizontal jet impingement by using the *VOF* formulation in *2D* geometry. To start using the open channel flow boundary condition, we have performed the following:

## 5.1 Problem definition

The physical problem is based on the open channel flow by providing the square cross-section *2D* obstruction at the fully-developed region of the channel bed. The length of the open channel is 18 m and the height is 0.4 m. The square (0.025 m  $\times$  0.025 m) is provided at a distance 11 m from the inlet of the bed. As the flow passes over this square obstruction, it generates a pronounced re-circulation zone that extends significantly into the wake region. The depth average velocity

of the mainstream, denoted as  $u_m$  is maintained at 0.35 m/s. The schematic representation of this model can be observed in Fig. 5.1. A jet panel with a series of upright  $2D$  wall jets each 0.002 m openings and varying jet panel length ( $l = nd$ , where  $d$  is the height of the square obstruction and  $n = 2, 4, 6$ ), is placed just after the square obstruction. The channel specification is shown in Table 5.1. All the details of the hydrodynamic parameters for without and with jets are presented in Table 5.2 and Table 5.3, respectively. In the study, a standard Volume-of-Fluid (*VOF*) model, both the water (secondary) and air (primary) phases are set at equal depths, precisely 0.2 meters, at a position halfway within the channel. This choice of depth ensures that the air phase's influence does not affect the water phase, which is our primary focus. Salaheldin et al. (2003)[40] previously documented that maintaining an air depth-to-water depth ratio greater than 0.5 results in no discernible impact from the upper boundary. In our current investigation, we deliberately maintained an aspect ratio below 0.5 to prevent any interference from the channel walls on the square obstacle.

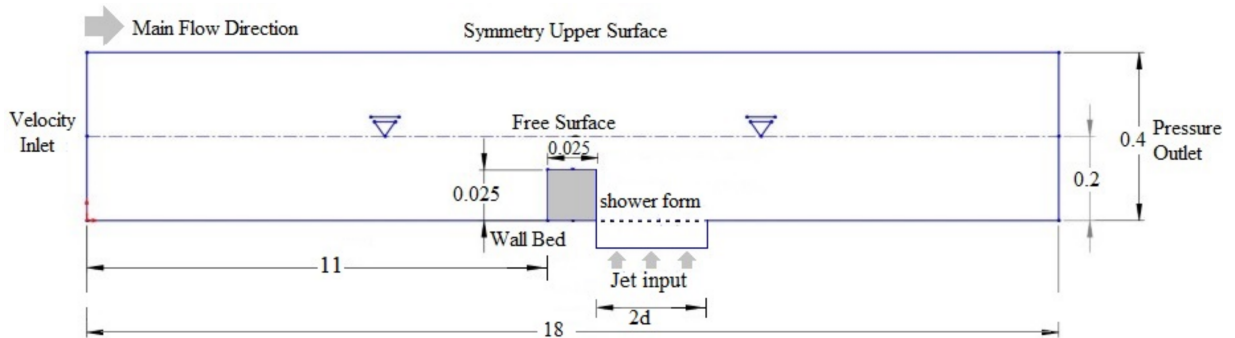


Figure 5.1: Schematic diagram of the computational setup with boundary conditions

### 5.1.1 Boundary conditions

For the solution of the present problem in the CFD domain four boundary conditions have been introduced for the open channel and one boundary condition is taken for the jet discharge. These are as follows.

- Symmetry for upper Surface

## 5.2 Mathematical Formulation

---

Table 5.1: specification of the Channel

Channel parameters	Dimensions
The channel length, $l$ (m)	18
The channel height, $h$ (m)	0.4
The arm of the square obstruction, $a$ (m)	0.025
Area of the square obstruction, $A$ (m <sup>2</sup> )	$0.025 \times 0.025$
Jet opening square hole each, (m)	0.002
Jet panel length, $l = nd$ , where $n = 2, 4, 6$ (m)	0.05, 0.10, 0.15

Table 5.2: Hydrodynamic parameters of open channel without jet

Parameters	Values
Reynolds number, $Re = uh/\gamma$	70,000
Streamwise depth average velocity $u$ (m/s)	0.35
The depth of mean flow, $h$ (m)	0.20
Friction velocity (computed from the log law) $u_*$ (m/s)	0.012
Froude number, $Fr$	1.2

- Pressure inlet for inlet of the channel
- Pressure outlet for the outlet of the channel
- Wall for the bottom surface
- Velocity inlet for jet

## 5.2 Mathematical Formulation

We employ the time-averaged Reynolds-averaged Navier–Stokes equations to analyze the flow patterns within an open channel. These equations are primarily utilized to depict turbulent fluid flows. In tensor notation (Cartesian form), the Navier–Stokes equations for the motion of a viscous, incompressible fluid can be expressed as:

$$\frac{\partial u_i}{\partial x_i} = 0 \tag{5.1}$$

## Ch 5: Square Duct Flow with Suction Panel

Table 5.3: Hydrodynamic parameters for open channel with jets

Parameters	Values
Reynolds number, $Re = uh/\gamma$	70,000
Streamwise depth average velocity $u$ (m/s)	0.35
The depth of mean flow, $h$ (m)	0.20
Friction velocity (computed from the log law) $u_*$ (m/s)	0.012
Jet Velocity, $u_i$ (m/s)	0.30, 0.70, 1.05
First set of jet Reynolds numbers, $Re_i = u_i l/\gamma (l = 2d)$	15487, 30973, 46460
Second set of jet Reynolds numbers, $Re_i = u_i l/\gamma (l = 4d)$	30973, 61947, 92920
Third set of jet Reynolds numbers, $Re_i = u_i l/\gamma (l = 6d)$	46460, 92920, 139381

$$\frac{\partial u_i}{\partial t} + u_j \frac{\partial u_i}{\partial x_j} = F_i - \frac{1}{\rho} \frac{\partial p}{\partial x_i} + \nu \frac{\partial^2 u_i}{\partial x_j \partial x_j} \quad (5.2)$$

To obtain approximations relying on the characteristics of turbulent flow, the time-averaged form is derived from Eq. 5.1 and Eq. 5.2

$$\frac{\partial \bar{u}_i}{\partial x_i} = 0 \quad (5.3)$$

$$\frac{\partial \bar{u}_i}{\partial t} + \bar{u}_j \frac{\partial \bar{u}_i}{\partial x_j} = F_i - \frac{1}{\rho} \frac{\partial \bar{p}}{\partial x_i} + \nu \frac{\partial^2 \bar{u}_i}{\partial x_j \partial x_j} - \frac{\partial \overline{u'_i u'_j}}{\partial x_j} \quad (5.4)$$

Where  $\overline{(u'_i u'_j)}$  term is the Reynolds stress which is the very important parameter based on the turbulent Eddy viscosity model. It makes the fundamental connection with the velocity gradient and represented as

$$\tau_{ij} = \overline{u'_i u'_j} = \frac{2}{3} k \delta_{ij} - \nu_t \left( \frac{\partial \bar{u}_i}{\partial x_j} + \frac{\partial \bar{u}_j}{\partial x_i} \right) \quad (5.5)$$

Where  $k$  is the average kinetic energy and represented as

$$k = \frac{1}{2} \overline{u'_i u'_i} \quad (5.6)$$

and  $\delta_{ij}$  is the Kronecker delta. The eddy viscosity term  $\nu_t$  is expressed as

$$\tau_t = C_\mu \frac{k^2}{\epsilon} \quad (5.7)$$

## 5.2 Mathematical Formulation

---

Where the value of  $C_\mu = 0.09$ . The modified equations may contain additional unknown variables that must be determined using a standard turbulent model and known quantities. In this study, we employ the widely used standard  $k - \omega$  shear stress transport (SST) model. The standard  $k - \omega$  SST model stands out as the simplest and most frequently used turbulence model, effectively meeting the demands for numerical solutions. This model represents a hybridization of the  $k - \epsilon$  and  $k - \omega$  models. Specifically, the  $k - \omega$  model developed by Wilcox (1998a) [41], is well-suited for the near-wall region, while the standard  $k - \epsilon$  model introduced by Launder and Spalding (1974) [42], is applied in the outer wake region, where turbulence is free-flowing. This model is grounded in the gradual transition from the  $k - \epsilon$  model to the  $k - \omega$  model, with this transition occurring progressively from locations near the wall to regions significantly farther away from it [43]. The  $k - \omega$  SST model equation is the modified version of the Wilcox's  $k - \omega$  where  $\omega$  value yields  $k$  times of  $\omega$  and finally takes the form as follows:

$$\frac{\partial(\rho\omega)}{\partial t} + \nabla \cdot (\rho\omega U) = \nabla \cdot \left[ \left( \mu + \frac{\mu_t}{\sigma_\omega} \right) \nabla(\omega) \right] + \nu_2 \left( 2\rho S_{ij} S_{ij} - \frac{2}{3} \mu\omega \frac{\partial U_i}{\partial x_j} \delta_{ij} \right) - \beta_2 \rho \omega^2 + 2 \frac{\rho}{\sigma_{\omega,2} \omega} \frac{\partial k}{\partial x_k} \frac{\partial \omega}{\partial x_k} \quad (5.8)$$

Incorporating this adjustment introduces an additional term referred to as cross-diffusion, denoted as the final term in Eq. 5.8. It can be further refined using a blending function. Consequently, this modification serves to mitigate numerical instabilities that may arise between computed values and the standard model. Empirical experiments have revealed notable enhancements stemming from the adoption of this modified model. Primarily, it results in a revision of the model's constants, which can be expressed as follows:

$$\sigma_k = 1, \quad \sigma_{\omega,1} = 2, \quad \sigma_{\omega,2} = 1.77, \quad \gamma_2 = 0.44, \quad \beta_2 = 0.0835 \text{ and } \beta^* = 0.09$$

Furthermore, the model constant is redefined by incorporating the inherent constants from both the  $k - \omega$  and  $k - \epsilon$  models, modulated by the blending function

FC. Notably, this redefined constant exhibits a unique characteristic of remaining effectively zero in close proximity to the boundary wall while gradually approaching unity in the far-field region. In the intermediate region, situated approximately midway between the boundary wall and the boundary layer's outer edge, this redefined constant facilitates a seamless transition. Consequently, this approach allows for a comprehensive treatment that combines the advantageous near-wall behavior of the  $k - \omega$  model with the robustness of the  $k - \epsilon$  model, thereby ensuring a balanced and effective solution across the entire range.

### 5.3 Free Surface Equation

In this context, the channel is characterized by being half-filled with water, which is treated as the secondary phase within the Volume of Fluid (VOF) model. Throughout the entire computational domain of the channel, and over the course of the computational iterations, the free surface level remains constant. We are hypothesizing that there will be negligible variation at the point of injection of the jets within the wake region, as these jets take the form of a spray within the primary flow domain. The temporal evolution of the mean flow depth, represented as  $[h = f(x, y, t)]$  is governed by the kinetic model equation presented below, given that the free surface moves with the streamwise velocity  $u$ .

$$\frac{\partial h}{\partial t} = (\hat{n} \cdot u) \sqrt{\sigma} \quad (5.9)$$

Here  $\hat{n}$  represents the surface normal vector and

$$\sigma = 1 + \left(\frac{\partial h}{\partial x}\right)^2 + \left(\frac{\partial h}{\partial y}\right)^2 \quad (5.10)$$

### 5.4 Numerical Procedure

The governing equations exhibit strong nonlinearity and are coupled with another equation. To obtain a solution, an iterative approach is employed until convergence is achieved. Convergence is defined with a stringent criterion of reaching a convergence criterion of residuals below  $1 \times 10^{-5}$ .

## 5.4 Numerical Procedure

---

Given the high Reynolds number within the flow domain, we employ Fourier stability analysis, also referred to as von Neumann stability analysis, in the implicit numerical simulation scheme. This approach guarantees unconditional stability throughout the entirety of the iterative process.

The finite difference method employed in this scheme offers the advantage of accommodating significantly larger time-step values while maintaining an acceptable range of errors. The formulation of the time step is inherently based on an empirical relationship established by Katopodes in 2018. [44]

$$\Delta t < \frac{(\Delta x)^2}{4\gamma} \quad (5.11)$$

The projection method, since it belongs to the pressure-based algorithms, has been employed to address the solution of equations as documented in the work of Wilcox in 1998 [41]. Specifically, the commercial computational fluid dynamics (*CFD*) software *ANSYS FLUENT* was utilized, employing the pressure-based solver algorithm known as *SIMPLE* algorithm. Additionally, the QUICK scheme was employed to resolve the governing equations [45].

The pressure correction method essentially derives a pressure equation from the governing equation. This pressure equation plays an essential role in resolving constraints within the continuity equation for the velocity field. The numerical solution is achieved by decoupling the interrelated terms present in the governing equation, a process inherently facilitated by the pressure-based solver integrated into the *CFD* package.

In the context of simulating open channel-based flow scenarios, a Volume-of-Fluid (*VOF*) approach has been devised for numerical computations involving multi-phase flow. This technique proves particularly valuable for accurately tracking the interface between two immiscible fluids, namely air and water, and determining their respective proportions within the computational cells as they pertain to the shared set of momentum equations.

The *VOF* formulation hinges on a phase interface model that delineates the fraction of water occupying each cell element. Consequently, it provides a representation of the free surface, which is a function of both two-dimensional spatial

coordinates  $(x, y)$  and time  $(t)$ . The formulation can be expressed as follows:

$$\frac{\partial \psi}{\partial t} + u \cdot \nabla \psi = 0 \quad (5.12)$$

Here the parameter  $\psi$ , denoting the liquid volume fraction, ranges from 0 (representing air) to 1 (representing water). The simulation employs a  $2D$  mathematical modeling approach, grounded in a set of assumptions governing the variation of problem variables and their successive relationships. Fig. 5.1 illustrates all calculations pertaining to the boundary domain.

In line with established practices for most open channel flow systems, we adhere to the scaling law as proposed by Russo and Basse (2016) [46]. In this framework, two crucial parameters, namely turbulent intensity ( $I$ ) and turbulent length scale ( $l$ ), play a pivotal role, as highlighted by Chang et al. (2020) [47].

$$I = 0.16 \times Re^{-\frac{1}{8}} \quad (5.13)$$

$$l = 0.038d_h \quad (5.14)$$

where  $d_h$  represents the hydraulic diameter.

## 5.5 Grid Independent Test

A grid independence test was conducted to assess the ideal mesh density for computational simulations while maintaining precision in the obtained results. Within the fully developed region, data was extracted to analyze the normalized stream-wise velocity profiles under various mesh node configurations in the computational domain. In Fig. 5.2, we present the plot of normalized velocity (normalized using the friction velocity,  $u_*$ ) against normalized flow depth (normalized with the channel's water depth) for different levels of mesh refinement. Close to the channel bed, viscous effects dominate within the boundary layer. Therefore, meticulous mesh refinement is essential to ensure optimal results. Fig. 5.2 clearly demonstrates that, for three different mesh element numbers, the velocity profiles closely align across most of the flow region. This convergence of results indicates that the computational fluid dynamics (*CFD*) model employed in this study exhibits

## 5.5 Grid Independent Test

grid independence. For this investigation, data derived from a mesh comprising 77,432 elements were utilized in the computations, and the subsequent results are presented herein. The mesh domain is shown in the Fig. 5.3.

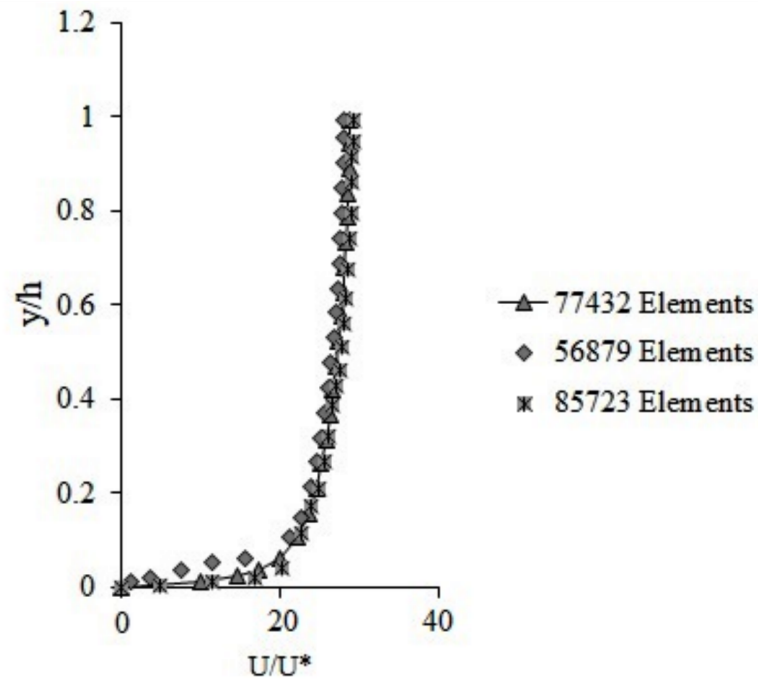


Figure 5.2: Normalized streamwise velocity plot for different grid elements

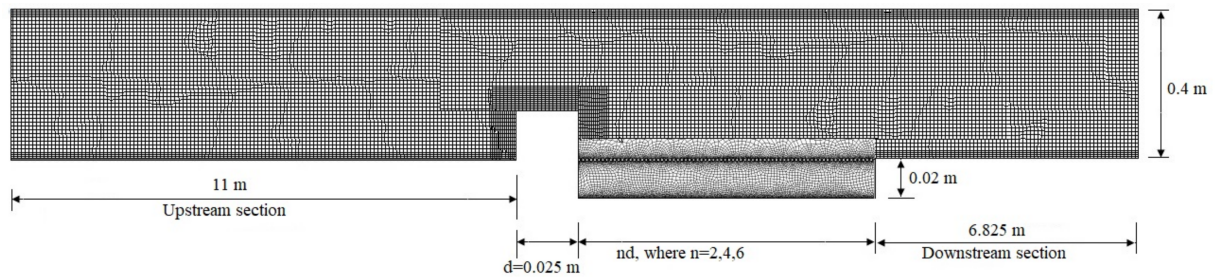


Figure 5.3: Schematic of the simulation domain with mesh

## 5.6 Validation of Velocity Profile with Log Law

The numerical model has been validated against experimental data at a Reynolds number of approximately  $Re \approx 70,000$  and compared with the logarithmic law. The normalized streamwise velocity ( $U = u/u_*$ ) from the numerical simulation is plotted on a logarithmic scale. The friction velocity, calculated from a wall shear stress of 0.027 Pa, is 1.2 cm/s. Figure 4 features a straight line representing the normalized logarithmic law, where  $U = u/u_*$  values are computed using von Karman's constant  $k = 0.41$  and  $A = 5.29$  as per Nezu and Nakagawa (1994) [48]. The comparison between the current results and the logarithmic law aligns well except in the near-wall area. This discrepancy in the near-wall region is consistent with findings by Banerjee and Singh (2022) [49], and is attributed to the linear law in the viscous sublayer, which aligns with fundamental theories. Additionally, deviations in the near-surface area are consistent with Coles' wake law in the turbulent outer layer.

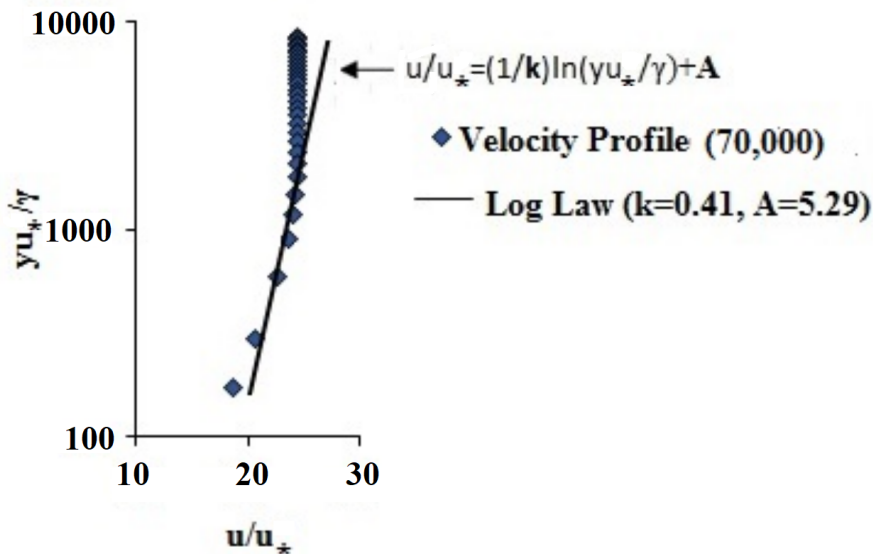


Figure 5.4: Validation with the Log-Law

### 5.7 Validation with Experimental Results

This section presents the validation of simulation results for normalized streamwise mean velocity  $U = u/u_*$  by comparing them with experimental data at three stream-wise locations, as illustrated in Fig. 5.5. The validation was performed at three positions relative to the obstacle: upstream, directly above, and downstream. The experiments were conducted in a square-mounted open-channel flume with dimensions of 18.3 m in length, 0.9 m in width, and 0.9 m in depth. The flume bed had a net cement finish and was maintained at a constant slope of 0.00025, ensuring hydraulically smooth bed flow under the tested conditions without any obstacles.

A vertical turbine pump with a discharge capacity of  $0.3 \text{ m}^3/\text{s}$  supplied water from a sump with dimensions of 30 m  $\times$  3 m  $\times$  2 m (length, width, and depth). Flow control was achieved using a valve between the pump and the flume inlet, with synchronized control between the discharge valve and the tailgate valve to maintain a constant desired flow depth throughout the channel. Wire meshes at the upstream side of the flume ensured smooth and uniform flow. Velocity time series data were collected using a 16 MHz Acoustic Doppler Velocimeter (*ADV*).

The experiments were performed with a submerged square in the flume, under identical flow conditions to those used in the numerical simulations, but without a jet. Measurements were taken in a fully developed turbulent zone at longitudinal locations  $x/d = -5, 0$ , and  $5$ , where  $x$  is the longitudinal distance from the square's center and  $d$  is the square's height. The free stream velocity at the upstream location was  $U_m = 35 \text{ cm/s}$ , resulting in a Reynolds number ( $Re_h$ ) of 70000 and a Froude number ( $Fr$ ) of 0.2, based on the flow depth ( $h = 20 \text{ cm}$ ).

Fig. 5.5 compares the numerical and experimental data for the streamwise mean velocity at different locations. The numerical results generally agree well with the experimental data, except near the bed. It is important to note that *ADV* measurements cannot be reliably performed very close to the bed, particularly within the viscous sublayer, for high Reynolds number turbulent flows. Nonetheless, the numerical simulation results show reasonable conformity with the experimental velocity profiles in the presence of the obstacle.

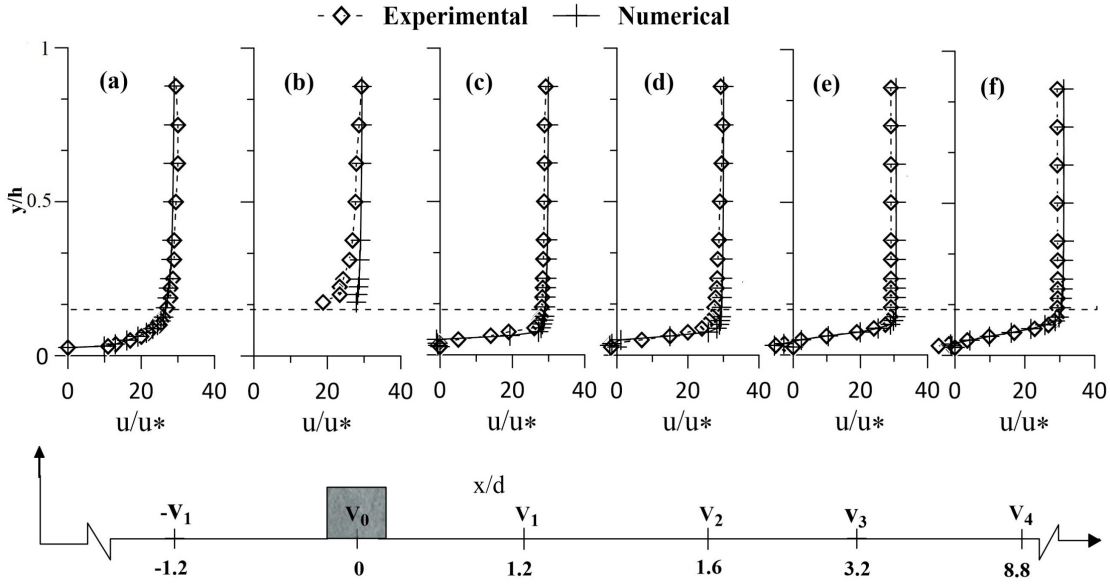


Figure 5.5: Validation of the Normalised x-velocity  $U = u/u_*$  at different positions relative to the obstruction

## 5.8 Result and Discussion

### 5.8.1 Variation of Vertical Normalized Mean-Velocity ( $U = u/u_*$ ) Component along x-Direction

The normalized longitudinal mean velocity ( $U = u/u_*$ ) is plotted in Fig.5.6 as a function of  $y/h$ , where  $h$  represents the constant water depth for a flow Reynolds number  $Re = 70,000$ . The normalized mean-velocity profile ( $U = u/u_*$ ) of a square-mounted bed without a jet is compared against jet-induced profiles where the jet velocities ( $u_i$ ) are maintained as integer multiples of the mean depth-averaged velocity, specifically at 35 cm/s, 70 cm/s, and 105 cm/s. Additionally, the effect of jet spread distance ( $l$ ) is investigated at  $l = 2d, 4d$ , and  $6d$  downstream of the obstacle. The resulting velocity profiles are presented at various stream-wise locations denoted as  $V_1, V_0, V_1, V_2, V_3$  and  $V_4$ , which are situated before, on, and after the square obstacle (refer to Fig.5.6). Fig.5.6 is organized into three rows corresponding to the jet velocities ( $u_i$ ) of 35 cm/s, 70 cm/s and 105 cm/s, respectively. For each with jet cases, the impact of jet spread distance ( $l$ ) on the

## 5.8 Result and Discussion

---

modulation of the re-circulation zone is compared at location  $V_1$  (upstream of the obstacle) and  $V_0$  (over the obstacle), as depicted in Fig.5.6( $a - n$ ). The velocity profiles for all cases converge, indicating that neither the jet velocity nor the jet spread affects the flow over and upstream of the obstacle.

Downstream of the obstacle, within the re-circulation zone, an irregular flow velocity pattern is observed. For the case of without a jet, a negative velocity is detected in the re-circulation zone. This region is characterized by the presence of vortices, as noted by Singh et al. (2019) [50]. In the first row (Fig.5.6( $a - f$ )), with a constant jet velocity of 35 cm/s, the influence of jet spread distance ( $l$ ) is evident in the velocity profiles downstream of the obstacle (Fig.5.6( $c - f$ )). A systematic effect of jet spread distance is observed, showing that the jet significantly shifts the negative velocity of the re-circulation zone (no-jet case) to positive longitudinal velocities.

In the second row (Fig.5.6( $i - l$ )), as the jet velocity is doubled to 70 cm/s, a prominent change in the flow pattern, particularly in the re-circulation zone, is observed. Negative velocities persist in the profile with a jet spread distance  $l = 5$  cm at locations  $V_3$  and  $V_4$ . Despite the lower velocity at  $l = 5$  cm, the profile shows maximum values at  $V_1$  and  $V_2$  locations (Fig.5.6( $i - j$ )) due to the smaller jet spread distance. When the jet velocity increases to three times the depth-averaged velocity (105 cm/s), retaining the same variations of jet spread distance ( $l$ ), the velocity profile variation is confined to the re-circulation zone up to an elevation of 5 cm (double the obstacle dimension) on the ordinates. As shown in Fig.5.6( $o - r$ ), no negative velocity prevails in the re-circulation zone under the influence of jets for all jet spread distances downstream of the obstacles.

This analysis indicates that a wall jet downstream of the obstacle effectively controls the re-circulation zone and mitigates negative pressure effects. Beyond 5 cm from the bottom, the influence of the jets becomes negligible. Thus, deploying wall jets downstream of obstacles serves as an efficient method for managing re-circulation zones and associated adverse pressure conditions.

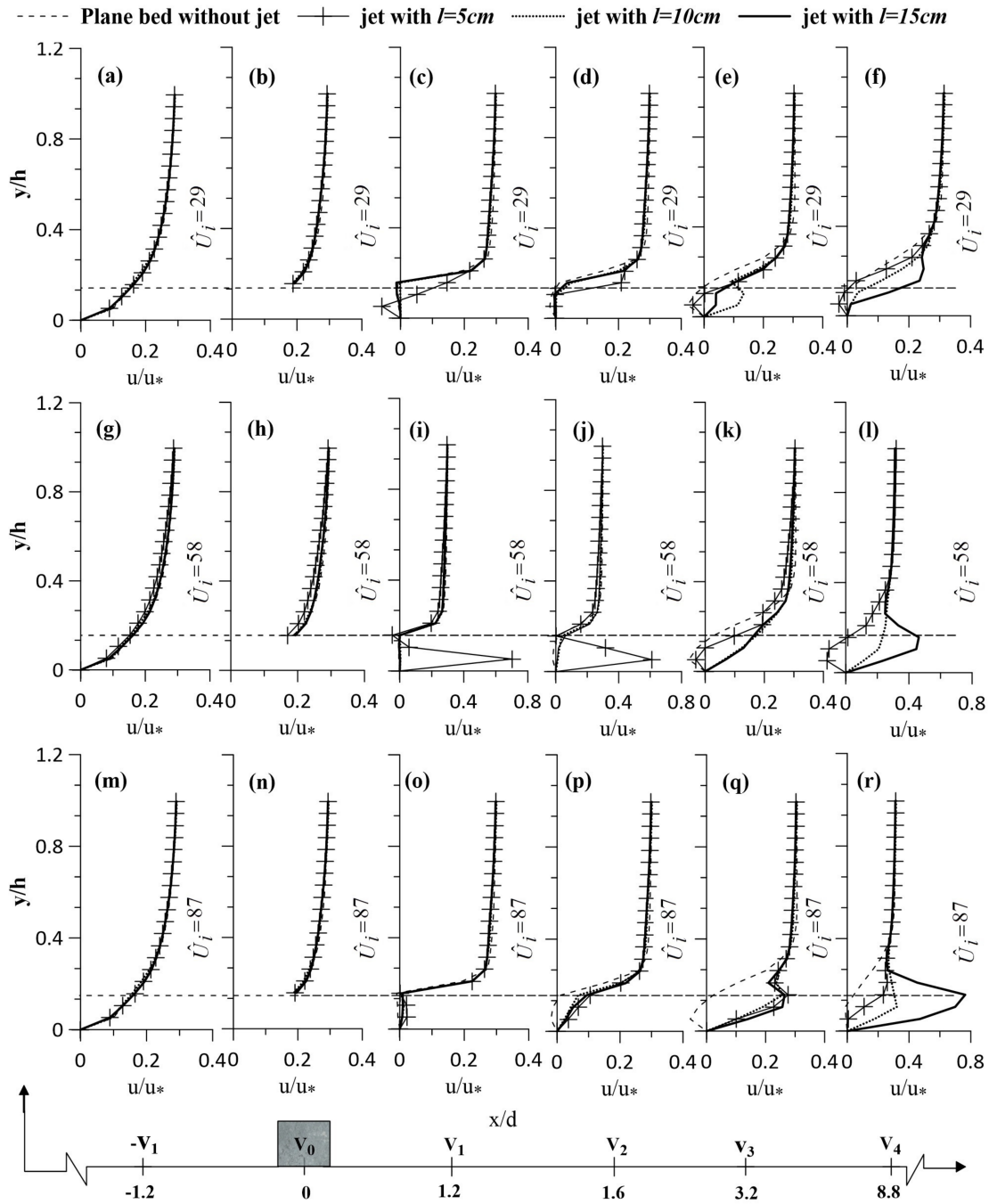


Figure 5.6: Variation of mean velocity along x-direction for without jet and with jet for a constant Reynolds number ( $Re = 70,000$ ) against the normalized vertical distance from the bed

### 5.8.2 Variation of Vertical Normalized Mean-Velocity( $V = v/u_*$ ) Component along y-Direction

As the problem is analyzed in the 2D domain, it is equally important to examine the variation of the vertical mean depth average velocity ( $V = v/u_*$ ) along the y-direction, as shown in Fig. 5.7. The location and configuration are exactly as depicted in Fig. 5.7. Across all rows, the modulation in velocity profiles due to jet induction is mainly observed in the wake region, influenced by the variation in jet velocity and the jet spread distance ( $l$ ). In the first row, the jet velocity is set at 35 cm/s, with the jet-spread distance varying at  $l = 5$  cm, 10 cm, and 15 cm. Notably, the velocity profiles for jet-induced cases become systematically less protruding with increasing jet-spread distance compared to the plane bed profile without the jet. The same variation in jet-spread distance ( $l$ ) is maintained for the other two rows, but the jet velocities are increased to 70 cm/s and 105 cm/s, respectively. The velocity profiles are more controlled in the re-circulation zone compared to the plane bed case without the jet, especially in the first row. The third row in Fig. 5.7( $o - q$ ) shows the maximum sequential elongation of the profiles compared to the other two rows. The upstream velocity profiles before the square obstacle match exactly with each other. This same pattern is observed in the flow structure over the obstacle and away from the re-circulation zone in the downstream region. The only variations occur in the re-circulation zone, where flow complexity arises due to turbulence mixing.

### 5.8.3 Contour Pattern of Velocity

The contour plot of longitudinal velocity is depicted in Fig. 5.8. The first row illustrates the contour plot for the longitudinal velocity structure past the obstacle without a jet. The second row displays the contour plots for jet-induced cases with varying jet-induced velocities studied here, with a constant jet spread distance of  $l = 5$  cm. The third and fourth rows represent the same for different fixed jet spread distances,  $l = 10$  cm and 15 cm respectively. In the without-jet case, a strong re-circulation zone in the wake region extends 22 cm downstream of the obstacle, indicated by the dark black region. This dark spot, showing flow reversal due to a high-pressure drop, is marked by the presence of vortex shedding [51].

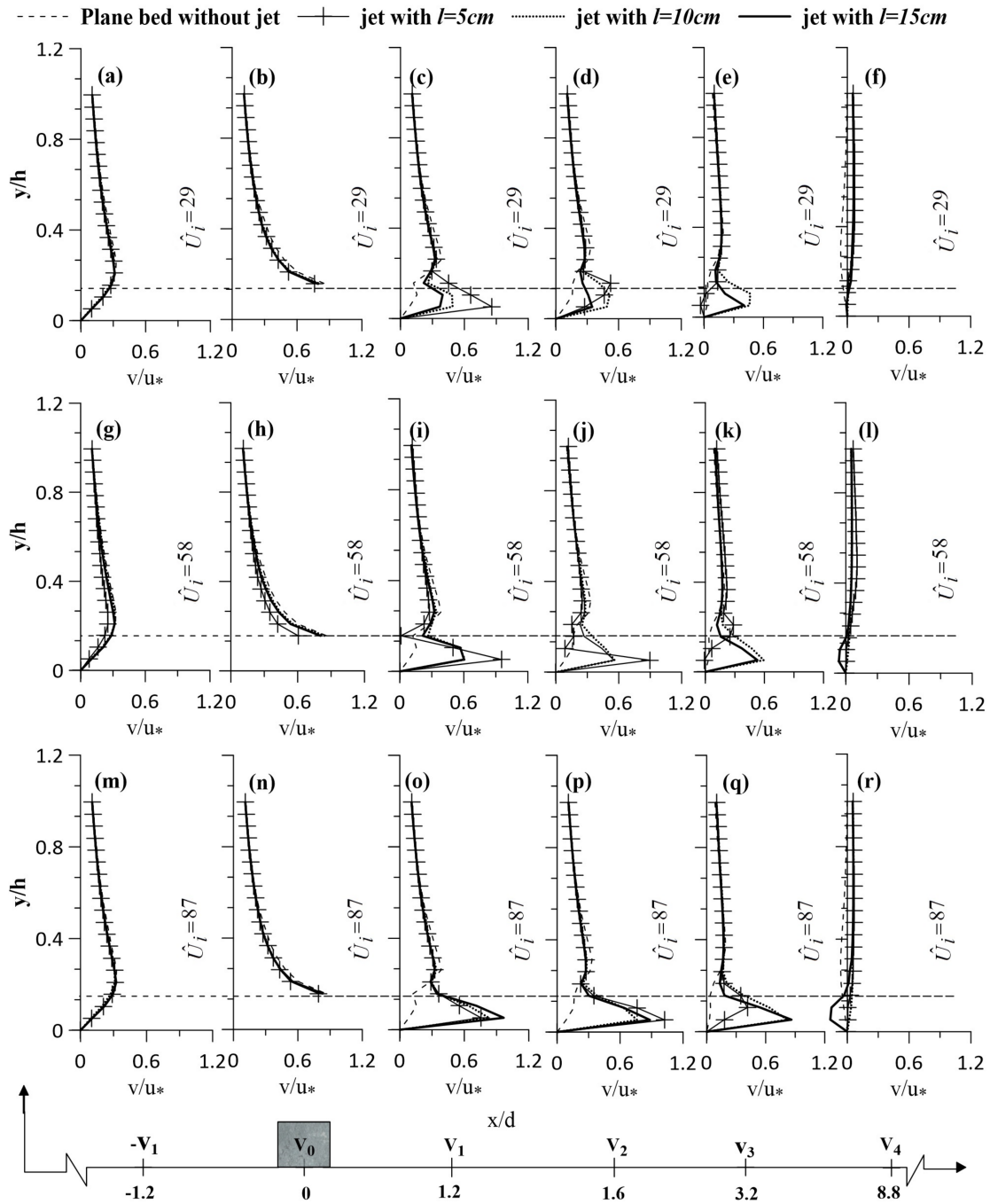


Figure 5.7: Variation of mean velocity along y-direction for without jet and with jet for a constant Reynolds number ( $Re = 70,000$ ) against the normalized vertical distance from the bed

## 5.8 Result and Discussion

---

Negative velocity ( $U = 0.01$ ) is observed in this area, indicating flow reversal. In the first row, the short jet-spread distance ( $l$ ) prevents the strong re-circulation zone from being fully extinguished, as shown in Fig. 5.8( $b - c$ ). A slightly varied contour is observed in Fig. 5.8( $d$ ) near the jet inlet point due to the higher jet velocity. Thus, no significant change is observed in the first row that could eliminate the re-circulation zone. Here, the thickness of the black spot is less than that in the plane bed without a jet profile.

The second row shows a notable modulation of the re-circulation zone by doubling the jet-spread distance ( $l = 10$  cm). With increased jet velocity, the negative velocity structure systematically disperses, as seen in Fig. 5.8( $f - g$ ). The last row in Fig. 5.8 shows significant modulation of the re-circulation zone with the jet-spread distance increased to three times the characteristic length of the obstacle ( $l = 15$  cm) downstream of the obstacle. A large part of the near-bed region shows a positive longitudinal velocity except for a few patches of negative velocity. In this region, the pressure drop induced by the jet is significantly reduced with the tripled jet-spread distance, thus freeing the wake region from the generation of eddies that cause vortex shedding.

### 5.8.4 Streamline Plot of the Flow Structure

The streamline plot of the flow structure, as depicted in Fig. 5.9 in this study, provides a visual representation of the flow behavior around a square obstruction with and without the introduction of jets. In the top row of 5.9( $a$ ), the streamline plot represents the flow structure without any jet input. A strong re-circulation wake region is observed behind the square obstruction. The core of the re-circulation zone is located approximately at  $x/d = 0.15$  downstream of the obstacle. The streamline plot shows the formation of eddies and vortices in the wake region, typical of flow patterns around bluff bodies. The introduction of jets plays a significant role in modifying the flow structure and controlling the re-circulation zone. By varying the jet-spread length and jet-injection velocity, the flow behavior can be altered to dampen the re-circulation zone. The combination of jet-spread length and jet-injection velocity leads to changes in the flow patterns, reducing the intensity of re-circulation behind the obstruction. In view of the Systematic

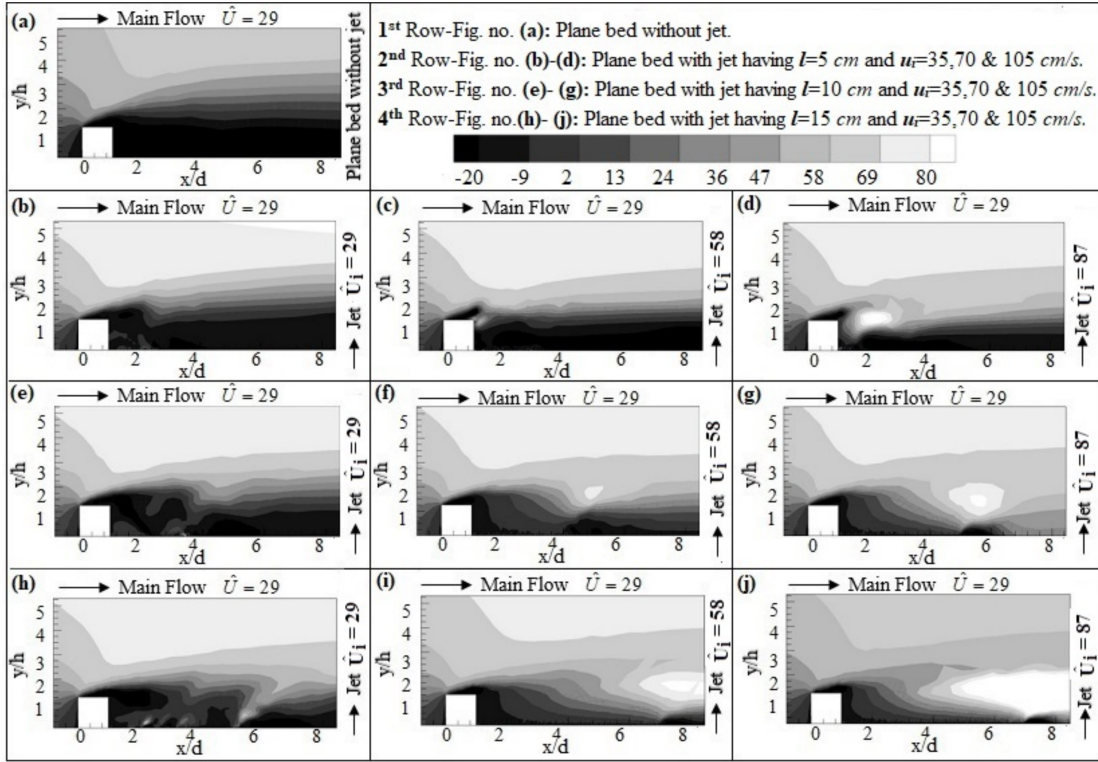


Figure 5.8: Contour plot of stream-wise vertical depth average velocity  $U$  in 2D against normalized horizontal distance along bed ( $x/d$ ) and the normalized vertical distance from the bed ( $y/h$ )

Behavior of Streamline Plots, the streamline plots exhibit systematic behavior as expected in response to the introduction of jets. The interaction between the jets and the flow field around the square obstruction results in changes in the flow direction and velocity distribution. The streamline plots visually demonstrate how the jets influence the flow patterns and help in mitigating the re-circulation zone. For control of re-circulation zone, the jet-spread distance is a critical factor in controlling the re-circulation zone and minimizing the generation of eddies that lead to vortex shedding. The streamline plots illustrate how adjusting the jet-spread length can influence the flow behavior and reduce the issues associated with vortex shedding.

The streamline plot analysis in Fig. 5.9 provides valuable insights into the impact of jet introduction on the flow structure around a square obstruction. It highlights the effectiveness of jets in modulating the re-circulation zone and

## 5.8 Result and Discussion

altering the flow patterns to mitigate vortex-induced vibrations and improve the overall flow characteristics in the wake region of the bluff body.

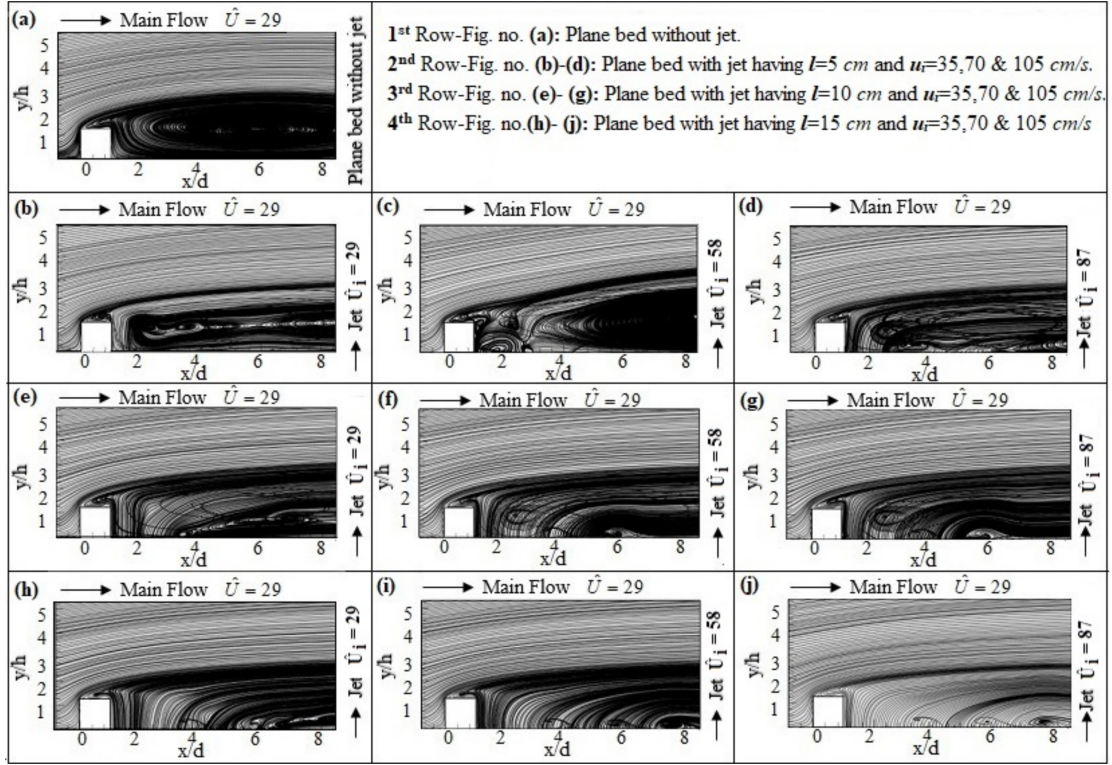


Figure 5.9: Streamline plot of stream-wise vertical depth average velocity ( $U$ ) in 2D against normalized horizontal distance along bed ( $x/d$ ) and the normalized vertical distance from the bed ( $y/h$ )

### 5.8.5 Contour plot of static pressure

The Static Pressure Contour plot in Fig. 5.10 shows the irregularities in the flow pattern, particularly in the wake region of the square obstruction. These irregularities are a result of the pressure difference generated by the form drag induced by the presence of the obstruction. The contour plot visually represents the variations in pressure levels across different regions of the flow domain. The re-circulation zone is marked by a large pressure drop, indicated by negative pressure values ( $\approx \Delta P = -18N/m^2$ ). In the absence of jets, the pressure distribution in the re-circulation zone shows significant pressure drop due to the flow behavior

around the obstruction. As jets are introduced into the re-circulation zone shown in the Fig. 5.10(*b – j*), changes in the pressure distribution are observed. The contour plot demonstrates how the negative pressure zone in the re-circulation region disperses systematically with the introduction of jets. In the second row [Fig. 5.10(*b – d*)], with the jet-spread distance kept constant at  $l = 5$  cm and varying jet injection velocities ( $u_i = 35, 70, 105$  cm/s), a systematic increase in pressure is observed as the negative pressure region disperses. The pressure recovery process is visualized as the jets interact with the flow field and modify the pressure distribution in the wake region. Increasing the jet-spread distance to  $l = 10$  cm for different jet velocity cases (5.10, third row) also shows a systematic increase in pressure recovery in the wake region; notably, the efficiency of pressure recovery improves for the same jet injection velocity with a longer jet-spread distance. In the last row, with parameters set to  $l = 15$  cm and  $u_i = 35, 70, 105$  cm/s, the pressure difference across the entire flow domain is controlled, resulting in complete recovery of the pressure field. The contour plot showcases the influence of jet parameters, such as jet-spread distance and jet injection velocity, on pressure recovery. By varying the jet-spread distance and jet injection velocity, the pressure field in the wake region can be controlled and optimized. Increasing the jet-spread length and adjusting the jet injection velocity lead to enhanced pressure recovery and a more uniform pressure distribution across the flow domain. The Static Pressure Contour plot provides insights into how the introduction of jets can influence the pressure field, reduce pressure differentials in the re-circulation zone, and improve the overall flow characteristics around the square obstruction. It visually demonstrates the effectiveness of jet modulation in controlling the pressure distribution and optimizing the flow patterns to mitigate vortex-induced vibrations and enhance flow stability.

### 5.8.6 Contour Plot of Turbulent Kinetic Energy

The Turbulent Kinetic Energy (*TKE*) contour plot of this research work provides insights into the distribution of turbulent energy in the flow field around the obstruction with and without the introduction of jets. The *TKE* contour plots for the cases without jet and with jet flow are presented in Fig. 5.11. *TKE*, or

## 5.8 Result and Discussion

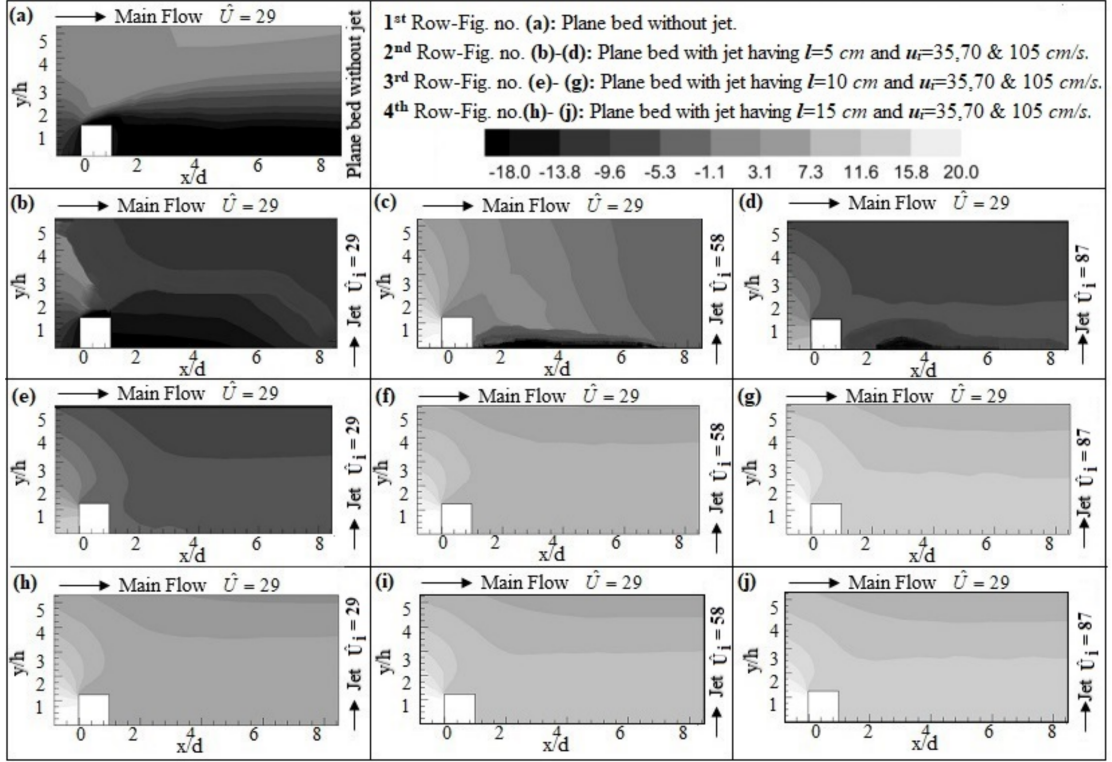


Figure 5.10: Contour plot of stream-wise static pressure ( $P$ ) in 2D against normalized horizontal distance along bed ( $x/d$ ) and the normalized vertical distance from the bed ( $y/h$ )

turbulent kinetic energy, is a crucial parameter representing the mean turbulent kinetic energy per unit mass in a turbulent flow with eddies. The  $TKE$  contour plot helps visualize the distribution of turbulent energy levels and how they vary across different regions of the flow domain. Near the wall,  $TKE$  variation is more pronounced ([52]) due to turbulence production influenced by the obstacle. The  $TKE$  contour plot helps visualize the distribution of turbulent energy levels and how they vary across different regions of the flow domain. In the case without jet flow, as shown in Fig. 5.11(a), most of the domain exhibits small  $TKE$  values, with minor modulations in the re-circulation zone. These small changes in  $TKE$  values result from mean flow instability and the complex flow structure in the re-circulation zone, leading to additional  $TKE$  production ([53]). Downstream of the obstacle and in the bottom wall region, the wall-normal jet may disrupt the viscous sublayer due to bursts of turbulent vortices ([54]). Consequently, the  $TKE$

variation does not follow a precise pattern. The  $TKE$  contour plot illustrates how the introduction of jets influences the distribution of turbulent energy in the flow field. In cases where jets are introduced, changes in  $TKE$  values are observed, especially in the wake region behind the obstruction. The interaction between the jets and the flow field leads to modifications in  $TKE$  levels, indicating the impact of jet-induced turbulence on the flow dynamics.

In Fig. 5.11(*a* and *c*), despite the influence of multiple jets, no significant changes are observed in  $TKE$  values. By adjusting jet parameters such as jet-spread distance and jet injection velocity, the  $TKE$  distribution can be modulated. Doubling the jet-spread distance to  $l = 10$  cm and varying jet velocities ( $u_i = 35, 70, 105$  cm/s) result in higher  $TKE$  values in the wake region. These higher  $TKE$  values indicate scale modulation dominated by large-scale eddies. It is suggested that the downstream jets introduce large-scale eddies into the system. Generally, a scale breakdown occurs when two flow systems collide. Here, the interaction between the jets and the main stream flow in a cross direction increases  $TKE$  values, potentially introducing additional turbulence scales and leading to a rise in  $TKE$ .

Additionally, a white feather-shaped patch is observed downstream of the recirculation zone at a height equivalent to the obstacle dimension. Away from the wall, the jet effect is prominent in the re-circulation zone, resulting in increased  $TKE$  values at a distance from the bed equivalent to the obstacle dimension. Despite the uniform intensity measures of the jet velocities for each row across all jet input profiles, noticeable changes occur due to variations in the jet-spread distance ( $l$ ) within the specified range.

### 5.8.7 Contour Plot of Turbulent Dissipation Rate ( $\epsilon$ )

The dissipation rate of turbulent kinetic energy ( $TKE$ ), known as the turbulent dissipation rate, is a key parameter that quantifies the conversion of turbulence energy into internal energy. The Turbulent Dissipation Rate, denoted as  $\epsilon$ , represents the rate at which turbulent kinetic energy dissipates into internal energy due to the action of small-scale turbulent eddies. In a system at equilibrium,  $TKE$  production equals the  $TKE$  dissipation rate. This equilibrium results in mixing

## 5.8 Result and Discussion

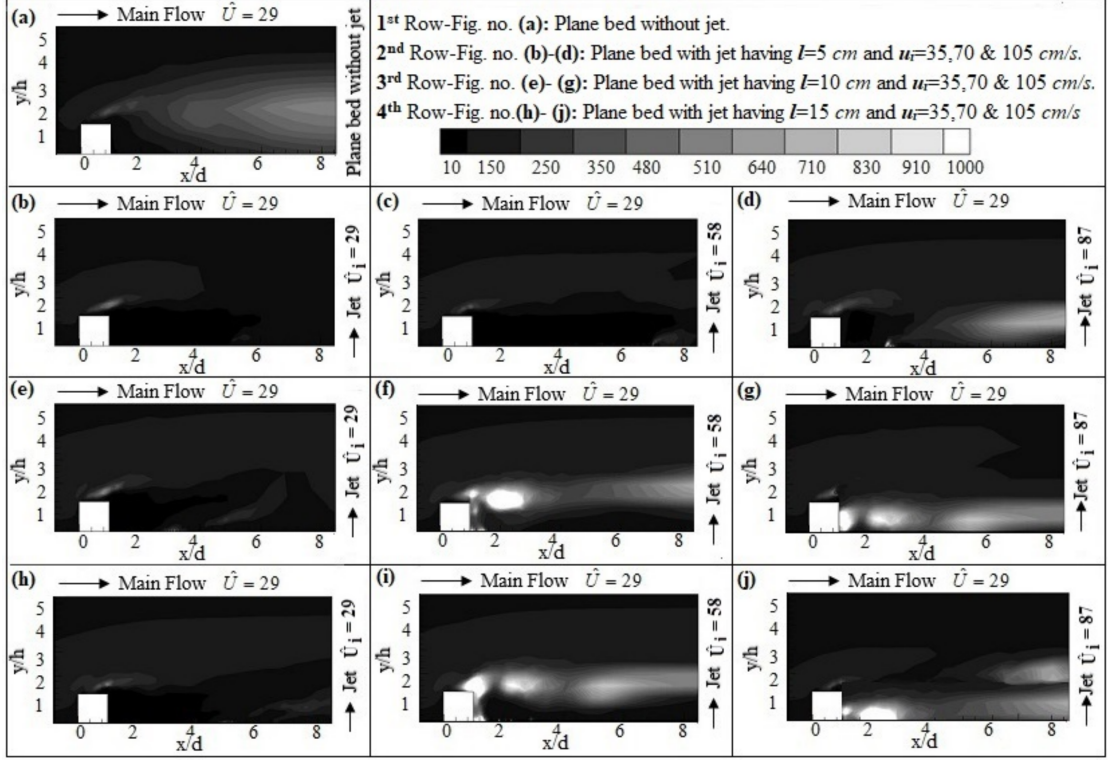


Figure 5.11: Contour plot of stream-wise turbulent kinetic energy ( $K$ ) profile in 2D against normalized horizontal distance along bed ( $x/d$ ) and the normalized vertical distance from the bed ( $y/h$ )

properties promoted by smaller eddies at the interface, influencing transport phenomena ([49, 55]). Fig. 5.12 presents a contour plot of the turbulent dissipation rate. The dissipation data is normalized with the square of the frictional velocity ( $u_*^2$ ) and plotted against the normalized horizontal distance along the bed ( $x/d$ ) and the normalized vertical distance from the bed ( $y/h$ ). The figure shows that changes in dissipation values are observed only in the re-circulation zone, which is highly prone to turbulence generation due to the transport phenomenon controlled by small eddies at the interface. ([19]) employed various methods to determine the turbulence energy dissipation rate; the  $2\rho S_{ij}S_{ij}$  term in Eq. 5.8 was used to obtain the turbulent dissipation rate per unit mass. For high Reynolds number flows, the turbulence dissipation rate in the small-scale energy cascade can be of the order of unity, regardless of the root mean square velocity ([56]). In Fig. 5.12, the square mounted bed without jet contour [Fig. 5.12(a)] is compared with the

multiple jet-input contours [Fig. 5.12( $b-j$ )], which vary according to the jet-input velocity ( $u_i$ ) and jet-spread distance ( $l$ ).

The dissipation value for the plain bed without jet is very low throughout the domain, with only minor changes observed in the re-circulation zone and above the obstacle. Since the jet covers most of the re-circulation zone in the bed, as shown in Fig. 5.12( $e-j$ ), dissipation values are highest near the bed. The turbulence field is a highly random quantity with its own probability density function domain ([57]), which intensifies with an increase in the jet Reynolds number. Intermittency in turbulent kinetic energy is present in the re-circulation zone, balancing production and destruction. The distribution of dissipation is a well-accepted phenomenon, described irrespective of the instantaneous fluctuating turbulence dissipative scale formation ([58]). In the cascade mode, the dissipation rate, which converts total kinetic energy into heat energy, shows very small values at high Reynolds numbers due to the predominance of viscous effects (except in the re-circulation zone) over inertia ([59]). From this maximum value, dissipation decreases abruptly beyond  $y/h = 3$  on the ordinate, with no significant changes observed in the flow field, resulting in consistently minimum values.

## 5.9 Conclusion

The primary objective of this work is to modulate the re-circulation zone behind a square cross-section  $2D$  obstacle using  $2D$  multiple wall jets ejected in a cross-flow direction, aiming for complete pressure recovery. The computational model framework is developed under a *VOF* framework, considering the two-dimensional analysis of an open channel with a square cross-section bottom obstacle.

The focus of this study is to identify the spreading of the re-circulation zone in the wake region behind the obstacle and to assess the jet spread length effective for its complete eradication. Additionally, the study investigates the behavioral changes of the main turbulent characteristics over the flow domain. For this purpose, the standard  $k - \omega$  *SST* turbulent closure model is solved. A detailed evaluation of flow characteristics in the re-circulation zone behind the square cross-section  $2D$  obstacle using turbulent multi-jets is conducted for three different sets of jet Reynolds numbers. This systematic analysis aims to understand the effect of

## 5.9 Conclusion

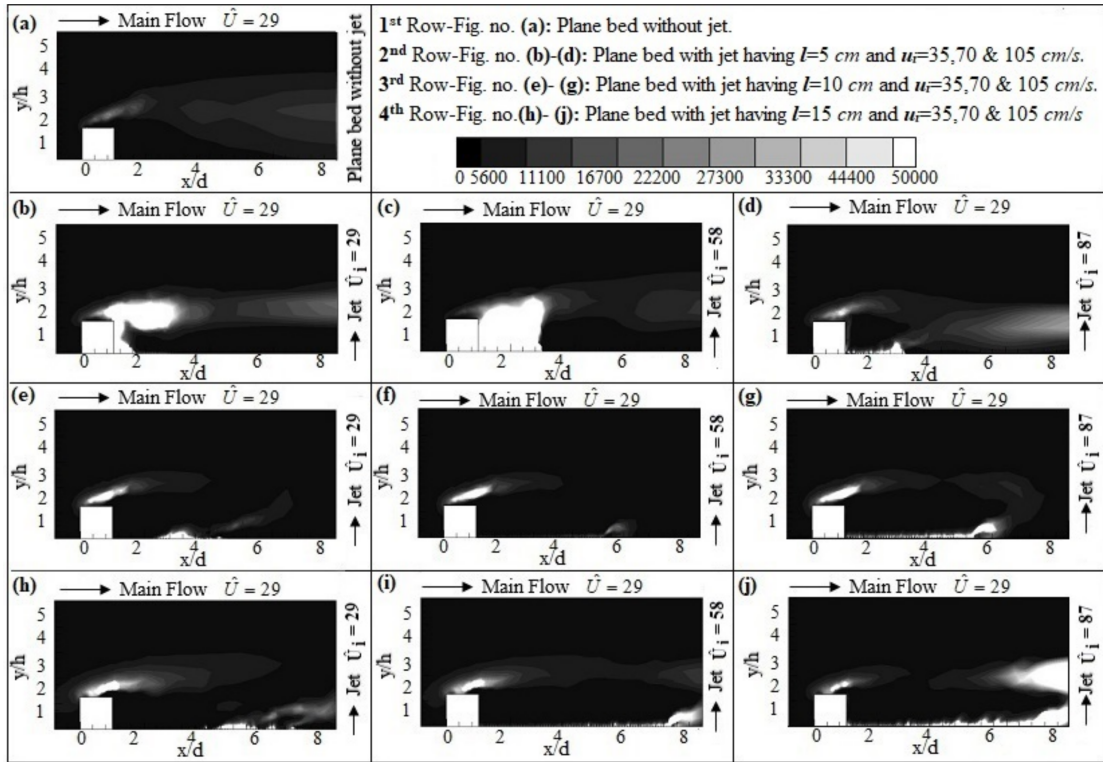


Figure 5.12: Contour plot of stream-wise vertical turbulent dissipation rate ( $\epsilon$ ) profile in 2D against normalized horizontal distance along bed ( $x/d$ ) and the normalized vertical distance from the bed ( $y/h$ )

downstream jet-spread length and jet efflux velocity on achieving pressure recovery and controlling the re-circulation region. The key findings are as follows:

The static pressure in the wake region behind the obstacle shows a negative value, indicating an adverse pressure gradient in the re-circulation zone for open channel flows over a submerged square cross-section  $2D$  obstacle without jets. This leads to vortex shedding in the re-circulation zone, generating unwanted vibrations that may be detrimental to the structure. The introduction of turbulent multi-jets creates more disturbances in the flow pattern in the re-circulation zone behind the square obstacle. Entrainment of ambient fluid starts from the transition zone of the multi-jets, leading to improved mixing. Consequently, there is an enhancement of the turbulent dissipation rate, especially in the recirculating zone. This study suggests that controlling the re-circulation zone could reduce the generation of unwanted vibrations in the object. Different sizes of square cross-section  $2D$

obstacles can be used to optimize the problem by varying jet Reynolds numbers. Changing the orientation of the multi-jets can help observe how phenomenological changes in turbulent properties are better visualized. This study also considers how softly or violently the jets are used to prevent the jets' effects on the object, rather than the issues arising in the re-circulation zone due to the main flow. This directly informs the required spacing among the jets to eradicate vortex-shedding effects and achieve a more satisfactory level of optimization. Future scope: This study focuses on a single square cross-section  $2D$  obstacle, but flow characteristics could be investigated using several similar obstacles. Creating a suction force by vacuuming the jet-input chamber may be incorporated to study the effects on the re-circulation zone. Additionally, a  $3D$  model could provide more proficiency in addressing real-life problems.

MODULATION OF  
RE-CIRCULATION ZONES  
BEHIND A SQUARE  
OBSTRUCTION BY  
BLOWER-INDUCED SUCTION  
FORCE

This study examines the use of suction force generated by a blower at high Reynolds numbers to manipulate and eliminate the re-circulation region behind a fully submerged  $2D$  square bluff body. An obstruction in the form of a square is placed in an open channel, followed by an array of small downstream openings. The strong re-circulation zone and vortex shedding in the wake can cause unwanted vortex-induced vibrations, potentially leading to structural damage. The research investigates controlling the re-circulation by varying both the suction force and the length of the suction panel. Numerical simulations use a 2-phase Volume of Fluid (*VOF*) model with open channel boundary conditions and the standard

$k - \epsilon$  turbulence model to solve the momentum and continuity equations. The re-circulation zone is identified by analyzing the negative mean stream-wise velocity and visualized through streamlined contour plots. Different suction velocities are tested to redistribute or eliminate the re-circulation region.

## 6.1 Formulation of the problem

A two-dimensional square obstruction ( $0.025 \text{ m} \times 0.025 \text{ m}$ ) is placed in the fully developed region of a rectangular cross-section channel ( $18 \text{ m} \times 0.4 \text{ m}$ ). When the flow passes over the square obstruction, a strong re-circulation zone is observed, spreading significantly in the wake region. The mainstream depth-averaged velocity  $u_m$  is maintained at  $0.35 \text{ m/s}$ . An array of suction panels with square openings of  $0.002 \text{ m}$  each and varying lengths ( $(l) = nd$ , where  $d$  is the height of the square obstruction and  $(n = 2, 4, 6)$ ) is arranged just before the obstruction, just beneath the channel bed. The depth of the suction panel is  $0.035 \text{ m}$ . The square obstruction is placed on the bed at a distance of  $11 \text{ m}$  from the channel entry, marked as zero for convenience in position analysis. The model schematic is represented in Fig. 6.1.

To perform a comprehensive analysis of the open channel flow, a commercial *CFD* solver, *ANSYS FLUENT*, is used to numerically solve the governing equations. The non-iterative time advancement *PISO* algorithm is employed with second-order accuracy. The computational domain is designed in *ANSYS Space Claim*. The channel specifications are shown in Table.6.1. All details of the hydraulic parameters for the square-mounted bed, both without suction and with suction, are provided in Table.6.2 and Table.6.3, respectively.

### 6.1.1 Boundary conditions

The boundary conditions of this computational problem are crucial for solving the governing equations in Ansys Fluent software. The objective is to numerically solve an open channel turbulent flow problem using simulation within a computational fluid dynamics (*CFD*) framework. The boundary conditions are configured in the pre-processor setup of Ansys Fluent.

## 6.1 Formulation of the problem

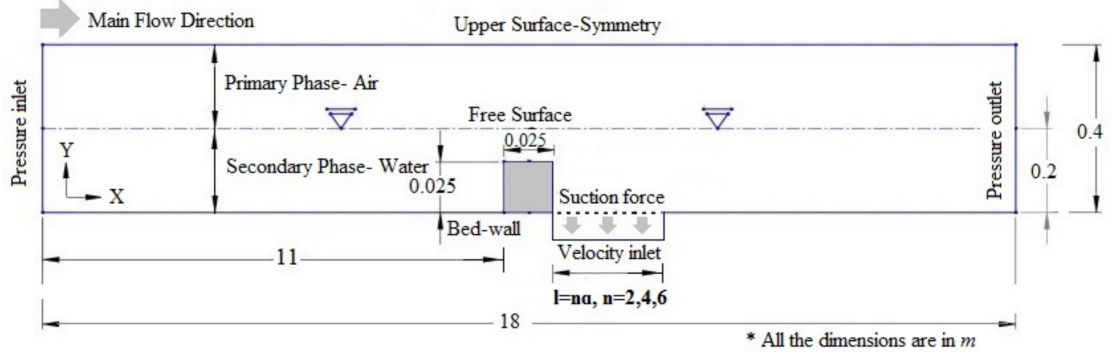


Figure 6.1: The diagrams of computational configuration with boundary conditions.

Table 6.1: specification of the Channel

Channel parameters	Dimensions
The channel length, $l$ (m)	18
The channel height, $h$ (m)	0.4
The arm of the square obstruction, $a$ (m)	0.025
Area of the square obstruction, $A$ (m <sup>2</sup> )	$0.025 \times 0.025$
Suction opening square hole each, ( $m$ )	0.002
Suction panel length, $l = na$ , where $n = 2, 4, 6$ (m)	0.05, 0.10, 0.15

This open-channel Ansys model incorporates four primary boundary conditions along with an additional one at the suction panel. As illustrated in Fig. 6.1, the boundary conditions are: symmetry at the top surface, pressure inlet at the channel inlet, pressure outlet at the channel outlet, and wall conditions for both the bottom surface and the square obstacle, applying the no-slip ( $u = 0$ ) and no-penetration ( $v = 0$ ) conditions with a standard wall function. The suction panel's boundary condition is defined as a velocity inlet. For the pressure and velocity inlet boundary conditions, the parameters are set using  $I = 0.16 \times Re^{-\frac{1}{8}}$  [60], where  $I$  and  $k_n$  represent the turbulent intensity and kinetic energy, respectively. Additionally, the turbulent energy dissipation  $\epsilon_n$  is related to  $\epsilon_n = \left(k_n^{3/2} C_\mu^{3/4}\right) / l$  [60] with  $l = 0.7$  according to Prandtl's mixing length model. In all simulations, the flow depth for both water (secondary phase) and air (primary phase) is set to 0.2 m. To prevent any influence of the air phase on the water phase, a sufficiently large depth of 0.2 m is chosen for the air phase. The standard *VOF* model is

Table 6.2: Hydrodynamic parameters for open channel without suction

Parameters	Values
Reynolds number, $Re = uh/\gamma$	70,000
Stream wise depth average velocity $u$ (m/s)	0.35
The depth of mean flow, $h$ (m)	0.20
Friction velocity (computed from the log law) $u_*$ (m/s)	0.012
Froude number, $Fr$	0.15

Table 6.3: Hydrodynamic parameters for open channel with suction

Parameters	Values
Reynolds number, $Re = uh/\gamma$	70,000
Stream wise depth average velocity $u$ (m/s)	0.35
The depth of mean flow, $h$ (m)	0.20
Friction velocity (computed from the log law) $u_*$ (m/s)	0.012
Suction panel sucking velocity, $u_i$ (m/s)	0.30, 0.70, 1.05
First set of Suction Reynolds numbers, $Re_i = u_i l / \gamma (l = 2d)$	15487, 30973, 46460
Second set of Suction Reynolds numbers, $Re_i = u_i l / \gamma (l = 4d)$	30973, 61947, 92920
Third set of Suction Reynolds numbers, $Re_i = u_i l / \gamma (l = 6d)$	46460, 92920, 139381

employed to account for the free surface boundary and the two phases of flow. Given the rectangular flow domain, the *VOF* model is appropriate for this study [61]. It is noteworthy that the ratio of the air to water depth is greater than 0.5 (equal to 1), indicating that the impact of the wall boundary at the top is negligible [40].

### 6.1.2 Governing Equations

Assuming an unsteady, two-dimensional, turbulent, and incompressible flow with isometric fluid properties, the time-averaged Reynolds-averaged Navier-Stokes (*RANS*) equations are solved to characterize the flow structure and predict the turbulent flow in an open channel. The Boussinesq hypothesis is employed to relate the Reynolds stress to the mean velocity gradient. The standard  $k - \epsilon$  turbulent model is used in this study. The continuity, momentum, and transport equations are expressed using non-dimensional variables based on the friction velocity ( $u_*$ )

## 6.1 Formulation of the problem

---

of the flow as follows

**Continuity equation:**

$$\frac{\partial U_i}{\partial X_i} = 0 \quad (6.1)$$

**Momentum equation:**

$$\frac{\partial U_i}{\partial \tau} + \frac{\partial}{\partial X_j} (U_j U_i) = -\frac{\partial}{\partial X_i} \left( P + \frac{2}{3} k_n \right) + \frac{1}{Re} \frac{\partial}{\partial X_j} \left[ (1 + \gamma_{t,n}) \frac{\partial U_i}{\partial X_j} \right] \quad (6.2)$$

where,

$$U_i = \frac{u_i}{u_*}, X_i = \frac{x_i}{d}, \tau = \frac{t}{d/u_*}, P = \frac{p - p_0}{\rho u_*^2}, k_n = \frac{k}{u_*^2} \quad (6.3)$$

**The  $k - \epsilon$  model transport equations:**

$$\frac{\partial k_n}{\partial \tau} + \frac{\partial}{\partial X_j} (U_j k_n) = \frac{1}{Re} \frac{\partial}{\partial X_j} \left[ \frac{\gamma_{t,n}}{\sigma_k} \frac{\partial k_n}{\partial X_j} \right] + G - \epsilon_n \quad (6.4)$$

$$\frac{\partial \epsilon_n}{\partial \tau} + \frac{\partial}{\partial X_j} (U_j \epsilon_n) = \frac{1}{Re} \frac{\partial}{\partial X_j} \left[ \frac{\gamma_{t,n}}{\sigma_\epsilon} \frac{\partial \epsilon_n}{\partial X_j} \right] + C_{1\epsilon} \frac{\epsilon_n}{k_n} G - C_{2\epsilon} \frac{\epsilon_n^2}{k_n} \quad (6.5)$$

where,  $G$  is the production term and  $\gamma_{t,n}$  is eddy viscosity. These two terms are related as

$$G = \frac{\gamma_{t,n}}{Re} \left[ \frac{\partial U_i}{\partial X_j} + \frac{\partial U_j}{\partial X_i} \right] \frac{\partial U_i}{\partial X_j}, \gamma_{t,n} = C_\mu Re \frac{k_n^2}{\epsilon_n} \quad (6.6)$$

The model constant are  $\sigma_k = 1$  and  $\sigma_\epsilon = 1.30$ ,  $\sigma_{1\epsilon} = 1.44$  and  $\sigma_{2\epsilon} = 1.92$  [62]

### 6.1.3 Grid independence test

To perform a grid independence test and analyze discretization errors, several key aspects need to be considered. The Grid Convergence Index (GCI), which is calculated as  $GCI = F_s \times E_{u,k}$ , where  $F_s$  is the safety factor and  $E_{u,k}$  represents the errors on the target grids, is used to determine the degree of acceptance of the test results [63]. For this analysis, three different grid densities (denoted as  $N_X \times N_Y$ ) were considered: Grid-1 ( $1512 \times 34$ ), Grid-2 ( $1760 \times 43$ ) and Grid-3 ( $1848 \times 52$ ). These grids contain 54,263, 81,452, and 115,256 elements, respectively, within the

computational domain, as summarized in Table. 6.4. The grid refinement ratio  $r_k$ , which is the ratio of the number of control volumes ( $h$ ) for successive refined meshes, is fixed at approximately 1.5 (i.e.  $r_k = h_2/h_1 = h_3/h_2$ ). From the plot shown in Fig. 6.2, the normalized depth average velocities were calculated to be 26.49, 25.35, and 24.89 for each of the grid samples. The error was calculated using the formula  $E_{u,k} = (S_i - S_j)/S_j(r_k^p - 1)$ , where  $S_i$  and  $S_j$  are the solutions at successive steps of grid refinement. Given that the governing equations are second-order, the value of  $p$  is taken as 2, and the safety factor  $F$  is taken as 1.25. [63].

The calculated values of the Grid Convergence Index ( $GCI$ ) for the grids, in ascending order of grid density, are  $GCI_{12} = 4.49\%$  and  $GCI_{23} = 1.84\%$ . Since  $GCI_{23}$  is less than  $GCI_{12}$ , there is a continuous succession of grid refinement. Furthermore, the solution falls within the asymptotic range of convergence because  $GCI_{12}/r_k^p GCI_{23} = 1.08 \approx 1$ . The velocity profiles obtained from different grid densities indicate that the solutions for Grid-1 and Grid-2 differ from those obtained for Grid-3. As a result, the grid independence test conducted for this research is deemed acceptable. The final solution is based on the data obtained through CFD analysis using Grid-3, as illustrated in Fig. 6.3. Additionally, the mesh for the wall boundary layer was created by employing mesh inflation and adding multiple layers, ensuring that the  $y^+$  value remains below 1.

Table 6.4: Grid convergence index test for grid density refinement

Grid	$N_X \times N_Y$	No. of Elements	$u/u_*$	$r_k$	$P$	%GCI	$GCI_{12}/r_k^p GCI_{23}$
Grid-1	$1512 \times 34$	54,263	26.49	1.5		—	
Grid-2	$1760 \times 43$	81,452	25.35	1.5	2	4.49	$1.08 \approx 1$
Grid-3	$1848 \times 52$	115,256	24.89	1.5		1.84	

## 6.1 Formulation of the problem

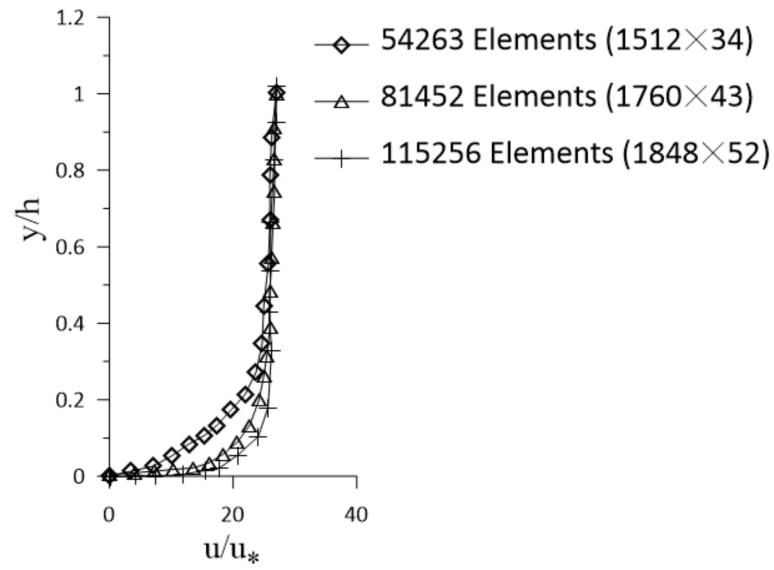


Figure 6.2: Stream-wise normalized velocity profile plot for three different grid elements

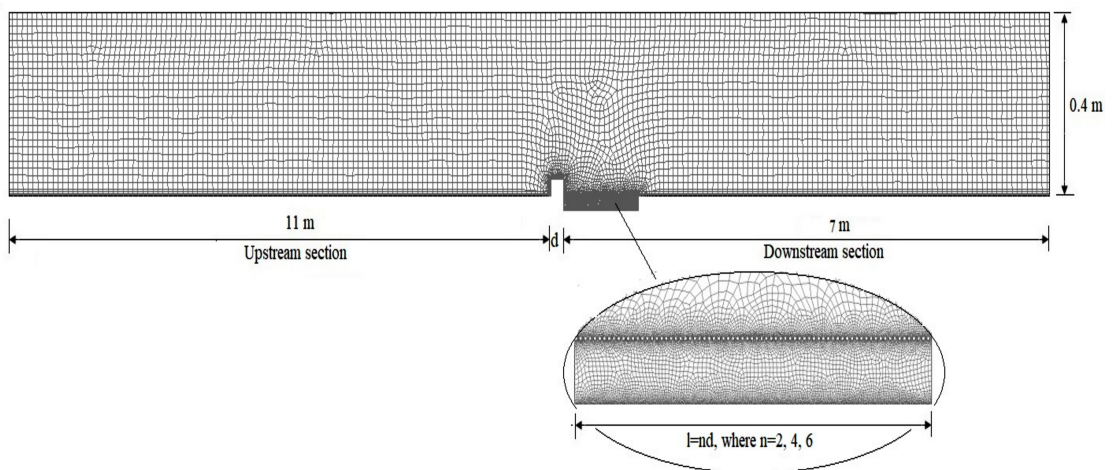


Figure 6.3: Diagram of the simulation domain featuring a mesh (Grid-3(1848 × 52))

## 6.2 Results and Discussion

### 6.2.1 Verification of the velocity profile using the log-law principle

The validation of the log-law principle in this study involved comparing the numerical model results with the standard logarithmic law of wall for turbulent flow. The log-law principle is a fundamental concept used to validate numerical data in turbulent flow problems. The computational domain was set up to simulate high Reynolds numbers ( $Re \approx 70,000$ ) and replicate the boundary conditions. In this study, the stream-wise velocity ( $u$ ) profile is plotted on a logarithmic scale against the height from the bed ( $y$ ), with normalization using the friction velocity ( $u_*$ ). The friction velocity was calculated to be 0.012 m/s, derived from a wall shear stress value of 0.027 N/m<sup>2</sup>. In Fig.6.4, the straight line illustrates the normalized log-law profile, with the standard ( $u/u_*$ ) values calculated using the von Karman constant (0.41) and an integration constant (5.29), as proposed by Nezu and Nakagawa [48]. These constants are universally applicable for high Reynolds number flows [64]. Within this framework, the simulated velocity profile closely matches the standard straight-line curve, except near the wall and close to the free surface. The deviation near the wall is due to the linear law within the viscous sub-layer, which is consistent with fundamental theory. Additionally, the deviation observed near the free surface conforms to the wake law in the turbulent outer layer.

### 6.2.2 Validation with the experimental results

In this work we have validated the numerical data with experimental data, as illustrated in Fig. 6.5. The normalized stream-wise mean x-velocity, stream-wise mean y-velocity, and turbulent kinetic energy obtained from the numerical simulation were compared with corresponding experimental data at both upstream and downstream locations. The simulation results were validated against the experimental data provided by [65], as shown in Fig. 6.5. The experiments were carried out in a water open channel facility with dimension 18.3 m  $\times$  0.9 m  $\times$  0.9 m. The flat bed of the flume was made from strong concrete and had a consistent slope of 0.00025. A vertical turbine pump was there to get a consistent flow rate through

## 6.2 Results and Discussion

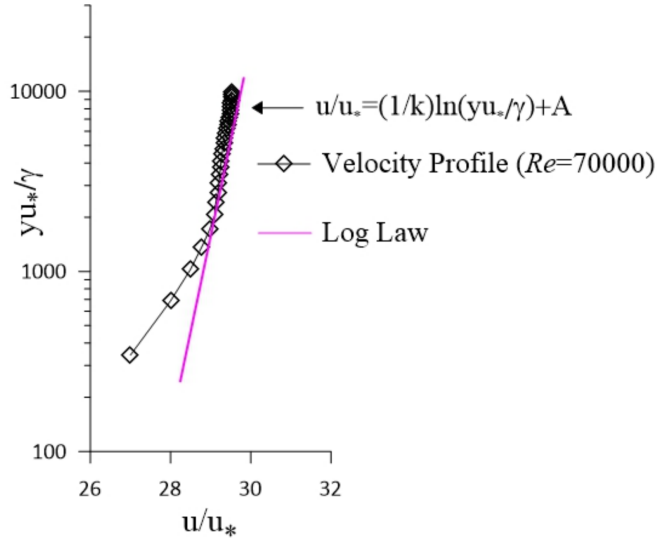


Figure 6.4: Verification of the numerical model through comparison with the standard logarithmic law of wall

the channel. The volume flow rate was controlled with a flow control valve installed between the pump and the channel. The depth of the flow was consistently kept constant throughout the entire channel by coordinating the flow control valve and the tailgate. Measurements of velocity over time were taken with a 16 MHz Acoustic Doppler velocimeter. To replicate the background flow conditions of the numerical simulation, the flow passed through a square placed on the flume bed. Five positions were selected for analysis: the first position ( $-V_1$ ) before the square and four positions ( $V_1, V_2, V_3,$  and  $V_4$ ) after the square, located at distances of 2 m, 0.038 m, 0.0955 m, 0.25 m, and 1 m, respectively, from the centre of the square. All positions were normalized using the square side ( $a = 0.025$  m). The experiments were performed with a free stream velocity of  $u = 0.35$  m/s, resulting in Reynolds number ( $Re = uh/\gamma$ ) and Froude number ( $Fr = u/\sqrt{gh}$ ) values of 70,000 and 0.15, respectively, based on the flow depth ( $h = 0.2$  m). Figure. 6.5 indicated that the simulation results and experimental data coincided at the upstream and top of the square. However, slight variation was observed near the bed at the downstream location. Moreover, the numerical data closely followed the trend of variation observed in the experimental data and provided a reasonable estimation of physical variables. The percentage of disagreement in the stream-wise velocity

profile between the numerical and experimental results, particularly in proximity to the square, was less than 8%. Conversely, at the upstream and far downstream locations, the numerical data exhibited good agreement with the variation trend observed in the experimental data, offering a reliable approximation of the physical variables.

### 6.2.3 Variation of normalized mean velocity along $x$ -direction

In Fig. 6.6, the mean stream-wise normalized velocities ( $\hat{u} = u/u_*$ ) are plotted as a function of  $y/h$ , where  $h$  denotes the constant water depth, for a flow with a Reynolds number of  $Re = 70,000$ . The graph compares the mean normalized velocity ( $\hat{u}$ ) profiles of an open channel both without suction and with suction from the suction panel. The suction velocities are varied as multiples of the mean depth-average velocity ( $u_j = 0.35, 0.70$ , and  $1.05$  m/s). Furthermore, the influence of the suction-panel distance ( $l$ ) is analyzed by considering distances of  $l = 2d, 4d$ , and  $6d$  downstream of the square obstacle. The diagrams represent different stream-wise locations:  $-V_1, V_0, V_1, V_2$ , and  $V_3$ , corresponding to positions before, on, and after the square obstacle, as depicted in Fig. 6.6.

Figure. 6.6 is organized into three rows. The first row represents the case with a suction velocity of  $0.35$  m/s, the second row with  $0.70$  m/s, and the third row with  $1.05$  m/s. By comparing the effects of different suction-panel lengths ( $l$ ) for each velocity case, insights into the modulation of the re-circulation zone are obtained. Specifically, Fig. 6.6 panels (a), (b), (g), (h), (m), and (n) display velocity profiles at locations  $-V_1$  (upstream of the square) and  $V_0$  (over the square). These profiles show perfect alignment across all cases, indicating that neither the suction velocity nor the suction-panel length affects the region upstream and directly over the obstacle. However, a disruption in the flow pattern becomes noticeable downstream within the re-circulation zone. In the absence of suction, the channel bed exhibits a negative velocity within the re-circulation zone, characterized by the presence of numerous vortices [66].

In the first row of Fig. 6.6 (a – e), with a constant suction velocity of  $0.35$  m/s, the effect of suction-panel length ( $l$ ) is particularly evident when examining the velocity profiles downstream of the square in panels (c and d). A systematic

## 6.2 Results and Discussion

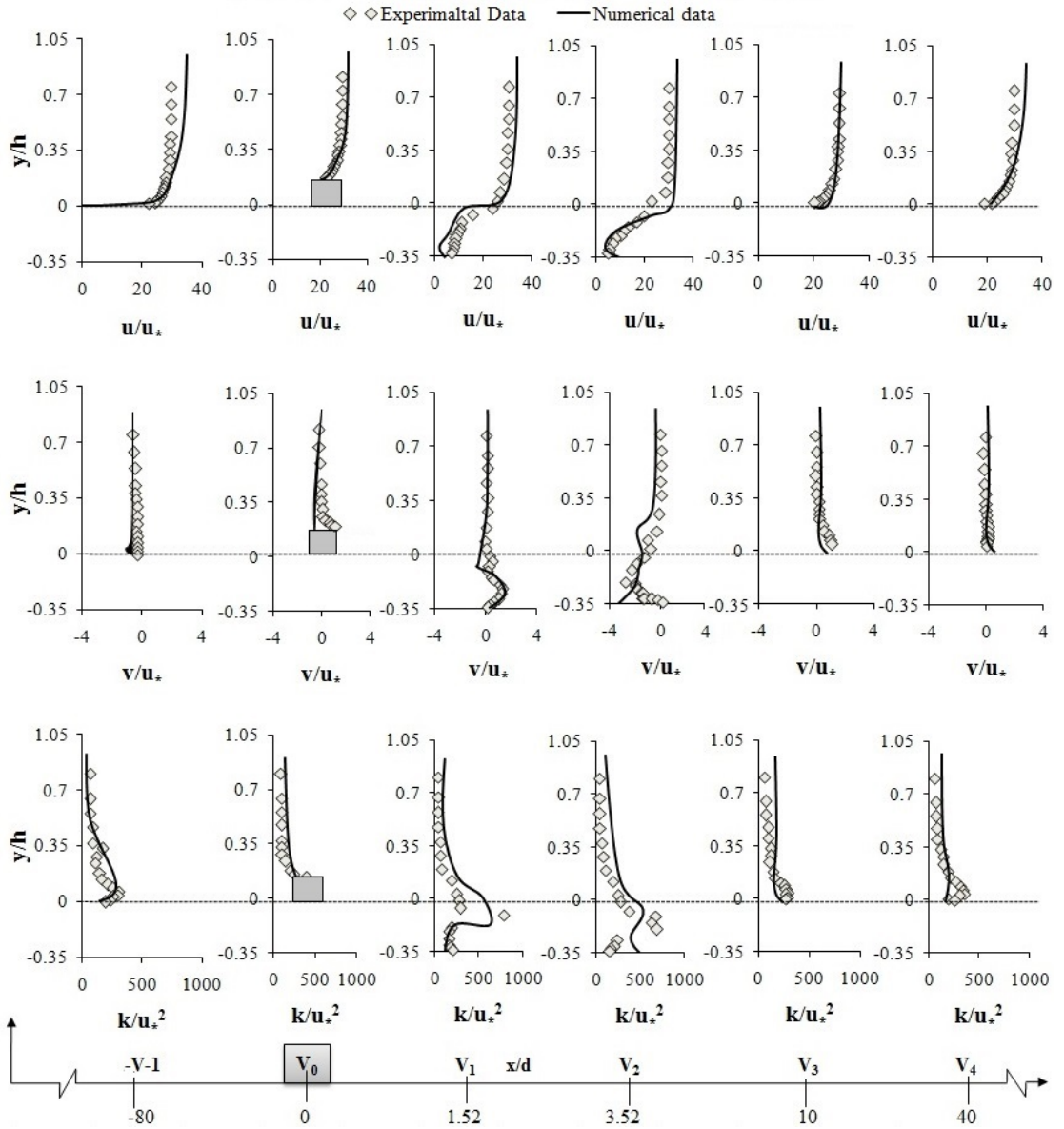


Figure 6.5: Validation of normalized mean-velocity along x-direction ( $u/u_*$ ), along y-direction ( $v/u_*$ ) and normalized turbulent kinetic energy ( $k/(u_*^2)$ ) with experimental results (adopted from Singh and Debnath 2016) at various normalized locations relative to the square obstruction.

influence of the suction-panel length ( $l$ ) emerges, highlighting the role of the suction force in transforming the negative velocity within the re-circulation zone to a positive one.

In the second row, focusing on locations  $V_1$  and  $V_2$  (Fig. 6.6 ( $h-i$ )), with the suction velocity doubled, a pronounced change in the flow structure is observed, especially within the re-circulation zone. A negative velocity persists in the wake when the suction-panel length is  $l = 0.05$  m at locations  $V_1$  and  $V_2$ .

In the third row, with the suction velocity increased to three times the depth-averaged velocity (1.05 m/s) and maintaining the same suction-panel distance variations ( $l$ ), variations in the velocity are observed solely within the re-circulation zone. This indicates that a suction force in the wake near the square can effectively control the re-circulation behind the square obstacle.

Overall, these findings underscore the significance of suction-panel distance ( $l$ ) and velocity in shaping flow patterns within and around the re-circulation zone, offering valuable insights for controlling and managing such zones.

### 6.2.4 Variation of normalized mean velocity along $y$ -direction

To comprehensively understand the impact of the problem within the 2-D domain, it is essential to analyze the changes in the average vertical depth-averaged velocity ( $\hat{v} = v/u_*$ ) along the  $y$ -direction, as illustrated in Fig. 6.7. The configuration and positioning of each plot remain consistent with those shown in Fig. 6.6. Across all rows, the velocity profiles are primarily influenced by suction effects in the wake region. This influence is due to variations in both the suction velocity and the suction-panel length ( $l$ ). In the first row, the suction velocity is held constant at 0.35 m/s, while the suction-panel length varies as follows:  $l = 0.05$  m, 0.10 m, and 0.15 m. Notably, as the suction spread-length systematically increases, the velocity profiles intensify, particularly in the re-circulation region, compared to the profile without suction. For the other two cases, the velocity profiles exhibit significant fluctuations in the re-circulation zone compared to the profile without suction. The third row in Fig. 6.7 ( $m,n$ ) demonstrates the most pronounced zig-zag patterns in the profiles compared to the other two rows. It is observed that, upstream of the square, the velocity profiles converge sharply for all cases. A similar pattern is observed for the velocity profile over the square and in the downstream region, away from the re-circulation zone. Variations become prominent only within the re-circulation zone, where the flow exhibits increased complexity due to turbulent

## 6.2 Results and Discussion

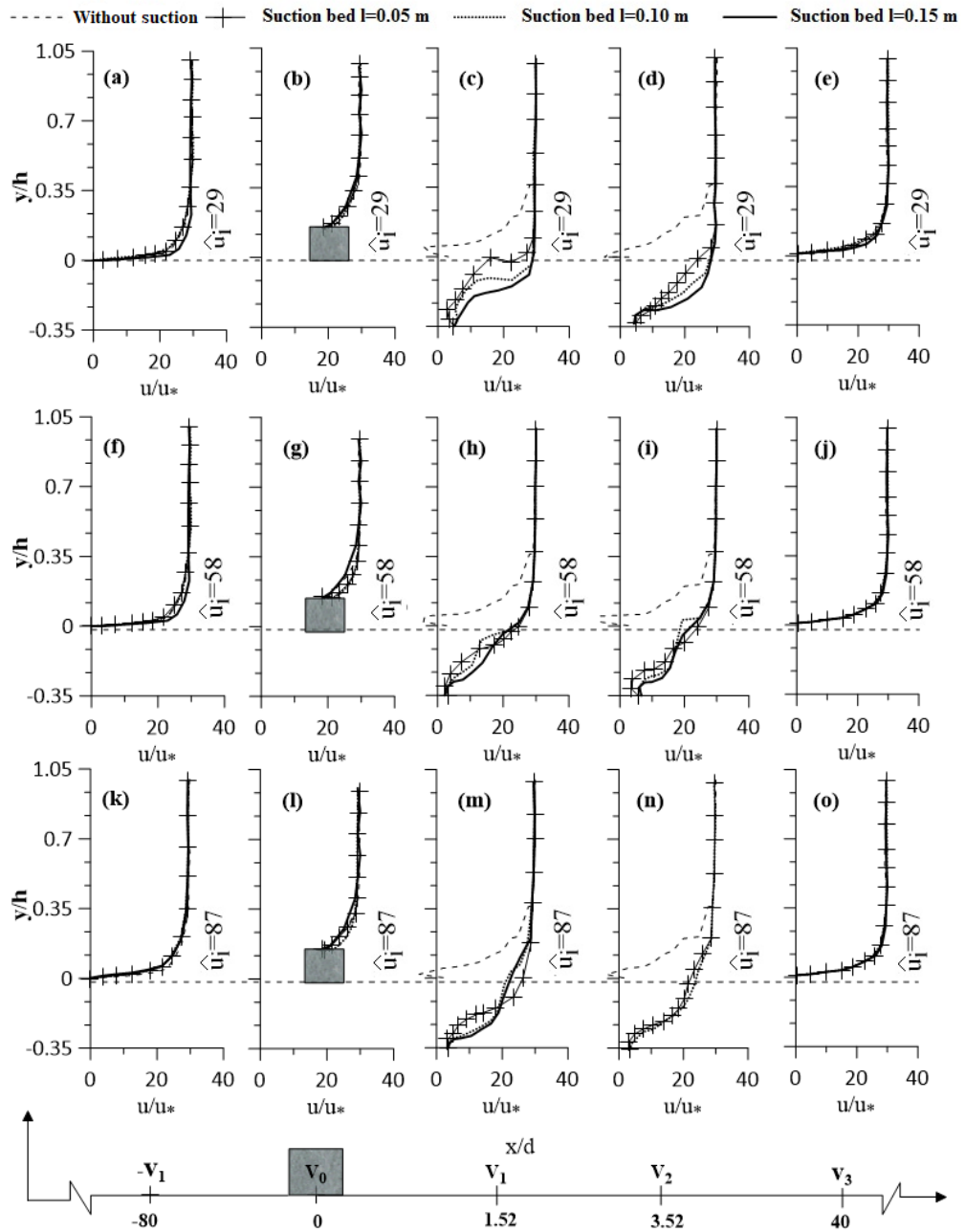


Figure 6.6: Representation of mean velocity along x- direction ( $u/u_*$ ) for bed without and with suction against  $y/h$  from the bed.

mixing.

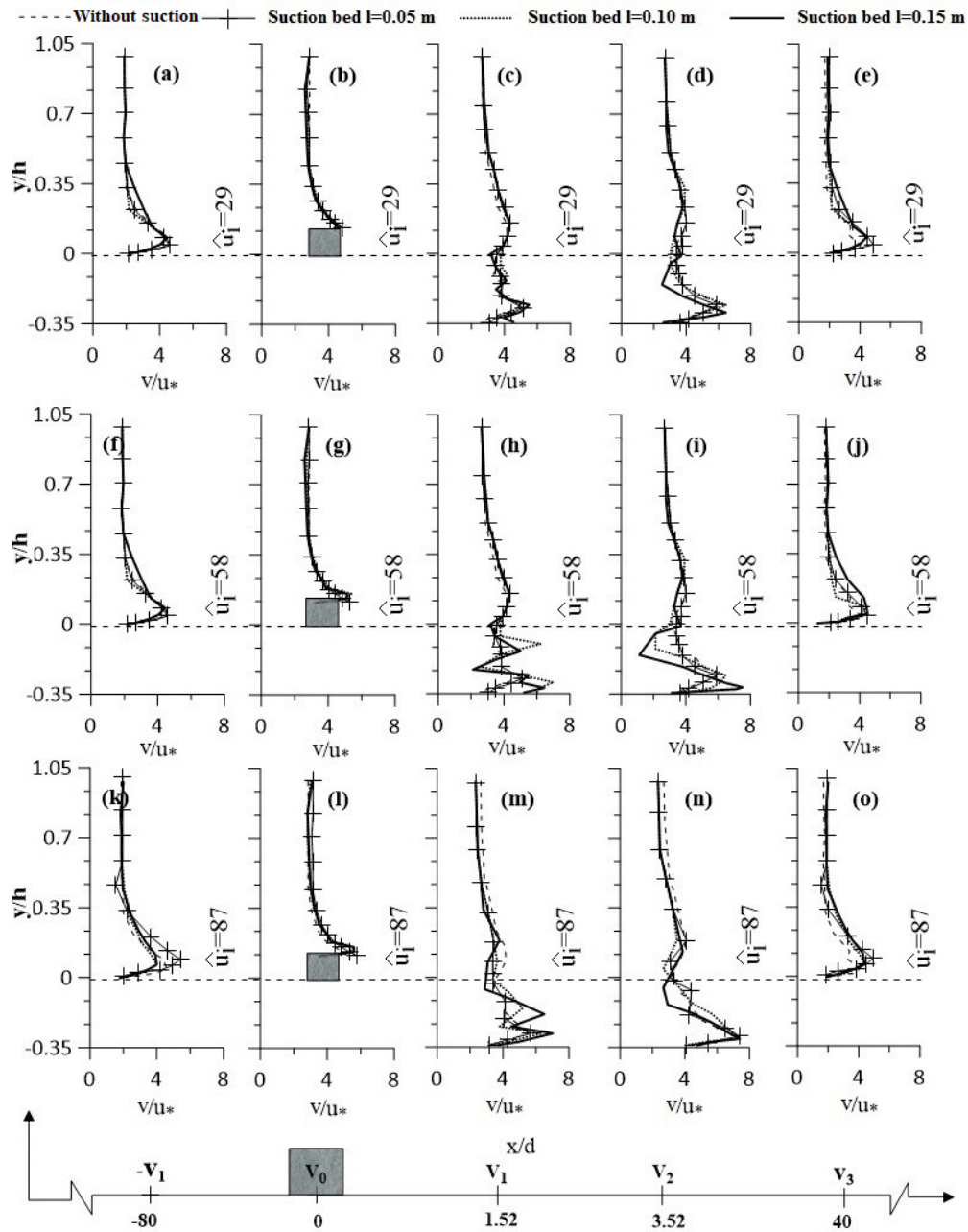


Figure 6.7: Representation of mean velocity along  $y$ - direction ( $v/u_*$ ) for bed without and with suction against  $y/h$  from the bed.

### 6.2.5 Contour plot of normalized mean velocity along $x$ -direction

The analysis of the contour plot of normalized mean velocity along the  $x$ -direction, as illustrated in Fig. 6.8. The presentation is structured into four rows, each row depicting a specific scenario related to the suction effects on the flow field.

In the initial row of Fig. 6.8, the contour plot showcases the longitudinal velocity structure behind the obstacle in the absence of suction. Subsequently, the second row of plots in Fig. 6.8 portrays the impact of suction at varying velocities while maintaining a constant suction-panel length ( $l$ ) of 0.05 m. Moving forward, the third and fourth rows of the figure present similar scenarios but with different fixed suction-panel lengths of 0.10 m and 0.15 m, respectively.

In the absence of suction, the prominent dark black region in the first row indicates a significant re-circulation zone in the wake area, extending up to 0.22 m downstream of the square. This re-circulation zone features flow reversal, attributed to a notable pressure drop and the onset of vortex shedding [51]. The observed negative velocity ( $\hat{u} = -3$ ) further confirms the presence of flow reversal. In the second row, with a smaller suction-panel length ( $l$ ), the re-circulation zone persists and cannot be entirely eliminated, as illustrated in Fig. 6.8 (b) and (c). Figure. 6.8 (d) shows a slightly different contour at the suction inlet, likely due to increased suction velocity. Consequently, the second row shows no substantial changes that could fully eliminate the re-circulation zone. However, the size of the black region is reduced compared to the case without suction.

The contour plots in Fig. 6.8 offer a visual representation of the distribution of longitudinal velocity in the wake region of the square obstacle under different suction conditions. The distinct patterns observed in the velocity contours elucidate the influence of suction on the flow structures, particularly in the regulation of the re-circulation zone behind the square obstacle. This detailed analysis provides valuable insights into the dynamics of the flow field and the efficacy of suction in controlling flow patterns.

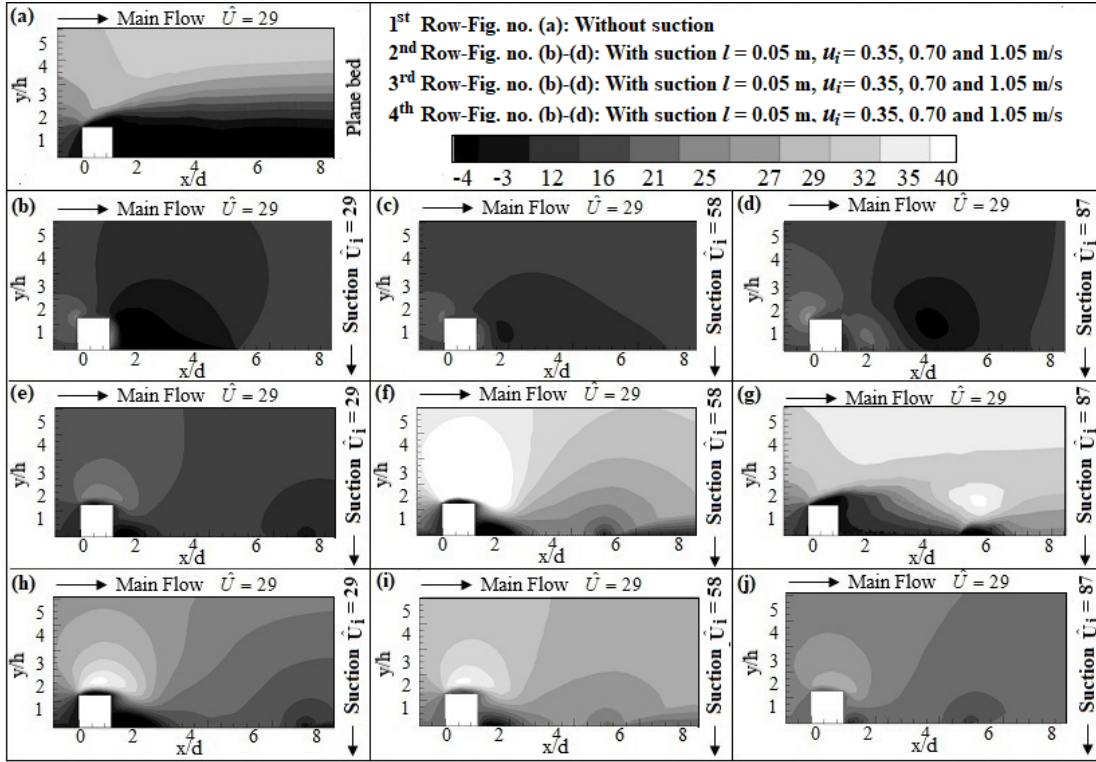


Figure 6.8: Representation of mean velocity along  $y$ - direction ( $v/u_*$ ) for bed without and with suction against  $y/h$  from the bed.

### 6.2.6 Representation of Streamlines of the flow pattern.

The plot illustrating streamlines is crucial for effectively depicting the local direction of the vector field at key points. Figure. 6.9 shows the streamlines for various flow scenarios analyzed in this study. The top row, specifically Fig. 6.9(a), depicts the streamlines for the scenario without suction, revealing a prominent re-circulation wake region with its core center located approximately at  $x/d = 8$  downstream of the square. The streamlines exhibit the expected systematic behavior. The graph demonstrates that the interaction between the suction-panel length ( $l$ ) and the suction velocity contributes to the reduction of the re-circulation zone. As both parameters increase in each subsequent row, significant structural changes in the flow patterns are observed. Consequently, in the final row, Fig. 6.9(j), the objective of this study is achieved, as the re-circulation is controlled or eliminated to an acceptable degree.

## 6.2 Results and Discussion

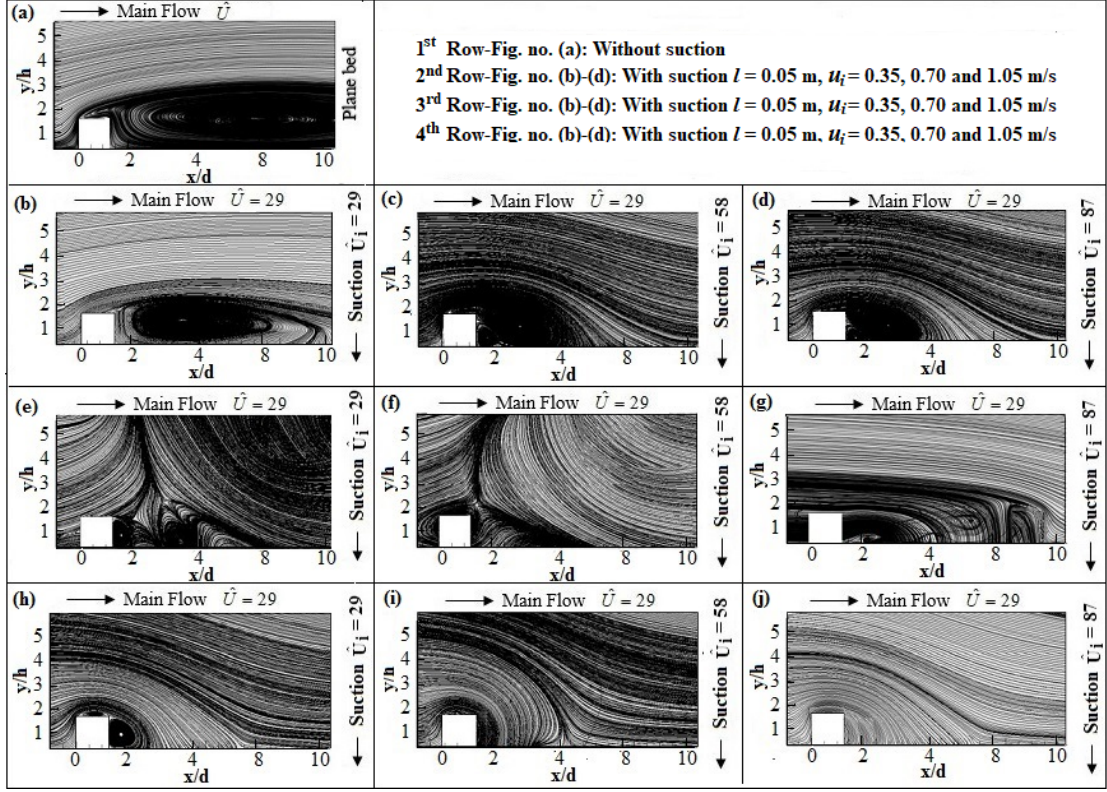


Figure 6.9: Stream-line plot of normalized mean velocity ( $u/u_*$ ) depth for without and with suction.

### 6.2.7 Instantaneous Vorticity Contours

The turbulent vorticity contour plot illustrates the regions of differential shear within a flow field. In this study, vorticity is defined as  $\omega = (\partial V/\partial X - \partial U/\partial Y)$  [67]. Figure. 6.10 presents the contour plots of instantaneous vorticity. The temporal progression of turbulent vorticity on the open channel bed without a suction profile is shown for time intervals of  $t = 1$  s, 8 s, 16 s, and 20 s in Fig. 6.10 (a – d), respectively. This time-dependent analysis is essential to reveal the underlying flow dynamics that contribute to the formation of a von Kármán-like vortex street within the re-circulation zone. The flow, particularly in the wake region behind the obstruction, transitions from a steady state to absolute instability, leading to the generation of vortex-shedding signals characterized by self-sustained periodic oscillations [68]. At this stage, even minimal disturbances in the flow field result in significant vortex growth. The figure clearly shows that

in the potential flow region, the vortices are small and gradually increase in size toward the bottom wall boundary within the re-circulation zone.

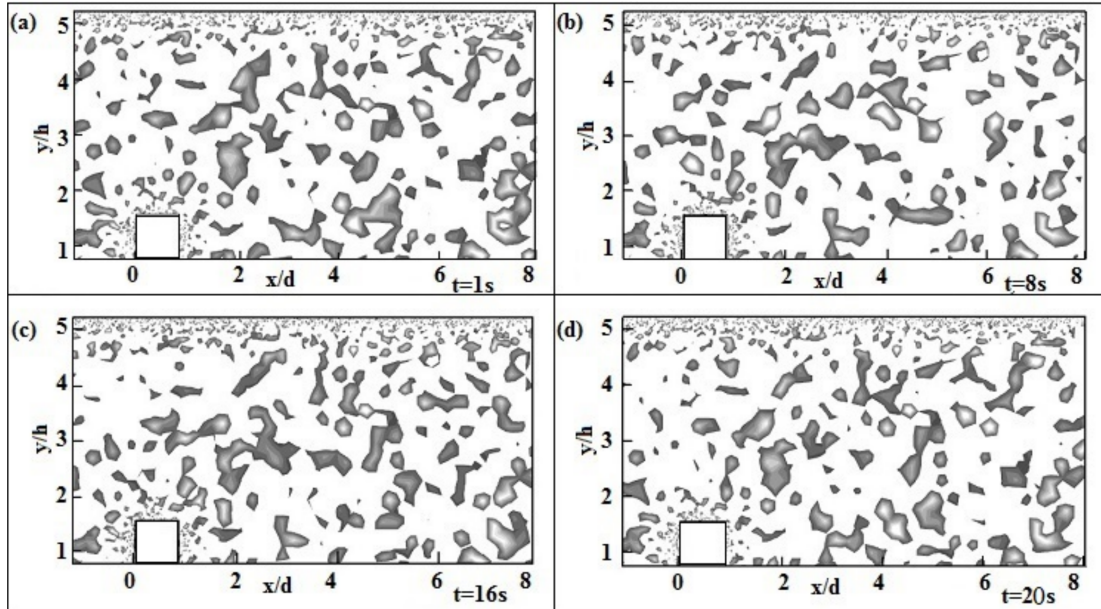


Figure 6.10: Instantaneous vorticity contours for (a)  $t = 1s$ , (b)  $t = 8s$ , (c)  $t = 16s$  and (d)  $t = 20s$

### 6.2.8 Time series of velocity components

The time series data of velocity components were analyzed at a specific point within the flow-sensitive region of the re-circulation zone. This analysis is crucial for understanding how the time-marching solution scheme progresses to reach a solution.

For solving the transient scheme, a time step size  $\Delta t = 0.02$  seconds was chosen, and the number of time steps was set to 1000. This results in a total solution time of 20 seconds ( $1000 \cdot 0.02 = 20$  seconds). Throughout this period, the changes in the velocity components in both the X-direction (denoted as  $u$ ) and the Y-direction (denoted as  $v$ ) were monitored. Figure 6.11 illustrates the progression of the velocity components  $u$  and  $v$  over the 20 second interval. This information is vital as it provides insights into the dynamic behavior of the flow within the re-circulation zone and helps in assessing the effectiveness and stability

## 6.2 Results and Discussion

---

of the time-marching solution scheme. The figure captures how these velocity components evolve, indicating the transient nature of the flow and allowing for a detailed analysis of the temporal characteristics of the fluid dynamics at the point of interest.

By studying these time series data, one can determine whether the chosen time step size and the number of time steps are appropriate for accurately capturing the transient phenomena in the flow. This analysis ensures that the numerical solution converges to a reliable and accurate representation of the physical flow behavior.

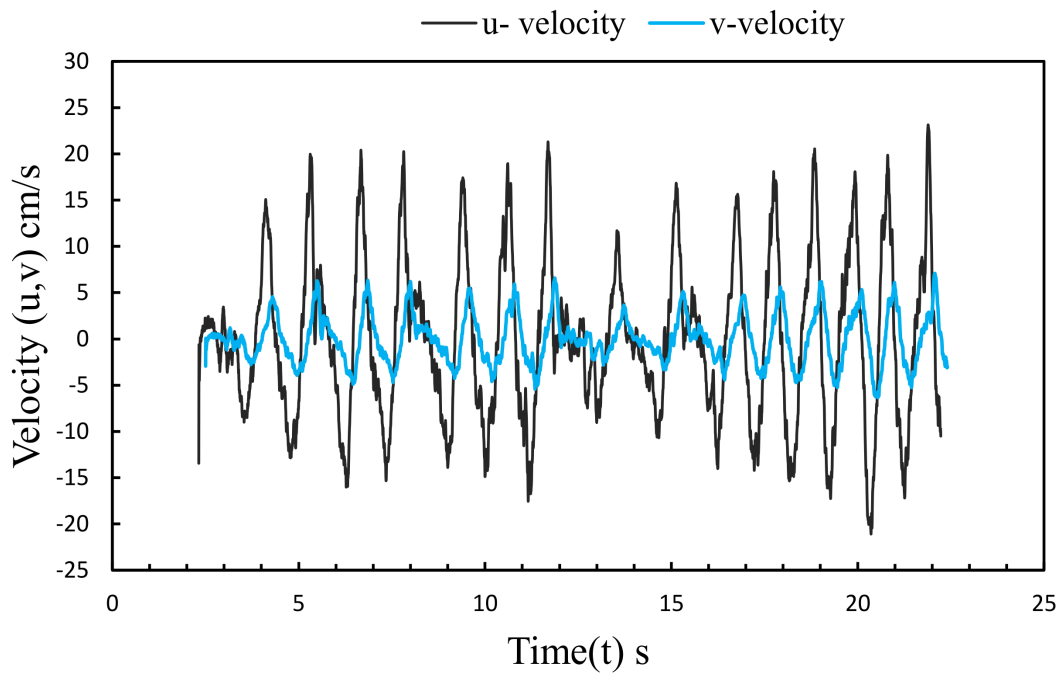


Figure 6.11: Time series analysis of stream-wise ( $u$ ) and transverse ( $v$ ) velocity component

### 6.2.9 Vorticity spectra analysis

In Fig. 6.12, the power spectral density ( $PSD$ ) analysis of vorticity magnitude offers a detailed examination of how vorticity signals are distributed across different frequencies within a flow field. The x-axis on these graphs corresponds to the vortex shedding frequency measured in Hertz, while the y-axis represents the

amplitude of the vorticity magnitude. Data for this analysis was collected from a point located 0.1 meters downstream from the right vertical side of a square obstacle and 0.01 meters above the bed in the re-circulation zone.

Panel (a) of Fig. 6.12 illustrates the *PSD* of vorticity magnitude without any suction applied. Here, the distribution of vorticity magnitudes is relatively uniform across the entire frequency range, from 0 Hz to 10,000 Hz. The PSD values span from  $(10^7)$  to  $(10^2)$ , indicating that the intensity of vorticity signals varies significantly across this range of frequencies.

In contrast, panels (b) to (d) in Fig. 6.12 display the *PSD* profiles when suction is applied. These panels reveal a noticeable reduction in the amplitude of vorticity magnitude under different suction conditions. This comparison highlights the effectiveness of suction in reducing vorticity magnitudes. Specifically, the range of *PSD* values in panel (d), which shows the most significant reduction, falls within  $(0 < PSD(m^2/s) < 10^4)$ . This substantial decrease underscores the influence of suction velocity ( $u_i$ ) and the length of the suction panel ( $l$ ) in modulating the magnitude of vortex shedding frequencies. These parameters play a crucial role in controlling the dynamics of the flow and the characteristics of turbulence.

By examining the *PSD* plots in Fig. 6.12, researchers can derive valuable insights into how suction impacts the distribution of vorticity and the frequencies at which vortex shedding occurs. This analysis enhances our understanding of flow behavior and demonstrates the effectiveness of suction mechanisms in controlling flow dynamics. Such insights are critical for the development and optimization of flow control applications, as evidenced by related studies in the field [67].

### 6.2.10 Static pressure contour

The variations in the flow pattern within a flow field are primarily influenced by differences in pressure. As depicted in Fig. 6.13, the irregularities in the flow pattern are mainly observed in the wake region behind the square obstacle. These irregularities arise due to pressure differences, which are influenced by several factors, including vortex formation and the dynamic behavior of the shear layer [69].

To analyze the data effectively, it is normalized using the parameter ( $\hat{p} =$

## 6.2 Results and Discussion

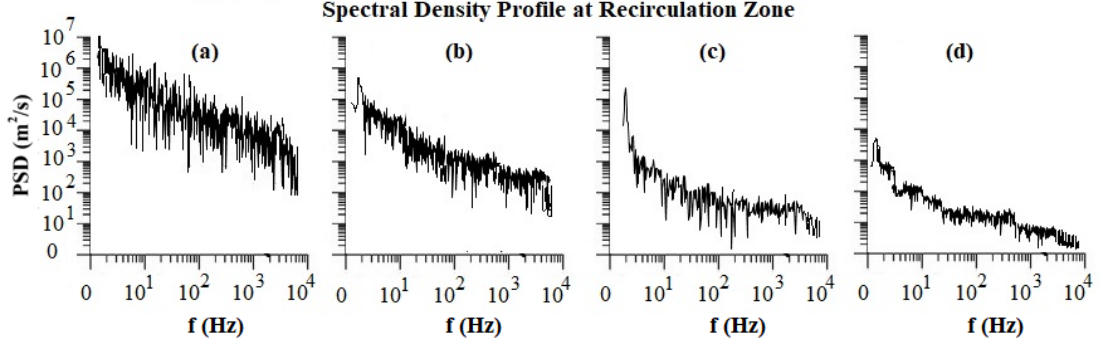


Figure 6.12: Power spectral density of vorticity magnitude (a). Without suction, (b). With suction  $l = 0.05$ ,  $u_i = 0.35, 0.70, 10.5$  m/s, (c). With suction  $l = 0.10$ ,  $u_i = 0.35, 0.70, 10.5$  m/s and (d). With suction  $l = 0.15$ ,  $u_i = 0.35, 0.70, 10.5$  m/s

$p/\rho.u_*^2$ ), where ( $p$ ) is the pressure, ( $\rho$ ) is the fluid density, and ( $u_*$ ) is friction velocity. This normalization transforms the data into a non-dimensional form, allowing for more straightforward comparisons.

In Fig. 6.13(a), a high negative pressure (approximately ( $\hat{p} = -20$ )) is observed in the re-circulation zone when there is no suction applied. This significant negative pressure indicates strong adverse pressure gradients and turbulent activity in the wake region.

However, when a suction force is introduced into the re-circulation zone, as shown in Fig. 6.13(b – d), the negative pressure zone gradually disperses. This dispersion is accompanied by a subsequent recovery in pressure, indicating that the suction force helps to stabilize the flow and reduce turbulence.

In the third row of Fig. 6.13, the effect of increasing the length of the suction panel to 10 cm is examined for various suction velocity cases. The results demonstrate a systematic increase in pressure recovery within the wake region as the suction panel length is increased. This implies that a longer suction panel can more effectively mitigate the negative pressure and improve the overall flow stability.

Finally, in the last row of Fig. 6.13, it is noteworthy that the efficiency of pressure recovery improves for the same suction velocity when the suction panel length is increased. This suggests that the length of the suction panel plays a crucial role in enhancing the effectiveness of suction in stabilizing the flow and

promoting pressure recovery in the wake region.

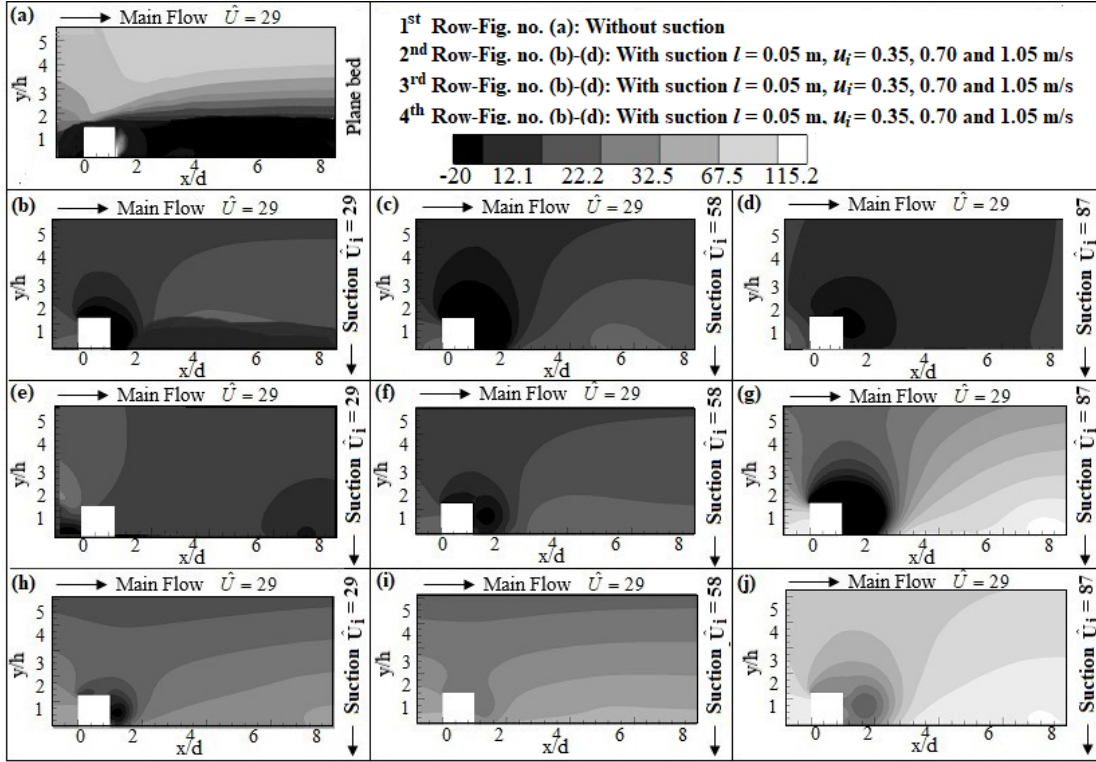


Figure 6.13: Contours of stream wise pressure ( $\hat{p}$ ) against non-dimensionlized abscissa along bed ( $x/d$ ) and the non-dimensionlized ordinate from bed ( $y/h$ )

### 6.2.11 Contours of Turbulent Kinetic Energy ( $TKE$ )

Turbulent Kinetic Energy ( $TKE$ ) represents the mean specific energy associated with turbulence in flows characterized by numerous eddies. According to the study, near-wall regions exhibit significant variations in  $TKE$  due to the turbulence production induced by obstacles [70]. In open channel beds without suction (refer to Fig. 6.14), most areas show low  $TKE$  values with minor fluctuations in the re-circulation zone. These  $TKE$  variations are attributed to the instability and complexity of the flow structure within the re-circulation zone, as well as the mean flow, both of which contribute to additional  $TKE$  production [53].

When a suction force is applied downstream of the obstacle and near the bottom wall, the expected pattern of  $TKE$  variation is disrupted. This disruption is

### 6.3 Conclusion

---

caused by the breakdown of the viscous sub-layer due to turbulent vortices bursting [54]. Figures. 6.14 ( $b - c$ ) illustrate that, despite the influence of suction on the flow, there are no significant changes in  $TKE$  values. However, increasing the length of the suction panel to ( $l = 0.10$ ) m and applying different suction velocities ( $u_i = 0.35, 0.70, 1.05$  m/s) result in localized patches of high  $TKE$  values in the wake region. These elevated  $TKE$  values indicate the presence of large-scale eddies, which are likely introduced by the downstream suction. It is important to note that when two flow systems intersect, scale breakdown typically occurs. In this case, the interaction between the suction flow and the mainstream flow in a cross direction leads to increased  $TKE$  values and the introduction of additional turbulence scales [71].

Furthermore, a distinct feather-shaped patch of high  $TKE$  values appears downstream of the re-circulation zone near the square obstacle. This indicates an increase in the maximum  $TKE$  values extending along the near-bed region in the suction panel. Despite the suction velocity intensity being the same for all rows and suction input profiles, changes in the suction panel length ( $l$ ) result in noticeable variations within the specified range. This suggests that the length of the suction panel plays a significant role in influencing the distribution and magnitude of  $TKE$  within the flow system.

### 6.3 Conclusion

The primary objective of this research is to manage the re-circulation zone that forms behind a square-shaped obstacle in a two-dimensional flow. This is achieved by utilizing suction forces through an array of small openings in the wall, which are positioned perpendicular to the main flow direction. The goal is to modulate the re-circulation zone and achieve complete pressure recovery.

To explore this, the study employs a computational model that simulates a two-dimensional open channel containing a square-shaped obstacle at the bottom. The model uses the Volume of Fluid ( $VOF$ ) method to account for the flow characteristics. The research focuses on two main aspects: identifying the extent of the re-circulation zone that spreads in the wake region behind the obstacle and determining the effective length of the suction panel required to eliminate this re-

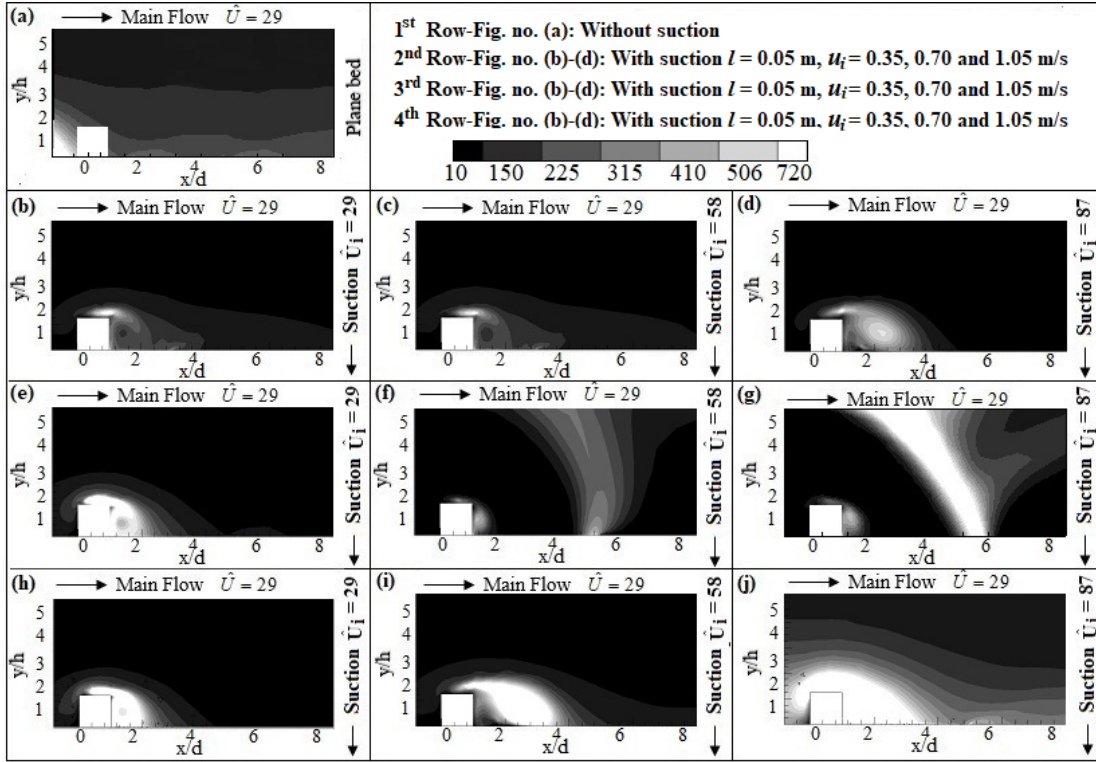


Figure 6.14: Contour plot of stream wise Turbulent Kinetic Energy ( $\hat{k}$ ) against normalized horizontal distance along bed ( $x/d$ ) and the normalized vertical distance from the bed ( $y/h$ ).

circulation. Additionally, the study examines how turbulent characteristics change throughout the flow domain.

The standard  $k - \epsilon$  turbulence model is used to solve the governing equations, providing insight into the flow dynamics and turbulence behavior.

A detailed investigation is conducted to evaluate the flow characteristics in the re-circulation zone behind the square-shaped obstacle when suction is applied. Three different sets of suction Reynolds numbers are considered in the study. The aim is to systematically understand the impact of two key parameters: the length of the downstream suction panel ( $l$ ) and the suction efflux velocity ( $u_i$ ). These parameters are analyzed to see how they affect pressure recovery and the modulation of the re-circulation zone.

The key findings from the study are summarized as follows:

### 6.3 Conclusion

---

- Without any suction applied, the wake behind a square object shows negative static pressure. This creates an adverse pressure gradient in the re-circulation zone, which leads to vortex shedding. Vortex shedding generates unwanted vibrations that can be harmful to structures.
- The introduction of suction plays a crucial role in disturbing the flow within the re-circulation zone. This suction pulls ambient fluid into the area starting from where the suction is applied, leading to better fluid mixing. This improved mixing increases the rate at which turbulent energy is dissipated. Therefore, the study indicates that the presence of suction forces in the re-circulation zone, irrespective of conditions in areas without suction, results in a higher rate of turbulent dissipation.
- By controlling the re-circulation zone, this study suggests that it is possible to reduce the generation of unwanted vibrations. This conclusion is based on a quantitative analysis of the vorticity magnitude and the frequencies at which vortices are shed within the re-circulation zone.
- The study recommends adjusting the orientation of the suction panel to observe changes in turbulent properties and to better understand the extent of the changes in the flow behavior. Additionally, it emphasizes the importance of considering the intensity of the suction force to mitigate problems arising specifically from the re-circulation zone, rather than from the main flow. This indicates a need to determine the optimal spacing between suction openings to eliminate the effects of vortex shedding and achieve better optimization.

Future research could focus on examining flow characteristics using multiple square-shaped two-dimensional obstacles. Another potential direction is optimizing the design parameters of arrays of small openings, such as their shape, size, and distribution pattern. Fine-tuning these parameters is crucial as it can significantly enhance the control and manipulation of the re-circulation zone, leading to improved performance in fluid flow systems. Additionally, exploring a three-dimensional model would provide greater insight and proficiency in solving real-world problems.



MODULATION OF  
RE-CIRCULATION ZONE  
BEHIND A SQUARE  
OBSTRUCTION BY SINGLE  
INCLINED TURBULENT WALL  
JET WITH VARYING ANGLE OF  
ATTACK

This numerical study focuses on the modulation of the re-circulation region behind a square obstruction using a single inclined turbulent wall jet with varying angles of attack. By visualizing the flow field through the simulation software's post-processing system, the effects on the re-circulation zone have been analyzed. The experiments conducted at various angles of attack and high Reynolds numbers reveal that the angle of attack of the wall jet significantly influences the re-circulation zone. Specifically, the maximum length of the re-circulation zone decreases as the angle of attack increases. Additionally, the angle of attack alters the strength and

position of vortex structures within the re-circulation zone. These findings offer valuable insights for engineering applications involving flow control and mixing enhancement using inclined wall jets. The numerical simulation utilizes a two-phase volume of fluid (*VOF*) model with open channel boundary conditions, and the Reynolds averaged equation is solved using the standard  $k - \omega$  *SST* turbulence model.

## 7.1 Formulation of the problem

In this study, we investigate the 2D open channel flow within an 18 m  $\times$  0.4 m channel, featuring a 2D square obstruction (0.025 m  $\times$  0.025 m) located 11 m from the inlet in a fully developed region. The mainstream flow maintains a depth-averaged velocity of  $u = 0.30$  m/s. An inclined wall jet, 0.020 m in diameter, is placed in the bottom right corner, as depicted in Figure 7.1. The blockage ratio of about 0.062, relative to the channel width, is below the critical value of 1, negating the need for pressure correction for near-wall effects. Previous studies suggest that blockage ratios above 1 impact the wake pressure coefficient [72].

Using *Ansys Fluent* software for *CFD* simulation, we solve the governing *PDEs* with a pressure-based numerical solver (*SIMPLE* algorithm). The setup involves a two-phase *VOF* approach with air as the primary phase and water as the secondary phase. Notably, the air-to-water depth ratio exceeds 0.5 (specifically, it is 1), indicating the negligible impact of the top wall boundary [40]. The *SIMPLE* algorithm, employing the *QUICK* scheme, is used for solving the equations. A time-advanced iterative approach is utilized, starting from an initial approximation. To ensure high precision, the residual target is set to  $10^{-5}$ . The time step size is 0.0002 seconds, and the simulation runs for 10,000 steps to ensure convergence. The implicit numerical scheme used does not impose restrictions on predefined time step sizes and mesh discretization [73]. Detailed specifications of the channel and hydraulic parameters are listed in Table 7.1.

## 7.1 Formulation of the problem

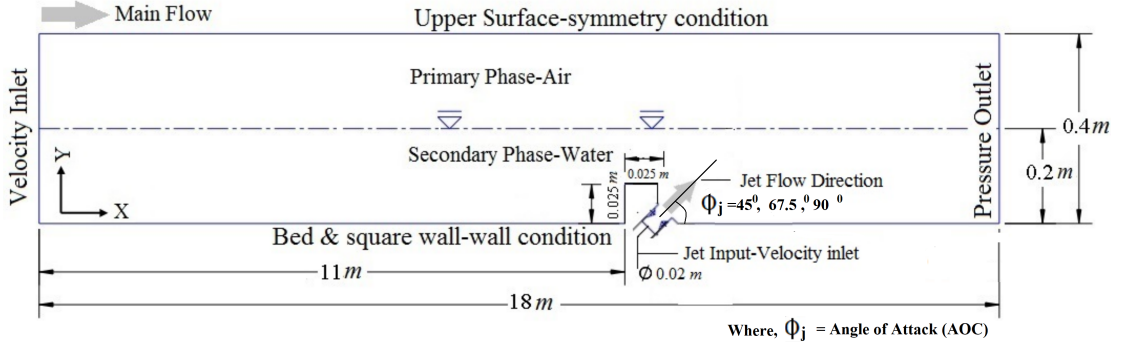


Figure 7.1: Schematic diagram of the computational set-up with boundary conditions With varying Angle of Attack ( $\Phi_j = 45^0, 67.5^0, \text{ and } 90^0$ ).

Table 7.1: specification of the Channel with hydraulic parameters

Channel parameters	Dimensions
The channel length, $l$ (m)	18
The channel height, $h$ (m)	0.4
The arm of the square obstruction, $d$ (m)	0.025
Area of the square obstruction, $A$ ( $m^2$ )	$0.025 \times 0.025$
Inclined jet Diameter $\phi$ , (m)	0.02
Reynolds number, $Re = uh/\gamma$	60,000
Stream wise depth average velocity $u$ (m/s)	0.30
The depth of mean flow, $h$ (m)	0.20
Friction velocity (computed from the log law) $u_*$ (m/s)	0.012
Froude number, $Fr$	0.15

### 7.1.1 Boundary Conditions

To solve the numerical problem, the computation domain is defined with boundary conditions detailed in Table 7.2. For the pressure and velocity inlet boundary conditions, the turbulent intensity ( $I$ ) and kinetic energy ( $k_n$ ) are specified as  $I = 0.16 \times Re^{-\frac{1}{8}}$  and  $k_n = 1.5I^2$  respectively [60]. Here,  $l = 0.7$  is based on Prandtl's mixing length model.

### 7.1.2 Turbulence model

This study adopts the  $k - \omega$  *SST* turbulence model, initially proposed by [43]. This hybrid model integrates Wilcox's  $k - \omega$  approach with the  $k - \epsilon$  model by

[62]. The  $k - \omega$  model is applied near the wall due to its accurate representation of boundary layer flows, whereas the  $k - \epsilon$  model is utilized away from the wall for its effectiveness in those regions. The *SST* model improves the prediction of adverse pressure gradients and reduces the sensitivity of the original  $k - \omega$  model to free stream flow conditions. The  $k - \omega$  *SST* model employs two transport equations, one for turbulence kinetic energy ( $k$ ) and another for turbulence specific dissipation rate ( $\omega$ ), providing a robust framework for turbulence modeling and ensuring enhanced accuracy across various flow scenarios.

The Standard Menter Shear Stress Transport (*SST*)  $k - \omega$  model is extensively used in computational fluid dynamics. The model's governing transport equations for turbulent kinetic energy  $k$  and specific dissipation rate  $\omega$  are expressed as follows:

**Turbulent Kinetic Energy  $k$  Equation:**

$$\frac{\partial(\rho k)}{\partial t} + \frac{\partial(\rho u_i k)}{\partial x_i} = \frac{\partial}{\partial x_j} \left[ \left( \mu + \sigma_k \frac{\mu_t}{\rho} \right) \frac{\partial k}{\partial x_j} \right] + P_k - \beta^* \rho k \omega + \frac{\partial}{\partial x_j} \left[ (\mu + \sigma_\omega \mu_t) \frac{\partial \omega}{\partial x_j} \right] + 2(1 - F_1) \rho \sigma_\omega \frac{\omega}{k} \frac{\partial k}{\partial x_j} \frac{\partial \omega}{\partial x_j} \quad (7.1)$$

**Specific Rate of Dissipation  $\omega$  Equation:**

$$\frac{\partial(\rho \omega)}{\partial t} + \frac{\partial(\rho u_i \omega)}{\partial x_i} = \frac{\partial}{\partial x_j} \left[ \left( \mu + \sigma_\omega \frac{\mu_t}{\rho} \right) \frac{\partial \omega}{\partial x_j} \right] + \frac{\beta \rho \omega^2}{k} - \frac{\beta^* \rho \omega^2}{k} + 2(1 - F_2) \sigma_\omega \rho \frac{\omega^2}{k} \quad (7.2)$$

Where, the constants are designated as:

- $\mu$ : Molecular viscosity
- $\mu_t$ : Turbulent eddy viscosity ( $= \rho \cdot \sigma_\omega \frac{k}{\omega}$ )
- $\sigma_k, \sigma_\omega$ : Model constants
- $P_k$ : Turbulent kinetic energy production term
- $\beta^*$ : Beta star coefficient ( $= 0.09$ )
- $F_1, F_2$ : Blending functions defined as:

$$F_1 = \tanh \left[ \left( \frac{\sqrt{k}}{\beta^* \omega d} \right)^2 \right]$$

## 7.1 Formulation of the problem

---

$$F_2 = \tanh \left[ \left( \frac{\sqrt{k}}{\beta^* \omega d} \right)^2 \left( 1 - \frac{\mu_t}{\rho k \omega} \left( \frac{d\omega}{dy} \right)^2 \right) \right]$$

Table 7.2: solution domain with required boundary conditions

Sl No.	Position of the channel	Boundary Conditions
1.	Upper Surface	Symmetry
2.	Inlet	Pressure Inlet
3.	Outlet	Pressure Outlet
4.	Channel Bed and square obstruction wall	Wall [No-slip ( $u = 0$ ) and no-penetration ( $v = 0$ )]
5.	Jet Input	Velocity Inlet

### 7.1.3 Governing Equation

In this research on 2D open channel flow, we assume a two-dimensional, transient, turbulent, and incompressible flow. We employ the  $k - \omega$  Shear Stress Transport (*SST*) turbulence model to numerically solve the partial differential equations (*PDEs*). The primary governing equations include the continuity equation, the momentum equations in both the x and y directions, and the transport equations for turbulent kinetic energy ( $k$ ) and the specific rate of dissipation ( $\omega$ ), as presented in the above model equations.

#### Continuity Equation:

$$\frac{\partial \rho}{\partial t} + \frac{\partial(\rho u)}{\partial x} + \frac{\partial(\rho v)}{\partial y} = 0 \quad (7.3)$$

#### Momentum Equations (x-directions):

$$\frac{\partial(\rho u)}{\partial t} + \nabla \cdot (\rho \mathbf{u}u) = -\frac{\partial p}{\partial x} + \nabla \cdot \boldsymbol{\tau}_x + \rho f_x \quad (7.4)$$

#### Momentum Equations (y-directions):

$$\frac{\partial(\rho v)}{\partial t} + \nabla \cdot (\rho \mathbf{u}v) = -\frac{\partial p}{\partial y} + \nabla \cdot \boldsymbol{\tau}_y + \rho f_y \quad (7.5)$$

When solved numerically along with appropriate boundary conditions, these equations provide a framework for simulating turbulent 2D open channel flow using the  $k - \omega$  SST turbulence model.

### 7.1.4 Free surface equation

In this study, we examine a half-filled channel with water, using it as the secondary phase in the Volume of Fluid (VOF) model. Throughout the iterative processes, the free surface level remains constant across the entire computational domain of the channel. Our analysis assumes negligible variations in the injection region of the jets within the wake region. This assumption is based on the observation that the jet emerges within the primary flow domain. The temporal evolution of the mean flow depth [ $h = f(x, y, t)$ ] is described by the kinetic model equation provided below. This formulation is essential for capturing the dynamic behavior of the free surface, which moves in tandem with the stream-wise velocity ( $u$ ) [74].

$$\frac{\partial h}{\partial t} = (\hat{n}u)\sqrt{\sigma} \quad (7.6)$$

Where  $\hat{n}$  represents surface normal vector and

$$\sigma = 1 + \left(\frac{\partial h}{\partial x}\right)^2 + \left(\frac{\partial h}{\partial y}\right)^2 \quad (7.7)$$

### 7.1.5 Grid Independence Test

In this study of numerical simulations, we perform a discretization error analysis to conduct a grid independence test. The Grid Convergence Index ( $GCI$ ), defined as ( $GCI = F_s \times E_{u,k}$ ), is crucial for evaluating the reliability of the results. Here, ( $F_s$ ) represents the safety factor, and ( $E_{u,k}$ ) signifies the errors related to the target grids [63].

Three different grid densities were used for the grid convergence analysis, labeled as Grid-1 ( $900 \times 24$ ), Grid-2 ( $1200 \times 31$ ), and Grid-3 ( $1600 \times 36$ ), with element counts of 43,856, 56,981, and 72,630, respectively. The grid refinement ratio ( $r_k = \frac{h_2}{h_1} = \frac{h_3}{h_2}$ ), where ( $h$ ) denotes the number of control volumes in the mesh, was maintained at approximately 1.5. Depth-averaged velocity was numer-

## 7.1 Formulation of the problem

ically determined for each grid configuration, yielding values of 26.01, 25.31, and 25.01, as shown in Fig. 7.2.

The error was computed using ( $E_{u,k} = \frac{(\bar{u}_i - \bar{u}_j)}{\bar{u}_j(r_k^p - 1)}$ ), where ( $\bar{u}_i$ ) and ( $\bar{u}_j$ ) are the solutions at different grid refinements, and ( $p$ ) denotes the order of the governing equations (with ( $p = 2$ ) for second-order spatial accuracy). A safety factor ( $F$ ) was set to 1.25 [63].

The  $GCI$  was calculated for the transition from Grid-1 to Grid-2, resulting in ( $GCI_{12} = 2.76\%$ ), and from Grid-2 to Grid-3, yielding ( $GCI_{23} = 1.19\%$ ). Notably, ( $GCI_{23} < GCI_{12}$ ), indicating a progressive grid refinement. The ratio ( $\frac{GCI_{12}}{r_k^p GCI_{23}} = 1.02$ ), approximately equal to 1, suggests that the solution is within the asymptotic range of convergence. The percentage differences between Grid-1 and Grid-2, and Grid-2 and Grid-3, were found to be 2.76% and 1.57%, respectively, confirming the adequacy of the grid independence assessment in this study.

The analysis focused on the  $CFD$  results obtained for Grid-3 ( $1600 \times 36$ ), as shown in Fig. 7.3. The wall boundary layer is constructed with multiple layers having a  $y^+$  value less than 1.

Table 7.3: Grid convergence index test for grid density refinement

Grid	$N_X \times N_Y$	No. of Elements	$\hat{U}$	$r_k$	$P$	%GCI	$GCI_{12}/r_k^p GCI_{23}$
Grid-1	$900 \times 24$	43,856	25.01				
Grid-2	$1200 \times 31$	56,981	25.31	1.5	2	2.76	$1.024745 \approx 1$
Grid-3	$1600 \times 36$	72,630	26.01			1.19	

### 7.1.6 Variation of $y^+$ values

The  $y^+$  values for Grid-3 shown in Fig. 7.4 are obtained using the standard  $k - \omega$  model with standard wall function ( $SWF$ ), and are approximately 1. This allows for the resolution of the viscous sub-layer and buffer regions, as illustrated in Fig. 7.4. The variations observed in the curves are due to the obstacle present in the flow path. This obstacle acts as a physical barrier or obstruction, influencing the flow characteristics and leading to the observed fluctuations in the simulation results [75]. The Wall  $y^+$  parameter is crucial for this specific turbulence model used in computational fluid dynamics simulations to manage near-wall flow.

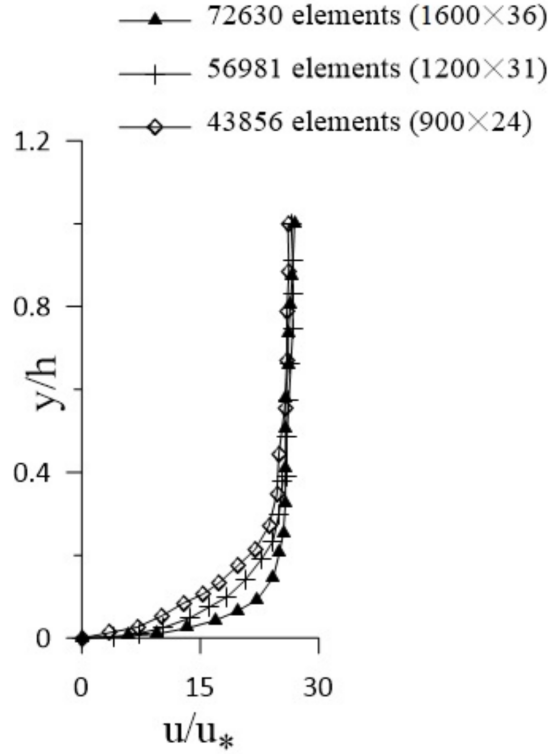


Figure 7.2: Normalized velocity profile plot for three different grids.

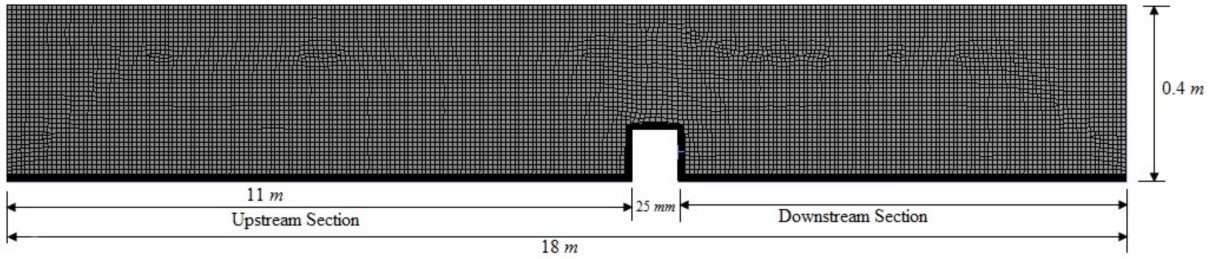


Figure 7.3: Schematic of the simulation domain with mesh.

## 7.2 Result and Discussion

### 7.2.1 Validation of velocity profile against log-law

The computed model solution data is compared with the log-law at a high Reynolds number ( $Re \approx 60,000$ ), as depicted in Fig. 7.5. The plot utilizes  $u^+$  (i.e.,  $u/u_*$ ) for the x-axis and  $y^+$  ( $yu_*/\nu$ ) for the y-axis. The friction velocity ( $u_* = 0.012$  m/s) is

## 7.2 Result and Discussion

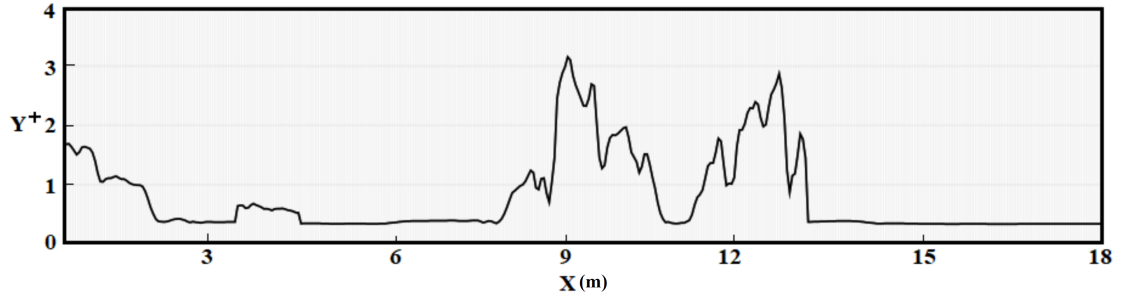


Figure 7.4: Wall  $y^+$  for Grid-3 along x-direction

determined from the wall shear stress value ( $\tau = 0.027 \text{ N/m}^2$ ). The standard  $u^+$  values are calculated using the Von Karman constant of 0.41 and an integration constant of 5.29 [48]. The velocity profile is also plotted based on the current data as a straight line, as shown below. It is noted that the majority of the data (90%) aligns with the straight line.

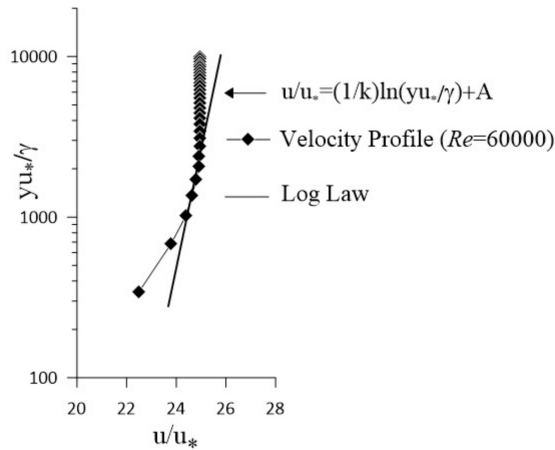


Figure 7.5: Validation of *VOF* model against the law of wall

### 7.2.2 Validation with the experimental results

A comparative analysis was conducted between the numerical results and experimental data in the validation process, as shown in Fig. 7.6. The study focused on examining normalized stream-wise mean x-velocity and stream-wise mean y-velocity derived from numerical simulations. These values were systematically compared against corresponding experimental measurements at both upstream

and downstream locations. The numerical results were validated using experimental data collected by researchers [76], graphically represented in Fig. 7.6. The experiments took place in a water channel facility measuring 18.3 m in length, 0.9 m in width, and 0.9 m in depth. The channel bed was constructed with reinforced concrete and maintained a constant slope of 0.00025. A vertical turbine pump ensured a consistent flow rate through the channel, with a flow control valve positioned between the pump and the channel to regulate the flow. The flow depth was controlled to ensure uniformity along the channel length, achieved by coordinating the flow control valve and the tailgate. Velocity-time measurements were conducted using a high-frequency (16 MHz) Acoustic Doppler velocimeter.

In the present study, five distinct positions were chosen for meticulous analysis, denoted as  $-V_1$  (located before the square),  $V_1$ ,  $V_2$ , and  $V_3$  (situated at distances of 2 m, 0.038 m, 0.088 m, and 1 m, respectively from the square). All positions were normalized to the square side length ( $d = 0.025$  m). Experimental investigations were conducted under conditions of a free-stream velocity,  $u$ , equal to 0.30 m/s. This parameter established Reynolds number ( $Re = uh/\gamma$ ) and Froude number ( $Fr = u/\sqrt{gh}$ ) values of 60,000 and 0.15, respectively. These values were determined based on the flow depth ( $h = 0.2$  m).

The comparison between simulation results and experimental data, as illustrated in Fig. 7.6, revealed a harmonious agreement at the upstream and upper regions of the square. Nonetheless, noticeable deviations were observed in the vertical velocity ( $v$ ) near the bed at the downstream location, particularly in the region influenced by suction. Unlike the experimental trend, the numerical results exhibit a downward velocity component that is not captured in the measured data. This discrepancy may arise from limitations in experimental resolution close to the wall, idealized boundary conditions in the simulation, or the sensitivity of vertical velocity prediction to turbulence modeling and mesh refinement.

Notably, the stream-wise velocity profile disparity between numerical and experimental results, particularly near the cube, was less than 8%. In contrast, at the upstream and far downstream locations, the numerical data exhibited commendable concordance with the variation trends observed in the experimental data, thereby offering a reliable approximation of the physical variables.)

## 7.2 Result and Discussion

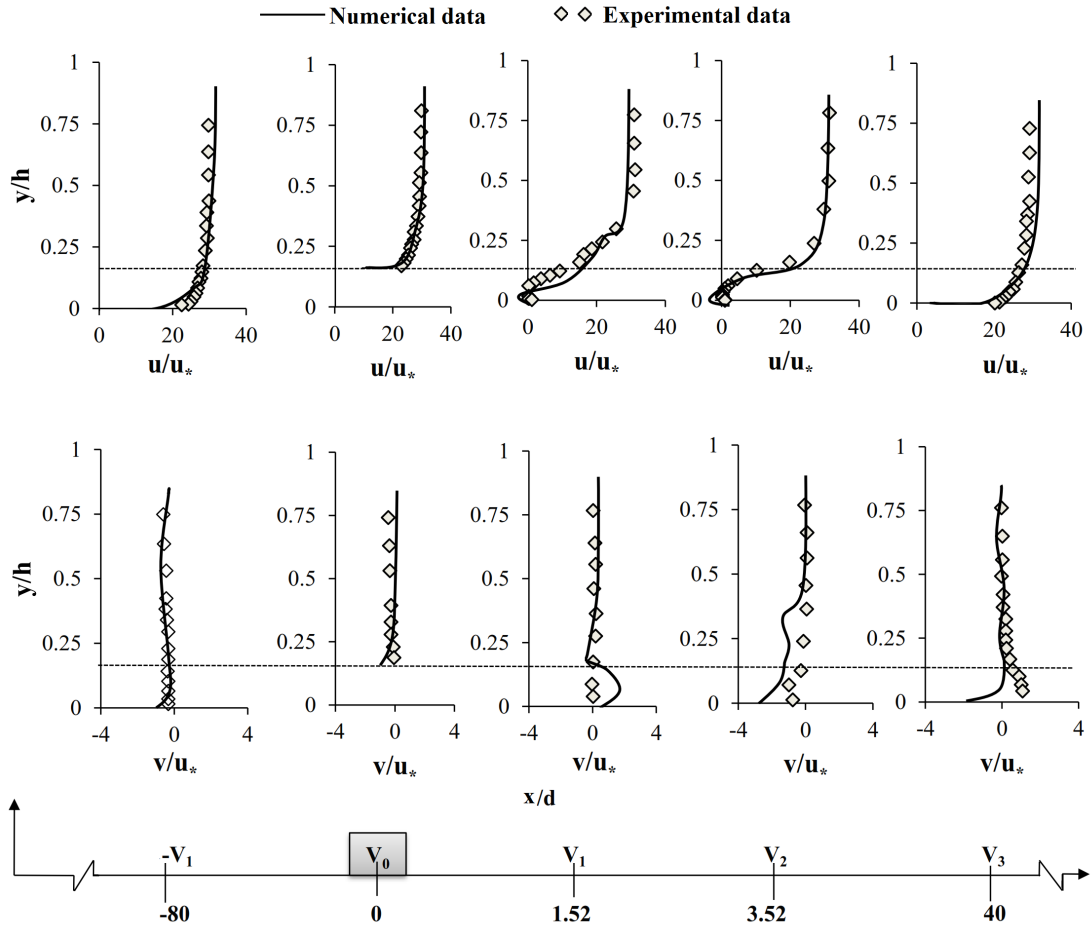


Figure 7.6: Validation of non-dimensionalized mean-velocity along  $x$ -direction ( $\hat{u}$ ), non-dimensionalized mean-velocity along  $y$ -direction ( $\hat{v}$ ) with experimental results

### 7.2.3 Velocity profile

The figure presented as Fig. 7.7 displays the normalized depth-averaged  $x$ -directional velocity component ( $\hat{U} = u/u_*$ ). The  $y$ -axis measures the height above the bed, normalized by the water depth ( $h = 0.2$  m). This graph contrasts the velocity profiles for a plane bed without a jet and with the inclusion of a jet at varying angles of attack ( $AOA$ ). At normalized bed positions ( $x/d$ ) both upstream and downstream, the velocity profiles are illustrated. The free stream velocity and the jet input velocity are constant at  $0.30$  m/s for all conditions. At the points labeled

$\hat{V}_1$  and  $V_3$  in Fig. 7.7 panels a and b, all four velocity profiles converge, showing no impact from jet-induced re-circulation or other effects. Negative velocities are noted in the wake zone, indicative of a pressure decrease.

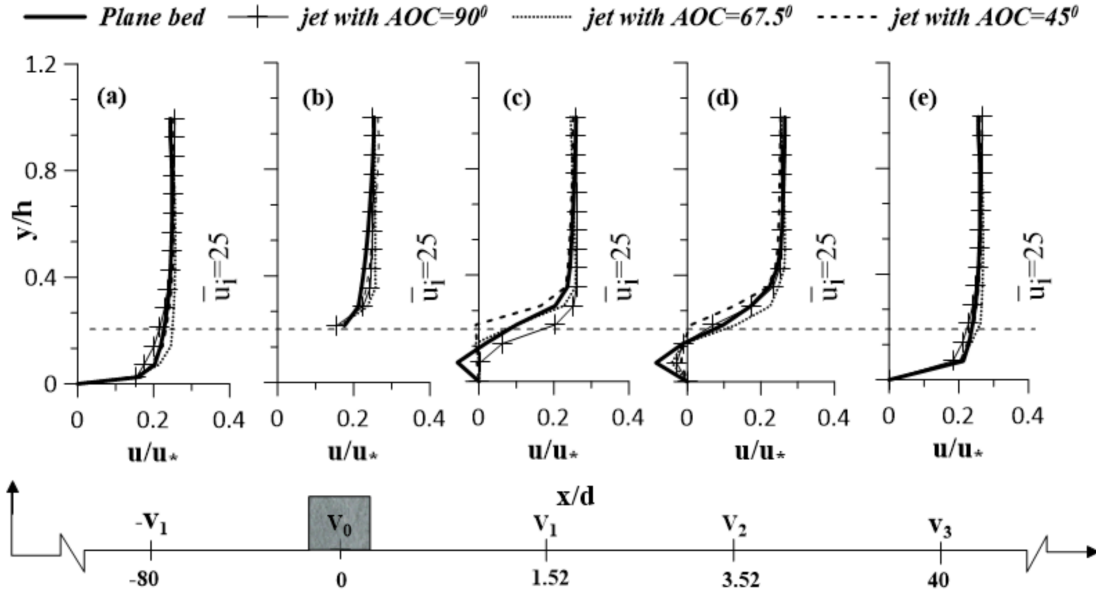


Figure 7.7: Stream wise vertical velocity  $\hat{U}$  profile along x- direction for a constant Reynolds number ( $Re = 60000$ ) of main flow with jet having three different angles of attacks

### 7.2.4 Streamline plot of the flow structure

The streamline plot is used to identify the flow pattern. Figure 7.8 below depicts the changes in the flow structure's behavior in the wake zone for a plane bed without a jet, as well as the corresponding jet input profiles. In the plane bed profile (Fig. 7.8a), a dark, coiled re-circulation area is observed. Figures 7.8(b – d) illustrate the jet input profiles with a constant jet velocity input but varying angles of attack. It is evident that as the angle of attack increases, the streamlines gradually become more linear, eventually eliminating the re-circulation at an angle of attack ( $AOC$ ) of 90 degrees. The upward curvature of streamlines suggests vertical flow induced by wake recovery and jet interaction. Although the free surface is modeled as a symmetry boundary, this behavior reflects potential

## 7.2 Result and Discussion

surface-directed flow in a physical scenario.

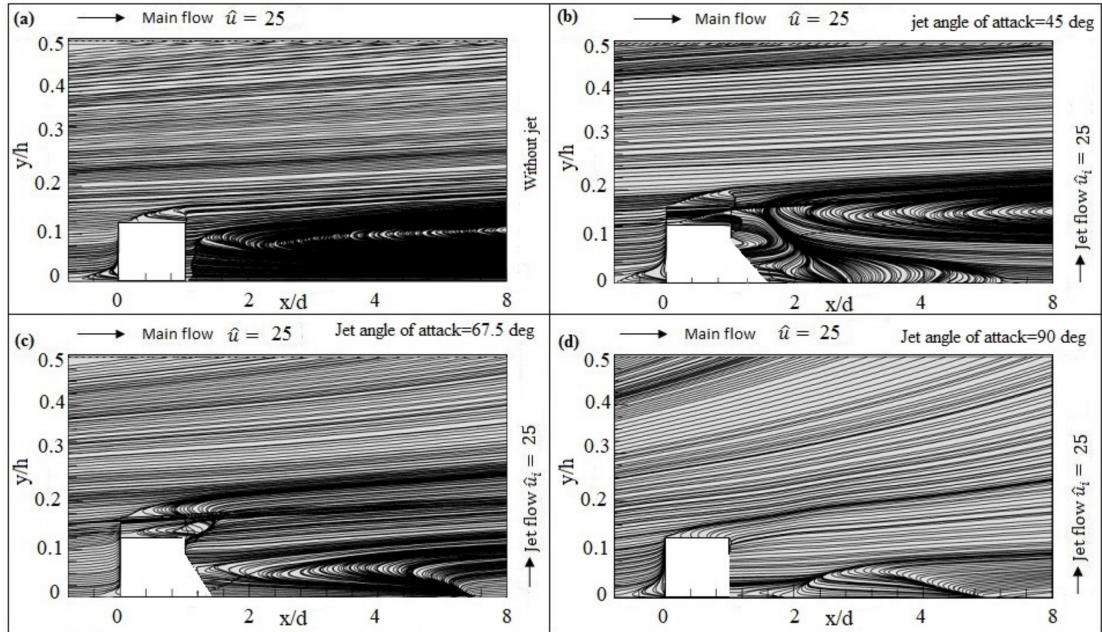


Figure 7.8: Stream line plot of streamwise vertical velocity  $\hat{U}$  (a) without jet, (b) Flow with jet velocities  $\hat{U}_i = 25^0$  and  $AOA 45^0$  (c) Flow with jet velocities  $\hat{U}_i = 25^0$  and  $AOA 67.5^0$  (d). Flow with jet velocities  $\hat{U}_i = 25^0$  and  $AOA 90^0$

### 7.2.5 Pressure Contour Plot

The contour plot of static pressure is depicted in Fig. 7.9 below. Pressure, a crucial parameter in the flow domain, is directly linked to flow velocity and its behavioral changes. The actual data has been normalized using the divisor  $\rho u^2$  to achieve a non-dimensional form. The dark spot in the re-circulation zone for a plane bed without a jet indicates the presence of high negative pressure  $\hat{P}$  ( $p/\rho u^2 = -138$ ), as shown in Fig. 7.9(a). For other jet input profiles, as the angle of attack increases, the pressure increases significantly, as illustrated in Fig. 7.9(a – d).

### 7.2.6 Variation of turbulent kinetic energy (TKE)

Figure 7.10 presents the turbulent kinetic energy (TKE) variations for two flow conditions: one without a jet and one with an inclined jet interacting with the flow.

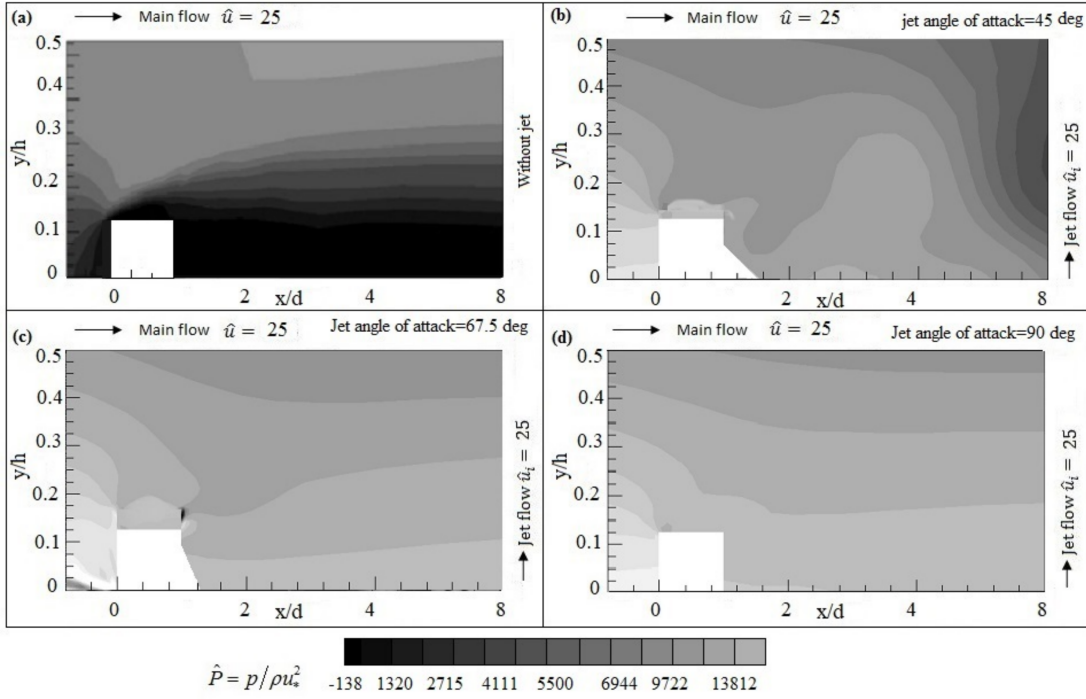


Figure 7.9: Contour plot of streamwise static pressure  $\hat{P}$  (a) without jet, (b) Flow with jet velocities  $\hat{U}_i = 25^0$  and AOA  $45^0$  (c) Flow with jet velocities  $\hat{U}_i = 25^0$  and AOA  $67.5^0$  (d). Flow with jet velocities  $\hat{U}_i = 25^0$  and AOA  $90^0$

To enhance understanding of  $TKE$  variations, we compared the  $TKE$  profiles for the flow without a jet with jets at different angles of attack (AOA) at specific stream-wise locations relative to a submerged obstacle. The  $TKE$  values have been normalized by the square of the frictional velocity ( $u_*^2$ ). The profiles exhibit notable variations at specific locations, specifically  $V_1$  and  $V_2$ . These changes are mainly due to velocity alterations and the behavior of flow structures within the re-circulation zones.

At the upstream location before the square obstacle ( $-V_1$ ), on the obstacle ( $V_0$ ), and at a downstream location ( $V_3$ ), the  $TKE$  profiles are closely aligned, showing minimal differences. Just downstream of the square,  $TKE$  is significantly higher than in the outer layer ( $y/h = 0.8$ ), with the highest  $TKE$  generated just above the square ( $y/h = 0.2$ ) compared to the near-bed region ( $y/h = 0$ ). Within the re-circulation zone, characterized by flow instability, there is significant  $TKE$  production. The  $TKE$  profiles without a jet show maximum values around 5000

## 7.2 Result and Discussion

at  $x/d = 1.52$ .

Due to the jet's influence on flow characteristics in the re-circulation zone,  $TKE$  values decrease systematically with varying  $AOA$  ( $\hat{k} \approx 5000$ ,  $\hat{k} \approx 2500$ ,  $\hat{k} \approx 1250$ ). Moving away from the re-circulation zone, the  $TKE$  magnitude decreases further downstream. This rapid change in  $TKE$  downstream indicates distinctive near-wake motion, highlighting a fundamental difference between near-wake and far-wake motion [77].

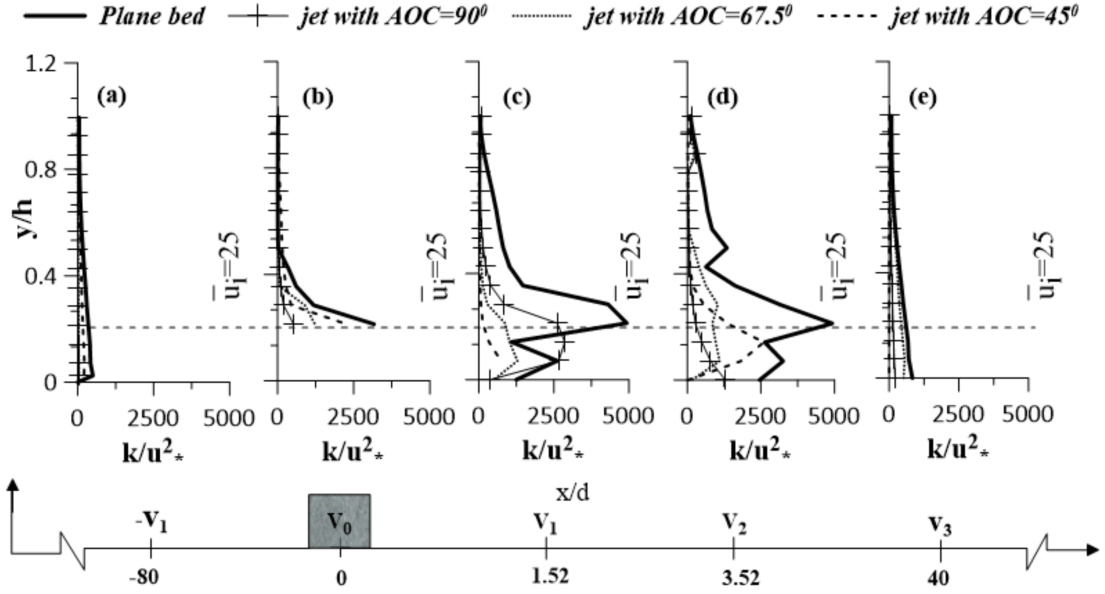


Figure 7.10: Stream wise plot of  $TKE$   $\hat{K}$  (a) without jet, (b) Flow with jet velocities  $\hat{U}_i = 25^\circ$  and  $AOA 45^\circ$  (c) Flow with jet velocities  $\hat{U}_i = 25^\circ$  and  $AOA 67.5^\circ$  (d). Flow with jet velocities  $\hat{U}_i = 25^\circ$  and  $AOA 90^\circ$

### 7.2.7 Contours of Turbulent Kinetic Energy ( $TKE$ )

In turbulent flows, characterized by the presence of numerous eddies, the parameter  $TKE$  represents the mean specific turbulent kinetic energy. This parameter provides a comprehensive quantitative analysis of various constituents originating from different turbulent mechanisms. These mechanisms include the  $TKE$  production rate,  $TKE$  dissipation rate,  $TKE$  diffusion rate, pressure energy diffusion rate, and viscous diffusion rate, which together maintain the dynamic equilibrium

within turbulent flows [70]. The data, normalized by  $u_*^2$ , is presented against the corresponding normalized coordinates as shown in Fig. 7.11. This study underscores significant variations in  $TKE$  near the wall, primarily due to turbulence production induced by an obstacle. For a square mounted without a jet [as illustrated in Fig. 7.11(a)], most of the area exhibits relatively low  $TKE$  values. However, drastic changes in  $TKE$  are observed in the re-circulation zone. This region of high turbulence, with elevated  $TKE$ , is caused by the formation of coherent large-scale vortices [78]. These fluctuations in  $TKE$  can be attributed to the intricate flow dynamics in the re-circulation zone, as well as the influence of the mean flow, resulting in additional  $TKE$  production [79].

With the introduction of the jet into the re-circulation zone, variations in the  $TKE$  values are observed. These variations also depend on the angle of attack. The square obstruction in the wake induces flow instability, generating additional  $TKE$  [53]. This deviation can be attributed to the disruption of the viscous sub-layer caused by turbulent vortices bursting [54]. As depicted in Fig. 7.11(b – c), changing the angle of attack of the jet results in  $TKE$  values returning to their main background flow values near the wall and around the square. When the angle of attack is  $90^\circ$ , as shown in Fig. 7.11(d), the white spot disperses from the re-circulation zone, and the  $TKE$  approaches lower levels.

### 7.2.8 Instantaneous vorticity variation

The vorticity contour plot, defined by  $\omega = (\partial V/\partial X - \partial U/\partial Y)$ , is utilized to visualize shear layers within a flow field. Instantaneous vorticity contours at  $t = 2$  s are presented for all cases in Fig. 7.12(a – d). These plots depict distinct shear layers within the core of vortex clusters in the wake zone, showing regions of concentrated vorticity with successive vortex generations. Fig. 7.12(a) shows that without jets, robust vortex generation occurs after the flow is obstructed by the square, within the re-circulation zone at  $0 \leq x/d \leq 12$ . A closer view reveals two vortices with opposite signs, shown as alternating thin layers of continuous and dotted lines. In the absence of external influence, vortices are generated, grow, and move downstream due to vortex dilutions [80]. The study investigates vortex shedding suppression by varying the jet angle of attack ( $AOA$ ). Jets impinging

## 7.2 Result and Discussion

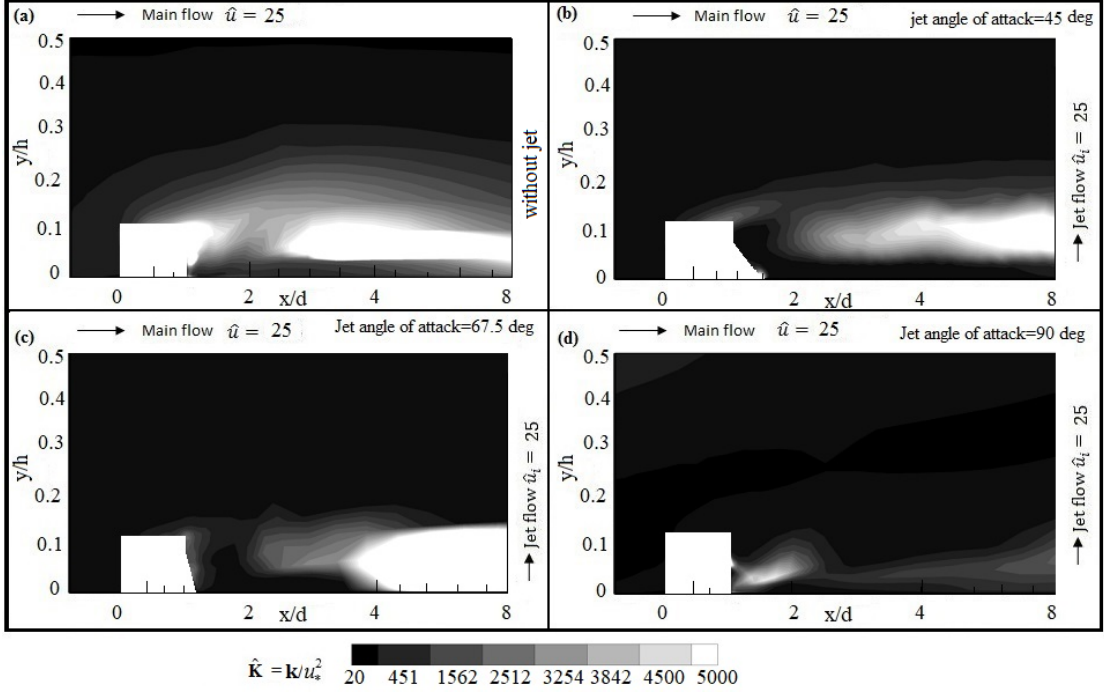


Figure 7.11: Contour plot of streamwise static turbulent kinetic energy  $\hat{K}$  (a) without jet, (b) Flow with jet velocities  $\hat{U}_i = 25$  and  $AOA = 45^\circ$  (c) Flow with jet velocities  $\hat{U}_i = 25$  and  $AOA = 67.5^\circ$  (d). Flow with jet velocities  $\hat{U}_i = 25$  and  $AOA = 90^\circ$

into the wake disrupt and weaken the shear layers of vortices [81]. This results in weaker vortices, transforming into smaller, well-defined vortices downstream where viscous effects gradually become dominant [82]. Increasing the jet angle of attack ( $AOA$ ) further enhances the separation of shear layers, leading to fewer, more concise vortices, as seen in Fig. 7.12(b – c). Finally, in Fig. 7.12(d), at an  $AOA$  of  $90^\circ$ , there is a marked reduction in vortex magnitude, evidenced by the reduced number and size of vortices, underscoring the effectiveness of this approach.

### 7.2.9 Spectral analysis of vorticity magnitude

In this study, we conduct a vorticity spectra analysis to evaluate the Power Spectral Density ( $PSD$ ) and pinpoint the vortex shedding frequency. The  $PSD$  plot's x-axis denotes the vortex shedding frequency in Hz, while the y-axis represents the

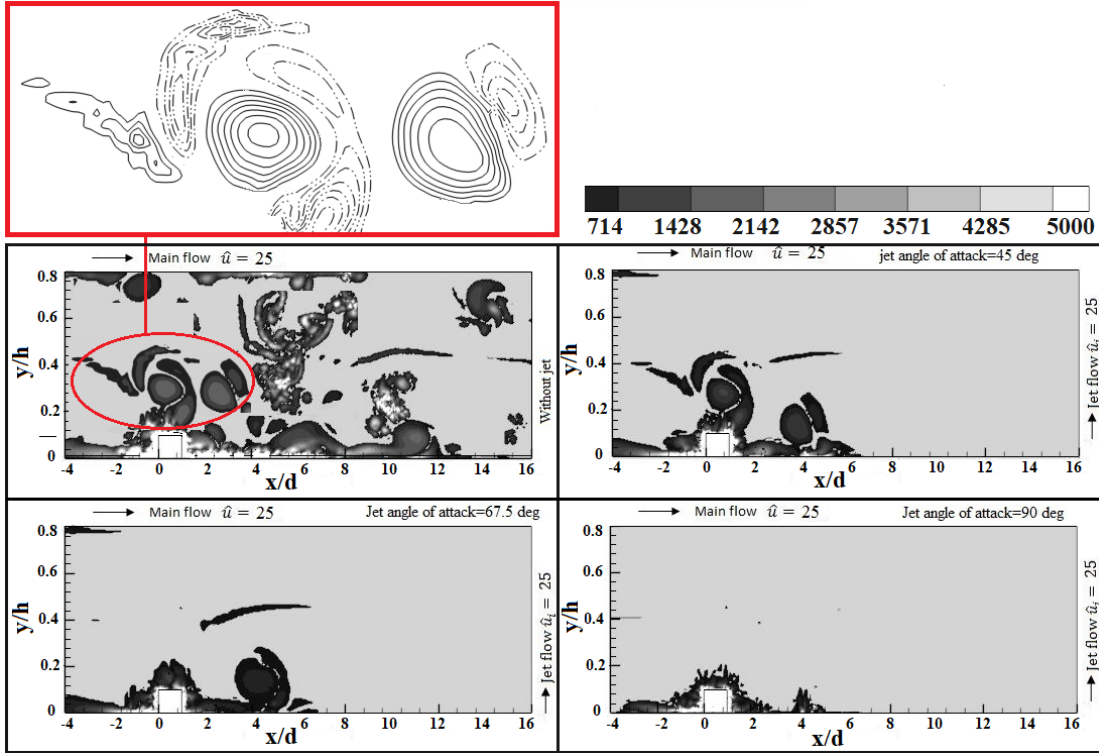


Figure 7.12: Instantaneous vorticity (a) without jet, (b) Flow with jet velocities  $\hat{U}_i = 25$  and  $AOA = 45^\circ$  (c) Flow with jet velocities  $\hat{U}_i = 25$  and  $AOA = 67.5^\circ$  (d). Flow with jet velocities  $\hat{U}_i = 25$  and  $AOA = 90^\circ$

amplitude of vorticity magnitude [67]. We specifically analyze data from the recirculation zone, particularly near the initial jet injection point by the square, to observe *PSD* variations under two conditions: without the jet [as depicted in Fig. 7.13(a)] and with the jet [as shown in Fig. 7.13(b–d)]. Notably, the amplitude of vorticity magnitude peaks uniformly across the specified frequency range. Without the jet, the amplitude lies within  $10^4 < PSD < 10^6$  as illustrated in Fig. 7.13(a). Introducing the jet results in a significant decrease in vorticity magnitude ( $10^2 < PSD < 10^4$ ), with a marked inclination in the same frequency range. As shown in Fig. 7.13(d), the amplitude of vorticity magnitude is minimized when the jet angle of attack (*AOA*) is  $90^\circ$ . This observation highlights the crucial influence of *AOA* variation in regulating the magnitude of the vortex shedding frequency [83].

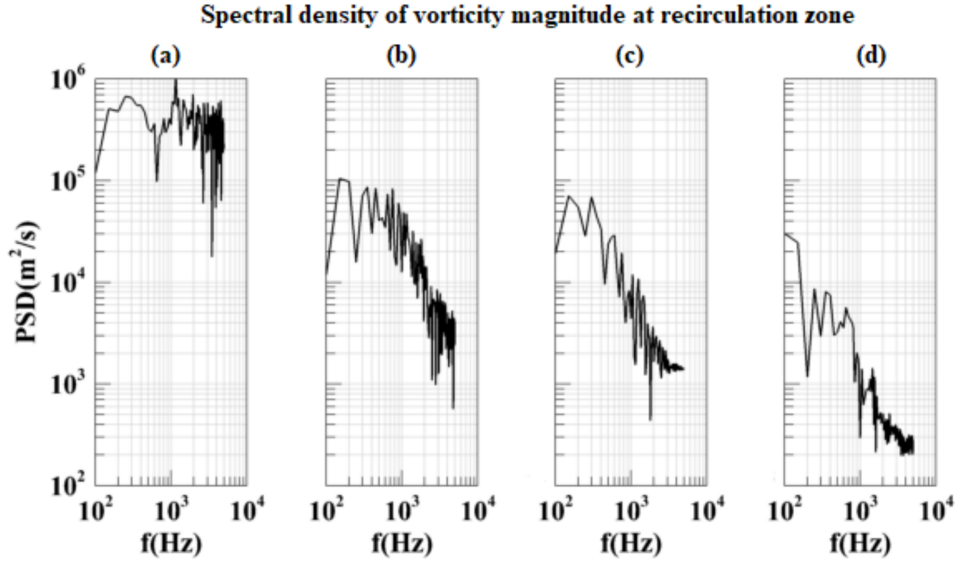


Figure 7.13: Power spectral density of vorticity magnitude (a) without jet, (b) Flow with jet velocities  $\hat{U}_i = 25$  and  $AOA = 45^\circ$  (c) Flow with jet velocities  $\hat{U}_i = 25$  and  $AOA = 67.5^\circ$  (d). Flow with jet velocities  $\hat{U}_i = 25$  and  $AOA = 90^\circ$ .

### 7.3 Conclusion

The research explored how a single inclined turbulent wall jet, adjusted at different angles of attack, affects the re-circulation zone formed behind a square obstruction. The findings reveal that altering the angle of attack significantly influences the re-circulation zone's dimensions and position. Specifically, as the angle of attack increases, the re-circulation zone diminishes in size and shifts further from the obstruction.

The study underscores the crucial role of the re-circulation zone in shaping the pressure distribution around the obstruction. Due to flow separation, this zone exhibits negative pressure. Additionally, the investigation showed that the turbulent wall jet is adept at shrinking the re-circulation zone and mitigating vortex effects. The jet creates a turbulent mixing layer near the re-circulation zone, disrupting vortex formation and decreasing the zone's size. This suggests that a single inclined turbulent wall jet serves as an effective flow control mechanism to manage the re-circulation zone behind a square obstruction. Notably, an approximate 80% reduction in vorticity magnitude indicates successful vorticity suppression.

Conclusively, the study shows that varying the angle of attack of a single inclined turbulent wall jet can be an efficient method to control the re-circulation zone behind a square obstruction. The results have significant implications for engineering applications, such as optimizing heat exchanger performance and minimizing vehicle drag.

# MODULATION OF RE-CIRCULATION ZONE BEHIND A SUBMERGED SQUARE OBSTRUCTION BY DUAL TURBULENT WALL JETS

This numerical study primarily aims to modulate the re-circulation region and suppress vortex shedding by investigating the flow behavior behind a square obstruction placed at the bottom surface of an open channel flow's fully developed region. The study involves testing two plane wall turbulent jets with three different jet Reynolds number combinations. These jets are directed vertically from the bottom surface into the wake zone, just downstream of the square obstruction. To ensure the entire re-circulation zone is covered, a specific gap is maintained between the jets. The re-circulation patterns are visualized using streamline contour plots, where negative mean stream-wise velocity signifies the re-circulation region. Upon introducing the first set of dual jets (varying in jet velocity), the main convoluted streamline pattern divides into three parts and relocates to dif-

ferent positions away from the jet injection points. A significant suppression of vortex shedding is achieved using dual jets set at a jet velocity ratio of 2 relative to the mainstream velocity.

### 8.1 Formulation of the problem

In this study, we investigate the behavior of open channel flow when a  $2D$  square obstruction is placed in the fully-developed region on the channel bed. The focus is on capturing the re-circulation zone in the wake region. The depth-averaged stream-wise velocity  $u$  is set to 0.30 m/s, which is considered the mainstream velocity. Two plane turbulent dual jets, with variable input velocities, are introduced vertically from two separate nozzles, each with a fixed diameter of 0.02 m. The open channel dimensions are 18 m in length and 0.4 m in width. An obstacle with a square cross-section of 0.025 m by 0.025 m is positioned 11 m from the channel inlet. The blockage ratio, based on the cross-sectional area, is 6.25%. It is noted that a blockage ratio greater than 1% can affect the wake pressure coefficients of bluff bodies, as demonstrated in wind-tunnel experiments by Noda (1995) [72]. However, the relatively small blockage ratio in this study is expected to have only a marginal or negligible effect on the results. A blockage ratio less than 1% indicates that pressure corrections due to wall effects are unnecessary.

For ease of analysis, the upstream edge of the obstacle is designated as the origin. The dual jets are placed 0.02 m and 0.08 m from the right-hand side of the obstacle on the bed. The gap between the jets is 0.04 m. The positions of the first jet, the gap, and the second jet follow a geometric progression with a geometric mean of 0.04 and a common ratio of 2. Figure 8.1 illustrates the developed model. The numerical solution of the governing equations was carried out using the commercial *CFD* software, *Ansys Fluent*. The computational framework was designed using the design module of *Ansys Fluent*. Detailed specifications of the channel and hydraulic parameters are listed in Table 8.1.



jets.

Dual plane wall jets, each with a diameter of 0.02 m, are introduced from the bed at right angles to the main stream. These jets are positioned on the bed at distances of 0.02 m and 0.08 m from the right vertical arm of the square obstruction, maintaining a 0.04 m gap between them. For both water (secondary phase) and air (primary phase), the depth of flow is set at 0.2 m in all models. For the air phase, a depth of 0.2 m is chosen to ensure that the air phase does not affect the water phase, which is the primary phase of interest. The transient (time-dependent) solution scheme is employed with initial conditions set for  $t = 0$  and a volume fraction ( $F = 1$ ).

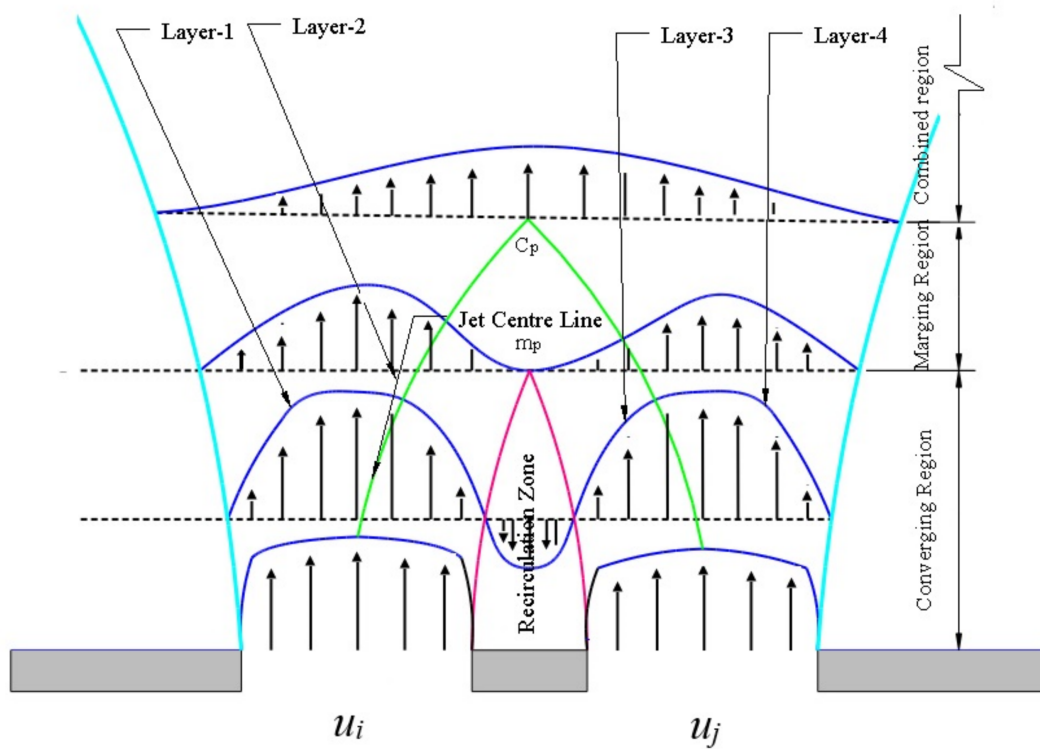


Figure 8.2: Schematic of the jet behavior in the flow field

## 8.1 Formulation of the problem

---

Table 8.2: Hydrodynamic parameters for plane bed open channel

Parameters	Values
Reynolds number, $Re = uh/\gamma$	60,000
Depth average stream wise velocity $u$ (m/s)	0.3
Mean flow depth, $h$ (m)	0.2
Friction velocity (computed from the log law) $u_*$ (m/s)	0.012
Froude number, $Fr$	0.15

Table 8.3: Hydrodynamic parameters for open channel with jet

Parameters	Values
Reynolds number, $Re = uh/\gamma$	60,000
Depth average stream wise velocity $u$ (m/s)	0.30
Mean flow depth, $h$ (m)	0.2
Friction velocity (computed from the log law) $u_*$ (m/s)	0.012
First set of jet velocity, $u_i = n \times u$ where $n = 1, 2, 3$ (m/s)	0.30, 0.60, 0.90
Second set of jet velocity, $u_j = n \times u$ where $n = 1, 2, 3$ (m/s)	0.15, 0.30, 0.45
First set of jet Reynolds numbers, $Re_i = u_i d/\gamma$	5971, 11943, 17914
Second set of jet Reynolds numbers, $Re_j = u_j d/\gamma$	2986, 5971, 8957

### 8.1.2 Governing Equations

Under the assumption of unsteady, two-dimensional, turbulent, and incompressible flow with isometric fluid properties, the Unsteady Reynolds-Averaged Navier-Stokes (URANS) equations are employed to solve and predict the turbulent characteristics of flow in an open channel. For turbulence modeling, the Standard  $k^\vee \epsilon$  model is utilized, known for its numerical stability and accuracy. It has been reported that the standard  $k^\vee \epsilon$  turbulence model is robust, economical, and accurate across a wide range of turbulent flows in industrial applications [84]. The continuity, momentum, and transport equations are formulated based on non-dimensional variables using the friction velocity ( $u_*$ ) of the flow as follows:[85].

**Continuity equation:**

$$\frac{\partial U_i}{\partial X_i} = 0 \quad (8.1)$$

**Momentum equation:**

$$\frac{\partial U_i}{\partial \tau} + \frac{\partial}{\partial X_j} (U_j U_i) = -\frac{\partial}{\partial X_i} \left( P + \frac{2}{3} k_n \right) + \frac{1}{Re} \frac{\partial}{\partial X_j} \left[ (1 + \gamma_{t,n}) \frac{\partial U_i}{\partial X_j} \right] \quad (8.2)$$

where,

$$U_i = \frac{u_i}{u_*}, X_i = \frac{x_i}{d}, \tau = \frac{t}{d/u_*}, P = \frac{p - p_0}{\rho u_*^2}, k_n = \frac{k}{u_*^2} \quad (8.3)$$

**The  $k - \epsilon$  model transport equations:**

$$\frac{\partial k_n}{\partial \tau} + \frac{\partial}{\partial X_j} (U_j k_n) = \frac{1}{Re} \frac{\partial}{\partial X_j} \left[ \frac{\gamma_{t,n}}{\sigma_k} \frac{\partial k_n}{\partial X_j} \right] + G - \epsilon_n \quad (8.4)$$

$$\frac{\partial \epsilon_n}{\partial \tau} + \frac{\partial}{\partial X_j} (U_j \epsilon_n) = \frac{1}{Re} \frac{\partial}{\partial X_j} \left[ \frac{\gamma_{t,n}}{\sigma_\epsilon} \frac{\partial \epsilon_n}{\partial X_j} \right] + C_{1\epsilon} \frac{\epsilon_n}{k_n} G - C_{2\epsilon} \frac{\epsilon_n^2}{k_n} \quad (8.5)$$

where,  $G$  is the production term and  $\gamma_{t,n}$  is eddy viscosity. These two terms are related as

$$G = \frac{\gamma_{t,n}}{Re} \left[ \frac{\partial U_i}{\partial X_j} + \frac{\partial U_j}{\partial X_i} \right] \frac{\partial U_i}{\partial X_j}, \gamma_{t,n} = C_\mu Re \frac{k_n^2}{\epsilon_n} \quad (8.6)$$

The model constant are  $\sigma_k = 1$  and  $\sigma_\epsilon = 1.30$ ,  $\sigma_{1\epsilon} = 1.44$  and  $\sigma_{2\epsilon} = 1.92$  [62]. The computational domain measures 18 meters in the  $x$  direction and 0.4 meters in the  $y$  direction. The bottom surface of the channel is designated as a wall where no-slip ( $u = 0$ ) and no-penetration ( $v = 0$ ) conditions are enforced. At the channel's inlet, a Dirichlet-type velocity boundary condition is applied. The turbulent intensity ( $I$ ) is determined using the relation  $I = 0.16 \times Re^{-\frac{1}{8}}$ , and the turbulent kinetic energy ( $k_n$ ) is calculated via  $k_n = 1.5I^2$  [60]. The dissipation rate ( $\epsilon_n$ ) at the inlet is given by  $\epsilon_n = \left( k_n^{3/2} c_\mu^{3/4} \right) / l$  [60], with  $l = 0.7$  based on Prandtl's mixing length model. At the outlet, a pressure outlet boundary condition is set, with all parameters assuming zero values. The open upper surface of the channel is modeled using a symmetry boundary condition.

## 8.1 Formulation of the problem

---

### 8.1.3 Free surface equation

In this study, the channel is modeled with a half-filled water configuration, serving as the secondary phase in the Volume of Fluid (VOF) model. Throughout the iterative simulations, the free surface level remains constant across the entire computational domain of the channel. Our methodology is based on the assumption that there are minimal variations in the jet injection region within the wake region. This assumption is supported by the observation that the jet forms within the primary flow domain. The temporal evolution of the mean flow depth, represented as  $[h = f(x, y, t)]$ , is governed by the kinetic model equation provided below. This formulation is especially relevant as it captures the dynamic characteristics of the free surface, moving synchronously with the streamwise velocity ( $u$ ) as described by Shi et al. (2000) [74].

$$\frac{\partial h}{\partial t} = (\hat{n}u)\sqrt{\sigma} \quad (8.7)$$

Where  $\hat{n}$  represents surface normal vector and

$$\sigma = 1 + \left(\frac{\partial h}{\partial x}\right)^2 + \left(\frac{\partial h}{\partial y}\right)^2 \quad (8.8)$$

### 8.1.4 Grid independence test

An study of discretization errors is crucial for carrying out the grid independence test. To accomplish the degree of acceptance, the grid convergence index ( $GCI = F_s \times E_{u,k}$ ), where  $E_{u,k}$  represents the errors on the target grids and  $F_s$  is the safety factor, is computed [63]. In order to perform the test, three distinct grid density ( $N_X \times N_Y$ ) are taken into consideration in the computational domain and are shown in table 8.4. These grid densities are Grid-1 ( $1636 \times 36$ ), Grid-2 ( $2005 \times 44$ ), and Grid-3 ( $2457 \times 54$ ), each of which contains 58896, 88220, and 132678 elements, respectively. With  $h$  representing the number of control volumes inside the mesh, the grid refinement ratio ( $r_k = \frac{h_2}{h_1} = \frac{h_3}{h_2}$ ) is fixed at 1.5 (approx.), where  $h$  is the mesh's total number of control volumes. The grid refinement ratio effectively captures the velocity gradient and is oriented from coarser to finer stages of refinement. Keeping the growth rate at 1.5 and the y-plus value at or around 1. The normalised numerical values of the depth average

velocity for each grid sample are determined from the plot (Fig.8.3) as 26.11, 25.09, and 24.68. The equation  $E_{u,k} = \frac{(\bar{u}_i - \bar{u}_j)}{\bar{u}_j(r_k^p - 1)}$  is the source of the inaccuracy. In the grid refinement process,  $\bar{u}_i$  and  $\bar{u}_j$  represent the solutions for the respective stages. The order of the governing equations is denoted by  $p$ , while second-order spatial accuracy is indicated by  $p = 2$ . Here,  $F$ , the safety factor, is taken into as 1.25 [63]. Grid convergence index values are computed as follows:  $GCI_{12} = 3.94\%$  for Grid-1 to Grid-2 and  $GCI_{23} = 1.69\%$  for Grid-2 to Grid-3. Given that  $GCI_{23} < GCI_{12}$ , a continuous grid refinement is indicated. The solution is found to reside within the asymptotic range of convergence, as shown by the  $\frac{(GCI_{12})}{r_k^p \times (GCI_{12})} = 1.03 \approx 1$  value. Figure.8.3 displays the test's visual examination. The depth average velocity profiles for various grid densities show that the Grid-3 solution differs from the Grid-1 and Grid-2 solutions. The grid independent test for the current job is therefore acceptable because the percentage differences across grids 1, 2, and 3 are 3.9% and 1.6%, respectively. The data used in this solution are derived from the CFD study of Grid-3(2257 × 54), as seen in Fig.8.4.

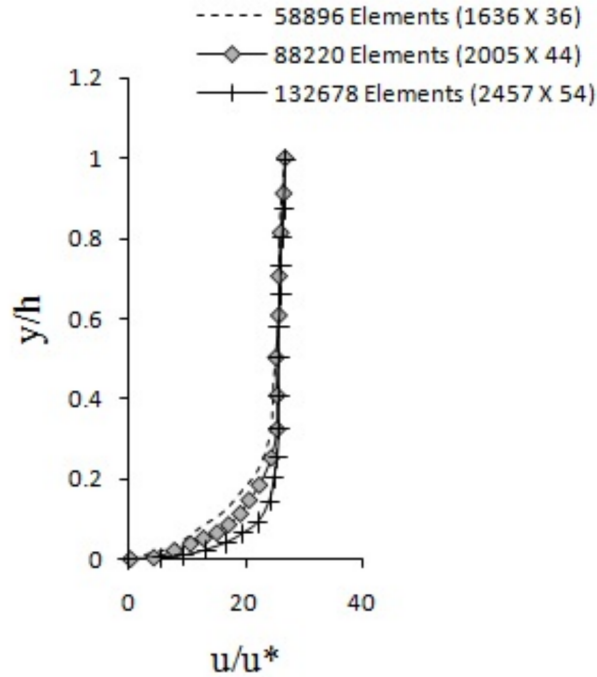


Figure 8.3: Stream-wise normalized velocity profile plot for three different grid elements

## 8.1 Formulation of the problem

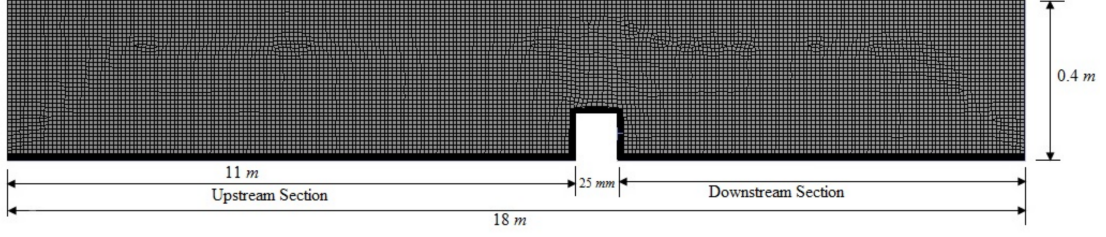


Figure 8.4: Schematic of the simulation domain with mesh (Grid-3( $2257 \times 54$ ))

Table 8.4: Grid convergence index test for grid density refinement

Grid	$N_X \times N_Y$	No. of Elements	$\hat{U}$	$r_k$	$P$	%GCI	$GCI_{12}/r_k^p GCI_{23}$
Grid-1	$1636 \times 36$	58,896	24.68				
Grid-2	$2005 \times 44$	88,220	25.09	1.5	2	3.94	$1.033632 \approx 1$
Grid-3	$2457 \times 54$	1,32,678	26.09			1.69	

### 8.1.5 Numerical procedure

The governing equations, being non-linear and coupled with each other, necessitate the use of iterative methods until convergence is achieved. To solve these equations, we utilized the projection method, a widely recognized pressure-based algorithm [86]. The pressure correction method, which derives the pressure equation from the governing equations, allows us to address the constraints imposed by the continuity equation on the velocity field. By segregating the coupled terms in the governing equations, the pressure-based solver inherently available in the *CFD* package facilitated the converged numerical solution.

Since time-advanced iterative methods based on initial approximations were employed, a residual target value of  $10^{-5}$  was set to ensure more accurate results. The time step size was set to 0.0002 seconds, with the number of time steps set to 10,000 to achieve convergence. In tackling the open channel-based flow problem, the *VOF* (Volume of Fluid) approach was adopted for the numerical calculations of multiphase flow. This technique is effective for surface tracking at the interface of two immiscible fluids, such as air and water, and for determining their fractional volumes within a computational cell using a common set of momentum equations.

In this numerical simulation, a *2D* mathematical model was employed, based on a set of assumptions regarding the variation of problem variables and their in-

terrelations. All boundary domain calculations are depicted in Fig. 8.1. For most open channel flow systems, scaling laws are utilized [46], making the turbulent intensity ( $I$ ) and turbulent length scale ( $l$ ) two critical parameters in this study [47].

$$I = 0.16 \times Re^{-\frac{1}{8}} \quad (8.9)$$

$$l = 0.038 \times d_h \quad (8.10)$$

where  $d_h$  is the hydraulic diameter. Again, for downstream boundary condition pressure outlet boundary condition is used specifying the static pressure as gauge pressure.

## 8.2 Results and Discussion

### 8.2.1 Validation of velocity profile with log-law

The log-law has been extensively studied as a fundamental principle for turbulent wall jets, receiving considerable attention from many researchers. This law has long been considered a milestone for validating numerical data. In the present study, the numerical model has been validated by comparing its data with the log-law. The computational domain was configured to simulate boundary conditions at a high Reynolds number ( $Re \approx 60,000$ ). The stream-wise velocity ( $u$ ) profile, normalized using the friction velocity ( $u_*$ ), is plotted against the height from the bed ( $y$ ) on a logarithmic scale. The friction velocity, calculated from a wall shear stress of 0.027 Pa, is 0.012 m/s.

Figure 8.5 shows a straight line representing the normalized log-law profile, with standard  $u^+$  values (i.e.,  $u/u_*$ ) derived using the Von Karman constant ( $= 0.41$ ) and an integration constant of 5.29, as outlined in [48]. The velocity profile in the same figure closely matches the standard straight-line curve, except near the wall and near the free surface. The deviation near the wall is attributed to the linear law in the viscous sub-layer, aligning with basic theory, while the variation near the free surface corresponds to the law of the wake in the turbulent outer layer.

## 8.2 Results and Discussion

---

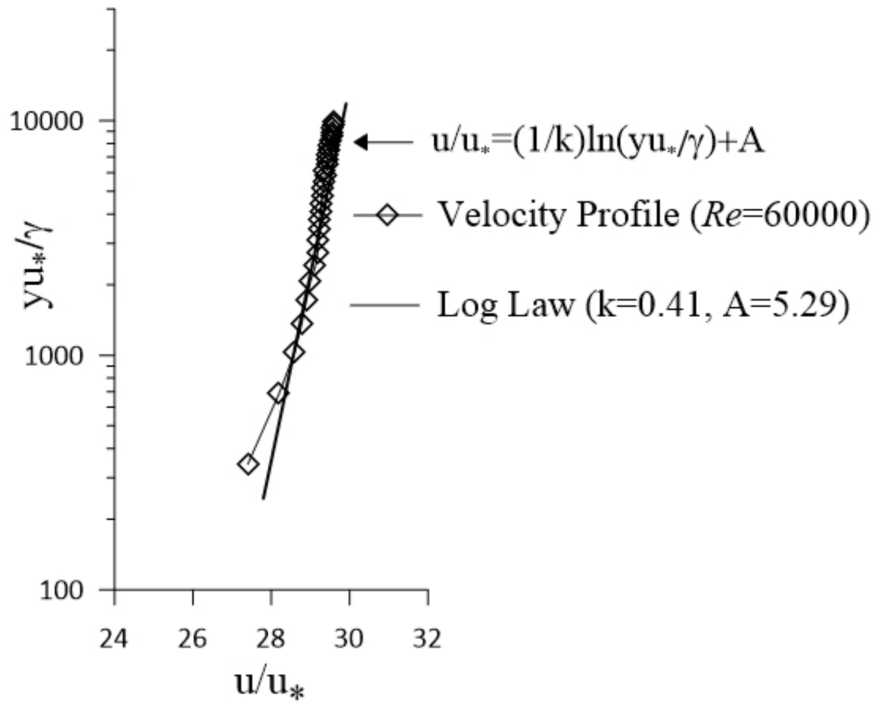


Figure 8.5: Validation of *VOF* model against log law

### 8.2.2 Validation with the experimental results

The validation of the numerical results was conducted using experimental data obtained from the fluid mechanics and hydraulics laboratory (FMHL) in the department of aerospace engineering and applied mechanics at the Indian Institute of Engineering Science and Technology (IEST), Shibpur, India, as depicted in Fig. 8.6. The comparison involved normalized stream-wise mean velocity data from both numerical and experimental sources at identical upstream and downstream locations. The experiments utilized a water channel facility measuring 18.3 m in length, 0.9 m in width, and 0.9 m in depth. The flume's flat bed, constructed from net cement, has a constant slope of 0.00025. A vertical turbine pump provided a steady flow through the channel, regulated by a flow control valve situated between the pump and the channel. Synchronizing the flow control valve with the tail gate maintained a consistent flow depth along the channel's length. Velocity-time measurements were taken using a 16 MHz Acoustic Doppler velocimetry device. The detailed description of the facility can be found in [65].

In the experimental setup, flow passed over an obstacle on the flume bed under conditions matching those of the numerical simulation. Position ( $A_{-1}$ ) was measured before the obstacle, while ( $A_1$ ,  $A_2$ ,  $A_3$ , and  $A_4$ ) were measured after the obstacle at distances of 0.08 m, 0.0325 m, 0.0525 m, 0.0925 m, and 0.4 m, respectively, from the obstacle's center. All positions on the channel bed were normalized to the jet diameter ( $d = 0.02$  m). The experiments were conducted with a free stream velocity of  $u_m = 0.30$  m/s, resulting in a Reynolds number ( $Re = u_m h / \nu$ ) of 60,000 and a Froude number ( $Fr = u / \sqrt{gh}$ ) of 0.15, based on a flow depth of  $h = 0.20$  m.

Figure 8.6 shows that numerical and experimental data closely match upstream and at the top of the square object ( $A_0$ ), though slight variations are observed near the bed downstream. The numerical results closely follow the experimental data trend, providing a reliable estimation of physical variables. The discrepancy in the stream-wise velocity profile between numerical and experimental results near the obstacle is less than 8%. Upstream and far downstream, the numerical data aligns well with the experimental trend, offering a reasonable approximation of physical variables.

### 8.2.3 Variation of Vertical Normalized Mean-Velocity ( $\hat{U}$ ) Component along x-Direction

The spatial evolution of the flow domain is depicted through the depth-averaged normalized mean velocity component ( $\hat{U} = u/u_*$ ) along the x-direction in Fig. 8.7. This velocity plot is presented against  $y/h$ , a normalized ordinate where  $h$  denotes the constant water depth. The normalized mean velocity ( $\hat{U}$ ) without the jet profile is compared to those with jet-induced profiles. To enhance representation, six specific normalized vertical positions in the bed are considered, marked as ( $A_{-1}$ ,  $A_0$ ,  $A_1$ ,  $A_2$ ,  $A_3$ , and  $A_4$ ). Three individual sets of dual jets with varying velocities are introduced vertically in the re-circulation zone from the bed, as illustrated in Fig. 8.7. For jet-1, the velocities are  $u_i = 0.30, 0.60,$  and  $0.90$  m/s at  $A_1$ , and for jet-2, they are  $u_j = 0.15, 0.30,$  and  $0.45$  m/s at  $A_3$ . The velocity ratio ( $v_k = v_2/v_1 = v_3/v_2$ ) is kept constant for both jets. Since the jets do not influence the locations  $A_{-1}$ ,  $A_0$ ,  $A_1$ , and  $A_4$ , the velocity profiles at these points are similar.

## 8.2 Results and Discussion

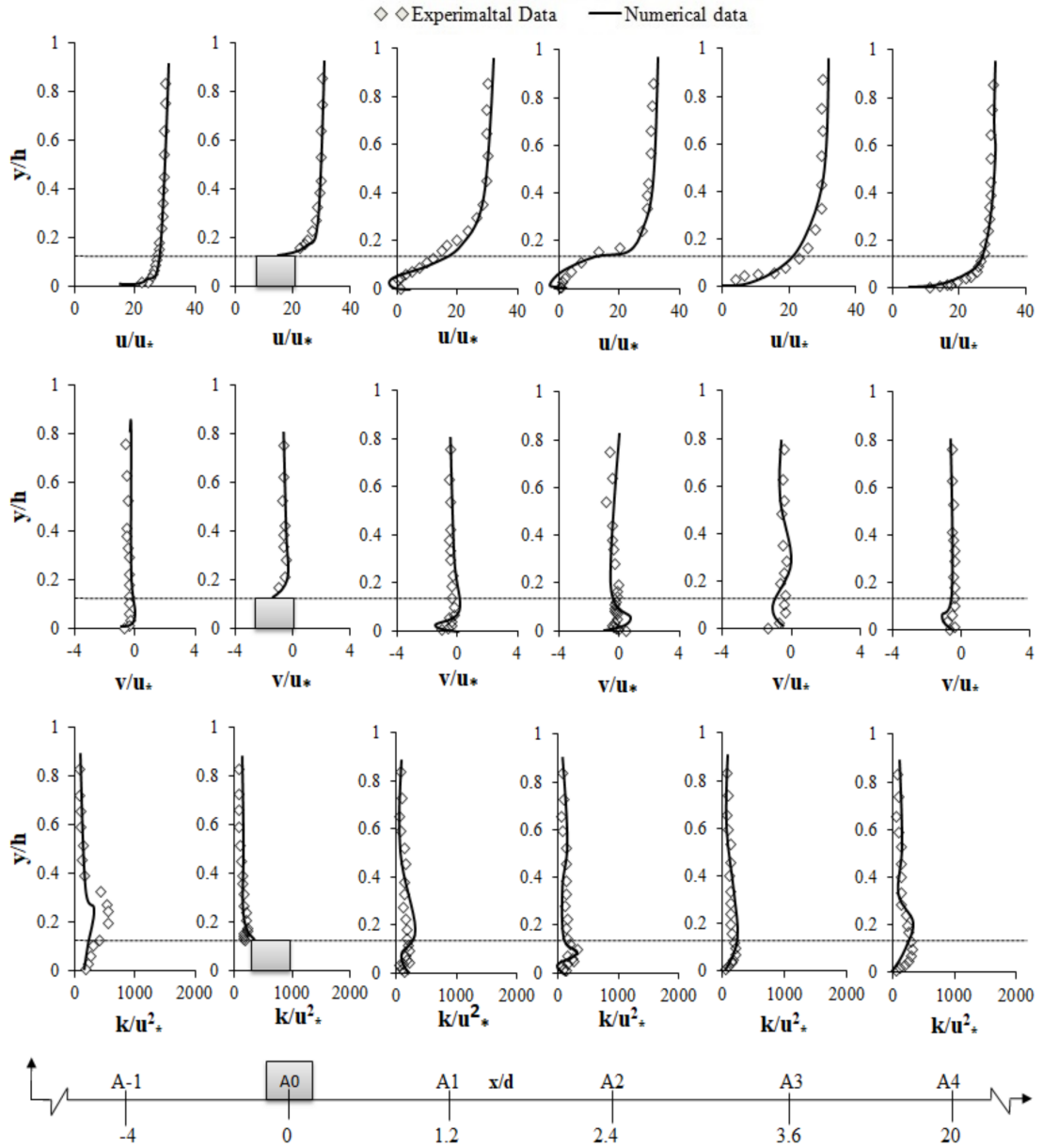


Figure 8.6: Validation of normalised mean-velocity along x-direction ( $u/u_*$ ), along y-direction ( $v/u_*$ ) and normalised turbulent kinetic energy ( $k/u_*^2$ ) with experimental results (from Singh and Debnath 2016) at different normalized locations relative to the square obstruction.

In the re-circulation zone, the presence of the jets leads to a proportional increase in jet inlet momentum ( $\int_0^1 u_m^2 dx$ ), resulting in a progressive velocity increase.

Consequently, a chaotic order in the velocity profile is observed near the bed in the re-circulation zone up to  $y/h = 0.3$ .

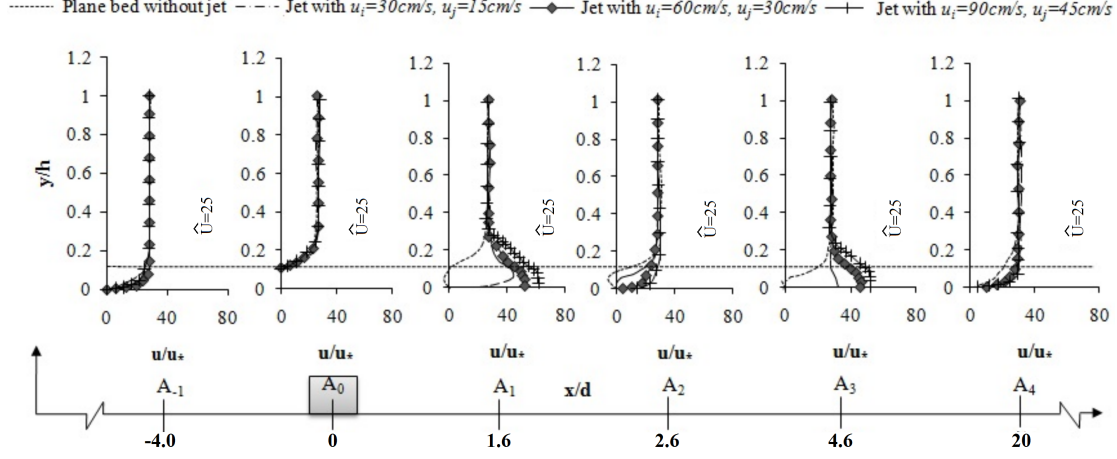


Figure 8.7: Normalized stream wise mean velocity  $\hat{U}$  profile against  $y/h$  for with and without jet.

### 8.2.4 Contour plot of velocity variation

Figure 8.8 presents the contour plot of the stream-wise mean velocity component for cases with and without the jet. To ensure a consistent comparison, the stream-wise and vertical distances are normalized using the jet diameter ( $d$ ) and flow depth ( $h$ ), respectively. In the flow without a jet, the dark spot in Fig. 8.7(a) indicates a significant reduction in mean velocity, with notable recirculation and flow reversal in the wake, caused by flow separation at the obstacle's edge, extending to approximately  $x/d = 4$ .

In contrast, Fig. 8.8(b) shows the flow when a jet is introduced with normalized velocities  $\hat{U}_i = 25$  and  $\hat{U}_j = 12.5$ . This introduction causes a slight perturbation in the target region, indicating a modest impact on flow modulation. Nevertheless, a small, cone-shaped re-circulation zone is still observed between the two jets. Figures 8.8(c) and 8.8(d) investigate the effect of increasing jet velocities on flow structures. The jet's momentum attainment ( $\int_0^1 u_m^2 dx$ ) is related to the jet's velocity. Consequently, increasing the jet velocities to  $\hat{U}_i = 50$ ,  $\hat{U}_j = 25$ , and then to  $\hat{U}_i = 75$ ,  $\hat{U}_j = 37.5$  leads to a gradual reduction of the dark spot.

## 8.2 Results and Discussion

However, for all the jet input velocity profiles considered, a dark spot persists in the space between the two jets, indicating the continued presence of the re-circulation zone up to the merging points ( $m_p$ ).

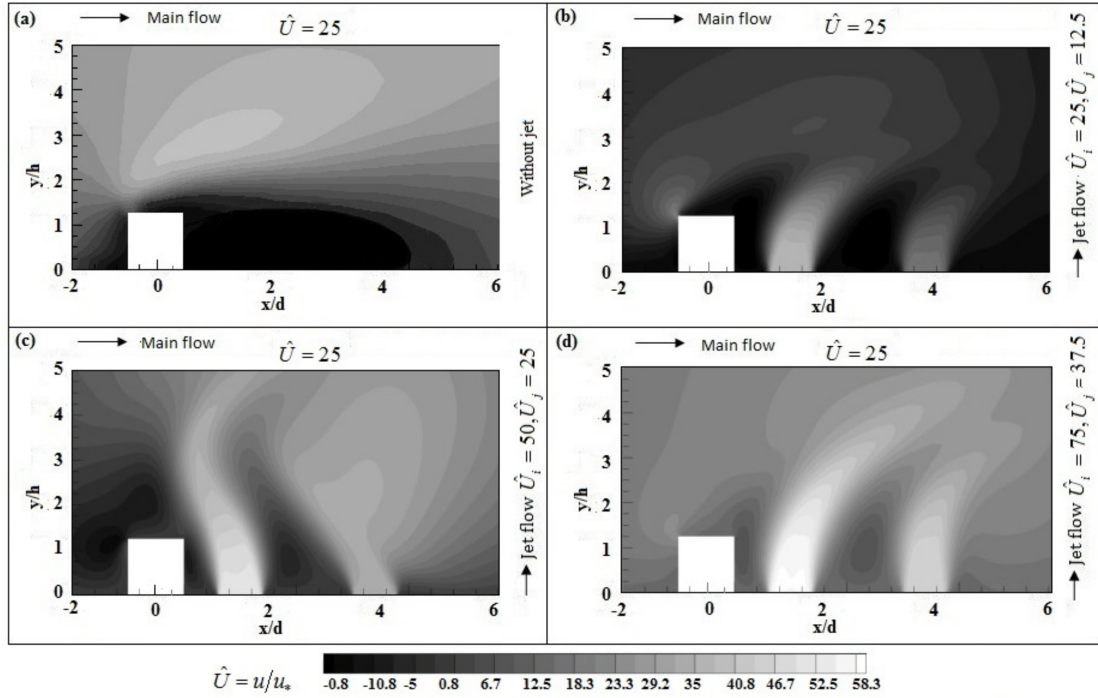


Figure 8.8: Contour plot of stream wise vertical velocity ( $\hat{U}$ ) (a). without jet (b). Flow with dual jet velocities  $\hat{U}_i = 25$  and  $\hat{U}_j = 12.5$  (c). Flow with dual jet velocities  $\hat{U}_i = 50$  and  $\hat{U}_j = 25$  and (d). Flow with dual jet velocities  $\hat{U}_i = 75$  and  $\hat{U}_j = 37.5$ .

### 8.2.5 Streamline plot of the flow structure

Figure 8.9 illustrates the local direction vector field in the wake of the obstacle, comparing scenarios with and without jet intervention. In Fig. 8.9(a), the streamline pattern at  $x/d = 3$  is concentric, with stable vortices positioned around the central point, resembling a coiled comet. This configuration emphasizes the significant role of the re-circulation zone in the wake region of the submerged obstacle. Each streamline follows an orderly pattern, gliding smoothly over one another without intersecting. To eliminate structural influences of flow irregularities, ex-

ternal artificial control forces are necessary [22, 18].

Upon introducing the first set of dual jets, as depicted in Fig. 8.9(b), the primary convoluted streamline pattern splits into three distinct parts, re-positioned away from the jet injection points, resembling a smaller, concise pattern. The orientation of the newly formed streamline near the square obstacle shifts vertically upward due to the higher velocity of the first jet pushing it in that direction. The middle streamline pattern, situated between the two jets, maintains its concise structure, while the last one reduces in size and exhibits similar behavior.

With the introduction of the second set of dual jets, as shown in Fig. 8.9(c), the last streamline patch completely disappears. The elliptical structure of the middle streamline is influenced by the increased jet velocities, although its volume remains unchanged. The application of the third set of dual jets results in nearly complete modulation of the re-circulation zone. Consequently, the dual jets effectively mitigate the formation of vortex shadings without impacting the square object.

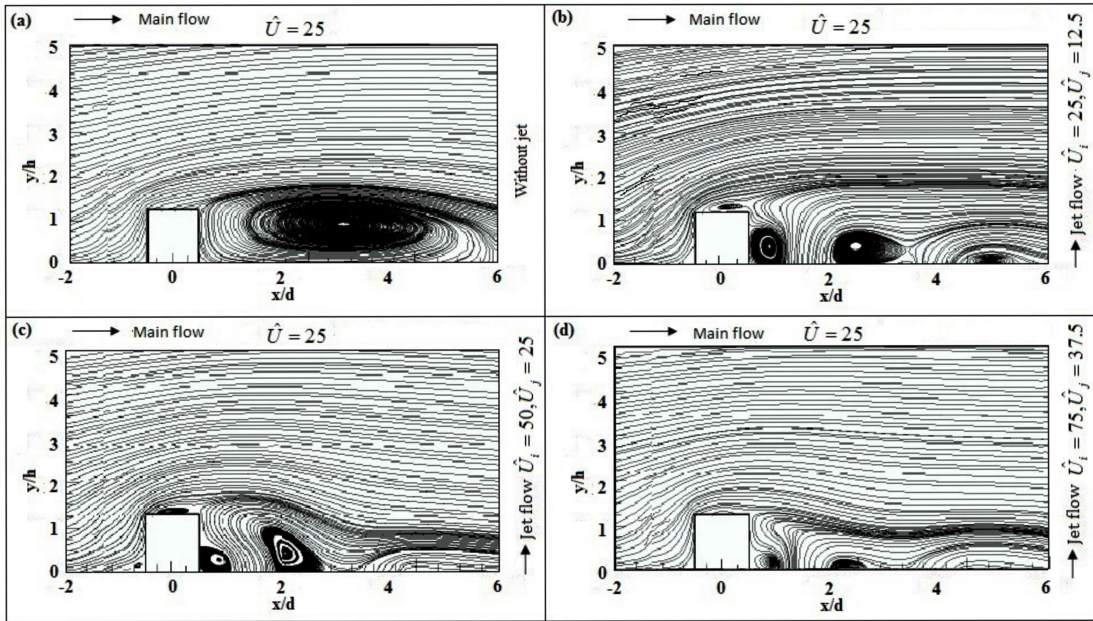


Figure 8.9: Stream line plot of stream wise vertical velocity ( $\hat{U}$ ) (a). without jet (b). Flow with dual jet velocities  $\hat{U}_i = 25$  and  $\hat{U}_j = 12.5$  (c). Flow with dual jet velocities  $\hat{U}_i = 50$  and  $\hat{U}_j = 25$  and (d). Flow with dual jet velocities  $\hat{U}_i = 75$  and  $\hat{U}_j = 37.5$ .

## 8.2 Results and Discussion

---

### 8.2.6 Instantaneous vorticity variation

The vorticity contour plot is a crucial tool for visualizing the shear layers within a flow field. In this study, vorticity is defined as  $\omega = (\partial V/\partial X - \partial U/\partial Y)$ . The plots of instantaneous vorticity contours are presented for the time period of  $t = 20$  s in all the cases shown in Fig. 8.10(a – d). These plots illustrate distinct shear layers within the cores of vortex chunks in the wake zone. As depicted in Fig. 8.10, areas of concentrated vorticity mark the presence of vortices in the flow field.

In Fig. 8.10(a), which represents the scenario without a jet, significant vortex generation is observed after the flow encounters the square obstruction in the re-circulation zone at  $0 \leq x/d \leq 7$ . A zoomed-in view of a specific region reveals two vortices with opposite signs, illustrated as alternating thin layers of continuous and dotted lines. These vortices form, grow, and are carried downstream due to vortex dilutions [80]. The variation in jet velocity is crucial for controlling vortex shedding suppression, making this study particularly insightful.

When jets are introduced into the wake, they disrupt and weaken the shear layers of the vortices [81]. Consequently, the vortices diminish in strength and transform into smaller, well-defined vortices further downstream, where viscous effects begin to dominate gradually [82]. As jet velocities increase, the momentum enhances the separation of shear layers, resulting in fewer and more compact vortices, as observed in Fig. 8.10(b – c). Ultimately, Fig. 8.10(d) demonstrates a significant reduction in vortex magnitude, indicated by fewer and smaller vortices, when dual jet velocities  $\hat{U}_i = 75$  and  $\hat{U}_j = 37.5$  are applied.

### 8.2.7 Vorticity spectra analysis

The power spectral density (*PSD*) of the vorticity magnitude signals is analyzed to detect the vortex shedding frequency. On the x-axis, the vortex shedding frequency (*Hz*) is plotted against the amplitude of the vorticity magnitude [67]. Data is collected from the re-circulation zone, specifically near the first jet injection point, to illustrate the *PSD* variations for scenarios without jet, as shown in Fig. 8.11(a), and with jet, as depicted in Fig. 8.11(b – d). The vorticity magnitude amplitude reaches its maximum uniformly within the specified frequency range. In cases with jet input, the vorticity magnitude declines sharply within the same

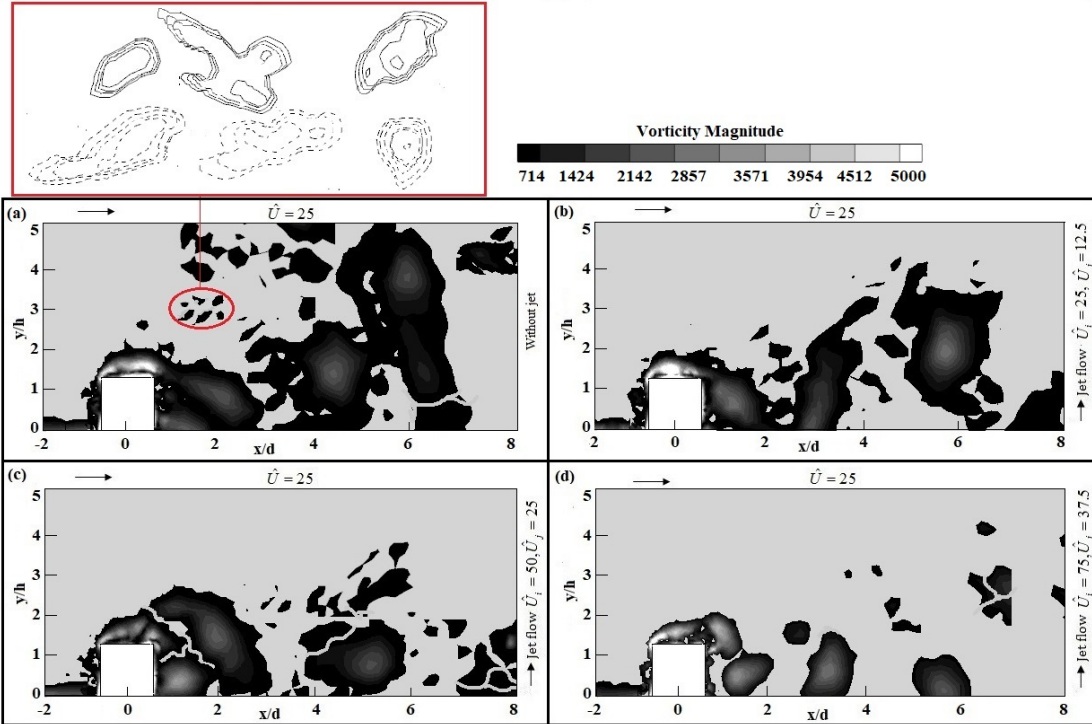


Figure 8.10: Instantaneous vorticity (a). without jet (b). Flow with dual jet velocities  $\hat{U}_i = 25$  and  $\hat{U}_j = 12.5$  (c). Flow with dual jet velocities  $\hat{U}_i = 50$  and  $\hat{U}_j = 25$  and (d). Flow with dual jet velocities  $\hat{U}_i = 75$  and  $\hat{U}_j = 37.5$ .

frequency ranges. Figure 8.11(d) clearly demonstrates that the amplitude of the vorticity magnitude is minimized for jet velocities  $\hat{U}_i = 75$  and  $\hat{U}_j = 37.5$ . This indicates that jet impingement velocity significantly influences the vortex shedding frequency magnitude [87]. The study thus highlights modulated re-circulation flow patterns through reduced vorticity magnitude.

### 8.2.8 Variation of pressure

The contours of static pressure variation depicted in Fig. 8.12 illustrate the scenarios with and without jet inputs. The data is normalized using the parameter  $(\rho u^2)$  to present it in a non-dimensional form. In Fig. 8.12(a), which represents the profile without jets, a notably high negative pressure  $\hat{P}(p/\rho u^2 = -434)$  is observed within the re-circulation zone of the obstacle. This area is characterized by a dark spot on the contour plot, indicating a substantial pressure drop.

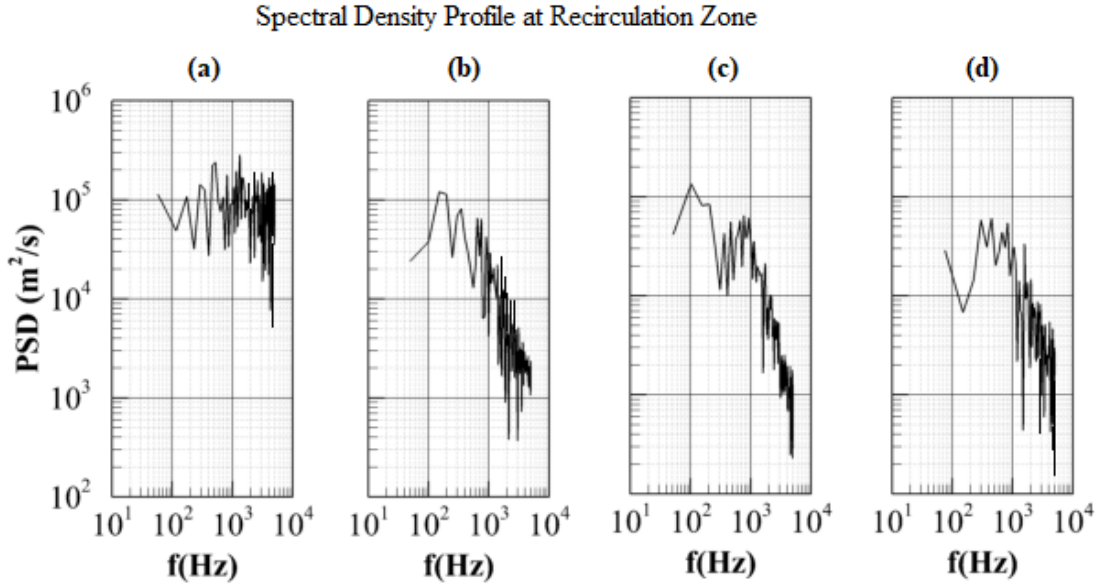


Figure 8.11: Power spectral density of vorticity magnitude (a). without jet (b). Flow with dual jet velocities  $\hat{U}_i = 25$  and  $\hat{U}_j = 12.5$  (c). Flow with dual jet velocities  $\hat{U}_i = 50$  and  $\hat{U}_j = 25$  and (d). Flow with dual jet velocities  $\hat{U}_i = 75$  and  $\hat{U}_j = 37.5$ .

The contour plots of the static pressure with dual jet inputs are shown in Fig. 8.12(b – d). The introduction of jets into the re-circulation zone significantly reduces the extent of the dark spot region. This reduction suggests that the jets alter the flow dynamics in the wake region, leading to a redistribution of pressure. Additionally, an increase in jet velocity results in a notable rise in pressure compared to the case without jets, as demonstrated in Fig. 8.12(c) and Fig. 8.12(d). Higher jet velocities drastically change the flow field, resulting in elevated pressure levels within the region.

### 8.2.9 Variation of turbulent kinetic energy ( $TKE$ )

The variation of turbulent kinetic energy ( $TKE$ ) is illustrated in Fig. 8.13 for the scenario without jets and compared with the dual jet scenario in the flow. For enhanced visualization, the plot for the no-jet flow is superimposed with the other three plots (representing the dual jet flow) at the same stream-wise locations relative to the submerged obstacle. The  $TKE$  is normalized by the square of the

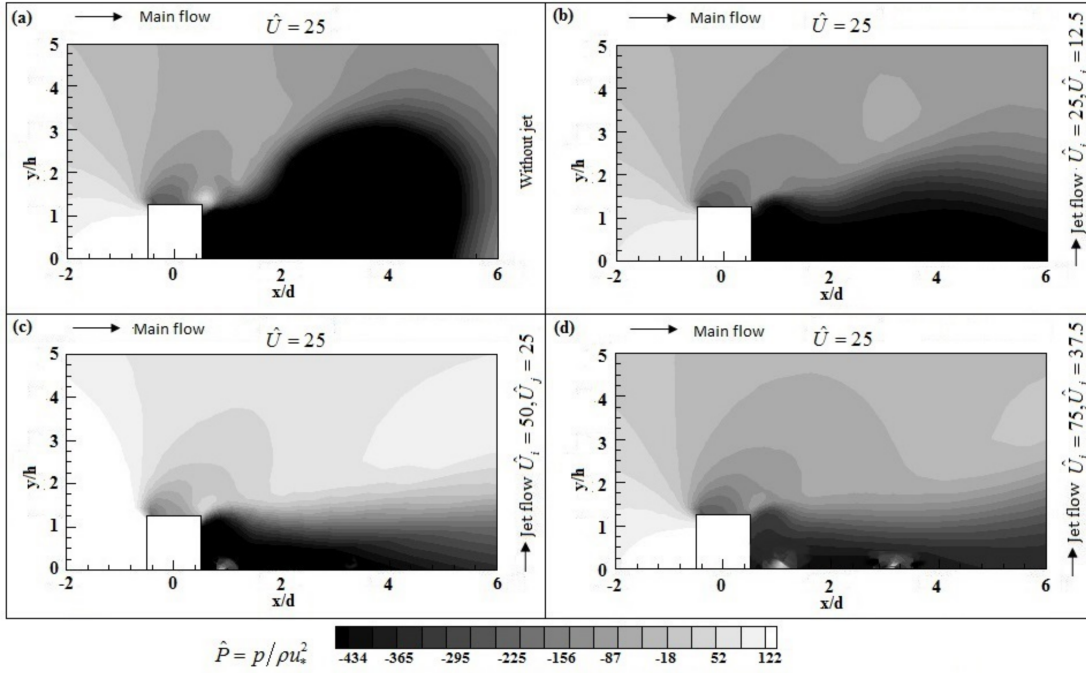


Figure 8.12: Contour plot of stream wise static pressure ( $\hat{P}$ ) (a). without jet (b). Flow with dual jet velocities  $\hat{U}_i = 25$  and  $\hat{U}_j = 12.5$  (c). Flow with dual jet velocities  $\hat{U}_i = 50$  and  $\hat{U}_j = 25$  and (d). Flow with dual jet velocities  $\hat{U}_i = 75$  and  $\hat{U}_j = 37.5$ .

frictional velocity ( $u_*^2$ ). Variations in  $TKE$  are noticeable only at locations  $A_1$ ,  $A_2$ , and  $A_3$ , mainly due to changes in velocity and the behavior of flow structures, particularly in the re-circulation zones. At upstream locations before the square ( $A_{-1}$ ), on the square ( $A_0$ ), and far downstream from the square ( $A_4$ ), the  $TKE$  profiles align exactly with each other. In the re-circulation zone, the instability of the mean flow leads to obvious  $TKE$  production, while viscous stresses contribute to  $TKE$  dissipation [88, 52]. At location  $A_1$ , the maximum  $TKE$  values ( $\hat{k} \approx 1600$ ) are observed due to Jet-1, which has the highest sequence of jet velocities. At Jet-2 location ( $A_3$ ), only minor changes are noted ( $\hat{k} \approx 250$ ) because the jet velocity is lower than that of Jet-1. In the area between the two jets, at location  $A_2$ , there is minimal  $TKE$  variation as this region is less affected by the jets. Changes in  $TKE$  at other locations, such as  $A_{-1}$  and  $A_4$  (outside the re-circulation zone), are observed near the bed due to flow roughness [89].

## 8.2 Results and Discussion

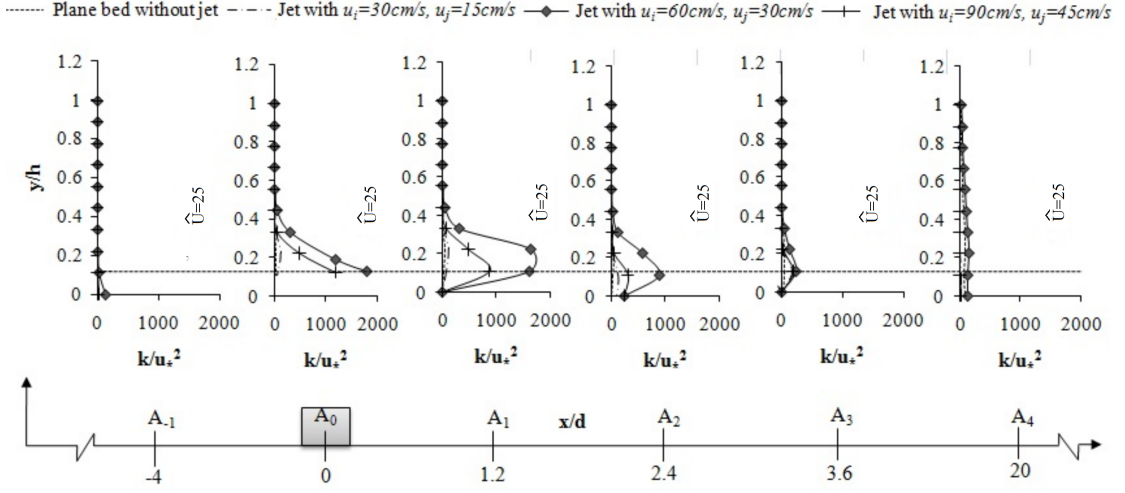


Figure 8.13: Contour plot of stream wise static pressure ( $\hat{P}$ ) (a). without jet (b). Flow with dual jet velocities  $\hat{U}_i = 25$  and  $\hat{U}_j = 12.5$  (c). Flow with dual jet velocities  $\hat{U}_i = 50$  and  $\hat{U}_j = 25$  and (d). Flow with dual jet velocities  $\hat{U}_i = 75$  and  $\hat{U}_j = 37.5$ .

### 8.2.10 The $TKE$ contour plots

The turbulent kinetic energy ( $TKE$ ) contour plots shown in Fig. 8.14 illustrate the variation in  $TKE$  within the flow for the baseline case without jets and for three different dual jet configurations. To enhance clarity, the normalized  $TKE$  values are presented within a range of 21 to 2084. In Fig. 8.14(a), the majority of the domain displays minimal  $TKE$  values, with significant variation observed in the re-circulation zone. This occurs because the flow is obstructed around the square, leading to turbulence production and higher  $TKE$  values [90].

In the presence of the first set of dual jets, as shown in Fig. 8.14(b), notable  $TKE$  variation is observed at the top of the obstacle and within the re-circulation zone. The square obstruction influences the flow stability, resulting in additional  $TKE$  generation around the square [53]. At the jet injection points, the  $TKE$  values are minimal since the flow within the jet potential core remains largely unchanged, varying only with velocity changes [91].

Similar  $TKE$  contour plots are observed for the other dual jet configurations, as depicted in Fig. 8.14(c) and 8.14(d). When the flow encounters the square obstruction, it experiences retardation, leading to higher  $TKE$  values just above

the square, as shown in Fig. 8.14(c) and 8.14(d). However, in both cases, the  $TKE$  values remain minimal at the jet injection points.

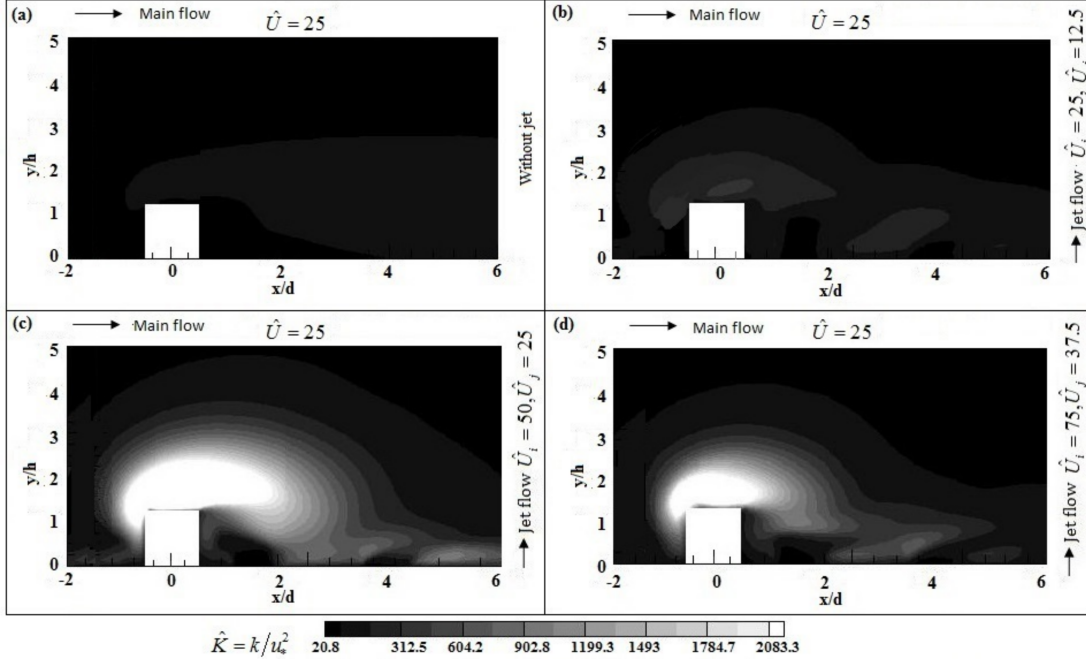


Figure 8.14: Contour plot of stream wise Turbulent Kinetic Energy ( $TKE$ ) ( $\hat{K}$ ) (a). Plane bed without jet (b). Flow with dual jet velocities  $\hat{U}_i = 25$  and  $\hat{U}_j = 12.5$  (c). Flow with dual jet velocities  $\hat{U}_i = 50$  and  $\hat{U}_j = 25$  and (d). Flow with dual jet velocities  $\hat{U}_i = 75$  and  $\hat{U}_j = 37.5$ .

### 8.2.11 Variation of Turbulent dissipation rate ( $TDR$ ) ( $\epsilon$ )

The specific portion of turbulent kinetic energy in its rate form is termed the rate of dissipation. This term counterbalances the production term in the overall rate of turbulent kinetic energy ( $TKE$ ) to maintain its actual value. The profile plot of the turbulent dissipation rate is illustrated in Fig. 8.15 for both with and without jet scenarios. Figure 8.15 indicates that changes in dissipation values are noticeable only in the re-circulation zone, which is characterized by vortices and a highly in-homogeneous and an-isotropic flow field. At positions  $A_{-1}$ ,  $A_3$ , and  $A_4$ , the turbulent dissipation rates for all four cases are minimal and coincide with the ordinate. Significant variations are observed within the normalized stream-wise

## 8.2 Results and Discussion

position range of  $0 \leq x/d \leq 2.5$ , as the diffusion and production terms contribute notably in the thin shear layer [7]. The dissipation peaks at position  $A_0$  for the dual jet input flow with velocities  $\hat{U}_i = 50$  and  $\hat{U}_j = 25$ . This peak precedes that of the third jet profile set, with velocities  $\hat{U}_i = 75$  and  $\hat{U}_j = 37.5$ . From this maximum value, it decreases linearly with a constant slope, reaching a distance of  $y/h = 0.3 m$ . At the first jet injection point,  $A_1$ , dissipation values start from zero, peak, and then intersect the ordinate at the same height. At position  $A_2$ , dissipation values start at certain levels and meet the y-axis at the height of the square. No significant influence on turbulent dissipation is observed at the second jet injection point.

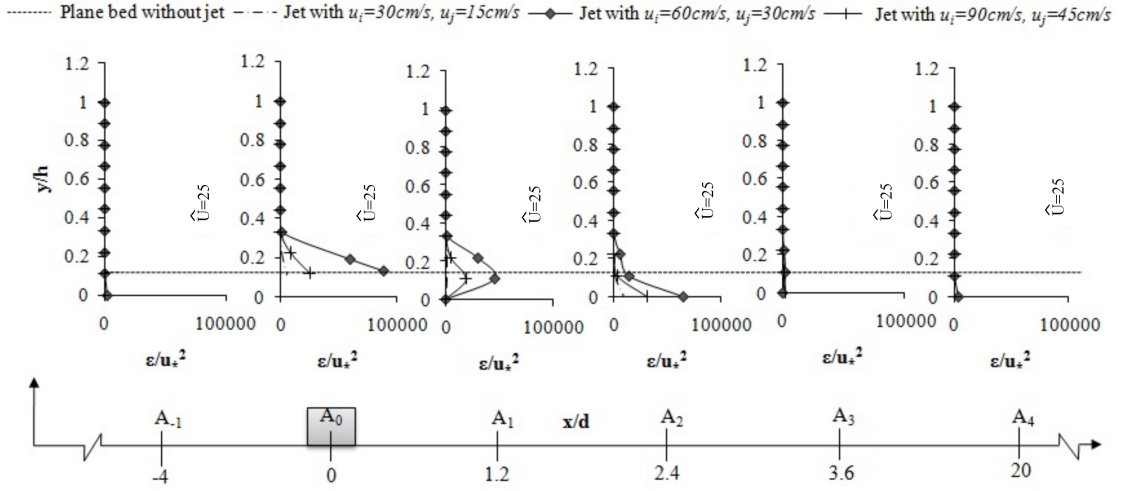


Figure 8.15: Stream wise vertical Turbulent Dissipation Rate ( $\hat{\epsilon}$ ) profile along  $x$ -direction for with and without jet.

### 8.2.12 The *TDR* contour plots

The contour plots depicting turbulent dissipation for scenarios with and without jet injection are illustrated in Fig. 8.16. These visualizations focus on the area surrounding the square obstruction. In the case without jet injection, the normalized energy dissipation is generally low throughout the domain, except for a significant variation observed in the re-circulation zone (see Fig. 8.16(a)). At high Reynolds numbers, the dissipation associated with the cascade of kinetic energy into heat is minimal due to the dominance of viscous effects over inertial effects,

except in the re-circulation zone [92]. Notably, the jet injection points present two dark spots indicating low turbulent dissipation values. Additionally, the contour plots for dual jet injection are displayed in Fig. 8.16(c) and Fig. 8.16(d). A distinctive feather-like structure, indicating higher dissipation rates, is observed just above the square obstruction.

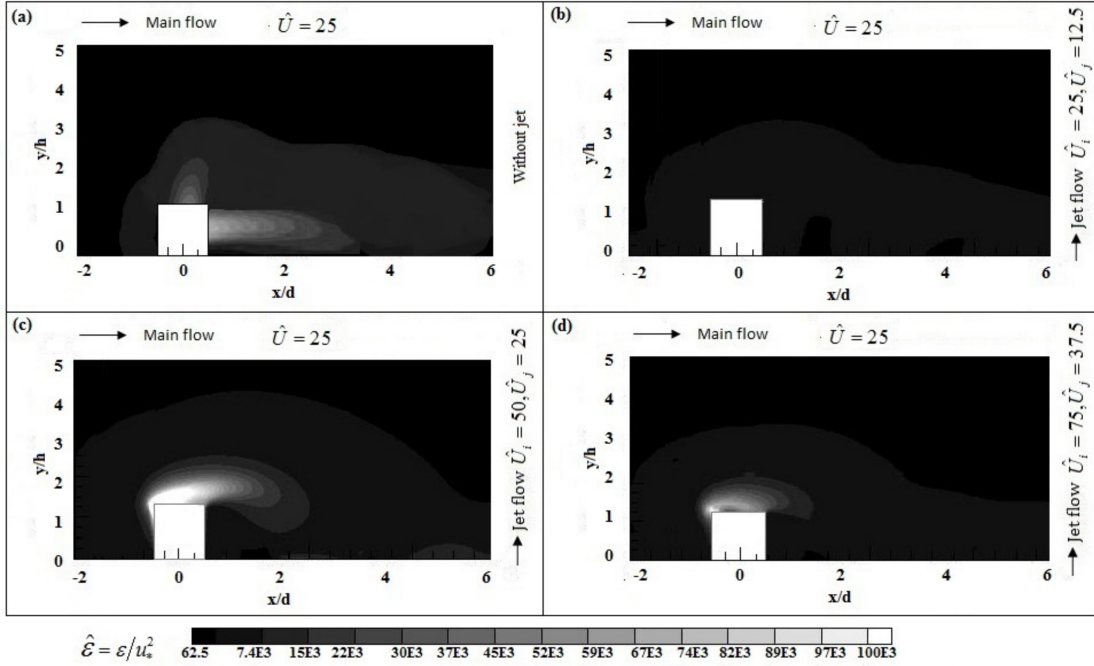


Figure 8.16: Contour plot of stream wise Turbulent Dissipation Rate ( $TDR$ ) ( $\hat{\epsilon}$ ) (a). without jet (b). Flow with dual jet velocities  $\hat{U}_i = 25$  and  $\hat{U}_j = 12.5$  (c). Flow with dual jet velocities  $\hat{U}_i = 50$  and  $\hat{U}_j = 25$  and (d). Flow with dual jet velocities  $\hat{U}_i = 75$  and  $\hat{U}_j = 37.5$ .

### 8.3 Conclusion

The primary goal of this research is to identify and eliminate the re-circulation zone behind a two-dimensional square object using plane vertical turbulent dual wall jets. This study focuses on understanding the flow physics of two-dimensional open channel flow over a fully submerged bed-mounted square cross-section obstacle. Key elements of this forward time-marched numerical solution include the use of

### 8.3 Conclusion

---

a turbulence model, multi-phase *VOF* techniques, and the *SIMPLE* algorithm. The primary aim is to determine the extent of the re-circulation zone in the wake region behind the obstacle and to find the optimal positioning of dual jets to eliminate it. Additionally, the research explores the changes in main turbulent characteristics throughout the flow domain as a secondary objective.

The standard ( $k-\epsilon$ ) model is utilized for a background flow Reynolds number of 60,000. Comprehensive analysis has been conducted to evaluate the flow characteristics in the re-circulation zone behind the obstacle using turbulent dual jets at different Reynolds numbers. A significant negative static pressure is observed downstream of the obstacle, indicating flow separation and the presence of a re-circulation region. In this area, a negative stream-wise mean velocity is noted, which is prominent up to the height of the square obstacle. The application of the jets reduces vortex shedding in the wake region behind the obstruction, achieving an approximately 88% reduction in vorticity magnitude, suggesting effective vorticity suppression. The dissipation of turbulent kinetic energy is found to be minimal at high Reynolds numbers due to the negligible viscous effect compared to inertia. Additionally, two dark spots in the turbulent dissipation rate contour are identified at the jet injection points.

This study demonstrates the effectiveness of dual jets in controlling the re-circulation zone behind square cross-section bluff bodies, potentially reducing unwanted vortex-induced vibrations. Future research should focus on bluff bodies of various shapes and different dual jet intensity combinations to optimize the jet injection velocity ratio for completely controlling the re-circulation zone in different shaped bluff bodies.

### Future Scope and Practical Considerations

While this study is primarily numerical, it offers insight into flow control strategies that may be adapted for real-life canal systems. The implementation of submerged jets or suction in practice may be feasible in certain localized regions, such as downstream of bridge piers, sluice gates, or other hydraulic structures, by using embedded nozzles or perforated bed systems. Energy requirements for such active flow control should be balanced against the potential benefits, including suppres-

sion of flow-induced vibrations, reduced scour potential, and improved structural integrity. Further studies involving cost-benefit analysis and low-energy or passive alternatives may enhance the practical relevance of this approach.

# ANSYS FLUENT – THE CFD TOOL

## A.0.1 General

*ANSYS FLUENT* is an advanced software application designed to simulate fluid flow, heat transfer, and chemical reactions in complex geometries. Designed with the C programming language, *ANSYS FLUENT* leverages the power of C to provide dynamic memory allocation, efficient data organization, and flexible solution control. This makes the software robust and scalable.

One of the key features of *ANSYS FLUENT* is its client/server architecture, which can run as a separate, concurrent process on multiple machines. This design means that this client can run on desktop workstations and computers overall complex servers, facilitating efficiency and connection management regardless of operating system or device characteristics.

The software provides a more flexible mesh, supporting solutions to flow problems with unstructured meshes that can be smoothed around complex geometries. Supported mesh types include 2D triangular tetrahedral meshes, and 3D tetrahedral, hexagonal, pyramid, wedge, polyhedral meshes, and more. Flow to *ANSYS FLUENT* users of the solution can optimize or simplify its mesh on a basis, making simulations more accurate and responsive well. Once a mesh is imported into *ANSYS FLUENT*, all subsequent tasks are conducted within the software. These tasks include establishing boundary conditions, specifying fluid properties, running the solution, refining the mesh, and post-processing to view the results. The

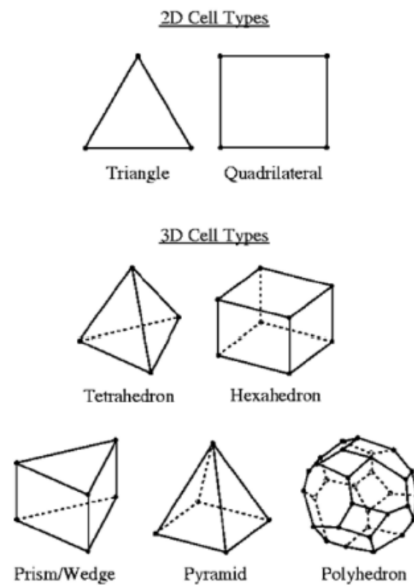


Figure A.1: Some elements of FLUENT uses

*ANSYS FLUENT* serial solver handles file input and output, data storage, and flow field calculations through a single solver process on one computer. *ANSYS FLUENT* utilizes a utility called Cortex to manage the user interface and basic graphical functions.

For more complex computations, *ANSYS FLUENT*'s parallel solver allows for the use of multiple processes, which can run on a single computer or across different computers within a network. Parallel processing involves collaboration between *ANSYS FLUENT*, a host process, and several compute-node processes. The Cortex utility facilitates the interaction between *ANSYS FLUENT*, the host process, and the compute nodes, ensuring efficient parallel computation.

## A.0.2 Components of fluent

FLUENT package includes the following products:

- *FLUENT*, the solver.
- *GAMBIT*, the preprocessor for geometry modeling and mesh generation.
- *TGrid*, an additional preprocessor that can generate volume meshes from existing boundary meshes.
- Filters (translators) for import of surface and volume meshes from *CAD/CAE* packages such as *ANSYS*, *CGNS*, *I-deas*, *NASTRAN*, *PATRAN*, and others.

The organization structure of these components is shown below in Fig. A.2

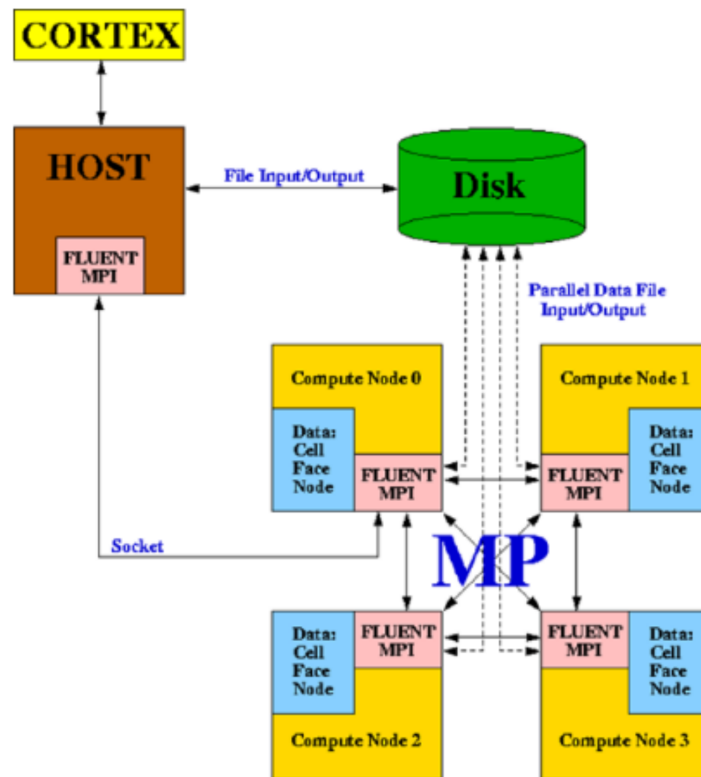


Figure A.2: Basic program structure of *FLUENT*

### A.0.3 Programming capabilities

The *ANSYS FLUENT* solver has the following modeling capabilities:

- ★ Capable of simulating 2D planar, 2D axisymmetric, 2D axisymmetric with swirl (rotationally symmetric), and 3D flows.
- ★ Supports various mesh types including quadrilateral, triangular, hexahedral (brick), tetrahedral, prism (wedge), pyramid, polyhedral, and mixed element meshes.
- ★ Handles both steady-state and transient flow simulations.
- ★ Accommodates incompressible and compressible flows across all speed regimes: low subsonic, transonic, supersonic, and hypersonic.
- ★ Simulates inviscid, laminar, and turbulent flows.

- ★ Models Newtonian and non-Newtonian fluids.
- ★ Works with ideal and real gas models.
- ★ Manages heat transfer scenarios including forced, natural, and mixed convection, conjugate (solid/fluid) heat transfer, and radiation.
- ★ Facilitates chemical species mixing and reactions, supporting both homogeneous and heterogeneous combustion models as well as surface deposition/reaction models.
- ★ Provides models for free surface and multi-phase flows including gas-liquid, gas-solid, and liquid-solid interactions.
- ★ Calculates Lagrangian trajectories for dispersed phases such as particles, droplets, and bubbles, including coupling with the continuous phase and spray modeling.
- ★ Includes cavitation and phase change models for melting/solidification processes.
- ★ Models porous media with non-isotropic permeability, inertial resistance, solid heat conduction, and porous-face pressure jump conditions.
- ★ Features lumped parameter models for components like fans, pumps, radiators, and heat exchangers.
- ★ Predicts flow-induced noise using acoustic models.
- ★ Operates within both inertial (stationary) and non-inertial (rotating or accelerating) reference frames.
- ★ Simulates multiple moving frames and uses sliding mesh options for dynamic interactions.
- ★ Utilizes a mixing-plane model for rotor-stator interactions, torque converters, and similar turbo-machinery applications, offering mass and swirl conservation options.
- ★ Supports dynamic mesh modeling for domains with moving and deforming meshes.
- ★ Incorporates volumetric sources of mass, momentum, heat, and chemical species into simulations.

- 
- ★ Includes a comprehensive material property database for various simulation needs.
  - ★ Offers a population balance module for detailed particle size distribution and interaction modeling (documented separately).

The specific internal response and interaction with the flow and the surrounding potential field are unique to each scenario. For instance, solid particles of varying sizes but made from the same material can be considered different phases. This distinction is because particles of the same size exhibit similar dynamic behavior when interacting with the flow field. In the context of channel contraction studies, water-air flow scenarios have been utilized to explore these interactions. Open

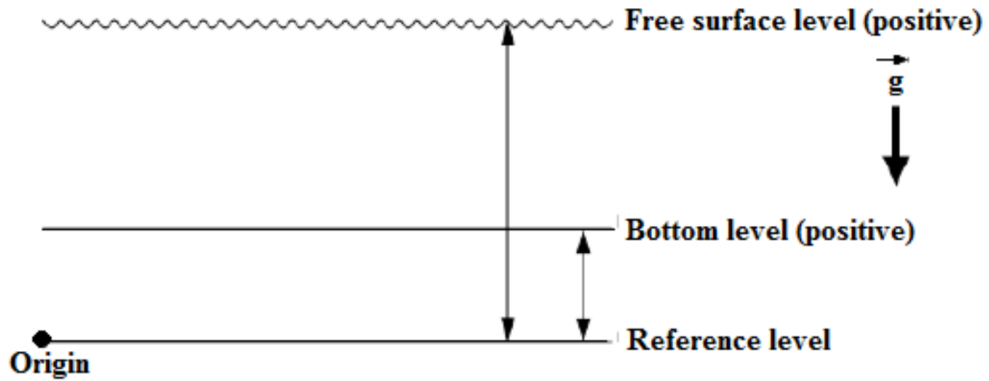


Figure A.3: Duct flow defining parameters

Duct flow is characterized by the dimensionless Froude Number, which is defined as the ratio of inertia force and hydro-static force.

$$Fr = \frac{V}{\sqrt{gy}} \quad (\text{A.1})$$

Where  $V$  is flow velocity magnitude,  $g$  is gravity and  $y$  is a length scale, here in the case of an open channel,  $y$  is the distance from the bottom of the channel to the free surface level. That's why flow depth in the case of the open channel is the most important parameter in the time of applying boundary conditions. The denominator in the above equation is the propagation speed of the wave. The wave speed as seen by the fixed observer is defined as

$$V_w = V \pm \sqrt{gy} \quad (\text{A.2})$$

Based on the Froude Number the open channel flow can be classified into three categories.

- ✓ When  $Fr < 1$ , i.e.,  $V < \sqrt{gy}$  (thus  $V_w < 0$  or  $V_w > 0$ ), the flow is subcritical. In this regime, disturbances can travel both upstream and downstream. This means that changes or conditions downstream can influence the flow conditions upstream.
- ✓ When  $Fr = 0$  (thus  $V_w = 0$ ), the flow is known to be critical. At this critical state, waves generated upstream stay in place and do not propagate. This condition signifies a transition point where the flow changes its character.
- ✓ When  $Fr > 1$ , i.e.,  $V > \sqrt{gy}$  (thus  $V_w > 0$ ) the flow is known to be supercritical. In supercritical flow, disturbances cannot travel upstream, implying that downstream conditions do not affect the upstream flow.

#### A.0.4 Upstream boundary condition

There are two options available for upstream boundary conditions in open channel flow

- ❖ **Pressure Inlet**-Total pressure is the summation of static pressure and dynamic pressure. Where dynamic pressure  $P_d$  is expressed as

$$P_d = \frac{(\rho - \rho_0)}{2} V^2 \quad (\text{A.3})$$

and static pressure  $P_s$  is expressed as

$$P_s = (\rho - \rho_0) |\vec{g}| [\hat{g} \cdot (\vec{b} - \vec{a})] \quad (\text{A.4})$$

In this context,  $\vec{b}$  and  $\vec{a}$  represent the position vectors for the centroid of the face and any point on the free surface, respectively. The free surface is considered horizontal and perpendicular to the gravitational direction. The gravitational vector is denoted by  $\vec{g}$ , while  $|\vec{g}|$  signifies the magnitude of gravity, and  $\hat{g}$  is the unit vector in the direction of gravity. The velocity magnitude is indicated by  $V$ ,  $\rho$  represents the density of the mixture within the cell, and  $\rho_0$  is the reference density.

- ❖ **Mass flow rate**-Mass flow rate for each phase associated with open channel flow is

$$\dot{m}_{Phase} = \rho_{Phase} (Area_{Phase}) (Velocity) \quad (\text{A.5})$$

- ❖ **Volume fraction specification**-In open channel flows, Fluent determines the volume fraction using the parameters provided in the Boundary Conditions panel. As a result, this option is not available for manual adjustment

---

### A.0.5 Downstream boundary condition

There are two options available for downstream boundary conditions in open channel flow.

- ❖ **Pressure Outlet-** The determination of static pressure at a pressure outlet is based on the chosen Pressure Specification Method. The static pressure is defined accordingly when using the Free Surface Level approach. If this method is not used, the static pressure must be provided as gauge pressure.
- ❖ For subcritical outlet flows ( $Fr < 1$ ), involving only two phases, the pressure is derived from the specified pressure profile along the boundary. If there are more than two phases, the pressure is taken from the adjacent cell. In the case of supercritical flows ( $Fr > 1$ ), the pressure is always determined by the adjacent cell.
- ❖ **Back flow volume fraction specifications-**Fluent calculates the volume fraction values at the outlet boundary based on the values from neighboring cells, rendering this option inactive for manual adjustment.



# References

---

- [1] J. Southard, *Introduction to fluid motions, sediment transport and current-generated sedimentary structures*, 2006.
- [2] W. Alawadi, T. Prasad, and O. Al-Salih, “Assessing the impact of velocity dip and wake coefficients on velocity prediction for open channel flows,” *Research Journal of Applied Sciences, Engineering and Technology*, vol. 16, no. 1, 2019.
- [3] P. Koumoutsakos, J. Freund, and D. Parekh, “Evolution strategies for parameter optimization in jet flow control,” 03 1999.
- [4] A. Assoudi, N. Mahjoub Saïd, H. Bournot, and G. Le Palec, “Comparative study of flow characteristics of a single offset jet and a turbulent dual jet,” *Heat and Mass Transfer*, vol. 55, pp. 1109–1131, 2019.
- [5] A. Abdel-Rahman, “A review of effects of initial and boundary conditions on turbulent jets,” *WSEAS transactions on Fluid Mechanics*, vol. 5, no. 4, pp. 257–275, 2010.
- [6] S. K. Singh, K. Debnath, and B. S. Mazumder, “Turbulence statistics of wave-current flow over a submerged cube,” *Journal of Waterway, Port, Coastal, and Ocean Engineering*, vol. 142, no. 3, p. 04015027, 2016.
- [7] H. J. Hussein and R. Martinuzzi, “Energy balance for turbulent flow around a surface mounted cube placed in a channel,” *Physics of Fluids*, vol. 8, no. 3, pp. 764–780, 1996.
- [8] D. Sumner, “Two circular cylinders in cross-flow: A review,” *Journal of fluids and structures*, vol. 26, no. 6, pp. 849–899, 2010.
- [9] H. Zhang, J.-m. Yang, L.-f. Xiao, and H.-n. Lü, “Large-eddy simulation of the flow past both finite and infinite circular cylinders at  $re=3900$ ,” *Journal of Hydrodynamics*, vol. 27, no. 2, pp. 195–203, 2015.
- [10] J. Derakhshandeh and M. M. Alam, “A review of bluff body wakes,” *Ocean Engineering*, vol. 182, pp. 475–488, 2019.
- [11] H. C. Lim, T. Thomas, and I. P. Castro, “Flow around a cube placed in a simulated turbulent boundary layer,” in *JWE: The Forth International Symposium on Computational Wind Engineering, Yokohama, (108)*, 2006, pp. 625–628.
- [12] R. Porteous, D. J. Moreau, and C. J. Doolan, “A review of flow-induced noise from finite wall-mounted cylinders,” *Journal of Fluids and Structures*, vol. 51, pp. 240–254, 2014.
- [13] C. D. Daniel, S. Laizet, and J. Vassilicos, “Direct numerical simulation of the interaction of a wall-attached cube with a turbulent boundary layer.”

- 
- [14] F. Scarano, C. Benocci, and M. Riethmuller, "Pattern recognition analysis of the turbulent flow past a backward facing step," *Physics of Fluids*, vol. 11, no. 12, pp. 3808–3818, 1999.
- [15] N. N. Bouda, C. Rey, J. Rosant, and T. Benabid, "Turbulent wall jet interaction with a backward facing step," in *Engineering Turbulence Modelling and Experiments 6*. Elsevier, 2005, pp. 471–480.
- [16] F. Mardkari, M. Aghakhani, and E. Esmailzad, "Experimental study of fluid flow around cylinder in the presence of ehd actuators," *Journal of Applied Sciences*, vol. 12, no. 1, pp. 90–95, 2012.
- [17] H. Deylami, N. Amanifard, S. Hosseini-zhad, and F. Dolati, "Numerical investigation of the wake flow control past a circular cylinder with electrohydrodynamic actuator," *European Journal of Mechanics-B/Fluids*, vol. 66, pp. 71–80, 2017.
- [18] S. Roy, S. Ghoshal, K. Barman, V. Das, S. Ghosh, and K. Debnath, "Modulation of the recirculation region due to magneto hydrodynamic flow," *Engineering Science and Technology, an International Journal*, vol. 22, no. 1, pp. 282–293, 2019.
- [19] G. Wang, F. Yang, K. Wu, Y. Ma, C. Peng, T. Liu, and L.-P. Wang, "Estimation of the dissipation rate of turbulent kinetic energy: A review," *Chemical Engineering Science*, vol. 229, p. 116133, 2021.
- [20] I. Korkischko and J. R. Meneghini, "Suppression of vortex-induced vibration using moving surface boundary-layer control," *Journal of Fluids and Structures*, vol. 34, pp. 259–270, 2012.
- [21] M. K. Bhukta, G. K. Bose, and K. Debnath, "Study of turbulent plane circular jet for modulation of recirculation zone behind a cubical obstruction," in *Advanced Applications in Manufacturing Engineering*. Elsevier, 2019, pp. 231–249.
- [22] M. K. Bhukta, S. K. Singh, K. Debnath, and S. Majumder, "Modulation of recirculation zone behind a cubical obstruction by the vertically placed turbulent multijets in the form of shower," *International Journal of Fluid Mechanics Research*, vol. 50, no. 1, 2023.
- [23] Y. Masip, A. Rivas, G. S. Larraona, R. Anton, J. C. Ramos, and B. Moshfegh, "Experimental study of the turbulent flow around a single wall-mounted cube exposed to a cross-flow and an impinging jet," *International Journal of Heat and Fluid Flow*, vol. 38, pp. 50–71, 2012.
- [24] G. Artana, R. Sosa, E. Moreau, and G. Touchard, "Control of the near-wake flow around a circular cylinder with electrohydrodynamic actuators," *Experiments in Fluids*, vol. 35, pp. 580–588, 2003.
- [25] D. Arcas and L. Redekopp, "Aspects of wake vortex control through base blowing/suction," *Physics of Fluids*, vol. 16, no. 2, pp. 452–456, 2004.
- [26] W.-L. Chen, D.-B. Xin, F. Xu, H. Li, J.-P. Ou, and H. Hu, "Suppression of vortex-induced vibration of a circular cylinder using suction-based flow control," *Journal of Fluids and Structures*, vol. 42, pp. 25–39, 2013.
- [27] L. H. Feng, J. J. Wang, and C. Pan, "Effect of novel synthetic jet on wake vortex shedding modes of a circular cylinder," *Journal of Fluids and Structures*, vol. 26, no. 6, pp. 900–917, 2010.
- [28] Y. Qu, J. Wang, M. Sun, L. Feng, C. Pan, Q. Gao, and G. He, "Wake vortex evolution of square cylinder with a slot synthetic jet positioned at the rear surface," *Journal of Fluid Mechanics*, vol. 812, pp. 940–965, 2017.

- 
- [29] K. Hannemann and H. Oertel Jr, “Numerical simulation of the absolutely and convectively unstable wake,” *Journal of Fluid Mechanics*, vol. 199, pp. 55–88, 1989.
- [30] E. Forthmann, “Turbulent jet expansion,” Tech. Rep., 1936.
- [31] M. Glauert, “The wall jet,” *Journal of Fluid Mechanics*, vol. 1, no. 6, pp. 625–643, 1956.
- [32] P. Bakke, “An experimental investigation of a wall jet,” *Journal of Fluid Mechanics*, vol. 2, no. 5, pp. 467–472, 1957.
- [33] W. Schneider, “Decay of momentum flux in submerged jets,” *Journal of Fluid Mechanics*, vol. 154, pp. 91–110, 1985.
- [34] D. Liepmann and M. Gharib, “The role of streamwise vorticity in the near-field entrainment of round jets,” *Journal of Fluid Mechanics*, vol. 245, pp. 643–668, 1992.
- [35] T. Craft, J. Kidger, and B. Launder, “Three-dimensional modelling of turbulent free-surface jets,” in *Engineering Turbulence Modelling and Experiments 4*. Elsevier, 1999, pp. 73–82.
- [36] S. Pramanik and M. K. Das, “Numerical study of turbulent wall jet over multiple-inclined flat surface,” *Computers & Fluids*, vol. 95, pp. 132–158, 2014.
- [37] J. Nikuradse, “Stromungsgesetze in rauhen rohren,” *vti-forschungsheft*, vol. 361, p. 1, 1933.
- [38] F. M. White and J. Majdalani, *Viscous fluid flow*. McGraw-Hill New York, 2006, vol. 3.
- [39] W. P. Jones and B. E. Launder, “The prediction of laminarization with a two-equation model of turbulence,” *International journal of heat and mass transfer*, vol. 15, no. 2, pp. 301–314, 1972.
- [40] T. M. Salaheldin, J. Imran, and M. H. Chaudhry, “Numerical modeling of three-dimensional flow field around circular piers,” *Journal of Hydraulic Engineering*, vol. 130, no. 2, pp. 91–100, 2004.
- [41] D. Wilcox, “Turbulence modeling for cfd (vol. 2, pp. 103-217),” *La Canada, CA: DCW Industries*, 1998.
- [42] W. P. Jones and B. Launder, “The calculation of low-reynolds-number phenomena with a two-equation model of turbulence,” *International Journal of Heat and Mass Transfer*, vol. 16, no. 6, pp. 1119–1130, 1973.
- [43] F. R. Menter, “Performance of popular turbulence model for attached and separated adverse pressure gradient flows,” *AIAA journal*, vol. 30, no. 8, pp. 2066–2072, 1992.
- [44] N. D. Katopodes, *Free-surface flow: computational methods*. Butterworth-Heinemann, 2018.
- [45] T. Hayase, J. A. Humphrey, and K. Morita, “A new finite-difference scheme for incompressible flow using a two-step fractional step method,” *International Journal for Numerical Methods in Fluids*, vol. 15, no. 6, pp. 385–403, 1992.
- [46] F. Russo and N. T. Basse, “Scaling of turbulence intensity for low-speed flow in smooth pipes,” *Flow Measurement and Instrumentation*, vol. 52, pp. 101–114, 2016.
- [47] C.-K. Chang, J.-Y. Lu, S.-Y. Lu, Z.-X. Wang, and D.-S. Shih, “Experimental and numerical investigations of turbulent open channel flow over a rough scour hole downstream of a ground sill,” *Water*, vol. 12, no. 5, p. 1488, 2020.

- 
- [48] I. Nezu, H. Nakagawa, and G. H. Jirka, "Turbulence in open-channel flows," *Journal of Hydraulic Engineering*, vol. 120, no. 10, pp. 1235–1237, 1994.
- [49] A. K. Banerjee and S. K. Singh, "Parametric investigation of spatio-temporal variability of submerged body hydrodynamics," *Applied Ocean Research*, vol. 123, p. 103152, 2022.
- [50] S. K. Singh, P. K. Raushan, and K. Debnath, "Role of multiple flow stages over submerged structure," *Ocean Engineering*, vol. 181, pp. 59–70, 2019.
- [51] B. Zhang, S. Gong, S. Dong, Z. Xiong, and Z. Zhang, "Vortex shedding induced vibration of thin strip in confined rectangular channel," *Progress in Nuclear Energy*, vol. 141, p. 103951, 2021.
- [52] K. Hanjalić and B. E. Launder, "Contribution towards a reynolds-stress closure for low-reynolds-number turbulence," *Journal of fluid mechanics*, vol. 74, no. 4, pp. 593–610, 1976.
- [53] N. Apsilidis, P. Diplas, C. L. Dancy, and P. Bouratsis, "Time-resolved flow dynamics and reynolds number effects at a wall-cylinder junction," *Journal of Fluid Mechanics*, vol. 776, pp. 475–511, 2015.
- [54] X. Nie, Y. Zhang, T. Zhang, L. Li, and J. Xu, "Comparative analysis and numerical simulation about six low reynolds number  $k-\varepsilon$  models in nearwall shear flow," *Proceedings of the CSEE*, vol. 24, pp. 7247–7254, 2017.
- [55] J. C. Lamont and D. Scott, "An eddy cell model of mass transfer into the surface of a turbulent liquid," *AIChE Journal*, vol. 16, no. 4, pp. 513–519, 1970.
- [56] K. Sreenivasan, "On the fine-scale intermittency of turbulence," *Journal of Fluid Mechanics*, vol. 151, pp. 81–103, 1985.
- [57] H. Mouri, M. Takaoka, A. Hori, and Y. Kawashima, "Probability density function of turbulent velocity fluctuations," *Physical Review E*, vol. 65, no. 5, p. 056304, 2002.
- [58] K. N. Morshed, S. K. Venayagamoorthy, and L. P. Dasi, "Intermittency and local dissipation scales under strong mean shear," *Physics of Fluids*, vol. 25, no. 1, 2013.
- [59] P. Lynch, "Weather prediction by numerical process," *The Emergence of Numerical Weather Prediction*, vol. 11, no. 3, pp. 1–27, 2006.
- [60] G. Biswas and V. Eswaran, *Turbulent flows: fundamentals, experiments and modeling*. CRC Press, 2002.
- [61] T. Patel and L. Gill, "Volume of fluid model applied to curved open channel flows," *WIT Transactions on Engineering Sciences*, vol. 52, 2006.
- [62] B. E. Launder and D. B. Spalding, "The numerical computation of turbulent flows," in *Numerical prediction of flow, heat transfer, turbulence and combustion*. Elsevier, 1983, pp. 96–116.
- [63] P. J. Roache, "Perspective: a method for uniform reporting of grid refinement studies," 1994.
- [64] I. Marusic, J. P. Monty, M. Hultmark, and A. J. Smits, "On the logarithmic region in wall turbulence," *Journal of Fluid Mechanics*, vol. 716, p. R3, 2013.
- [65] S. K. Singh and K. Debnath, "Combined effects of wave and current in free surface turbulent flow," *Ocean Engineering*, vol. 127, pp. 170–189, 2016.

- 
- [66] S. Singh, J. Chowdhury, S. Ghosh, P. Raushan, K. Debnath, and P. Kumar, "Experimental and numerical investigation of flow characteristics in an open rectangular cavity," *ISH Journal of Hydraulic Engineering*, vol. 28, no. sup1, pp. 1–13, 2022.
- [67] T. Mondal, M. K. Das, and A. Guha, "Transition of a steady to a periodically unsteady flow for various jet widths of a combined wall jet and offset jet," *Journal of Fluids Engineering*, vol. 138, no. 7, 2016.
- [68] G. S. Triantafyllou, K. Kupfer, and A. Bers, "Absolute instabilities and self-sustained oscillations in the wake of circular cylinders," *Physical review letters*, vol. 59, no. 17, p. 1914, 1987.
- [69] A. Hemmati, D. H. Wood, and R. J. Martinuzzi, "Wake dynamics and surface pressure variations on two-dimensional normal flat plates," *AIP Advances*, vol. 9, no. 4, p. 045209, 2019.
- [70] S. Dey, D. Swargiary, S. Sarkar, H. Fang, and R. Gaudio, "Turbulence features in a wall-wake flow downstream of a wall-mounted vertical cylinder," *European Journal of Mechanics-B/Fluids*, vol. 69, pp. 46–61, 2018.
- [71] R. Krpan and B. Končar, "Simulation of turbulent wake at mixing of two confined horizontal flows," *Science and Technology of Nuclear Installations*, vol. 2018, pp. 1–12, 2018.
- [72] M. Noda, H. Utsunomiya, and F. Nagao, "Basic study on blockage effects in turbulent boundary layer flows," *Journal of wind engineering and industrial aerodynamics*, vol. 54, pp. 645–656, 1995.
- [73] J. D. Anderson, G. Degrez, E. Dick, and R. Grundmann, *Computational fluid dynamics: an introduction*. Springer Science & Business Media, 2013.
- [74] J. Shi, T. Thomas, and J. Williams, "Free-surface effects in open channel flow at moderate froude and reynold's numbers," *Journal of Hydraulic Research*, vol. 38, no. 6, pp. 465–474, 2000.
- [75] M. Ariff, S. M. Salim, and S. C. Cheah, "Wall  $y^+$  approach for dealing with turbulent flow over a surface mounted cube: part 1–low reynolds number," in *Seventh international conference on CFD in the minerals and process industries*. CSIRO Australia, 2009, pp. 1–6.
- [76] S. K. Singh, P. K. Raushan, and K. Debnath, "Combined effect of wave and current in rough bed free surface flow," *Ocean Engineering*, vol. 160, pp. 20–32, 2018.
- [77] A. Samanta, M. Sarkar, H. Mondal, R. Das, and S. Sarkar, "Turbulence anisotropy in a wall-wake flow downstream of two horizontal cylinders," *Flow Measurement and Instrumentation*, vol. 94, p. 102456, 2023.
- [78] B. Van Oudheusden, F. Scarano, N. Van Hinsberg, and E. Roosenboom, "Quantitative visualization of the flow around a square-section cylinder at incidence," *Journal of wind engineering and industrial aerodynamics*, vol. 96, no. 6-7, pp. 913–922, 2008.
- [79] N. Apsilidis, P. Diplas, C. L. Dancy, and P. Bouratsis, "Effects of wall roughness on turbulent junction flow characteristics," *Experiments in Fluids*, vol. 57, pp. 1–16, 2016.
- [80] A. K. Saha and A. Shrivastava, "Suppression of vortex shedding around a square cylinder using blowing," *Sadhana*, vol. 40, pp. 769–785, 2015.

- 
- [81] A. Teimourian and H. Teimourian, "Vortex shedding suppression: a review on modified bluff bodies," *Eng*, vol. 2, no. 3, pp. 325–339, 2021.
- [82] T. Mondal, M. K. Das, and A. Guha, "Numerical investigation of steady and periodically unsteady flow for various separation distances between a wall jet and an offset jet," *Journal of Fluids and Structures*, vol. 50, pp. 528–546, 2014.
- [83] A. Kilavuz, F. Sarigiguzel, M. Ozgoren, T. Durhasan, B. Sahin, L. Kavurmacioglu, H. Akilli, E. Sekeroglu, and B. Yaniktepe, "The impacts of the free-surface and angle of attack on the flow structures around a torpedo-like geometry," *European Journal of Mechanics-B/Fluids*, vol. 92, pp. 226–243, 2022.
- [84] S. Yayla, K. Kamal, S. Bayraktar, and M. Oruç, "Two phase flow separation in a horizontal separator by inlet diverter plate in oilfield industries," *Int J Mech Prod Eng*, vol. 5, no. 10, pp. 97–100, 2017.
- [85] T. P. Singh and A. Dewan, "Heat transfer characteristics of a periodically transient flow for turbulent wall-bounded dual jet," *Engineering Science and Technology, an International Journal*, vol. 36, p. 101146, 2022.
- [86] A. J. Chorin, "Numerical solution of the Navier-Stokes equations," *Mathematics of Computation*, vol. 22, no. 104, pp. 745–762, 1968.
- [87] J. H. Fransson, P. Konieczny, and P. H. Alfredsson, "Flow around a porous cylinder subject to continuous suction or blowing," *Journal of Fluids and Structures*, vol. 19, no. 8, pp. 1031–1048, 2004.
- [88] S. Banerjee, D. Scott, and E. Rhodes, "Mass transfer to falling wavy liquid films in turbulent flow," *Industrial & Engineering Chemistry Fundamentals*, vol. 7, no. 1, pp. 22–27, 1968.
- [89] W. Alawadi and T. Prasad, "Comparison of performance of simplified rans formulations for velocity distributions against full 3d rans model," *International Journal of Hydraulic Engineering*, vol. 7, no. 2, 2018.
- [90] J. H. Ferziger and M. PeriC, "Computational methods for fluid dynamics," 2002.
- [91] N. Uddin, S. O. Neumann, B. Weigand, and B. A. Younis, "Large-eddy simulations and heat-flux modeling in a turbulent impinging jet," *Numerical Heat Transfer, Part A: Applications*, vol. 55, no. 10, pp. 906–930, 2009.
- [92] L. F. Richardson, *Weather prediction by numerical process*. University Press, 1922.

# Publications from this Thesis

---

---

## Journals

- **Bhukta, M.K.**, Singh, S.K., Debnath, K., and Majumder, S., "Modulation of recirculation zone behind a cubical obstruction by the vertically placed turbulent multijets in the form of shower," in *International Journal of Fluid Mechanics Research*, 2022, DOI: 10.1615/InterJFluidMechRes.2023046305.
- **Bhukta, M.K.**, Singh, S.K., Majumder, S., and Debnath, K., "Modulation of re-circulation zones behind a square obstruction by blower-induced suction force" in *Journal of the Brazilian Society of Mechanical Sciences*, 2024, DOI: 10.1007/s40430-024-04976-x
- **Bhukta, M.K.**, Singh, S.K., Majumder, S., and Debnath, K., "Modulation of re-circulation zone behind a square obstruction by single inclined turbulent wall jet with varying angle of attack" in *Engineering Research Express*, 2024, <https://doi.org/10.1088/2631-8695/ad6af3>.

## Conferences

- **Bhukta, M.K.**, Singh, S.K., Debnath, K., and Majumder, S., "Modulation of re-circulation zone behind a square obstruction by single inclined turbulent wall jet with varying angle of attack" 2nd International Conference on Energy Resources and Technologies for Sustainable Development (ICERTSD 2023), organized by the Department of Mechanical Engineering IEST, Shibpur

---

## Submitted Papers

- **Bhukta, M.K.**, Singh, S.K., Majumder, S., and Debnath, K., "Modulation of recirculation zone behind a submerged cube obstruction by dual turbulent plane jets." at Journal of Fluid Engineering, The American Society of Mechanical Engineers, ASME.org . (under review)

# MODULATION OF RECIRCULATION ZONE BEHIND A CUBICAL OBSTRUCTION BY THE VERTICALLY PLACED TURBULENT MULTIJETS IN THE FORM OF SHOWER

Manas Kumar Bhukta,<sup>1</sup> Santosh Kumar Singh,<sup>2,\*</sup> Koustuv Debnath,<sup>3</sup> & Snehamoy Majumder<sup>4</sup>

<sup>1</sup>Department of Mechanical Engineering, Haldia Institute of Technology, Haldia-721657, India

<sup>2</sup>Department of Mechanical Engineering, SRM Institute of Science and Technology, Kattankulathur-603203, Chennai, India

<sup>3</sup>Department of Aerospace Engineering and Applied Mechanics, Indian Institute of Engineering Science and Technology, Shibpur-711103, India

<sup>4</sup>Department of Mechanical Engineering, Jadavpur University, Kolkata, India

\*Address all correspondence to: Santosh Kumar Singh, Department of Mechanical Engineering, SRM Institute of Science and Technology, Kattankulathur-603203, Chennai, India; Tel.: +919433054519, E-mail: santoshk@srmist.edu.in

Original Manuscript Submitted: 9/30/2022; Final Draft Received: 12/19/2022

The present numerical work reports the application of jets for modulating and eradicating the recirculation zone in the wake region behind a fully submerged two-dimensional square cross-section bluff body for high Reynolds number flow. The wake region of the bluff body is characterized by a strong recirculation zone and vortex shedding, leading to unwanted vortex-induced vibrations that may instigate structural damage. Jets of varying Reynolds number and center-to-center distance are explored to look into the most effective jet Reynolds number and jet spread in completely modulating the recirculation region. The numerical simulation is based on a two-phase volume-of-fluid model with open channel boundary conditions. The standard  $k-\omega$  SST two-equation turbulence model is applied to close the time-averaged-momentum and continuity equations. The negative mean streamwise velocity signifies the recirculation region, and streamline contour plots are made to identify it. The variation in discharge velocity of the jet series is carried out for reallocation or complete disappearance of the recirculation region.

**KEY WORDS:** open channel, turbulent jet, jet-spread distance, Reynolds number

## 1. INTRODUCTION

The structure of turbulence of a free surface flow under the influence of a submerged obstruction is greatly modulated. Turbulent flows are marked by random and fluctuating flow fields, and researchers are still challenged to characterize and model such flows. Though the square cross-section rib is simple in geometry, the flow field in the wake region is complex and composed of zone-of-flow separation, recirculation, and reattachment. The resistance to the flow by the presence of the obstruction introduces a remarkable increase in turbulence intensities, turbulent kinetic energy, and dissipation rate. Furthermore, vortices are constantly shed at the wake of the square cross-section 2D obstacle due to a significant pressure drop in the wake region. The characterization and understanding of the turbulent flow over a submersed square cross-section 2D obstacle find application in many areas of science



# Modulation of re-circulation zone behind a square obstruction by blower-induced suction force through an array of small openings in the bed

Manas Kumar Bhukta<sup>1</sup> · Santosh Kumar Singh<sup>2</sup> · Snehamoy Majumder<sup>3</sup> · Koustuv Debnath<sup>4</sup>

Received: 19 October 2023 / Accepted: 11 May 2024

© The Author(s), under exclusive licence to The Brazilian Society of Mechanical Sciences and Engineering 2024

## Abstract

This study focuses on using suction force generated by a blower at high Reynolds numbers to manipulate and eliminate the re-circulation region behind a fully submerged 2D square bluff body. A square obstruction is introduced in an open channel, followed by an array of small downstream openings. The presence of a strong re-circulation zone and vortex shedding in the wake can lead to unwanted vortex-induced vibrations, posing a risk of structural damage. The investigation explores the control of the re-circulation by the variation of both suction force and suction-panel length. Numerical simulations employ a 2-phase volume of fluid (VOF) model with open channel boundary conditions and the standard  $k - \epsilon$  turbulence model for solving momentum and continuity equations. The re-circulation zone is identified by analyzing the negative mean stream-wise velocity and visualizing it through streamline contour plots. Various suction velocities are examined to redistribute or completely eliminate the re-circulation region.

**Keywords** Open channel · Square obstruction · Suction-panel length ( $l$ ) · Reynolds number · Numerical simulation

Technical Editor: Daniel Onofre de Almeida Cruz.

S. K. Singh, S. Majumder, K. Debnath have contributed equally to this work.

✉ Manas Kumar Bhukta  
manasbhukta14@gmail.com

Santosh Kumar Singh  
fmsks84@gmail.com

Snehamoy Majumder  
smrmsmsm@gmail.com

Koustuv Debnath  
debnath\_koustuv@yahoo.com

<sup>1</sup> Department of Mechanical Engineering, Haldia Institute of Technology, HIT Campus, Hatiberia, Haldia, West Bengal 721657, India

<sup>2</sup> Department of Mechanical Engineering, SRM Institute of Science and Technology, SRM Nagar, Kattankulathur, Chennai, Tamil Nadu 603203, India

<sup>3</sup> Department of Mechanical Engineering, Jadavpur University, Raja S.C. Mallick Rd, Calcutta, West Bengal 700032, India

<sup>4</sup> Department of Aerospace Engineering and Applied Mechanics, Institute of Engineering Science and Technology, Botanical Garden Rd, Shibpur, West Bengal 711103, India

## 1 Introduction

The flow behind submerged objects has become an ever-interesting topic since the physics of flow relates to the many practical problems. Due to the high pressure decrease in the wake zone, vortex shedding is a frequent phenomenon that happens there. This vortex shedding creates flow-induced vibration (FIV), such as vortex-induced vibration (VIV), wake-induced vibration (WIV) and galloping [9, 13, 39]. This causes adverse effects on the structures in the wake region and a significant control of the flow in that region is highly needed for stable structure. Identification of the re-circulation zone behind the objects is the major interest of many researchers to control the flow structure. In order to study these issues, a number of experimental techniques, including laser Doppler anemometer (LDA), acoustic Doppler velocimeter (ADV), laser Doppler velocimeter (LDV), etc., were applied [6, 19, 26] to study the flow structure behind the different shapes of bluff bodies. For e.g., Lacey and Renny [14], Singh et al., [33] and others investigated the flow structure behind the submerged obstacle experimentally using ADV at multiple flow stages and highlighted the importance of submergence on wake structure. Besides these experimental studies, numerous numerical methods

## Engineering Research Express



### PAPER


# Modulation of re-circulation zone behind a square obstruction by single inclined turbulent wall jet with varying angle of attack

RECEIVED  
23 April 2024

REVISED  
24 July 2024

ACCEPTED FOR PUBLICATION  
1 August 2024

PUBLISHED  
13 August 2024

Manas Kumar Bhukta<sup>1</sup> , Santosh Kumar Singh<sup>2</sup>, Snehamoy Majumder<sup>3</sup> and Koustuv Debnath<sup>4</sup>

<sup>1</sup> Department of Mechanical Engineering, Haldia Institute of Technology, Haldia-721657, West Bengal, India

<sup>2</sup> Department of Mechanical Engineering, SRM Institute of Science and Technology, Kattankulathur-603203, Chennai, India

<sup>3</sup> Department of Mechanical Engineering, Jadavpur University, Kolkata, India

<sup>4</sup> Department of Aerospace Engineering and Applied Mechanics, Indian Institute of Engineering Science and Technology, Shibpur-711103, India

E-mail: [manasbhukta14@gmail.com](mailto:manasbhukta14@gmail.com)

**Keywords:** open channel, turbulent jet, Reynolds number, numerical simulation, angle of attack (AOA)

### Abstract

The modulation of the re-circulation region is one of the primary interests of this numerical study. This study investigates the modulation of the re-circulation zone behind a square obstruction by a single inclined turbulent wall jet with varying angles of attack. The flow field is visualized using the post-processing system of the simulation software and the results have been analyzed. The experiments are carried out for different angles of attack of the wall jet and a range of high Reynolds numbers. The results show that the re-circulation zone is significantly affected by the angle of attack of the wall jet. The maximum length of the re-circulation zone decreased with increasing angle of attack. The wall jet angles of attack (AOA) also affect the strength and position of the vortex structures in the re-circulation zone. The results of this study provide insights into the use of inclined wall jets for controlling the flow field behind obstructions in engineering applications such as flow control and mixing enhancement. The numerical simulation is based on a two-phase volume of fluid (VOF) model with open channel boundary conditions. The standard  $k-\omega$  SST turbulence model is applied to solve the Reynolds averaged equation.

### 1. Introduction

Turbulent, since it is complicated and demands lots of unsolved and undiscovered problems to be solved in the years ahead (Ishihara *et al* 2009), has now become an important topic of research works. The current study focuses on detecting the re-circulation zone behind the wall-mounted square obstruction of an open channel flow followed by its consequent effects. Modulation of the re-circulation zone is essential for minimizing the impact on the objects. Such problems have a lot of applications in the field of engineering and science (Miyata 2003), Wissink and Rodi (2008). Generated vortex shading in the wake region followed by the formation of flow-induced vibration (FIV), and wake-induced vibration (WIV) may cause detrimental influences on the objects (Forouzi Feshalami *et al* 2022). Several experimental techniques, as well as numerical approaches (LES), were involved in investigating the turbulent flow pattern past wall-mounted bluff bodies in an open channel (Bouda *et al* 2005, Ma and Mahesh 2022). Their works mainly focus on the flow pattern past the different geometrical-shaped obstructions, flow separation and reattachment, vortex structures, and their effects, etc Up to these extent, it would be significant to mention that, very few works are found to modulate the re-circulation zones behind the surface-mounted bluff bodies by adopting some control measures. Different control techniques like the use of magnetic forces (Deylami *et al* 2017, Roy *et al* 2019), the use of particles with varying diameters (Liu *et al* 2020), the use of jets with different impingement velocities (Bhukta *et al* 2019), and the different jet orientations i.e. Longitudinal horizontal (Bhukta *et al* 2019), lateral horizontal (Masip *et al* 2012), multiple jets (Bhukta *et al* 2023) and use of steady suction/ blowing techniques (Chen *et al* 2013) were used over the past decades. Besides dual parallel wall jets issued from two nozzles in vertically upward directions are also



**Paper ID: ICERTSD 210**

**Modulation of recirculation zone behind a square obstruction by single inclined turbulent wall jet with varying angle of attack.**

Manas Kumar Bhukta<sup>\*</sup>, Santosh Kumar Singh, Kaustav Debnath and Snehamoy Mazumder

<sup>\*</sup>Department of Mechanical Engineering, Haldia Institute of Technology, Haldia-721657,  
India

manasbhukta14@gmail.com

**Abstract**

The modulation of the recirculation region is one of the primary interests of this numerical study. This study investigates the modulation of the recirculation zone behind a square obstruction by a single inclined turbulent wall jet with varying angle of attack. The flow field is visualized using the post processing system of the simulation software and the results have been analyzed. The experiments are carried out for different angles of attack of the wall jet and a range of high Reynolds number. The results show that the recirculation zone is significantly affected by the angle of attack of the wall jet. The maximum length of the recirculation zone decreased with increasing angle of attack. The wall jet angle of attack also affects the strength and position of the vortex structures in the recirculation zone. The results of this study provide insights into the use of inclined wall jets for controlling the flow field behind obstructions in engineering applications such as flow control and mixing enhancement. The numerical simulation is based on two-phase volume of fluid (VOF) model with open channel boundary conditions. The standard k- $\epsilon$  two equation turbulence model is applied to solve the Reynolds averaged equation.

**Keywords:** Open channel, submerged cube, turbulent jet, Reynolds number, numerical simulation.

# Author's Biography

---

---

*Manas Kumar Bhukta* is a *Ph.D* scholar from the Department of Mechanical Engineering, Jadavpur University Kolkata. He completed his M.Tech degree in Applied Mechanics from *IEST* Shibpur during 2014 – 16. He is presently working as an Assistant Professor in the Department of Mechanical Engineering, Haldia Institute of Technology, Haldia.

## Contact Information

Permanent Address: Vill-Srikrishnapur, PO-Bikrampur, PS- Debra, PIN-721136, India.

Mobile: +91-7044063413

Email: [manasbhukta14@gmail.com](mailto:manasbhukta14@gmail.com)

## Research Interests

My research interest centers on the experimental and numerical investigation of suction effects on flow patterns around obstacles, focusing on understanding the underlying flow physics, optimizing design parameters, and enhancing flow control strategies for practical applications.

---

## Education

**Doctor of Philosophy (Ph.D)**, Mechanical Engineering

Jadavpur University, Kolkata, India

Thesis title: Modulation of re-circulation zone behind a submersed square Obstruction by different turbulent controlling forces

**Master of Technology (M. Tech)**, Engineering Mechanics, Specialization: Fluids Mechanics (Marks obtained: 69%) 2016

Indian Institute of Engineering Science and Technology, *IIST* Shibpur, India

Thesis title: Modulation of Re-circulation Zone behind a Cubical Obstruction by Turbulent Plane Jet

**Bachelor of Technology (B-Tech)**, Mechanical Engineering 2009

Haldia Institute of Technology (Marks obtain: 62.40%)

**12th**, from W. B. C. H. S. E (Marks obtained: 74.80%) 2005

**10th**, from W. B. S. E (Marks obtained:67.37%) 2002

## Awards & Honours

- Secured 439 Score in Mechanical engineering GATE 2013.

## Teaching Experience

**Assistant Professor**, Mechanical Engineering Department, Haldia Institute of Technology, Haldia. 2016-present

## Industrial Experience

**ENGINEER**, Mechanical Maintenance, Welspun Corp. Ltd, Mandya, Bengaluru 2009-2013